THE UNIVERSITY OF MICHIGAN
COLLEGE OF ENGINEERING
Aeronomy Program

Michigan Airglow Observatory Report No. 2

A THEORETICAL AND EXPERIMENTAL STUDY OF THE STABLE MID-LATITUDE RED ARC (SAR-ARC)

Raymond G. Roble

ORA Projects 08622 and 08953

under contract with:

NATIONAL SCIENCE FOUNDATION
GRANT NO. GA-1025 and GA-788
WASHINGTON, D. C.

administered through:
OFFICE OF RESEARCH ADMINISTRATION ANN ARBOR
March 1969

ACKNOWLEDGEMENTS

The author wishes to express his appreciation to Professors Paul B. Hays and Andrew F. Nagy for their guidance and assistance throughout this study. The author appreciates stimulating discussions with various members of his committee, Professors Leslie M. Jones, Gordon G. Shepherd, and Aksel Wiin-Nielsen, and would like to express his gratitude for their helpful suggestions.

In the development and construction of the Airglow Observatory the author is grateful to Messrs. H. A. Brooks, J. R. Cutler, S. J. Eberbach, E. Kaiser, H. Henry, G. Marsh, R. Pelkey, A. N. Shah, and V. Soden for their contributions.

Conversations with members of the High Altitude Engineering Laboratory, Messrs. L. Chaney, W. Hansen, L. Loh, H. Reichle, H. Schulte, E. Schaefer, and members of the Space Physics Research Laboratory, Drs. E. Fontheim, R. Stolarski, and Messrs. B. Campbell, D. Jones, G. Poole, W. Silvis, and R. Simmons, to name only a few were of great assistance.

Helpful colloquy with Professors K. D. Cole, J. Noxon, M. H. Rees, and J. C. G. Walker, Drs. M. Gadsden and G. Hernandez, and Messrs. E. Marovich and C. Purdy is also much appreciated.

In addition the author wishes to express his thanks to Mrs. M. Boissonneault, Mrs. L. Deakin, and Mrs. P. Burris for typing the drafts and the final manuscript and to Mr. J. Olivero for his review and suggestions.

The author is grateful to the National Science Foundation for support during the last two years by NSF grants GA-788 and GA-1025.

TABLE OF CONTENTS

LIST OF TABLES

LIST OF FIGURES

Figure Page

Figure Page

Figure Page

LIST OF SYMBOLS

a	half-width at half-height of the Airy function
$a(z)$	coefficient defined in equation (5-4)
A	collecting area of the photometer
$A(x)$	Airy function defined in equation (7-7)
A_D	Einstein level coefficient
A_i	ion mass in a. m. u.
A_n	Fourier coefficient defined in equation (7-36)
A_λ	Einstein transition coefficient
A_o	constant used in equation (7-36)
$B(\sigma)$	source function of an emission line
C	background level of recorded fringe profile
$\bar{C}_c$	mean value of the standard light spectral characteristics
$\bar{C}_s$	mean value of the filter transmission function
$C(\lambda)$	standard light spectral characteristics
C_p	specific heat of neutral gas at a constant pressure
$\frac{d}{dt}(\ )$	total derivative
d_f	half-width at half-height of the spherical defect function
d_g	half-width at half-height of the gaussian surface defect function
D	constant defined in equation (7-10)
$\vec{D}$	ion drag force
$D_f(x)$	spherical surface defect function
$D_g(x)$	gaussian surface defect function
$D_{x,y}$	x and y components of the ion drag

$\vec{E}$	viscous drag force
$E(\lambda_o)$	emission line intensity
$\bar{E}_c$	constant spectral intensity of the nightglow continuum
$E_c(\lambda)$	spectral intensity of the nightglow continuum
$E_{x, y}$	x and y components of the viscous drag
f	(in Chapter 6) coriolis parameter $(2\Omega \sin \theta)$
f	(in Chapter 7) half-width at half-height of the aperture function
F	focal length of the objective lens
F(x)	aperture function
g	half-width at half-height of the doppler source profile
$\vec{g}$	acceleration of gravity
g_{120}	acceleration of gravity at 120 km
G(x)	doppler source function
G_o	a constant defined by equation (7-16)
$G(\sigma)$	spectral density of a radiation source
h	a constant defined in equation (7-22)
$H(z, T_e)$	neutral heating function defined in equation (A-23)
$\bar{H}^*(z)$	gaussian neutral heating function defined in equation (C-3)
H_m	peak value of the gaussian profile used in equation (C-1)
$\vec{i}$	eastward directed unit vector
I	magnetic dip angle
$\vec{j}$	northward directed unit vector
k	(in Chapters 5 and 6) a constant defined in equation (5-12)
$\vec{k}$	(in Chapter 6) upward directed unit vector
k	(in Chapter 7) a constant relating the index of refraction to the pressure, $\mu = 1 + kp$

k^*	Boltzmann constant
$K^1(z)$	coefficient defined in equation (A-25)
K_e	thermal conductivity of the electron gas
K_{ee}	thermal conductivity of a completely ionized gas
K_{en}	thermal conductivity due to collisions of electrons with neutral particles, defined in equation (A-4)
K_n	thermal conductivity of the neutral gas
KR	kilorayleighs
L( )	loss rate of electrons with various atmospheric species
$L(z, T_e)$	energy loss processes in the electron gas
$L^*(z, T_n)$	the 63μ radiational loss term from the excited fine structure levels in the ground state of atomic oxygen
m	order of interference
m_i	molecular mass of constituent i
M	molecular weight of the emitting atom
m^*	a constant defined in section 7.2.3.1
n(x)	number density of atmospheric species x
n^*	a constant defined in section 7.2.3.1
N_{D_f}	spherical defect finesse
N_{D_g}	gaussian surface defect finesse
N_f	aperture finesse
N_i	number density of the ion gas
N_n	number density of the neutral gas
N_R	reflective finesse
n(i, z)	number density of i^{th} atmospheric species at altitude z
$\overline{P}$	constant spectral response of the photomultiplier

$P(\lambda)$	spectral characteristics of the photomultiplier tube
q	fraction of $O(^1D)$ atoms quenched
$Q(y, z)$	SAR-arc neutral heating function
Q'	non-adiabatic heating rate per unit volume
Q^*	non-adiabatic heating rate per unit mass
$\overline{Q}(y, z)$	assumed neutral heating function used in section (6.3)
$\overline{Q}^*(y, z)$	effective heating function defined by the sum of the assumed neutral heat input $\overline{Q}(y, z)$, and the heating and cooling resulting from the adiabatic terms in the thermodynamic equation
$Q_e(z)$	local electron heating
$Q_o(z)$	neutral heating required to maintain the thermospheric temperature profile
p	pressure
R	(in Chapter 7) reflectivity of the coated etalon plates
R	(in Chapter 6 and Appendix A) neutral gas constant
R_e	(in Appendix A) radius of the earth
s	(in Chapter 7) full width of doppler line at half-intensity points
s	(in Appendix A) variable defined in equation (A-16)
S_D	collisional deactivation coefficient
S_{cc}	calibration signal of the continuum filter
S_{cs}	night sky signal from the continuum filter
S_D	dark signal of the photomultiplier tube
S_{sc}	emission line filter calibration signal
S_{ss}	sky signal from emission line filter
t	(in Chapter 7) etalon plate spacing
t	(in Chapters 5 and 6) time

T	(in Chapter 7) transmission of etalon plate coatings
$T_B(z)$	basic thermospheric temperature profile defined in equation (A-17)
T_e	electron temperature
T_i	ion temperature
T_n	temperature of the neutral gas
$T_1(\lambda)$	emission line filter transmission function
T_{120}	neutral gas temperature at 120 km
T_∞	exospheric temperature
$T(\lambda)$	transmission function of the continuum filter
u	zonal component of the neutral wind, x-direction
U	light gathering power
v	meridional component of the neutral wind, y-direction
$\vec{V}$	neutral gas velocity vector
$\vec{V}_i$	velocity of the ion gas
$\vec{V}_n$	velocity of the neutral gas
V	potential defined in equation (C-2)
w	(in Chapters 5 and 6) vertical component of the neutral wind,
w	(in Chapter 7) half-width of the instrument function
W_o, W_1, W_2	statistical weights for the excitation energies of the ground state of atomic oxygen; equation (5-8)
$W(\sigma)$	Fabry-Perot instrument function
x	(in Chapter 6) east-west direction in a Cartesian coordinate system
x	(in Chapter 7) phase difference, defined in equation (7-8)
x	(in Appendix C) $= (z' - z_m) / \delta$; equation (C-17)
y	(in Chapter 6) north-south direction in a Cartesian coordinate system
y	(in Appendix A) variable defined in equation (A-26)

$Y(x)$	recorded function of the Fabry-Perot interferometer
$Y(\sigma)$	recorded function of the Fabry-Perot interferometer as a function of wavenumber
$Y^*(x)$	measured fringe profile
Y_m	total Fourier transform of recorded fringe profile
Y_{cm}	Fourier cosine transform of recorded fringe profile
Y_{sm}	Fourier sine transform of recorded fringe profile
z	vertical height direction in a Cartesian coordinate system
α	(in Appendix C) semi -major axis of an ellipse
α	(in Appendix A) thermal diffusion coefficient
α	(in Chapter 7) angle subtended by the aperture from the etalon plates
$\bar{\alpha}$	constant defined in section 7.2.2
β	semi-minor axis of an ellipse
γ	(in Chapter 7) a constant defined in equation (7-39)
γ	(in Appendix C) axis of an ellipsoidal level layer in equation (C-8)
γ'	constant defined in equation (A-18)
γ_{en}	electron-neutral collision frequency
δ	(in Chapter 7) phase difference
$\delta_{1,2}$	e-folding distance for gaussian profile used in equation (C-1)
δp	$p_i - p_{i-1}$, the pressure difference for the i^{th} step
$\delta\sigma$	effective limit of resolution of a Fabry-Perot interferometer
$\delta(\ )$	Dirac function
$\Delta\sigma$	free spectral range of the Fabry-Perot interferometer
Δp	pressure difference for the free spectral range

Δt	(in Chapter 7) sampling time of Fabry-Perot interferometer
Δt	(in Chapter 5) conduction time constant defined in equation (5-9)
$\Delta T_n(z)$	$T_n(z) - T_B(z)$, as used in equation (5-9)
Δx	free spectral range in units of optical path
∇^2	Laplacian
ϵ	ratio of semi-major to semi-minor axes used in equation (C-3)
$\epsilon_{o,\ 1,\ 2}$	excitation energies of the ground state of atomic oxygen; equation (5-8)
ξ	geopotential altitude
θ	(in Chapter 7) incident angle of radiation
θ	(in Chapter 6) the geographic latitude
ζ	root of equation (C-18)
ζ'	root of equation (C-19)
ζ^*	variable defined in equation (C-18)
ζ'^*	variable defined in equation (C-19)
λ	(in Appendix C) a parameter defined in equation (C-8)
λ	(in Chapter 7 and 8) wavelength of optical emission
λ	(in Chapter 6) ion drag parameter defined in equation (6-12)
μ	(in Chapter 7) optical index of refraction
μ	(in Chapter 6) kinematic viscosity
ν_i	ion-neutral collision frequency
$\pi(x)$	function defined in equation (7-12)
ρ	density of neutral gas
ρ_i	ion density
ρ_n	neutral density

σ	(in Chapters 7 and 8) wavenumber of radiation
σ	(in Appendix A) variable defined in equation (A-16)
λ_m	wavelength for constructive interference
$\sigma(y, z)$	charge distribution used in equation (C-2)
τ_A	transmission coefficient that includes the effects of absorption and/or scattering of the reflective coatings
Φ	viscous dissipation function
$\phi(y, z)$	a term related to the neutral gas temperature increase given in equation (5-14)
$\psi(x)$	normalized output profile of the Fabry-Perot interferometer
Ω_1	field of view of the photometer
Ω'	Fabry-Perot interferometer field of view
Ω	the rate of rotation of the earth
Ω^*	solid angle associated with the resolvance of the Fabry-Perot interferometer
$\mathcal{R}$	resolving power of a Fabry-Perot interferometer
$\partial(\ )$	partial derivative
$\langle \delta Y^2 \rangle$	parameter defined in equation (7-38)

ABSTRACT

The stable mid-latitude red arc (SAR-arc) is theoretically and experimentally examined in order to determine the nature of the arc and its role as a neutral gas heat source in the upper atmosphere during geomagnetic storms.

The SAR-arc is considered to be excited by energy flowing from the magnetosphere down along the geomagnetic field lines into the ionosphere. The energy heats the ambient F-region electrons which in turn excite the ^1D state of atomic oxygen by electron impact and gives rise to the 6300 Å emission characteristic of the SAR-arc. The electron heat conduction equation in the F-region of the ionosphere is solved for various heat flows from the magnetosphere in order to determine the atmospheric and ionospheric conditions and energy requirements for red arc formation. The electron temperature, ion temperature, 6300 Å emission rate, and neutral heating height profiles are determined and related to SAR-arc intensity. A two-dimensional model of the SAR-arc is constructed and the neutral heating rates for this model are used to calculate the neutral temperature increase and the atmospheric winds generated by the arc. The results indicate that a large thermal cell develops within the arc region and the peak neutral gas temperature increase within the arc is less than 70° K for a 10 kilorayleigh SAR-arc. The calculated circulation pattern generated by the SAR-arc is shown to produce certain atmospheric and ionospheric effects which are found to agree well with direct measurements made on satellites.

Two optical instruments were constructed to study the SAR-arc and the normal nightglow. The first instrument, a 6'' diameter Fabry-Perot interferometer was designed to measure the 6300 Å doppler temperature of atomic oxygen. The second instrument is an interference filter photometer which alternately positions 6 interference filters over a telescope and measures the intensity of various emission lines in the night sky. The theory, design, construction, performance tests, and data reduction procedure for both instruments are presented.

The observational results of the SAR-arcs of October 30/31 and October 31/November 1, 1968 are presented. The structure, intensity, and position of the SAR-arc were determined from photometer scan measurements which show that the arc was stable, persisted for more than 12 hours, moved southward during the night, and extended across the eastern part of the United States slightly tilted to lines of constant magnetic L-shells. The results of the doppler temperature measurements made by the Fabry-Perot interferometer show no measurable neutral gas temperature increase within the arc in agreement with the theory developed.

The satellite observations on the September 28/29, 1967 SAR-arc are used to theoretically calculate the structure of the arc. The calculated height of the peak emission, the total intensity, and the cross-sectional structure of the arc are in agreement with the ground based observational data.

I. INTRODUCTION

The stable mid-latitude red arc (SAR-arc) was first observed in the night sky by Barbier in 1957 from Haute Province in southern France (Barbier, 1958, 1960). During a geomagnetic storm he noted that his 6300 Å photometer, while performing almucanter scans at a fixed angle above the horizon, occasionally showed two conspicuous regions of enhanced brightness. The enhanced brightness was caused by what appeared to be a homogeneous arc of apparently monochromatic 6300 Å emission roughly aligned in an east-west direction. The arcs were unusual, because they occurred at mid-latitudes, well south of the auroral zones; they were also stable and generally persisted throughout the night quite unlike the more common aurora. Soon after this discovery, observers in Australia and the United States (Roach, Barbier, and Duncan, 1962) confirmed the existence and world-wide extent of these arcs. Barbier (1958) has summarized the morphology of these arcs thus: "At the time of a very strong auroral perturbation, a red arc is probably formed in the zone of maximum activity and shifts toward the south; it is then checked and becomes stationary at a latitude which is slightly higher than 45^{o} (geomagnetic), then later it disappears slowly in place without spreading and remaining unaffected by later recurrence of auroral activity."

There are many morphological features of the SAR-arc which suggest that the arcs are an optical manifestation of a slow leakage of energy from some vast reservoir of energy stored during a geomagnetic storm.

Strong geomagnetic control over these arcs is clearly indicated by the fact that they are observed during periods of increased magnetic activity and that their intensity increases with the magnetic activity index. Cole (1965) suggested that the SAR-arc is the major sink of energy for the magnetospheric ring current generated during a geomagnetic storm. He postulates that the energy of the energetic particles causing the main phase decrease, D_{st}, of the geomagnetic storm is transferred to the ambient low temperature plasma in the magnetosphere by coulomb collisions. The energy is then conducted down along the field lines, heating the F-region electrons which then in turn excite the atomic oxygen to the ^1D state leading to the 6300 Å emission which is characteristic of the SAR-arc. The magnetospheric processes responsible for the SAR-arc will not be examined in this thesis. Instead, the observed properties of the arc in the ionosphere are used to critically evaluate the various possible source mechanisms which lead to a self-consistent theory of the SAR-arc.

Walker and Rees (1968) have examined the four excitation hypotheses which have been suggested in the literature as the source of the SAR-arc and they have defined the conditions by which the arc forms for each mechanism. Only those mechanisms which are based upon the excitation of atomic oxygen to the ^1D state by thermal electron impact were considered because of the predominant 6300 Å emission associated with the arc. Their results indicate that the arc is most likely caused by a hot F-region electron gas which is heated by energy flowing from the magnetosphere.

Walker and Rees (1968) have examined this mechanism for the one-dimensional case in order to specify the energy requirements for arc formation. In this thesis, the two-dimensional structure of the SAR-arc is investigated and the optical data of Tohmatsu and Roach (1962) on the structure of the arc is used to construct a SAR-arc model according to the thermal conduction hypothesis in such a manner that the calculated and observed properties of the arc are in agreement. One of the characteristic features of the thermal conduction model is the hot-electron gas in the F-region of the ionosphere which is required to excite and sustain the SAR-arc during the geomagnetic storm. The hot electron gas is ultimately coupled to the neutral component of the atmosphere and in this study particular emphasis is placed upon the energy exchange and atmospheric response caused by this interaction.

Jacchia and Slowey (1964) have shown that significant over-all temperature changes occur in the upper thermosphere during times of geomagnetic storms. The contribution of the SAR-arc to this atmospheric heating process is investigated to determine the extent to which it is responsible for the observed thermospheric heating during the storm.

The neutral gas temperature is a significant parameter in determining the properties of the atmosphere and the instrumentation aboard geophysical satellites is not well suited to study the important question of neutral heating within the SAR-arc. One method of determining the neutral exospheric temperature is to measure the doppler broadening of the atomic oxygen red line.

Doppler temperature measurements made during quiet and disturbed conditions enables one to investigate the physical state of the upper atmosphere. These measurements reveal the atmospheric response to the complex interaction between the ionized and neutral components of the atmosphere. Therefore, ground based instruments which are capable of locating and making doppler temperature measurements of various optical emission regions of the night sky were built and these instruments were used to study the atmospheric response to the SAR-arc.

The theoretical and experimental investigation of the SAR-arc carried out leads to a self-consistent model of the arc which adds considerably to our understanding of this geophysical phenomenon which is associated with our planet.

II. OBSERVED SAR-ARC FEATURES

The observed features of the SAR-arc have been reported in the literature by several authors, Roach and Roach (1963), Megill and Carleton (1964), Cole (1965), Cruz, et. al. (1965), and Marovich (1966). The main features of the arc are summarized in this chapter for completeness and later reference.

The SAR-arcs have been observed to have the following properties:

1. The arcs generally occur in mid-latitudes, as shown in Fig. 1 (Roach and Roach, 1963), are stable, homogeneous, several hundred kilometers wide in the meridional direction, and extend from 300-700 km in height. Current evidence indicates that the arcs extend in longitude around the night side of the globe and even possibly around the earth (Roach, Barbier, and Duncan, 1962; Marovich and Roach, 1963) although no observations have been made to date on the day side. A meridional cross-section of the normalized 6300 Å intensity contours for a typical SAR-arc is shown in Fig. 2 (Tohmatsu and Roach, 1962).
2. The SAR-arc appears to be monochromatic with the wavelength of emission at 6300 Å. The 6300 Å emission is caused by the atomic oxygen transition from $O(^1D)$ metastable state to the ground state $O(^3P)$ with a transition probability of 0.0091 sec^{-1}. The other major emission lines observed in the aurora are not enhanced in the SAR-arc. The normal intensity ratio between the 6300 Å line and the 5577 Å line, which is the atomic oxygen transition from the $O(^1S)$ metastable state to the $O(^1D)$ state, is of the order of 50:1 in a SAR-arc (Roach and Roach, 1963). The excitation energies of the $O(^1D)$ and $O(^1S)$ states are 1.96 ev and 4.17 ev respectively; therefore the lack of 5577 Å emission implies

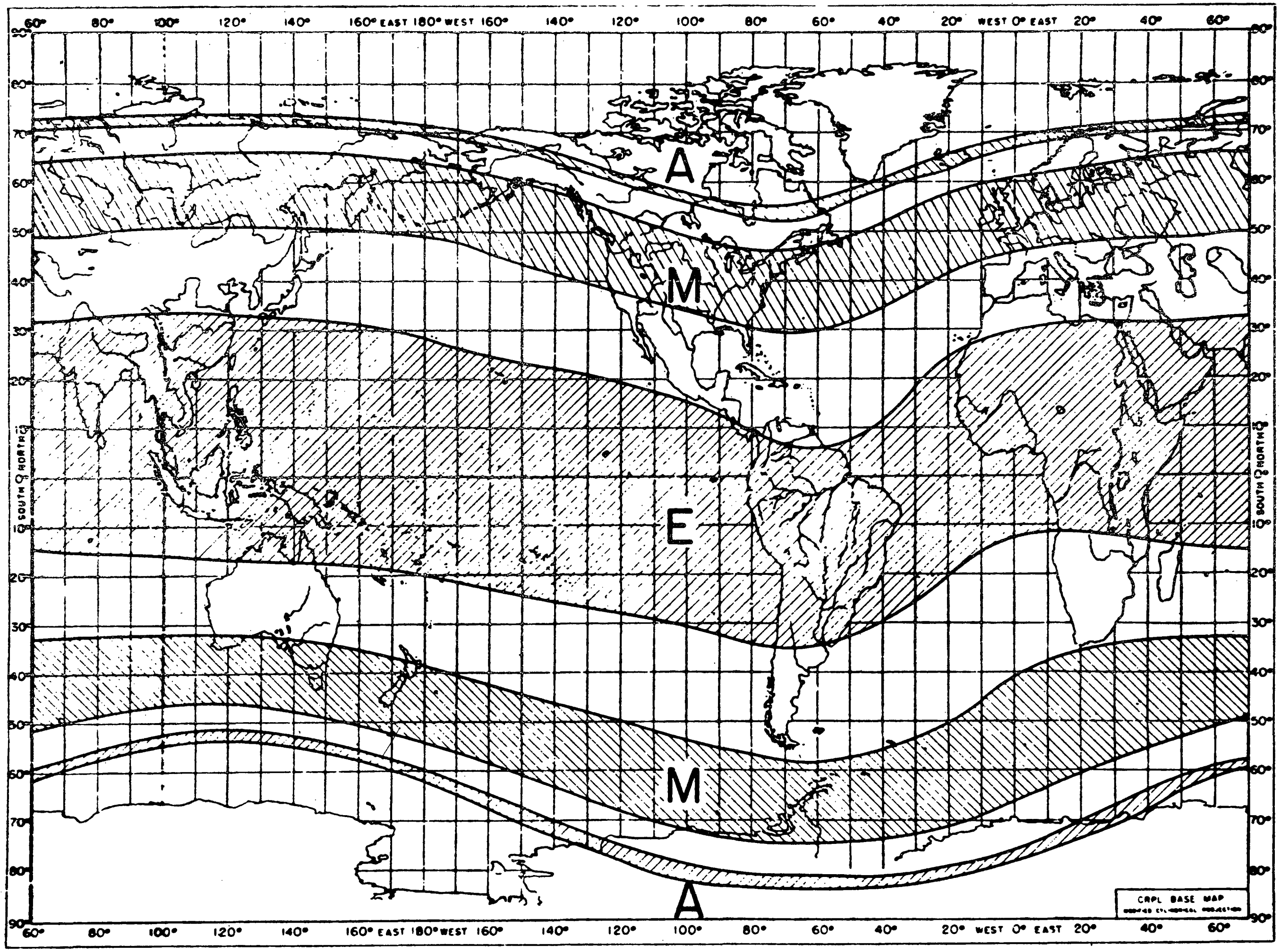

FIG. (1) ZONES OF CHARACTERISTIC 6300 Å ACTIVITY,
M REGION CORRESPONDS TO STABLE MID-LATITUDE RED ARC

Fig. 1. Zones of characteristic 6300Å activity, M region corresponds to Stable Mid-Latitude Red Arc (Roach and Roach, 1963).

a low energy source acting within the SAR-arc. There has also been no definite spectroscopic evidence to indicate an enhancement of the NI 5199 Å line (Carelton and Roach, 1965).

3. The absolute intensity of the SAR-arc ranges from several hundred Rayleighs to tens of kilorayleighs with the mean, during the last solar cycle maximum, being 6 KR. The arcs are subvisual because the sensitivity of the human eye is relatively weak at this wavelength. However, the arc may become perceptible at an intensity of 10 KR and a color impression becomes apparent at about 30 KR.

4. The lifetime of the SAR-arc is generally of the order of 10 hours or more.

5. The frequency of SAR-arc occurrence appears to follow the solar cycle. During the last solar cycle maximum, in 1958, Marovich (1966) reported SAR-arcs on 20% of the observing nights at Fritz Peak, Colorado. The frequency of the arcs has decreased following solar cycle maximum, and from about 1963 to 1967 no arcs have been reported from any of the geophysical observatories. SAR-arcs reappeared in September 1967, (Hoch, Marovich, and Clark, 1968) but up to the present time the number of arcs observed is considerably less than for the previous solar cycle. This is not too surprising because the solar activity for this solar cycle maximum is relatively low and there is a definite positive correlation between the occurrence of a SAR-arc and the solar activity (Roach and Roach, 1963).

6. The arcs are magnetically controlled and are, therefore, oriented along magnetic rather than geographic latitudes. They occur simultaneously in both the northern and southern hemisphere, indicating a conjugate phenomenon. (Reed and Blamont, 1968). They have been

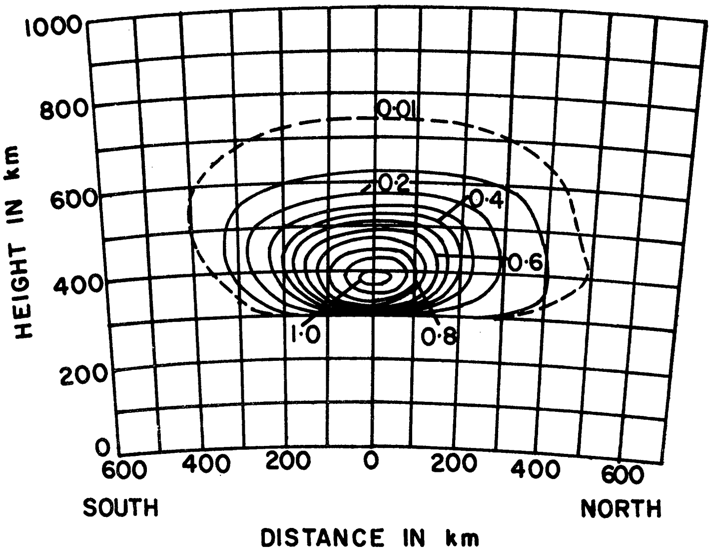

SAR-ARC 6300Å INTENSITY CROSS-SECTION

Fig. 2. Normalized 6300 Å isophotal representation of a SAR-arc cross-section (Tohmatsu and Roach, 1962).

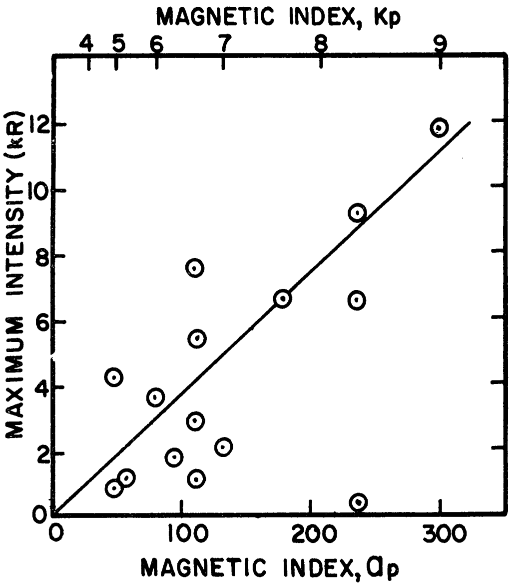

SAR-ARC INTENSITY VS MAGNETIC INDICIES

Fig. 3. Correlation between the maximum intensity of SAR-arcs and the magnetic indicies K_p and a_p (Roach and Roach, 1963).

observed in L shells 2 to 4, which lie approximately between geomagnetic latitudes of 40-60^o; the L shell on which they appear generally decreases with increasing magnitude of the geomagnetic storm. The arcs are observed only during periods of increased magnetic activity and the relationship of the arc intensity with the magnetic indices K_p and a_p is shown in Fig. 3.

Rees and Akasofu (1963) have called attention to a positive correlation between the magnetic storm parameter D_{st} and the SAR-arc intensity. D_{st} is the horizontal component of the storm time disturbance field, averaged over all local-time longitudes around a circle of geomagnetic latitude. Most of the D_{st} field change during the main phase of a magnetic storm may be attributed to a westward flowing ring current encircling the earth at several earth radii and this ring current field is the only storm-time field which has a time constant similar to that of the SAR-arc.

7. During large magnetic storms the SAR-arcs first appear south of the auroral zone against an auroral background in the north. The arcs, however, do not show any major changes in intensity when the polar aurorae to the north break up with rapid and large fluctuations in intensity (Roach and Marovich, 1959, 1960). The SAR-arc usually moves south to mid-latitudes where it persists throughout the night long after the aurora to the north has disappeared.

8. The mean height of the peak intensity of the SAR-arc occurs near 400 km (Roach and Roach, 1963). The height of an individual arc is determined from triangulation measurements performed simultaneously from two or more observing stations (Roach, et. al. 1960; Moore and Odencrantz, 1961; Hoch, Marovich, and Clark, 1968). Rees (1963),

using a method of obtaining both height and geographical position from a single station, studied 9 SAR-arcs observed at Fritz Peak, Colorado, and found heights varying from 390 to 560 km with an indication of greater heights for the more northerly arcs.

9. In the northern hemisphere the arc usually, but not universally, moves north to south at rates between 4 and 50 m/sec with the maximum observed rate at about 87 m/sec, (Roach and Roach, 1963). In certain cases multiple arcs form along different magnetic invariant latitudes and in these cases the southerly arcs are more stable.

10. The scintillation of radio stars viewed through the SAR-arc is highly correlated with the brightness of the arc (Roach and Roach, 1963).

11. During the last solar cycle maximum, when most of the SAR-arc observations were made, electron density height profiles within the SAR-arc could only be determined from ionosonde data. In general, the ionograms obtained during times of the SAR-arc were difficult to analyze due to spread-F, indications of more than one layer, oblique echoes, and generally confusing traces. In spite of these difficulties, King and Roach (1961) and Walker and Rees (1968) were able to deduce electron density profiles for the region within the SAR-arc.

King and Roach (1961) were able to obtain an electron density profile for the arc which appeared on November 28/29, 1959. The arc was centered some 200 km north of the ionosonde station but by comparing the vertical reflections and the oblique echo, which were received from a large irregularity in the F-layer near the region of the arc, they were able to conclude that: a) the critical frequency for the oblique echo is lower than for the overhead reflection, indicating a lower peak electron density in the arc than in the ionosphere adjacent to the arc, and b) the spread of the oblique echo is greater, suggesting that the reflection is due not to a simple reflecting layer but rather to a complex irregular region.

Walker and Rees (1968) have taken advantage of the proximity of the Fritz Peak Airglow Observatory to the Boulder ionosonde station to examine six ionograms, obtained when SAR-arcs were directly overhead. Their analysis showed that the bottomside ionograms for faint SAR-arcs yielded maximum electron densities which were not significantly different from undisturbed conditions, although there is some suggestion that the altitude of the maximum is usually high in the arcs. For the case of an arc exceeding an intensity of 1 KR the ionogram proved to be difficult to analyze. As a result of their study, they established an electron density profile representative of a faint SAR-arc by using ionogram readings between 260-400 km, an average nighttime profile below 260 km, and an extrapolated profile above 400 km with an appropriate scale height. The resulting profile is shown in Fig. 5.

The features of the SAR-arc listed above were determined from ground based measurements made on arcs which occurred during the last solar cycle maximum. The satellites in orbit at that time were not equipped with the proper instruments to effectively probe the topside structure of the arc. There are now a number of satellites in orbit which have the capability to determine the topside structure of the SAR-arc. However, because of the relatively low solar activity for the present solar cycle maximum, only a few arcs have been observed. Still some important satellite observations have been made on the SAR-arc and they include the following items:

12. Reed and Blamont (1968) have observed the conjugate nature of the September 28/29, 1967, SAR-arc with photometers aboard the OGO-B satellite. The arcs were observed to be oriented approximately along constant L-shells in conjugate hemispheres and they extended in longitude over the entire night portion of the globe.

13. Norton and Findlay (1969) obtained a topside sounding, during the SAR-arc which occurred on September 28/29, 1967, from both the Alouette I and II satellites and found an electron density depression in the vicinity of a SAR-arc while passing over it in a north-south direction. The topside ionogram also showed traces which could be interpreted as oblique echoes from slant electron density gradients.

14. Norton and Findlay (1969) have also observed a significant increase in the electron temperature at 1800 km measured by the Alouette II satellite as it passed over the arc. The region of the increased electron temperature was directly over the SAR-arc and it was broad enough to overlap the electron density depression lying just to the north of the enhanced 6300 Å emission. Satellite passes occurring before and after the observed SAR-arc do not reveal the increased electron temperature. Therefore, it appears likely that the increased electron temperature is related to the SAR-arc excitation mechanism.

In the next chapter the proposed excitation mechanisms of the SAR-arc are examined.

III. REVIEW OF PROPOSED EXCITATION MECHANISMS FOR A SAR-ARC

In this chapter the various excitation mechanisms which have been suggested for the SAR-arc are reviewed. These mechanisms are the recombination hypothesis, the electric field hypothesis, the soft electron flux hypothesis, and the thermal conduction hypothesis.

3.1 RECOMBINATION HYPOTHESIS

King and Roach (1961) have suggested that the SAR-arc is excited by increased dissociative recombination in the ionosphere. They have studied a SAR-arc which occurred on the night of November 28/29, 1959. Photometric data for this arc were obtained from the Fritz Peak Geophysical Observatory located near Boulder, Colorado, where observations were made with a birefringent filter photometer in three colors: the 5577Å and the 6300 Å lines of atomic oxygen, and the 5893Å line of sodium. Ionograms were obtained for the same arc from an ionosonde station at Boulder, 26km from the airglow observatory. From the ionosonde data King and Roach, (1961) were able to deduce an electron density profile in the near vicinity of the SAR-arc. They considered dissociative recombination of atomic oxygen in the F-region as the source of the 6300Å emission line and determined the atmospheric conditions which were necessary to excite the SAR-arc to the observed levels. The two important reactions which occur in the F-region and are capable of exciting atomic oxygen to the ^1D level are (Peterson, Van Zandt, and Norton, 1966)

$$\left.\begin{array}{l} O_2+O^+ \rightarrow O_2^++O \\ O_2^++e \rightarrow O+O \end{array}\right\} \quad +6.96\ \text{ev} \qquad (3\text{-}1)$$

and

$$\left.\begin{array}{l} N_2+O^+ \rightarrow NO^++N \\ NO^++e \rightarrow N+O \end{array}\right\} \quad +2.75\ \text{ev} \qquad (3\text{-}2)$$

Reaction (3-1) is sufficiently energetic to also excite the O(^{1}S) state of atomic oxygen giving rise to the 5577 Å green line (Hays and Walker, 1966). This line was not enhanced in the SAR-arc and therefore reaction (3-1) appeared as an unlikely candidate for the excitation mechanism. King and Roach (1961) have argued that reaction (3-2) is capable of exciting the 6300 Å line but not the 5577 Å and, therefore, this reaction is a likely mechanism if, by some means, a 400 fold increase over the normal concentration of N_2 takes place. They suggest that this increase in the N_2 density at high levels is due to a combination of enhanced heating and mixing during times of magnetic activity. Any increase in reaction (3-2) cannot be due to an increase in the electron density because the data obtained from the ionogram indicated a decrease of electron density within the arc.

There are two important reasons why this hypothesis appears unlikely. Rees (1962) has pointed out that in order that reaction (3-2) proceed at the rate suggested by King and Roach (1961), the F-region would have a characteristic lifetime of a mere 500 seconds instead of the observed lifetime of $1.4\text{x}10^4$ seconds. The second reason is that reaction (3-2) for the production of O(^{1}D) states is spin forbidden, (Dalgarno and Walker, 1964) and therefore it has a low reaction rate. These two strong arguments and the requirement of a 400 fold increase in the N_2 number density make the recombination hypothesis an unlikely candidate for the sole excitation mechanism responsible for the SAR-arc.

3.2 ELECTRIC FIELD HYPOTHESIS

Rees (1961), Megill, Rees, and Droppleman (1963), Megill and Carleton (1964), Megill and Van Zandt (1964), and Walker and Rees (1968) have all examined the mechanism of an electric field acting orthogonal to the geomagnetic field as an excitation source for the SAR-arc. In this mechanism an electric field perpendicular to the geomagnetic field lines provides sufficient energy to the ambient electrons in the ionosphere to excite the SAR-arc through collisions with atomic oxygen. The source of the electric field is not clear; however, it could conceivably be generated through the interaction of the rotating magnetosphere with the solar wind. The high conductivity along the magnetic field lines provides a good connection between the ionosphere and the magnetosphere, so that a transverse electric field applied anywhere across a given magnetic shell will also appear in the ionosphere.

Several mechanisms have been suggested by Megill and Carleton (1964) for the production of the electric field, and each requires a steady transport of charge perpendicular to the magnetic shells. The convective motions in the magnetosphere which cause the charge separation responsible for the electric field are not well defined and therefore, most authors assume that an electric field exists and then proceed to calculate the electron distribution function and the excitation rates of the atmospheric gases resulting from this field.

Rees and Walker (1968) have made a detailed study of the heating of ionospheric electrons by an electric field normal to the magnetic field, and later (Walker and Rees, 1968) applied the results to the question of the excitation of the SAR-arc. They have shown that, although there is some direct heating of the electrons, the major heating mechanism is due to elastic collisions of ions with electrons. The perpendicular electric fields heat the ions much more efficiently than the electrons, so that the ion temperature rises above the electron temperature over much of the lower ionosphere. Walker and Rees (1968) have solved the coupled electron temperature-ion temperature problem with allowance for heat conduction in the electron gas, but not the ion gas. The calculated electron and ion temperature profiles are shown in Fig. 4 for a range of assumed electric field strengths. This figure indicates extremely large ion temperatures especially at the lower altitudes. Since the ions transfer their energy to the neutrals through elastic and inelastic collisions, the high ion temperature implies a significant neutral heating. This heating would produce a large perturbation in the neutral atmosphere resulting in a large dynamic response and a significant increase in the neutral gas temperature. Walker and Rees (1968) have also shown that the volume emission rate height profiles, due to electric field heating, have a maximum near 350 km; independent of the magnitude of the field. This height is somewhat lower than the average height determined from observational data.

Cole (1965) has examined the data for some 19 SAR-arcs and found that the average time interval in which the atmosphere magnetically conjugate to the station observing the SAR-arc was sunlit is 3 hours and 5 minutes. During this time the sunlit conjugate E-region had considerably more ionization than the nighttime ionosphere of the station observing the SAR-arc. As a result, the electrical conductivity in the conjugate ionosphere is at least 400 times greater. An electric field of about 1 mv/cm is capable of exciting a small SAR-arc in the night hemisphere and, because of the good conductivity along the geomagnetic field lines, this electric field is also present in the conjugate hemisphere. Such a field would give rise to a magnetic bay of about 1400 γ in the conjugate geomagnetic field whereas in the nighttime ionosphere where the SAR-arc is present a magnetic bay of 3-4γ would occur. It appears unlikely that a magnetic bay of 1400γ in the sunlit hemisphere would go unnoticed, but yet no observation has been reported of such a disturbance occurring simultaneously with a SAR-arc. Current observational evidence does not support the atmospheric and ionospheric effects which would be caused by an electric field although the means of detecting the high ion

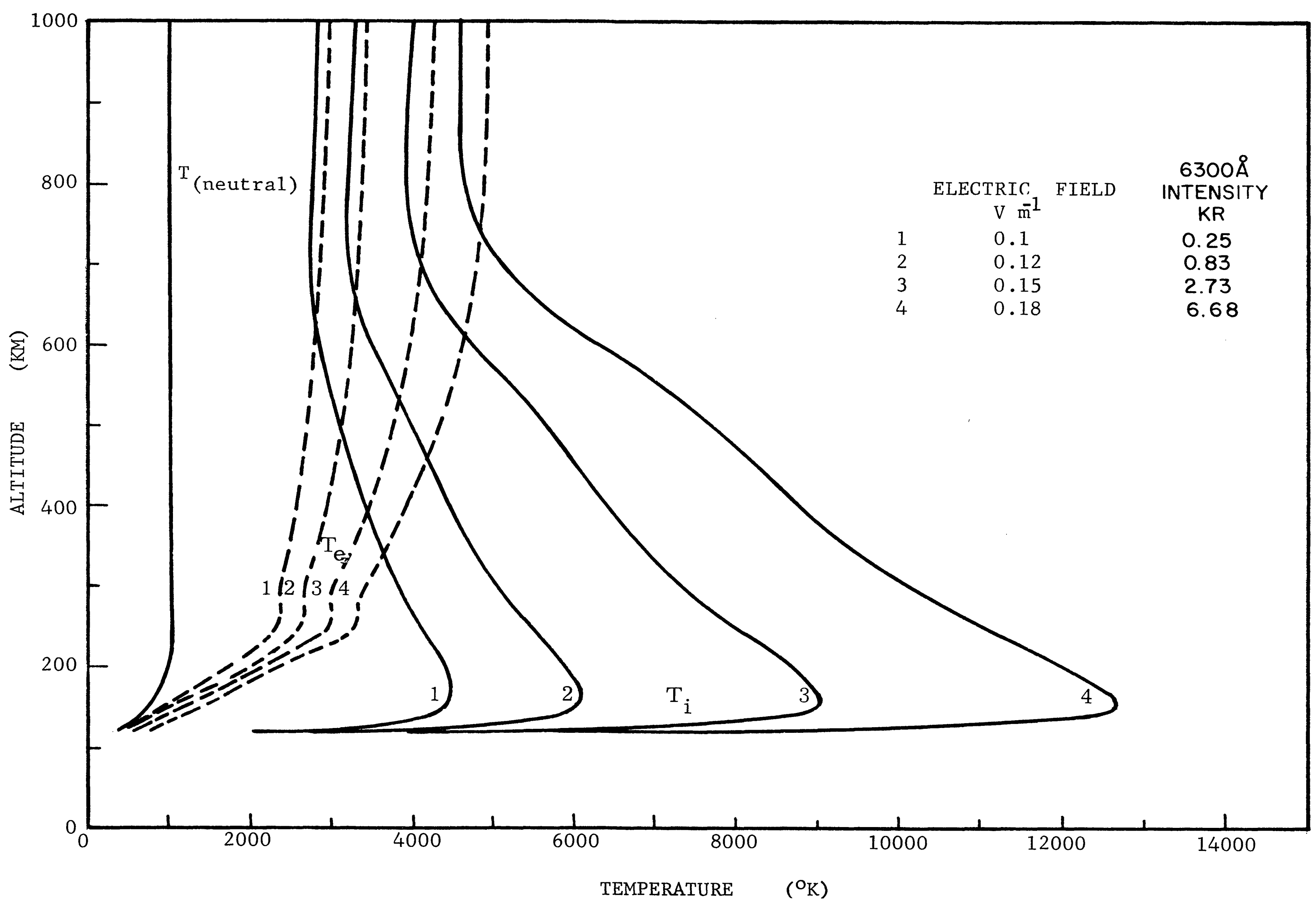

Fig. 4. Electron and ion temperature profiles which result from heating by a range of electric fields perpendicular to the magnetic field, (Walker and Rees, 1968).

and neutral temperatures were not available during the last solar cycle. It should be possible during the present solar cycle maximum to resolve the question of electric fields as an excitation mechanism by searching for high ion and neutral temperatures within the region of the SAR-arc, (see Chapter 8). It does appear unlikely that the very high ion temperatures resulting from the electric fields exist, and in view of the other arguments presented, electric fields are not likely to be the sole excitation mechanism responsible for the SAR-arc.

3.3 SOFT ELECTRON FLUX HYPOTHESIS

Dalgarno (1964) has postulated that an incident flux of electrons with an energy of about 400 ev is responsible for the type A red aurora and it is conceivable that a soft electron flux may also excite the SAR-arc. Walker and Rees (1968) have examined this mechanism in detail and found that a sufficiently soft electron flux can provide enough heat to the ambient F-region electron gas to excite the 6300 Å emission line of atomic oxygen by thermal impact, and yet not excite the other optical emissions normally present in an aurora. Because of the strong monochromatic nature of the SAR-arcs they had to set an upper limit of 15 ev on the initial energy of the bombarding electrons. Also, in order to excite the SAR-arc to any measurable degree, an electron flux of the order of 10^9 electrons $cm^{-2} sec^{-1}$ or more is required and this flux must be active over the 10 hour lifetime of the SAR-arc. This soft flux of electrons, with energies of a few ev or less, may turn out to be equivalent to a special form of magnetospheric thermal conduction which is discussed in the next section.

3.4 THERMAL CONDUCTION HYPOTHESIS

Cole (1965) has postulated that the SAR-arc is excited by electron impact of heated ambient F-region electrons with atomic oxygen. The F-region electron gas is kept hot by the conduction of heat from the magnetosphere, along geomagnetic field lines, into the ionosphere. According to this mechanism, the source of energy for the SAR-arc lies in ring currents developed in a magnetic storm. Cole (1964, 1965) suggests that the ring currents, giving rise to the main phase decrease of the geomagnetic field, D_{st}, are largely caused by the noisy geomagnetic fluctuations that occur within the ionosphere-magnetosphere medium during a storm. He suggests that the hot ambient plasma, (10-100 ev) observed by Serbu (1964) with the IMP 1 satellite in the outer magnetosphere during quiet times, is pumped deeper into the geomagnetic field by the electrostatic fields associated with geomagnetic fluctuations during storms. The observed geomagnetic fluctuations have been found to have sufficient energy and time to energize the magnetospheric plasma in order to cause a major part of the D_{st} main phase variation of the geomagnetic field. No theory is proposed as to how the noise is generated or distributed during a storm, but Cole (1965) starts from the observation that the noise exists and proceeds to account for the observed facets of the storm. Cole (1967) has shown that for a main phase decrease of the geomagnetic field, D_{st}, of 100γ, the ring current particles have to be energized to 200 to 2000 ev. If a fraction of the magnetospheric plasma is thermalized, with an energy of about 1 ev, then sufficient energy can be transferred from the ring current through coulomb collisions to the ambient plasma in order to maintain a flow of heat into the ionosphere and sustain the SAR-arc. In this manner, Cole (1965) claims that the SAR-arc is a major sink of the energy stored in the ring currents contributing to the main phase decrease. The strength of the ring current is reflected in the magnetic storm parameter D_{st}, and Rees and Akasofu (1962) have called attention to a positive correlation between this storm parameter and the SAR-arc intensity. Cole (1965) has shown that an electron temperature of only 3200°K in the F-region was sufficient to excite a 10 KR SAR-arc. Electron temperatures of this order are capable of exciting the 6300 Å emission but not the other atmospheric emission lines. He has also shown that the magnetospheric ambient electron temperature, for this particular SAR-arc, has to be of the order of 10,000 - 15,000°K in order to maintain a flow of heat, along the geomagnetic field lines into the ionosphere to excite the SAR-arc to the 10 KR level. This temperature corresponds to an average energy per thermalized particle of 1 to 1.5 ev. Because of the low electron density in the magnetospheric plasma, thermal conduction may depart from its conventional meaning and the energy flow may appear as a soft electron flux flowing down the geomagnetic field lines into the ionosphere. In this sense, the soft electron flux and thermal conduction hypotheses are equivalent.

The thermal conduction hypothesis of the SAR-arc appears to consistently explain most of the observed features of the SAR-arc described in Chapter 2. Taking the observed SAR-arc features in the order presented in Chapter 2, the thermal conduction model can explain the following properties:

1. The fact that the SAR-arc moves equatorward from the auroral zone and occurs in mid-latitudes can be explained by the inward development of the geomagnetic noise region in the magnetosphere during a storm. The SAR-arc forms at mid-latitudes because the magnetospheric ring current, which provides the energy for the arc, occurs at the inner face of the noise region which during strong magnetic storms is forced deeper into the magnetosphere. The position and extent of the arc is governed by the position of the ring current and may be expected to go all the way around the earth, thus accounting for the observed horizontal extent of the arc. The fact that it extends several hundred kilometers in the meridional direction and is diffuse can be explained by the fact that, projected from middle latitudes via the

field lines to the equatorial plane, the phenomenon is about 4000 km wide, and this is about equal to the observed scale height of the plasma distribution produced by the geomagnetic fluctuations (Cole, 1964, 1967).

The height distribution of the observed 6300 Å emission is determined by the atomic oxygen distribution and, at the lower boundary, by collisional deactivation of the excited $O(^1D)$ state.

2. The SAR-arc is monochromatic since the F-region electron temperature is sufficient for exciting the 6300 Å atomic oxygen emission line, but not the other major emission lines requiring a higher excitation energy.
3. The intensity of the arc is dependent upon the strength of the geomagnetic storm. A stronger storm will have a larger ring current and, therefore, the heat flux transferred to the F-region will cause an increased electron temperature resulting in a brighter SAR-arc.
4. The fact that the SAR-arc has a time constant of the order of 10 hours is consistent with the explanation that the arc is a major sink of energy for the D_{st} main phase and therefore a time constant similar to the recovery phase of the storm is expected.
5. The SAR-arc requires a strong geomagnetic storm to produce the high F-region electron temperatures in order to excite the arc. Therefore, the frequency of occurrence of SAR-arcs is related to the frequency of strong geomagnetic storms which follows the solar cycle.
6. The SAR-arcs are directly controlled by the geomagnetic field because the position of the ring currents are geomagnetically controlled. Also, because the energy in the magnetosphere can flow down both legs of the magnetic field lines in the form of heat, conjugate SAR-arcs are expected.

7. Cole (1967) suggests that since the geomagnetic field is seldom absolutely quiet, particularly in the polar cap region, the geomagnetic agitation will tend to heat the outer magnetosphere. As a result, a weak ring current and a depletion of plasma are expected to be quasi-permanent features of the outermost magnetosphere. During a geomagnetic storm, the inward progression of the geomagnetic noise region in the magnetosphere will cause the heated region in the ionosphere to move southward, out of the polar cap, across the aurora oval, and south to mid-latitudes. As the storm develops, the heated electrons become sufficiently hot to excite the 6300 Å atomic oxygen emission in the SAR-arc. As a result, the SAR-arc moves equatorward along with the inner movement of the ring current in the magnetosphere.

8. The height of the peak intensity of the SAR-arc is determined by a combination of the F-region parameters, involving the electron temperature profile resulting from heat conduction, the atomic oxygen distribution, and the density profile of the atmospheric species quenching the $O(^1D)$ state.

9. Cole (1965) suggests that the speed of SAR-arc movements is probably related to inward development of the noisy geomagnetic fluctuations in the magnetosphere. It is not, at this time, at all clear whether this mechanism is solely responsible for arc movement. It could conceivably be controlled, at least to a partial extent, by ionospheric conditions. It is also not clear, from the theory developed by Cole (1967) thus far, why multiple SAR-arcs should exist.

10. It is not apparent why irregularities should develop from the heat conduction hypothesis. However, Cole (1965) claims that irregularities within the arc may be explained by the fact that the inward development of the geomagnetic noise fluctuations, which are responsible for the main phase decrease in a geomagnetic storm, may be field-aligned. Therefore, perturbations in the magnetospheric

ring current could be present and these perturbations may appear in the SAR-arc.
11. The observed F-region electron density depression in the near vicinity of the SAR-arc is not explained by the theory.

The remainder of the satellite observations discussed in Chapter 2 are consistent with the theory. It therefore appears that the thermal conduction hypothesis is consistent with the observational data and offers a mechanism for the transfer of energy from the magnetosphere to the ionosphere.

Cole (1965) has performed an energy balance of a magnetic storm and compared the energy in the magnetospheric ring current to the energy required to sustain the SAR-arc. He considered the case of a geomagnetic storm with a 100-γ main phase decrease at the equator. According to Parker (1962) a storm of this magnitude requires a change of about 3×10^{22} ergs in the kinetic energy of the trapped magnetospheric particles. Cole (1965) has calculated an electron temperature of 3200°K to excite a 10 KR SAR-arc and when the rate of cooling of the electrons was integrated over the three dimensional volume of the arc the total loss rate was found to be between 4×10^{16} to 2×10^{17} ergs sec^{-1}. The energy lost in 6300 Å radiation for the SAR-arc was approximately 10^{15} ergs sec^{-1}. Therefore, if the 3×10^{22} ergs stored in the ring current of the geomagnetic storm was conducted to the ionosphere in about 10^{5} seconds, the order of the lifetime of the SAR-arc, the energy loss rate is of the order of 3×10^{17} ergs sec^{-1} in apparent agreement with the energy required to sustain the arc. This energy balance adds considerable support to the thermal conduction model of the SAR-arc.

3.5 SUMMARY OF EXCITATION MECHANISMS

Walker and Rees (1968) have examined the four mechanisms discussed above and have stated the conditions by which the SAR-arc may form. The difficulties with the enhanced recombination hypothesis of NO^{+} ions are convincing and have been presented in section 3.1. Electric fields of 0.1 to 0.2 volts m^{-1} have been found to be capable of producing the observed luminosity; however, the very high ion temperatures, of the order of $5000^{o}K$ and greater in low altitudes, and the resulting large neutral heating appear as unacceptable consequences of this mechanism. In addition, using the results of Walker and Rees (1968) shown in Fig. 4, the total energy loss rate to the neutral gas in the three dimensional volume of a 10 KR SAR-arc was calculated to be about $2.5x10^{18}$ ergs/sec. This value is an order of magnitude greater than the energy required to sustain the SAR-arc by the thermal conduction mechanism, and if the energy for the electric fields is derived by some means from the magnetospheric ring current, the expected lifetime of the SAR-arc will be shorter. The arguments against a soft electron flux, with energies of the order of 15 ev or less, are less convincing and it is not possible to rule out this mechanism completely. In fact, the soft electron flux at low energies can almost be considered as a special form of heat conduction. The heat conduction hypothesis is the most acceptable and does not appear to cause any effects which would conflict with the available observations. Therefore, in the next chapters the thermal conduction hypothesis is examined in detail. The energy requirements and ionospheric conditions necessary for the excitation of the SAR-arc are determined and the two-dimensional structure of the arc is examined. In later chapters, the neutral gas temperature increase and atmospheric response caused by heating within the SAR-arc are both examined. In this manner, the ultimate sink of the energy in the magnetospheric ring current will be investigated.

IV. THERMAL CONDUCTION MODEL OF A SAR-ARC

According to the thermal conduction model of the SAR-arc, proposed by Cole (1965) and reviewed in the previous chapter, the SAR-arc is the primary sink of the energy for the D_{st} main phase of a magnetic storm. Cole (1965) postulates that the energy of the energetic particles causing the main phase decrease is transferred to the ambient thermalized plasma in the protonosphere by coulomb collisions. The energy in the thermalized plasma is then conducted down along the geomagnetic field lines heating the F-region electrons to a level where the atomic oxygen is excited to the ^1D state by electron impact. In this chapter, heat conduction in the F-region of the ionosphere and the physical processes caused by the hot thermal electrons are examined in detail. The one-dimensional heat conduction equation for the electron gas in the ionosphere is solved for various atmospheric and ionospheric models in order to determine the energy requirements and conditions necessary for SAR-arc formation. The height profiles of electron temperature, ion temperature, 6300 Å volume emission rate, and neutral heating within the SAR-arc region are determined and related to the arc intensity. Next, a two-dimensional model of the SAR-arc is constructed in such a manner that the computed 6300 Å emission rate contours closely approximate the observed contours shown in Fig. 2. The properties of this SAR-arc model are then discussed and the energy required to sustain the observed global pattern of the SAR-arc is compared to the energy of the trapped particles in the magnetospheric ring current causing the magnetic storm.

4.1 ELECTRON HEAT CONDUCTION EQUATION

Thermal conduction in the F-region electron gas has been considered by several authors (Geisler and Bowhill, 1965; Dalgarno, McElroy and Walker, 1967; Nagy and Walker, 1967; Walker and Rees, 1968; Dalgarno, et. al., 1968). They have shown that heat conduction in the F-region electron gas is very important in determining the electron temperature height profile for day and night conditions. Banks (1967a, 1967b) has shown that conduction is not as important in determining the ion temperature below 600 km, but must be considered above that altitude. In this study where observations show that the bulk of the 6300 Å radiation in the SAR-arc occurs below 600 km, it is assumed that the temperature profiles exciting the arc can be obtained by considering conduction only in the electron gas, but not in the ion gas. The ion temperature is obtained from a balance between the rate at which the ions are heated in elastic collisions with the ambient electrons and the rate at which the ions cool in elastic collisions with the neutrals without considering conduction in the ion gas.

DaRosa (1966) has shown that the electron gas temperature in the F-region of the ionosphere accommodates itself fast enough to changing conditions so that it is, in effect, always in a "thermal quasi-steady state." According to the observations, discussed in Chapter 2, the SAR-arc is persistent and stable with a lifetime of 10 hours or greater. Therefore, it can be assumed that the steady state electron heat conduction equation adequately represents conditions existing within the SAR-arc.

Lateral heat conduction in the electron gas can also be neglected because the electrons are confined to the geomagnetic field lines resulting in a very low lateral thermal conductivity. Heat conduction along the geomagnetic field lines is important and therefore the steady state heat conduction equation for the electron gas in the ionosphere can be written as,

$$-\frac{d}{dz}\left[K_e(z,T_e)\frac{dT_e}{dz}\right] = Q_e(z) - L(z,T_e) \tag{4-1}$$

where T_e is the electron temperature, z is the altitude, and $K_e(z, T_e)$ is the theral conductivity as given by Dalgarno, McElroy, and Walker (1967). $Q_e(z)$ is the local heating of the electron gas at height z, and for a night-time SAR-arc it is assumed to be zero. $L(z, T_e)$ represents the energy loss term and includes the following collisional processes:

1. Elastic collisions of electrons with the various neutral constituents: N_2, O_2, O, H, and He.

2. Inelastic collisions of electrons with molecular nitrogen, exciting the various rotational and vibrational levels.

3. Coulomb collisions of electrons with the various ion species: O^+, He^+, H^+, NO^+, and O_2^+.

4. Collisions of electrons with atomic oxygen exciting the ^1D state.

5. Collisions of electrons with atomic oxygen exciting the fine structure of the ground state of atomic oxygen.

A detailed description of the various loss processes and the other terms used in the electron heat conduction equation is given in Appendix A.

The boundary conditions for the electron heat conduction equation require that the electron temperature be equal to the neutral gas temperature at 120 km, and that the heat flow into the topside ionosphere, at 1000 km, is specified.

4.2 IONOSPHERIC AND ATMOSPHERIC MODELS; Case (1)

At the present time there is not sufficient observational data on the arcs to completely formulate the atmospheric and ionospheric conditions within the arc. A model, which is consistent with the observed characteristics of the arc, is therefore assumed and the electron heat conduction equation is solved for these conditions. The main parameters of the model are also varied in order to determine their effect upon the properties of the SAR-arc.

The model atmosphere, used throughout the analysis, is the analytic model atmosphere derived by Bates (1959), as modified by Walker (1964). In the model the temperature height profile is analytically represented and the number density height profiles of N_2, O_2, O, and He are obtained by analytically integrating the diffusive equilibrium equation for a given set of boundary conditions. The boundary conditions which are used in all of the model atmospheres considered in this analysis, require that the neutral gas temperature at 120km be held fixed at 350°K, and the neutral particle densities at 120km are $n(N_2)=4\times10^{11}$, $n(O_2)=7.5\times10^{10}$, $n(O)=7.6\times10^{10}$, and $n(He)=3.4\times10^{7}cm^{-3}$. In addition, the number density profile of atomic hydrogen was obtained from the work of Donahue (1966). For the model atmosphere considered here, case(1), the exospheric temperature is set at 1500°K, which is appropriate for nighttime conditions near solar cycle maximum. With these boundary conditions the temperature and the neutral species number density height profiles are obtained from the analytic expressions given in Appendix A for all species except hydrogen. Table (I) gives the model atmosphere as a function of height.

The model ionosphere includes the electron and ion density height profiles determined by Walker and Rees (1968) who, after searching through numerous ionograms available at the Boulder, Colorado, ionosonde station, selected an electron density profile for a 600R SAR-arc as representative of the conditions of the ionosphere during a SAR-arc. This electron density profile is considered as the basic profile to be used in this study, and it is shown, as case (1), in Fig. 5. It was obtained by using the ionogram to establish the electron density profile between 260 and 400km, an average nighttime profile below 260km, and an extrapolated profile, having an appropriate scale height, for the topside ionosphere above 400km. The ion composition is also taken from Walker and Rees (1968) which in turn was derived from the work of Holmes, Johnson, and Young (1965) and Taylor, *et. al.*(1963). The model ionosphere for case (1) is listed in Table (II).

Table I

The Model Atmosphere for Case (1) Conditions

Z	TN	N2	O2	O	HE	H
0.10000D 09	0.15000D 04	0.14380D 04	0.20640D 02	0.60901D 06	0.10870D 07	0.27000D 05
0.98000D 08	0.15000D 04	0.20017D 04	0.30122D 02	0.73572D 06	0.11396D 07	0.27500D 05
0.96000D 08	0.15000D 04	0.27915D 04	0.44051D 02	0.88971D 06	0.11950D 07	0.28000D 05
0.94000D 08	0.15000D 04	0.39000D 04	0.64555D 02	0.10771D 07	0.12535D 07	0.28500D 05
0.92000D 08	0.15000D 04	0.54588D 04	0.94802D 02	0.13052D 07	0.13152D 07	0.29000D 05
0.90000D 08	0.15000D 04	0.76547D 04	0.13952D 03	0.15834D 07	0.13803D 07	0.29500D 05
0.88000D 08	0.15000D 04	0.10754D 05	0.20576D 03	0.19229D 07	0.14490D 07	0.30000D 05
0.86000D 08	0.15000D 04	0.15137D 05	0.30411D 03	0.23377D 07	0.15215D 07	0.30500D 05
0.84000D 08	0.15000D 04	0.21346D 05	0.45045D 03	0.28451D 07	0.15981D 07	0.31000D 05
0.82000D 08	0.15000D 04	0.30161D 05	0.66867D 03	0.34664D 07	0.16789D 07	0.31500D 05
0.80000D 08	0.15000D 04	0.42697D 05	0.99480D 03	0.42280D 07	0.17644D 07	0.32000D 05
0.78000D 08	0.15000D 04	0.60562D 05	0.14833D 04	0.51628D 07	0.18548D 07	0.32280D 05
0.76000D 08	0.15000D 04	0.86072D 05	0.22166D 04	0.63113D 07	0.19503D 07	0.32560D 05
0.74000D 08	0.15000D 04	0.12257D 06	0.33201D 04	0.77241D 07	0.20513D 07	0.32840D 05
0.72000D 08	0.15000D 04	0.17489D 06	0.49841D 04	0.94638D 07	0.21582D 07	0.33120D 05
0.70000D 08	0.15000D 04	0.25005D 06	0.74995D 04	0.11609D 08	0.22713D 07	0.33400D 05
0.68000D 08	0.15000D 04	0.35825D 06	0.11311D 05	0.14257D 08	0.23910D 07	0.33920D 05
0.66000D 08	0.15000D 04	0.51431D 06	0.17099D 05	0.17529D 08	0.25177D 07	0.34440D 05
0.64000D 08	0.14999D 04	0.73988D 06	0.25910D 05	0.21578D 08	0.26520D 07	0.34960D 05
0.62000D 08	0.14999D 04	0.10666D 07	0.39356D 05	0.26594D 08	0.27943D 07	0.35480D 05
0.60000D 08	0.14999D 04	0.15409D 07	0.59924D 05	0.32816D 08	0.29451D 07	0.36000D 05
0.58000D 08	0.14998D 04	0.22309D 07	0.91465D 05	0.40544D 08	0.31050D 07	0.36600D 05
0.56000D 08	0.14998D 04	0.32369D 07	0.13995D 06	0.50153D 08	0.32747D 07	0.37200D 05
0.54000D 08	0.14997D 04	0.47068D 07	0.21469D 06	0.62119D 08	0.34547D 07	0.37800D 05
0.52000D 08	0.14995D 04	0.68595D 07	0.33017D 06	0.77039D 08	0.36458D 07	0.38400D 05
0.50000D 08	0.14993D 04	0.10020D 08	0.50910D 06	0.95670D 08	0.38489D 07	0.39000D 05
0.48000D 08	0.14990D 04	0.14670D 08	0.78710D 06	0.11897D 09	0.40647D 07	0.39840D 05
0.46000D 08	0.14985D 04	0.21532D 08	0.12203D 07	0.14815D 09	0.42943D 07	0.40680D 05
0.44000D 08	0.14979D 04	0.31683D 08	0.18973D 07	0.18478D 09	0.45389D 07	0.41520D 05
0.42000D 08	0.14969D 04	0.46745D 08	0.29589D 07	0.23083D 09	0.47996D 07	0.42360D 05
0.40000D 08	0.14955D 04	0.69168D 08	0.46298D 07	0.28887D 09	0.50782D 07	0.43200D 05
0.38000D 08	0.14934D 04	0.10268D 09	0.72705D 07	0.36226D 09	0.53765D 07	0.44900D 05
0.36000D 08	0.14903D 04	0.15299D 09	0.11465D 08	0.45537D 09	0.56970D 07	0.46700D 05
0.34000D 08	0.14857D 04	0.22896D 09	0.18166D 08	0.57410D 09	0.60432D 07	0.48467D 05
0.32000D 08	0.14789D 04	0.34450D 09	0.28957D 08	0.72648D 09	0.64198D 07	0.50200D 05
0.30000D 08	0.14689D 04	0.52196D 09	0.46512D 08	0.92385D 09	0.68336D 07	0.52000D 05
0.28000D 08	0.14540D 04	0.79825D 09	0.75473D 08	0.11828D 10	0.72951D 07	0.56400D 05
0.26000D 08	0.14318D 04	0.12367D 10	0.12421D 09	0.15291D 10	0.78208D 07	0.60800D 05
0.24000D 08	0.13987D 04	0.19525D 10	0.20861D 09	0.20050D 10	0.84378D 07	0.68800D 05
0.22000D 08	0.13490D 04	0.31710D 10	0.36123D 09	0.26866D 10	0.91937D 07	0.80400D 05
0.20000D 08	0.12745D 04	0.53845D 10	0.65622D 09	0.37254D 10	0.10177D 08	0.92000D 05
0.18000D 08	0.11624D 04	0.98470D 10	0.12911D 10	0.54716D 10	0.11571D 08	0.11500D 06
0.16000D 08	0.99331D 03	0.20609D 11	0.29361D 10	0.89261D 10	0.13816D 08	0.15600D 06
0.14000D 08	0.73762D 03	0.57525D 11	0.90948D 10	0.18230D 11	0.18330D 08	0.25500D 06
0.12000D 08	0.35000D 03	0.40000D 12	0.75000D 11	0.76000D 11	0.34000D 08	0.65000D 06

Table II

The Model Ionosphere for Case (1) Conditions

Z	O+	HE+	H+	O2+	NO+	NE
0.10000D 09	0.82500D 04	0.66000D 04	0.16500D 04	0.0	0.0	0.16500D 05
0.98000D 08	0.89080D 04	0.64600D 04	0.16320D 04	0.0	0.0	0.17000D 05
0.96000D 08	0.98640D 04	0.64800D 04	0.16560D 04	0.0	0.0	0.18000D 05
0.94000D 08	0.10868D 05	0.64600D 04	0.16720D 04	0.0	0.0	0.19000D 05
0.92000D 08	0.11920D 05	0.64000D 04	0.16800D 04	0.0	0.0	0.20000D 05
0.90000D 08	0.13330D 05	0.64500D 04	0.17200D 04	0.0	0.0	0.21500D 05
0.88000D 08	0.14812D 05	0.64400D 04	0.17480D 04	0.0	0.0	0.23000D 05
0.86000D 08	0.16032D 05	0.62400D 04	0.17280D 04	0.0	0.0	0.24000D 05
0.84000D 08	0.17300D 05	0.60000D 04	0.17000D 04	0.0	0.0	0.25000D 05
0.82000D 08	0.19332D 05	0.59400D 04	0.17280D 04	0.0	0.0	0.27000D 05
0.80000D 08	0.20720D 05	0.56000D 04	0.16800D 04	0.0	0.0	0.28000D 05
0.78000D 08	0.23016D 05	0.54000D 04	0.15840D 04	0.0	0.0	0.30000D 05
0.76000D 08	0.25818D 05	0.52000D 04	0.14820D 04	0.0	0.0	0.32500D 05
0.74000D 08	0.27934D 05	0.47600D 04	0.13056D 04	0.0	0.0	0.34000D 05
0.72000D 08	0.30557D 05	0.43200D 04	0.11232D 04	0.0	0.0	0.36000D 05
0.70000D 08	0.33288D 05	0.38000D 04	0.91200D 03	0.0	0.0	0.38000D 05
0.68000D 08	0.36441D 05	0.36900D 04	0.86920D 03	0.0	0.0	0.41000D 05
0.66000D 08	0.39670D 05	0.35200D 04	0.80960D 03	0.0	0.0	0.44000D 05
0.64000D 08	0.43891D 05	0.33600D 04	0.74880D 03	0.0	0.0	0.48000D 05
0.62000D 08	0.47287D 05	0.30600D 04	0.65280D 03	0.0	0.0	0.51000D 05
0.60000D 08	0.51700D 05	0.27500D 04	0.55000D 03	0.0	0.0	0.55000D 05
0.58000D 08	0.57000D 05	0.25200D 04	0.36000D 03	0.0	0.0	0.60000D 05
0.56000D 08	0.65280D 05	0.23120D 04	0.13600D 03	0.0	0.0	0.68000D 05
0.54000D 08	0.71765D 05	0.19388D 04	0.0	0.0	0.0	0.74000D 05
0.52000D 08	0.78352D 05	0.14880D 04	0.0	0.0	0.0	0.80000D 05
0.50000D 08	0.87032D 05	0.96800D 03	0.0	0.0	0.0	0.88000D 05
0.48000D 08	0.96205D 05	0.79540D 03	0.0	0.0	0.0	0.97000D 05
0.46000D 08	0.10443D 06	0.56700D 03	0.0	0.0	0.0	0.10500D 06
0.44000D 08	0.11164D 06	0.35840D 03	0.0	0.0	0.0	0.11200D 06
0.42000D 08	0.12180D 06	0.19520D 03	0.0	0.0	0.0	0.12200D 06
0.40000D 08	0.13000D 06	0.0	0.0	0.0	0.0	0.13000D 06
0.38000D 08	0.14000D 06	0.0	0.0	0.0	0.0	0.14000D 06
0.36000D 08	0.14300D 06	0.0	0.0	0.0	0.0	0.14300D 06
0.34000D 08	0.14500D 06	0.0	0.0	0.0	0.0	0.14500D 06
0.32000D 08	0.14800D 06	0.0	0.0	0.0	0.0	0.14800D 06
0.30000D 08	0.14500D 06	0.0	0.0	0.0	0.0	0.14500D 06
0.28000D 08	0.14000D 06	0.0	0.0	0.0	0.0	0.14000D 06
0.26000D 08	0.15000D 05	0.0	0.0	0.20817D-12	0.20817D-12	0.15000D 05
0.24000D 08	0.18480D 04	0.0	0.0	0.17040D 03	0.38160D 03	0.24000D 04
0.22000D 08	0.74880D 03	0.0	0.0	0.33408D 03	0.83712D 03	0.19200D 04
0.20000D 08	0.17400D 02	0.0	0.0	0.34800D 03	0.13746D 04	0.17400D 04
0.18000D 08	0.0	0.0	0.0	0.26816D 03	0.13978D 04	0.16760D 04
0.16000D 08	0.0	0.0	0.0	0.20208D 03	0.14786D 04	0.16840D 04
0.14000D 08	0.0	0.0	0.0	0.13416D 03	0.15858D 04	0.17200D 04
0.12000D 08	0.0	0.0	0.0	0.63700D 02	0.17563D 04	0.18200D 04

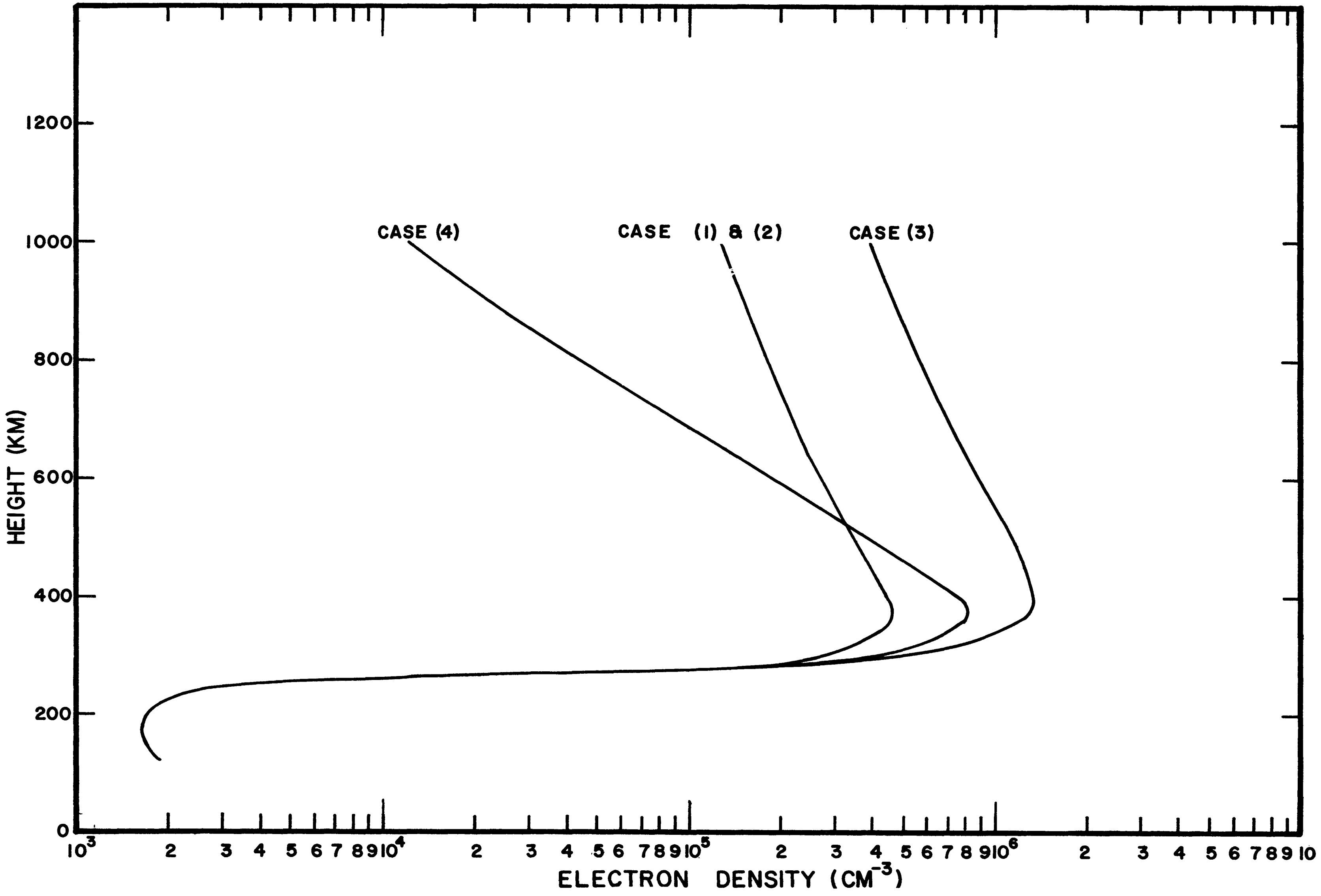

Fig. 5. Electron density height profiles for model ionospheres, cases (1) through (4).

4.3 METHOD OF SOLUTION

The computer program used to solve the electron heat conduction program appears in Appendix A and requires as inputs (a) an electron and ion density profile, (b) boundary conditions for the neutral model atmosphere, and (c) a heat flow rate into the ionosphere at the upper boundary. The program output gives the electron temperature, 6300Å volume emission rate, heat flow rate, neutral heating rate, and the various loss rates over the 1000 to 120 km height interval in the atmosphere.

The 6300 Å volume emission rate is obtained by a balance between the rate at which the oxygen atoms are raised to the ^1D level and by the rate at which they are collisionally deactivated. The neutral heating rate is obtained by summing the following elastic and inelastic collisional processes between neutrals and electrons and ions:

1. Polarization interactions between all of the neutral and ion species considered: O^+, H^+, He^+, NO^+, O_2^+ and O, H, He, O_2, N_2.

2. Resonance charge exchange interactions between the neutrals and ionized particles of a species: $O\text{-}O^+$, $H\text{-}H^+$, $He\text{-}He^+$, and $O_2\text{-}O_2^+$.

3. Elastic collisions between electrons and neutrals: N_2, O_2, O, He, and H.

4. Inelastic collisions between electrons and neutral species exciting the various rotational and vibrational states, which in turn are quenched before radiating (e.g. vibrational excitation of molecular nitrogen, fine structure cooling of atomic oxygen, and collisional quenching of the $O(^1D)$ state of atomic oxygen). The analytic expressions for the various processes described above are given in Appendix A.

4.4 DISCUSSION OF RESULTS; Case (1)

The electron heat conduction equation, with the atmospheric and ionospheric conditions given in section 4.2, is solved for various assumed heat flows into the topside ionosphere at 1000 km and the results are shown in Fig. 6. The total 6300Å

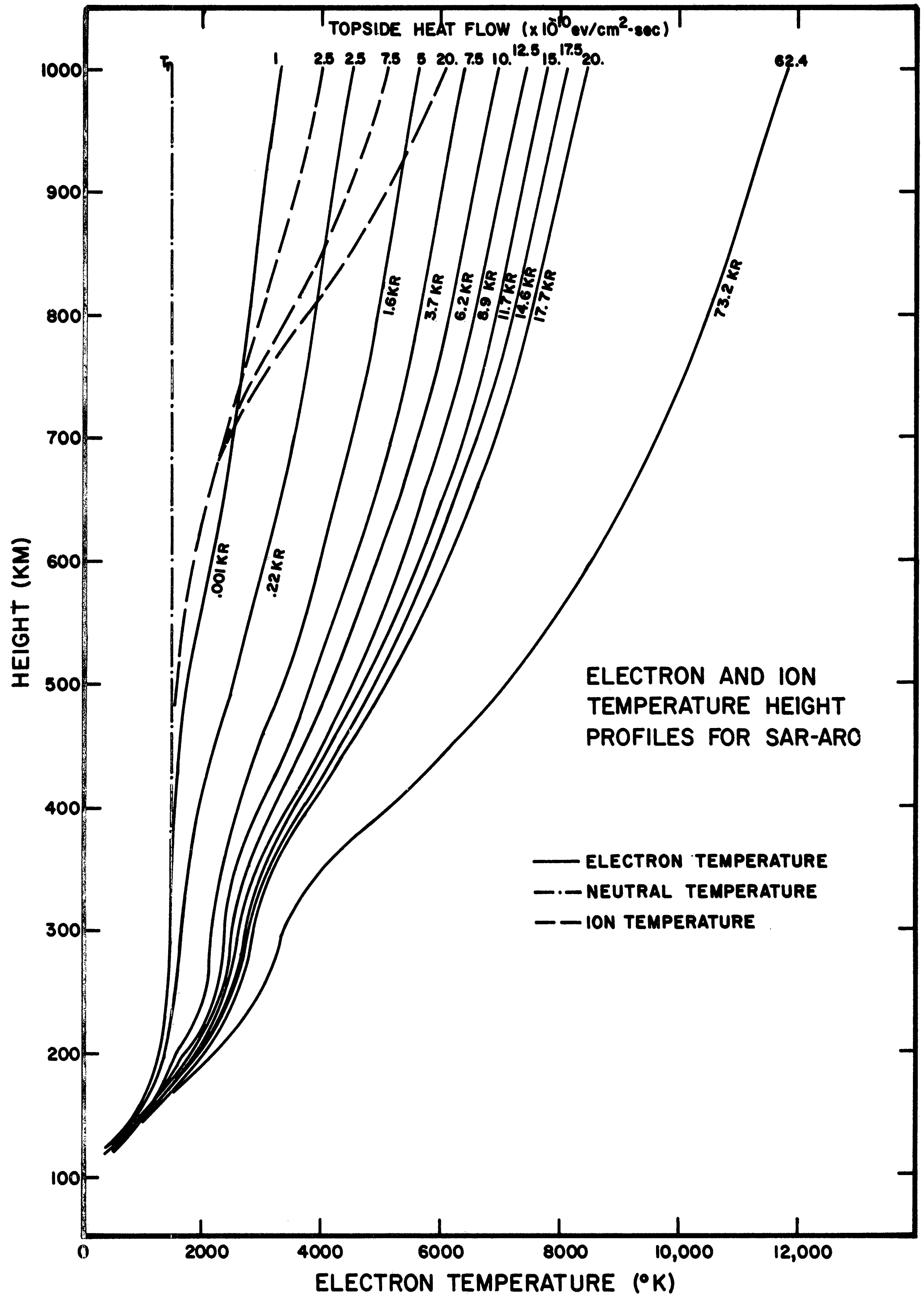

Fig. 6. Electron and ion temperature height profiles for SAR-arcs corresponding to case (1) conditions.

column emission rates resulting from these electron temperatures are indicated on the curves; they were obtained by integrating the 6300 Å volume emission rate (see Fig. 7) with respect to height. It is shown in this figure that the SAR-arc intensity is a strong function of the electron temperature and a relatively small increase in the electron temperature gives rise to a large change in the arc brightness. Assuming that the SAR-arc becomes detectable at an intensity of 100 R, then, for these particular atmospheric and ionospheric conditions, a topside heat flow of 2×10^{10} ev $cm^{-2} sec^{-1}$ or greater will cause a detectable SAR-arc to be excited. It was assumed in these calculations that the atmospheric and ionospheric conditions remained constant even for the brightest SAR-arc considered. However, some change would undoubtably be expected because the heating within the SAR-arc should cause a dynamic response and corresponding adjustment in the atmospheric and ionospheric models. Nevertheless, since the arc has been observed to be stable, it does seem unlikely that such a response would cause an atmospheric change large enough to significantly affect the excitation process. In Fig. 6, each electron temperature profile has an inflection near 300 km and this is due to a rapid change of the electron thermal conductivity with height in that region. The curve having the greatest topside heat flow represents a downward transport of energy from the magnetosphere of 1 erg $cm^{-2} sec^{-1}$. The ion temperature is also shown in Fig. 6. At high altitudes the magnitude of the ion temperature is in error because conduction in the ion gas was neglected. However, below about 600 km conduction is not important (Banks, 1967a) and the ion temperatures are, therefore, representative of conditions within the SAR-arc.

The 6300 Å volume emission rate height profile, excited by the ambient electron gas, is shown in Fig. 7. In the upper ionosphere the volume emission rate is low because the atomic oxygen number density is low, and in the lower ionosphere collisional deactivation by the neutral gas becomes important and the volume emission rate again decreases. Therefore, there exists a peak in the volume emission rate curve and it is seen to occur near 480 km. It is apparent,

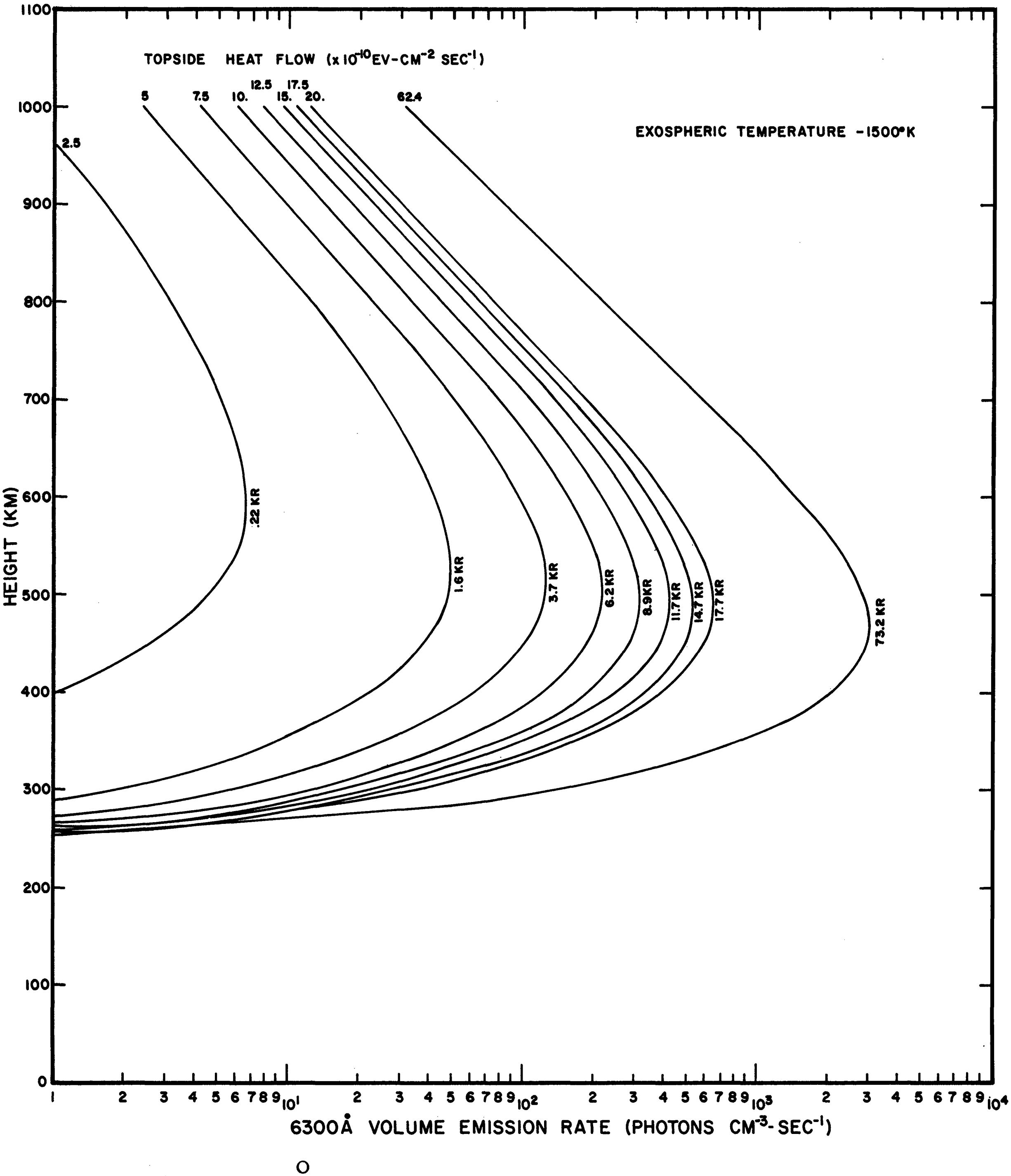

Fig. 7. 6300Å volume emission rate height profiles for SAR-arcs corresponding to case (1) conditions.

in the figure, that the peak volume emission rate progresses deeper into the atmosphere as the intensity first increases; however, beyond an arc intensity of 2 KR, the peak remains nearly constant. The height of the peak of the volume emission rate is slightly greater than the average, 400 km, usually reported in the literature. However, it is shown later that the peak height is dependent upon atmospheric conditions and as the exospheric temperature varies during the night a range of peak heights can be expected.

The neutral heating height profile due to an energy transfer from the electron and ion gas to the neutral gas within the SAR-arc is shown in Fig.8. The neutral heating peak occurs near 380 km and decreases quite rapidly below the peak because of the rapid decrease of electron temperature. Most of the energy in the electron gas is lost in the region of the neutral heating peak, and since no localized heat sources are present, the electrons are rapidly cooled through collisions with neutrals and ions. Above the peak, the electron temperature increases with height, however, because the neutral gas number density is decreasing at an exponential rate, the reduced collision frequency results in a decrease of the neutral heating. It is also shown in Fig. 8, that the height of maximum heating for a faint SAR-arc occurs at a high altitude and progresses downward as the arc intensity increases. Beyond a SAR-arc intensity of 1 KR the peak height and shape of the neutral heating height profile remains constant. This fact will be used when the two-dimensional structure of the SAR-arc and the neutral gas temperature increase caused by neutral heating are studied.

In Fig. 9, the height profiles of the more important electron loss rates are presented for a 1.6 KR SAR-arc having atmospheric and ionospheric conditions corresponding to case (1). It is seen that at high altitudes the electron-ion elastic collision loss rate dominates and at lower altitudes the loss rate to molecular nitrogen and the loss rate exciting the fine structure levels of atomic oxygen are most important. The production of the ^1D state of atomic oxygen peaks at an altitude of

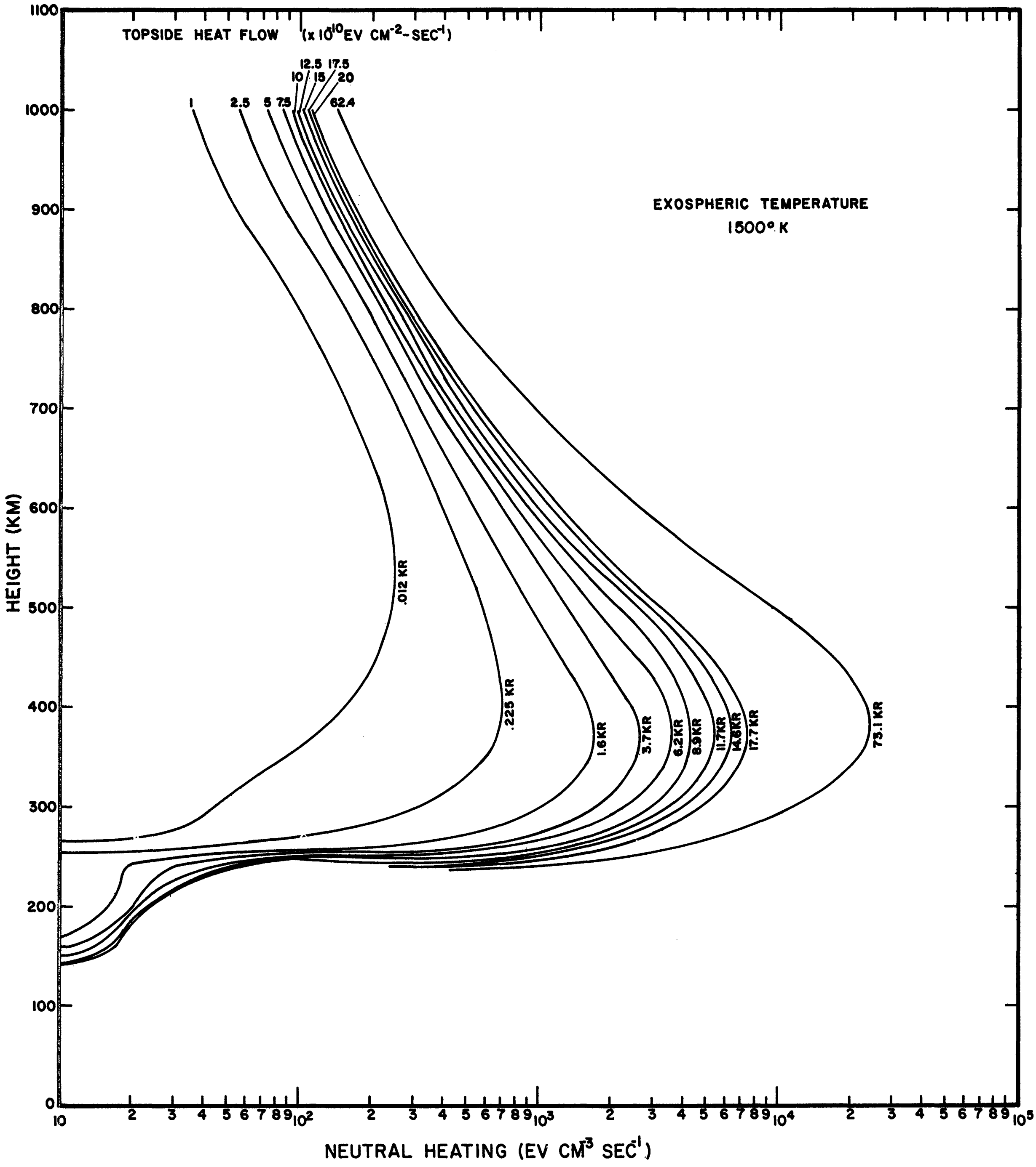

Fig. 8. Neutral heating rate height profiles for SAR-arcs corresponding to case (1) conditions.

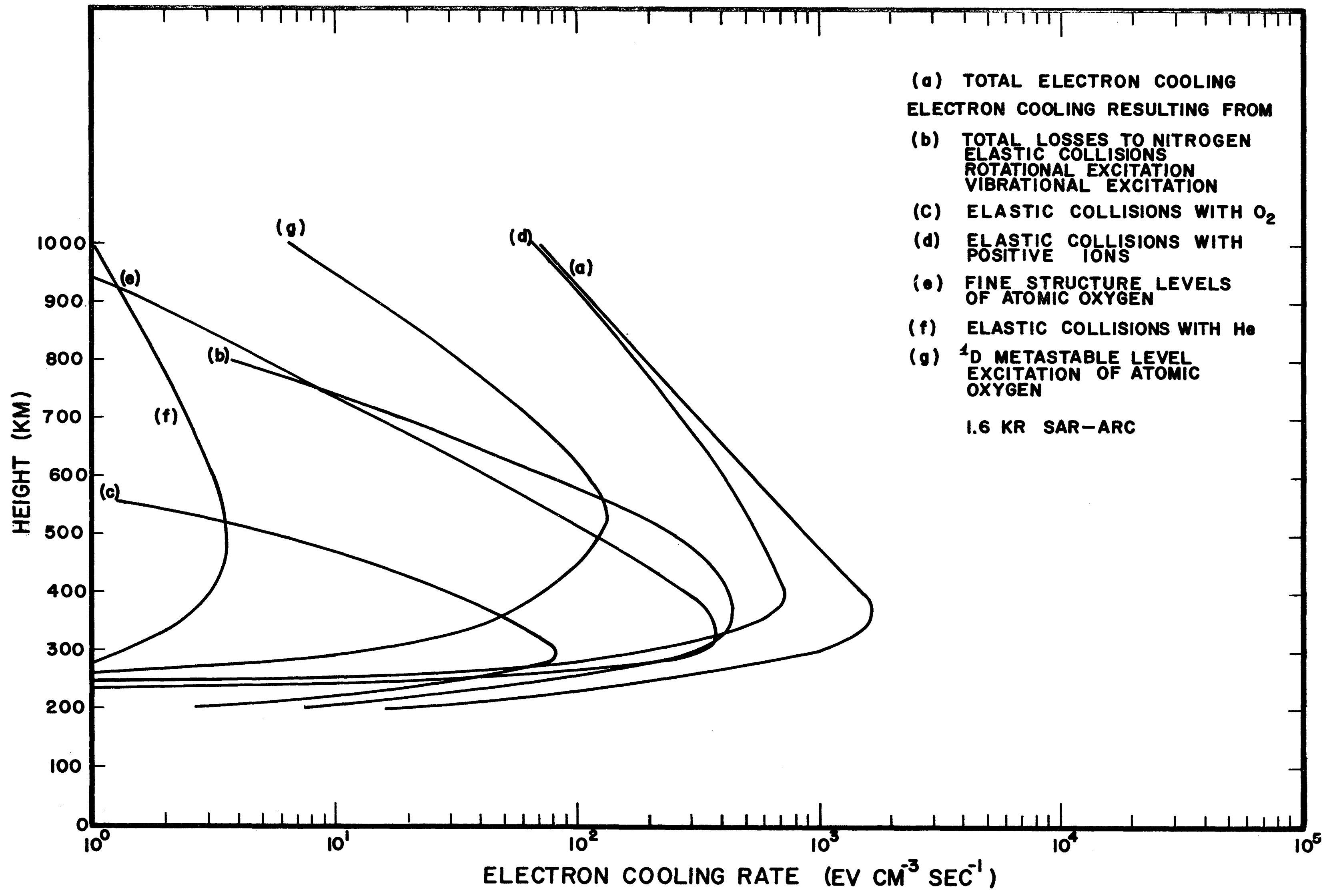

Fig. 9. Electron cooling rates appropriate to a 1.6 KR SAR-arc corresponding to case (1) conditions.

520km, which is identical to the calculated peak of the 6300Å volume emission rate shown in Fig. 7. Below that altitude collisional deactivation of the ^1D state becomes important which explains why the 6300Å volume emission rate decreases more rapidly with altitude than the production rate of the ^1D state. It is evident from these calculations that the 6300Å radiation of the SAR-arc may be excited by hot thermal electrons in the F-region; the resulting emission rate profile and spectral purity are in agreement with the observations.

4.5 RESULTS OF OTHER ATMOSPHERIC AND IONOSPHERIC MODELS

The main parameters affecting the atmospheric and ionospheric conditions within the SAR-arc region are varied in order to determine their influence upon the arc structure and the energy requirements for arc excitation. The model atmosphere and ionosphere discussed above was classified as case (1). In this section three other atmospheric models are examined:

1. Case(2): A neutral gas model atmosphere having an exopsheric temperature of 1061°K, similar to that which would exist during solar cycle minimum, and the same model ionosphere used in case (1).

2. Case(3): A neutral gas model atmosphere having an exospheric temperature of 1500°K and a model ionosphere having the case(1) electron and ion number density profiles increased by a factor of 3. This model can be considered to represent the conditions for a daytime SAR-arc.

3. Case(4): A neutral gas model atmosphere with an exospheric temperature of 1500°K, and a model ionosphere having an electron density profile, with the same total integrated number density as used in case(1), but with a topside scale height lower by a factor of 3. This model is used to study the influence of ionospheric structure on arc formation.

The electron density profile used in each of these cases is shown in Fig. 5. The same calculations were carried out for cases (2)-(4) as for case (1) and the results are given in Appendix B. Only the more important conclusions of this parametric study are outlined here:

1. The magnetospheric heat flow required to excite the SAR-arc to a given intensity is shown in Fig. 10 for the four cases considered. It is shown in this figure that the conditions specified for case (1) are most favorable for SAR-arc formation, requiring the least heat flow from the magnetosphere to excite the arc to a given intensity.

2. When the exospheric temperature is low, a greater topside energy flow is required to excite the SAR-arc to a detectable level. This may be partially responsible for the solar cycle variation of the SAR-arc frequency.

3. For a given set of ionospheric conditions, the height of the peak 6300 Å volume emission rate depends upon the exospheric temperature, as discussed in Appendix B. Therefore, if it is assumed that the ionospheric conditions and the energy flowing into the SAR-arc remain constant throughout the night, then the height of the peak 6300 Å volume emission rate and total SAR-arc intensity should decrease in accordance with the exospheric temperature decay.

4. It is also shown in Appendix B that the SAR-arc is most easily formed in a region having a reduced electron density. Therefore, a given heat flow from the magnetosphere will heat the ambient F-region electrons, in the depressed electron density region, to much higher temperatures than in the surrounding areas. Because the SAR-arc intensity is a very strong function of the electron temperature, a brighter arc will form.

5. It is shown in Fig. 10 that for an ionosphere with considerably more ionization a weaker arc will form for a given heat flow from the magnetosphere. Therefore, it can be expected that because the SAR-arc is believed to extend completely around the earth, the arc intensity on the dayside will be much fainter and occur at higher altitudes than the corresponding nighttime SAR-arc.

6. The results of case (4) show that the SAR-arc intensity may increase or decrease depending upon whether the electron scale height is increasing or decreasing. This effect may be caused by vertical and meridional neutral winds forcing ionization up and down the geomagnetic field lines.

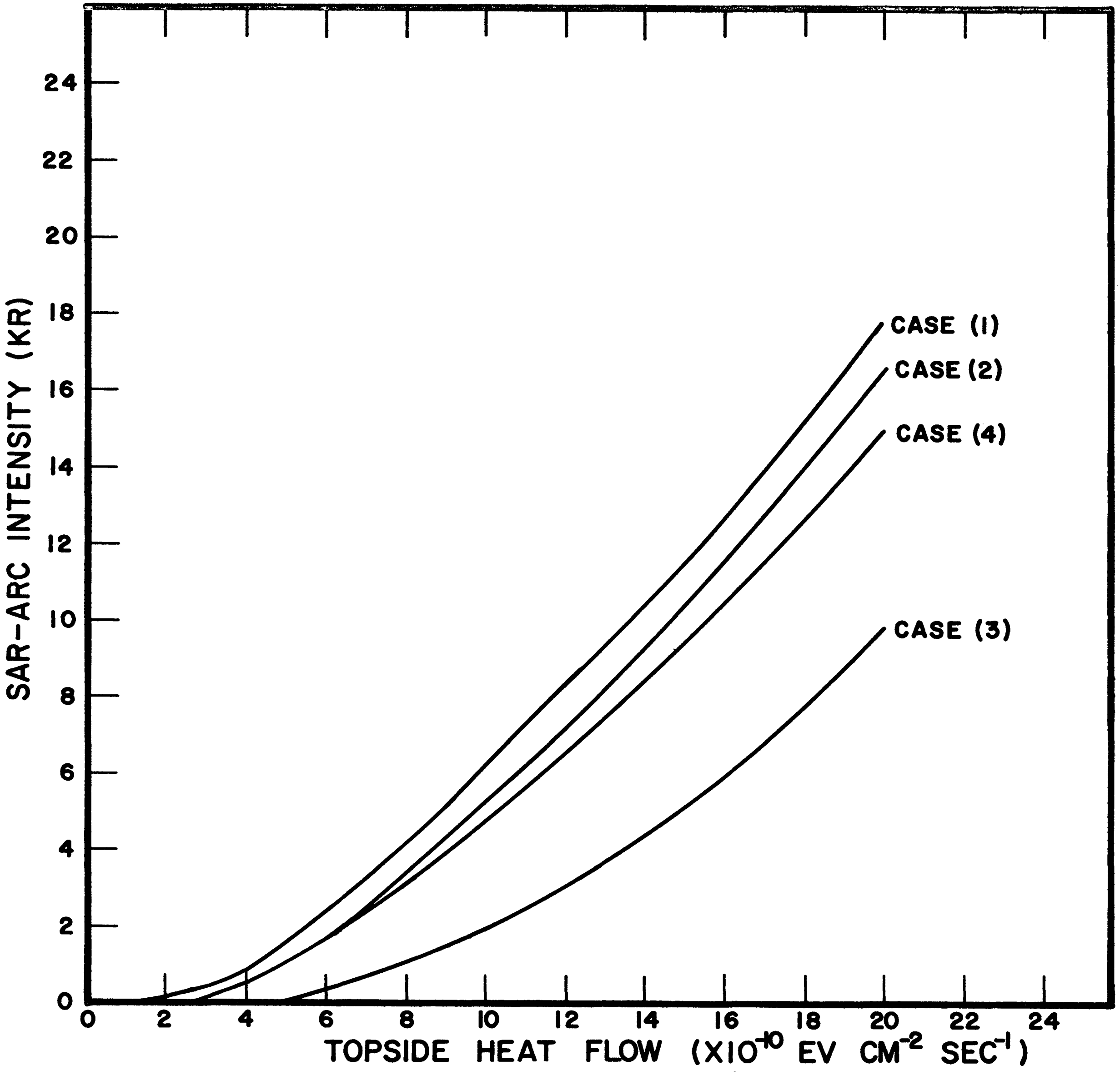

Fig. 10. Topside heat flow requirements to excite the SAR-arc to a given intensity for the four cases considered.

In the cases considered, it has been shown that the SAR-arc can be excited by electron impact of the ambient F-region electrons with atomic oxygen for almost any set of atmospheric and ionospheric conditions if sufficient heat flow from the magnetosphere occurs. There are certain conditions more favorable to SAR-arc formation and these were seen to depend strongly upon the model atmosphere and ionosphere chosen to represent the conditions within the arc. In spite of these variations, the consistency of the thermal conduction hypothesis appears to be well established causing no serious conflict between the model and observed features of the SAR-arc.

4.6 TWO DIMENSIONAL SAR-ARC STRUCTURE

The results described in the previous sections were obtained from a solution to the one-dimensional electron heat conduction equation along the geomagnetic field lines in the ionosphere. It is evident, however, from the morphology of the SAR-arc, described in Chapter 2, that the arcs form continuous rings around the earth with a north-south intensity cross section as shown in Fig. 2. Since lateral heat conduction in the electron gas is negligible, there are two obvious ways to obtain the two-dimensional SAR-arc structure from the results obtained thus far: (1) assume that the same vertical height profile of the electron density holds over the arc cross section and vary the topside heat flow across the ionosphere and (2) assume the presence of a constant heat flow across the top of the arc and have a meridional variation of the electron density height profile in the ionosphere. In the real case, some combination of the two is likely and the satellite data described in Chapter 2, indicate that variations in both the topside heat flow and electron density height profile were present for the SAR-arc of Sept. 28/29 1967. However, as will be shown in Chapter 8 where this particular SAR-arc is examined in detail, the electron density depression occurred 300-400 km north of the 6300 Å emission region and appeared to be a result rather than a contributing cause of the SAR-arc. The satellite recorded an enhanced electron temperature over the 6300 Å emission region indicating an enhanced topside heat flow into the vicinity of the SAR-arc. But beyond this region of enhanced 6300Å emission the electron temperature was considerably lower. Therefore, it appears that there is a relationship between the topside heat flow and the position of the SAR-arc. In the theoretical model of the SAR-arc presented here, it is assumed that the electron density height profile is constant across the arc and only the topside heat flow varies.

The 6300 Å volume emission rate height profile for case (2) shown in Appendix B, closely approximates the height distribution of the normalized 6300 Å volume emission rate contours, shown in Fig. 2, at a given meridional distance from the arc center. The height of the peak intensity and the intensity variation with height are both similar. The 6300 Å intensity cross section of the SAR-arc determined by Tohmatsu and Roach (1962), and shown in Fig. (2), represent an average cross section of several SAR-arcs occurring over a 5 year period after the last solar cycle maximum in 1958. In this study the SAR-arc at solar cycle maximum is being investigated and the atmospheric conditions are better represented by those given in case (1) having a high exospheric temperature. As a result, the 6300 Å volume emission rate profiles shown in Fig. 7 are assumed to represent the vertical intensity distribution; however, the same lateral intensity distribution, as shown in Fig. 2, is still considered to adequately represent the SAR-arc. Therefore, the SAR-arc model which is used for the rest of the study has atmospheric and ionospheric conditions corresponding to case (1) and 6300 Å intensity contours, as shown in Fig. 11. The major effect of such a modification is that the 6300 Å intensity peak will be 80 km higher and the contours will be slightly more elongated in the vertical direction. This difference does not fundamentally affect the problem and better approximates conditions existing during solar cycle maximum when the experimental measurements, described in Chapter 8 were made.

The two-dimensional SAR-arc structure is formed in the following manner. If it is assumed that the peak intensity of the SAR-arc, observed from the ground

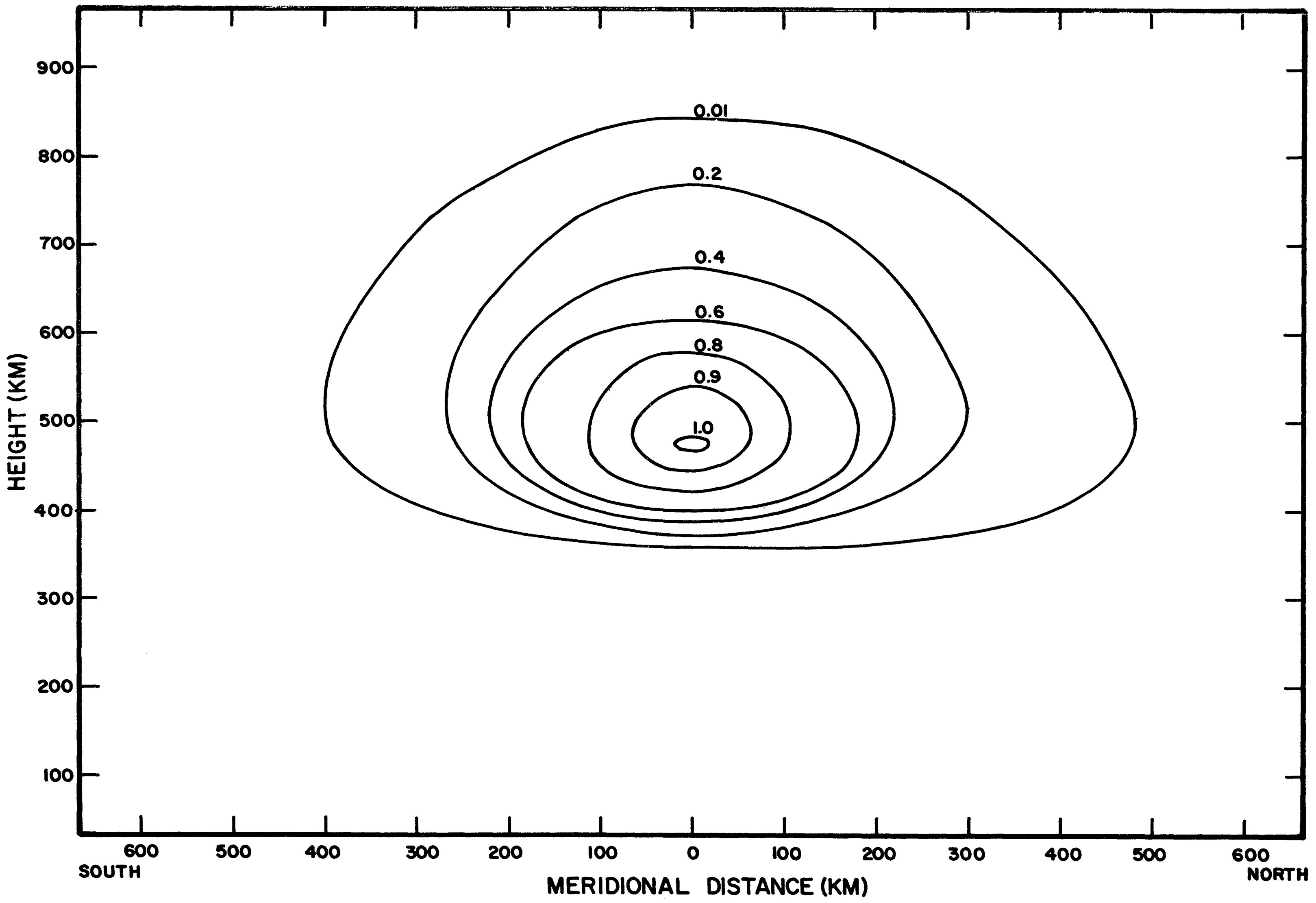

Fig. 11. Normalized 6300Å isophotal representation of the two-dimensional SAR-arc model.

is 10KR then, from Fig. 6, the heat flow into the upper ionosphere must be about 14×10^{10} ev $cm^{-2}sec^{-1}$ at the SAR-arc center in order to excite the arc to that intensity. For a vertical slice at a meridional distance 200km north of the arc center, the peak of the normalized volume emission rate is 0.4 as shown in Fig. 11. Because the 6300Å volume emission rate height profile for a 4 KR SAR-arc is similar to the emission rate profile for a 10KRarc, it can be used to represent the vertical intensity distribution at that position. The energy flow from the magnetosphere required to excite the SAR-arc at that location is 8×10^{10} ev $cm^{-2}sec^{-1}$ as shown in Fig. 6. By repeating this process of matching the 6300Å volume emission rate height profiles to the normalized values given at a meridional distance from the arc center, the entire two-dimensional structure of the SAR-arc can be determined. Fig. 12 shows the meridional distribution of the topside heat flow into the region of a 10KR SAR-arc having the normalized 6300Å volume emission rate contours which are shown in Fig. 11.

The integrated heat flow rate into the SAR-arc cross section is 5.9×10^{18} ev $sec^{-1}cm^{-1}$. The total amount of heat transferred out of the arc at the lower boundary is 8.2×10^{14} ev $sec^{-1}cm^{-1}$ and the total 6300Å energy radiated from the SAR-arc cross section is 1.6×10^{16} ev $sec^{-1}cm^{-1}$. The difference between the heat flow into the arc and the heat and radiative flux flowing out of the arc cross section appears as neutral heating and is 5.88×10^{18} ev $sec^{-1}cm^{-1}$.

According to Cole (1965), a 100γ decrease of D_{st} at the equator corresponds to a 10KR SAR-arc and is caused by trapped particles in the magnetosphere whose total kinetic energy is 3×10^{22} ergs. Cole(1965) also assumed that the ring current decayed in about 10^5 seconds, implying an energy loss rate of 3×10^{17} ergs sec^{-1}. If it is assumed that the SAR-arc forms complete rings of equal intensity around the earth at 45° latitude in both conjugate hemispheres, then for a heat flow rate of 5.9×10^{18} ev $sec^{-1}cm^{-1}$ the total energy flowing into the ionosphere at 1000km is 0.6×10^{17} ergs sec^{-1}. Thus it appears that there is sufficient energy in the ring current to sustain the

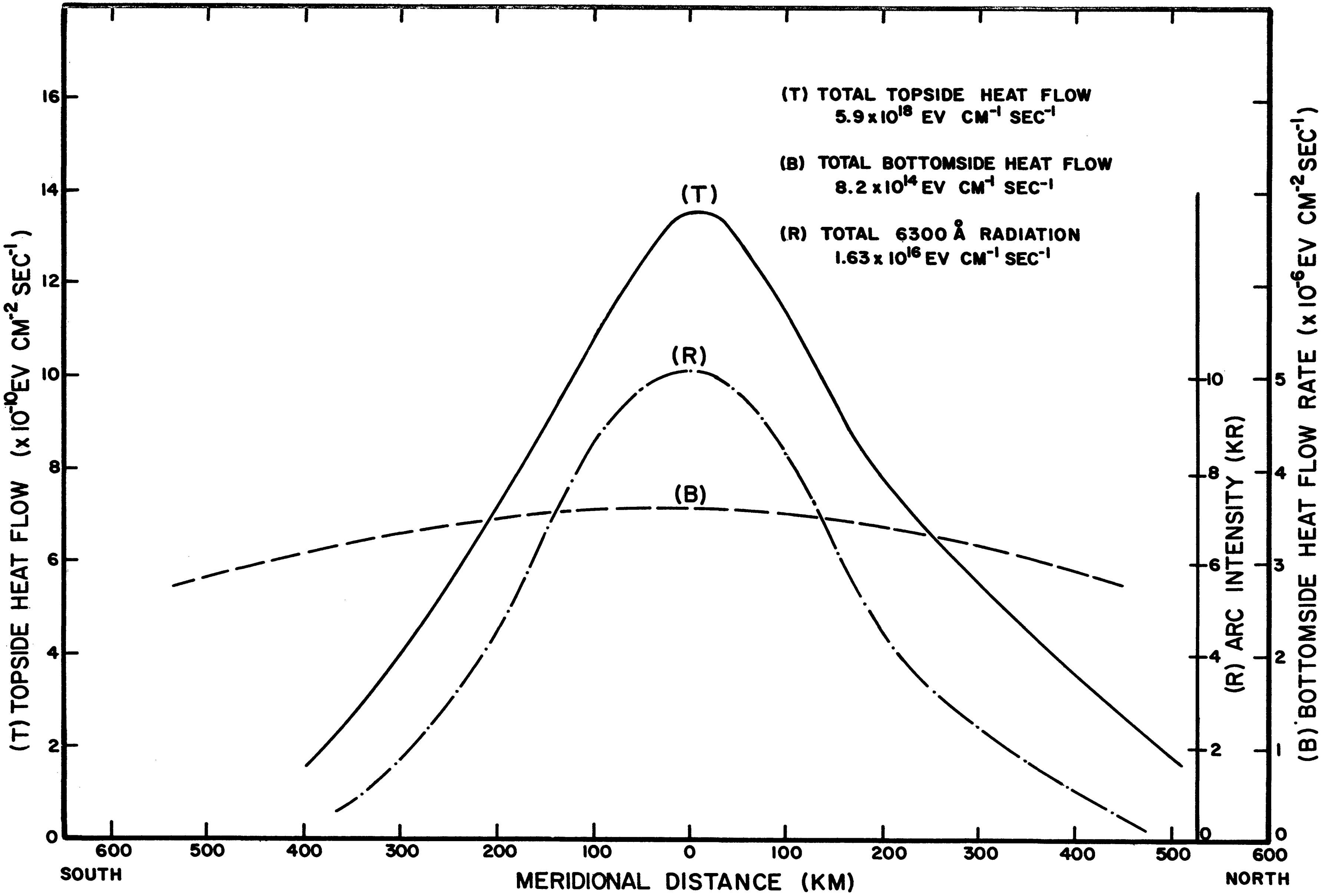

Fig. 12. Meridional energy flow distribution for a 10KR SAR-arc model.

SAR-arc throughout the night. This order of magnitude balance between the energy contained in the magnetospheric ring current and energy flow required to sustain the arc lends considerable support to the thermal conduction hypothesis.

The electron and ion temperature contours for this two-dimensional SAR-arc model are shown in Fig. 13. This figure indicates a considerable enhancement of the electron temperature in the topside ionosphere over the SAR-arc. A belt of high electron temperature should, therefore, exist along a constant magnetic latitude over the SAR-arc region which encircles the earth. The corresponding two-dimensional ion temperatures are also shown in Fig. 13 and significant departures from the neutral exospheric temperatures are noticeable only in the upper ionosphere. This is in sharp contrast to the ion temperatures obtained by the electric field theory, shown in Fig. 4, where very large ion temperatures are seen to exist in the lower ionosphere, near 200-300km. One way of resolving the SAR-arc excitation mechanism is by measuring the ion temperature at various altitudes within the SAR-arc.

In Fig. 7 and 8 the 6300 Å volume emission rate and neutral heating height profiles are seen to be similar in shape beyond an SAR-arc intensity of 1 KR. Therefore, it is possible to normalize the two-dimensional neutral heating contours because of the linear manner by which the SAR-arc model was constructed. The normalized neutral heating contours are shown in Fig. 14 and the peak value of the neutral heating is plotted as a function of SAR-arc peak intensities in the upper right hand corner of the figure. It is seen that the neutral heating contours closely approximate ellipses with a peak value occurring at a height of 380 km. This fact will be utilized in the next chapter where the neutral temperature increase is calculated using this heat source.

The results of this chapter indicate that the mechanism involved in the thermal conduction hypothesis is indeed capable of exciting the 6300 Å atomic oxygen emission if sufficient energy flows from the magnetosphere. The height,

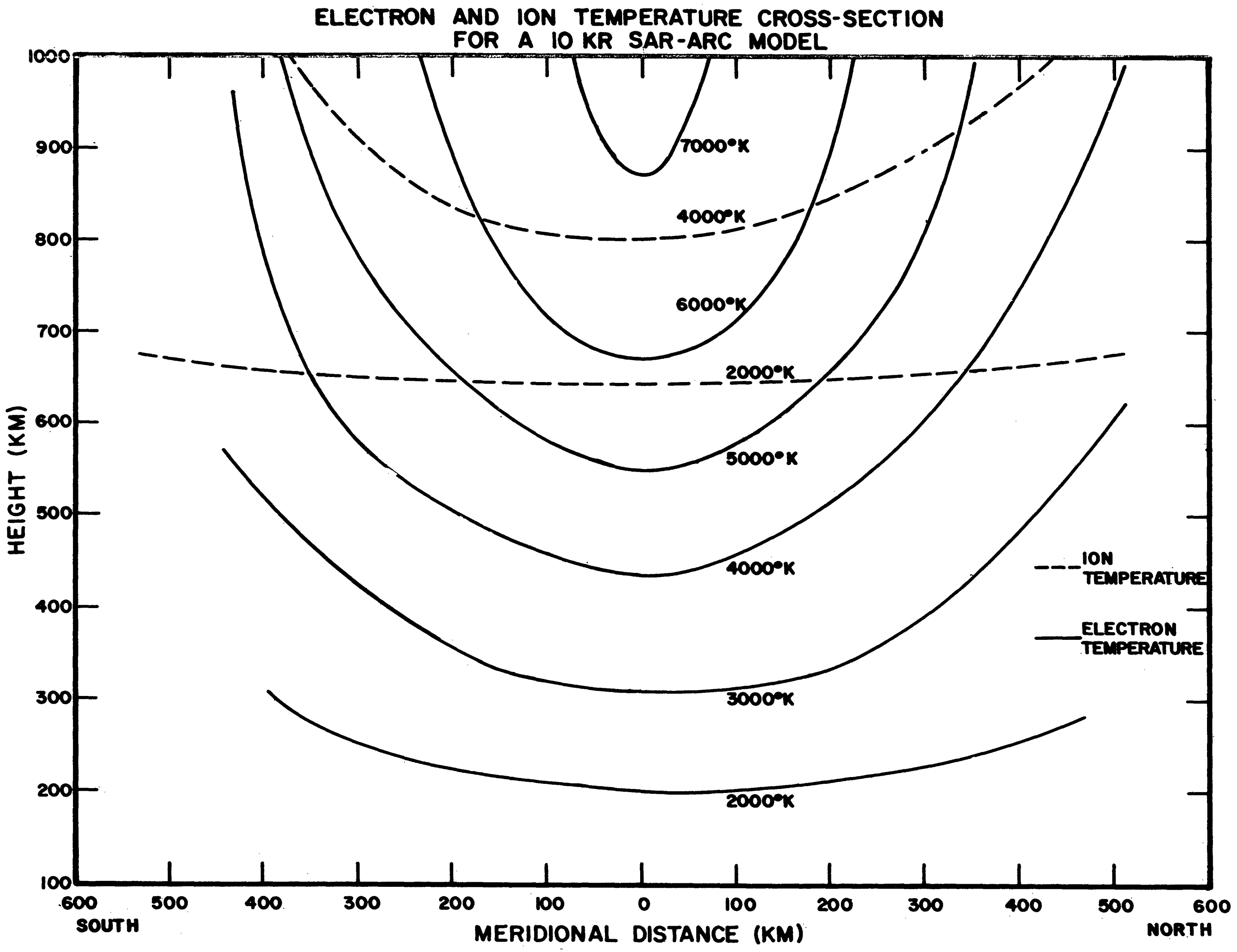

Fig. 13. Electron and ion temperature contours for a 10 KR SAR-arc model.

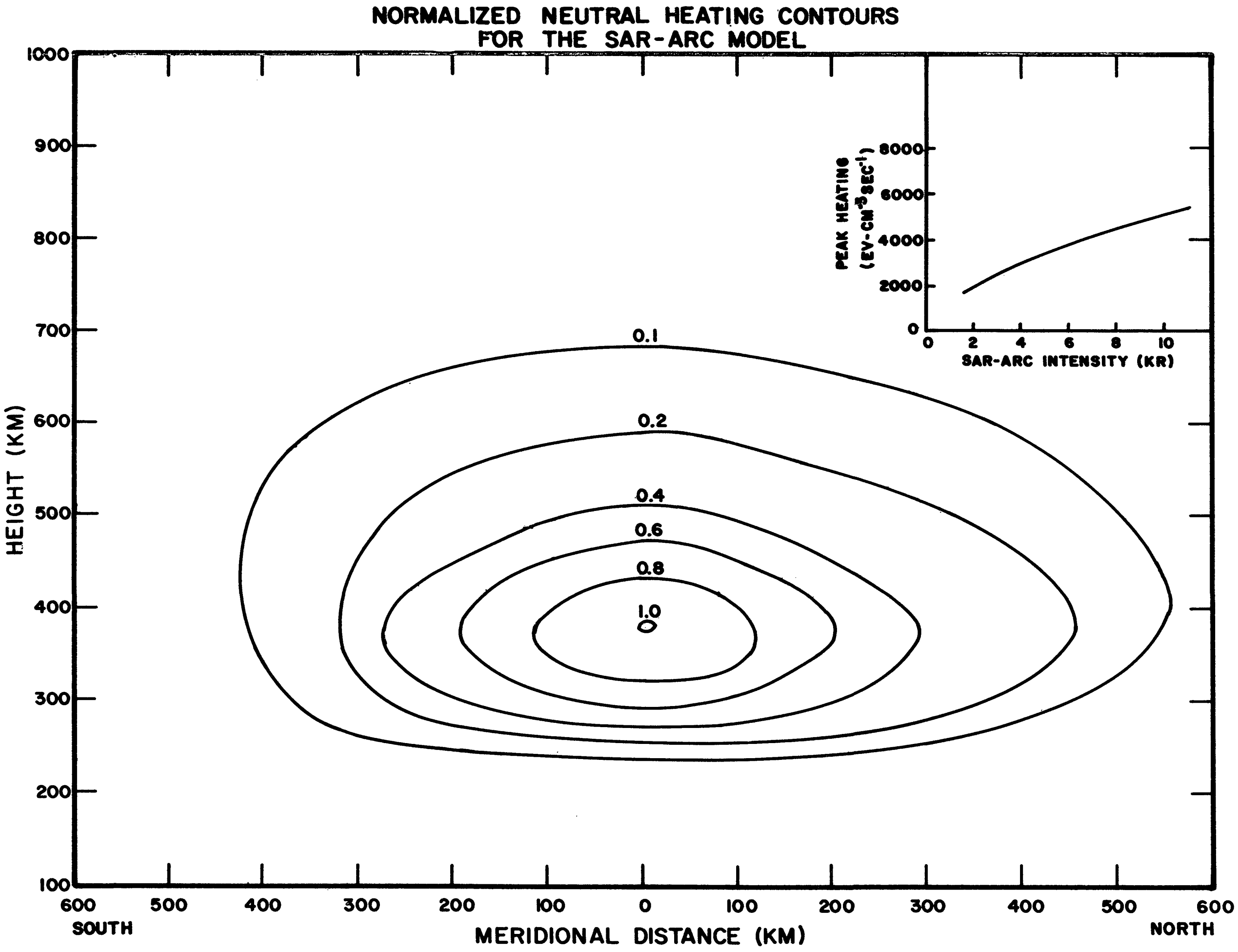

Fig. 14. Normalized neutral heating contours for the SAR-arc model

shape, width, and spectral purity of the SAR-arc can all be accounted for by the thermal conduction model and the agreement between the model and observed SAR-arc features is good. The two-dimensional model of the SAR-arc has been shown to adequately represent the conditions within the arc and, therefore, in the next chapters the neutral atmospheric temperature increase and dynamic response within the SAR-arc region will be investigated for the heating function generated by this model.

V. NEUTRAL TEMPERATURE INCREASE WITHIN THE SAR-ARC CONSIDERING CONDUCTION ALONE

Cole (1965, 1967) has argued that an atmospheric bulge should exist in the vicinity of the SAR-arc because of electron heating of the neutral gas within the arc. His estimate of the neutral gas temperature increase was based upon a solution to the one dimensional steady state neutral heat conduction equation and indicated a temperature rise of 100-700°K. In this chapter, the neutral gas temperature increase for the two-dimensional model of the SAR-arc, presented in Chapter 4, is calculated by considering thermal conduction alone. The heat conduction equation for the neutral gas, as it applies to the SAR-arc, is derived and various terms appearing in the equation are initially neglected in order to arrive at a steady state one-dimensional neutral heat conduction equation. This equation is solved and the relative importance of the neglected terms is then critically evaluated. These terms are (a) the 63μ radiational loss due to the excitation of the fine structure of the atomic oxygen ground state, (b) the time dependent terms, and (c) the term representing horizontal heat conduction within the SAR-arc. It will be shown that the first two terms can be neglected for the SAR-arc; however, the horizontal heat conduction term cannot. Therefore, the two-dimensional neutral heat conduction equation, appropriate to the SAR-arc model presented in Chapter 4, is analytically solved and the neutral gas temperature increase for this model is presented. Finally, the effect of this heating upon the neutral atmosphere is discussed.

5.1 HEAT CONDUCTION EQUATION FOR THE NEUTRAL ATMOSPHERE

The neutral heat conduction equation is derived from the first law of thermodynamics which can be expressed as (cf. Schlichting, 1962).

$$\rho C_p' \frac{dT_n}{dt} - \frac{dp}{dt} = \mathrm{div}\left(K_n \, \mathrm{grad}\, T_n\right) + \Phi + Q^* \qquad (5\text{-}1)$$

where ρ is the density, C_p' is the specific heat at a constant pressure, T_n is the neutral gas temperature, t is the time, p is the pressure, $\frac{d}{dt}$ is the total derivative $\left(\frac{\partial}{\partial t} + u\frac{\partial}{\partial x} + v\frac{\partial}{\partial y} + w\frac{\partial}{\partial z}\right)$, K_n is the conductivity of the neutral gas, Φ is a viscous dissipation function, and Q^* is a non-adiabatic heating rate per unit volume.

The SAR-arc has been observed to occur at mid-latitudes, extend over the night portion and possibly around the earth, and it has a 6300 Å intensity cross section as shown in Fig. 2. The two-dimensional model of the SAR-arc, discussed in Chapter 4, requires an enhanced electron temperature within the SAR-arc region to thermally excite the 6300 Å atomic oxygen emission line in the SAR-arc. The hot thermal electrons are cooled by elastic and inelastic collisions of electrons and ions with the neutrals thereby locally heating the neutral atmosphere in the SAR-arc region. The calculated neutral heating cross section, shown in Fig. 14, is assumed to remain constant in the longitudinal, or x, direction and extend around the earth, forming a mid-latitude belt of neutral atmospheric heating in the same region as the enhanced 6300 Å emission in the SAR-arc. Therefore, all derivatives with respect to x, the longitudinal direction, vanish. The u, v, and w components of the wind, appearing in equation (5-1) are neglected because only thermal conduction is considered in this chapter. The neutral gas heat conduction equation then becomes

$$\rho C_p' \frac{\partial T_n}{\partial t} - \frac{\partial p}{\partial t} = \frac{\partial}{\partial y}\left(K_n \frac{\partial T_n}{\partial y}\right) + \frac{\partial}{\partial z}\left(K_n \frac{\partial T_n}{\partial z}\right) + Q^* \qquad (5\text{-}2)$$

where $\frac{}{t}$ is the partial derivative with respect to time. Q^* here consists of three non-adiabatic quantities, (a) $L^*(z, T_n)$ the 63μ radiational loss from the excited fine structure levels in the ground state of atomic oxygen, (b) Q(y, z), the neutral heating caused by the SAR-arc, as given in Fig. 14, and (c) $Q_o(z)$, the heating required to maintain the basic thermospheric temperature profile. The importance of the various terms in this equation are now examined, but first the solution to the steady state one-dimensional neutral heat conduction equation for a neutral heating height profile given in Fig. 8 is determined.

5.2 SOLUTION TO THE STEADY STATE ONE-DIMENSIONAL NEUTRAL HEAT CONDUCTION EQUATION

The steady state one-dimensional neutral heat conduction equation is solved by assuming that the time dependent terms, the 63μ radiational loss term, $L^*(z, T_n)$, and the horizontal heat conduction terms in equation (5-2) can be neglected. The importance of each term is determined later, by using the neutral gas temperature profile obtained from the solution to this equation to evaluate the magnitude of each term. With these assumptions, the neutral heat conduction equation becomes

$$\frac{d}{dz}\left(K_n \frac{dT_n}{dz}\right) = -\left[Q(y,z) + Q_o(z)\right] \tag{5-3}$$

The thermal conductivity of the neutral gas is obtained from Harris and Priester (1962) and is

$$K_n(z) = \frac{\sum_i A_i\, n_i(z)}{\sum_i n_i(z)}\, T_n^{1/2}(z) = a(z)\, T_n^{1/2}(z) \tag{5-4}$$

where the coefficients for the major constituents have the values A(H) = 2.1×10^3, A(He) = 9×10^2, A(O) = 3.6×10^2, and $A(O_2) = A(N_2) = 1.8 \times 10^2$ ergs $\mathrm{cm}^{-1}\mathrm{sec}^{-1}\,{}^{\circ}\mathrm{K}^{-3/2}$.

Equation (5-3) can now be written as,

$$\frac{d}{dz}\left[\frac{2}{3}\, a(z)\, \frac{dT_n^{3/2}}{dz}\right] = -\left[Q(y,z) + Q_o(z)\right] \tag{5-5}$$

Integrating equation (5-5) with the requirement that no heat flows out of the upper atmosphere, $(dT_n^{3/2} / dz)_\infty = 0$, then

$$\frac{dT_n^{3/2}}{dz} = \frac{3}{2\,a(z)} \int_z^\infty \left[Q(y,z') + Q_0(z') \right] dz' \tag{5-6}$$

Integrating again and using the fact that $T^{3/2}(z_o)$, the temperature at the lower boundary, z_o, and $Q_o(z)$ combine to give the basic unperturbed thermospheric temperature $T_B(z)$ described in Appendix A, then the temperature height profile for the case of neutral heating within the SAR-arc becomes,

$$T_n(y,z) = \left[T_B^{3/2}(z) + \int_{z_o}^{z} \frac{3}{2a(z'')} \int_{z''}^{\infty} Q(y,z')\,dz'\,dz'' \right]^{2/3} \tag{5-7}$$

The neutral gas temperature increase for heating within the SAR-arc is obtained by evaluating equation (5-7), and using the neutral heating function given in Fig. 8 as the energy source. The results are shown in Fig. 15 for SAR-arcs of various intensities. The temperature increase is seen to be quite large but yet well within the 100-700°K range estimated by Cole (1967). An example which will be of interest later is for a 1.6KR SAR-arc which shows a neutral exospheric temperature increase of almost 200°K. The bulk of the 6300 Å atomic oxygen emission occurs near an altitude of 400 km and a large temperature increase occurs in that region. Because there is a velocity distribution of the emitting oxygen atoms which are associated with the neutral gas temperature, the 6300 Å emission line is doppler broadened. A measurement of the doppler width gives the temperature of the emitting region and this is a quantity of considerable interest. One way of experimentally determining the amount of neutral heating within the SAR-arc would be to measure the 6300 Å doppler profile in the

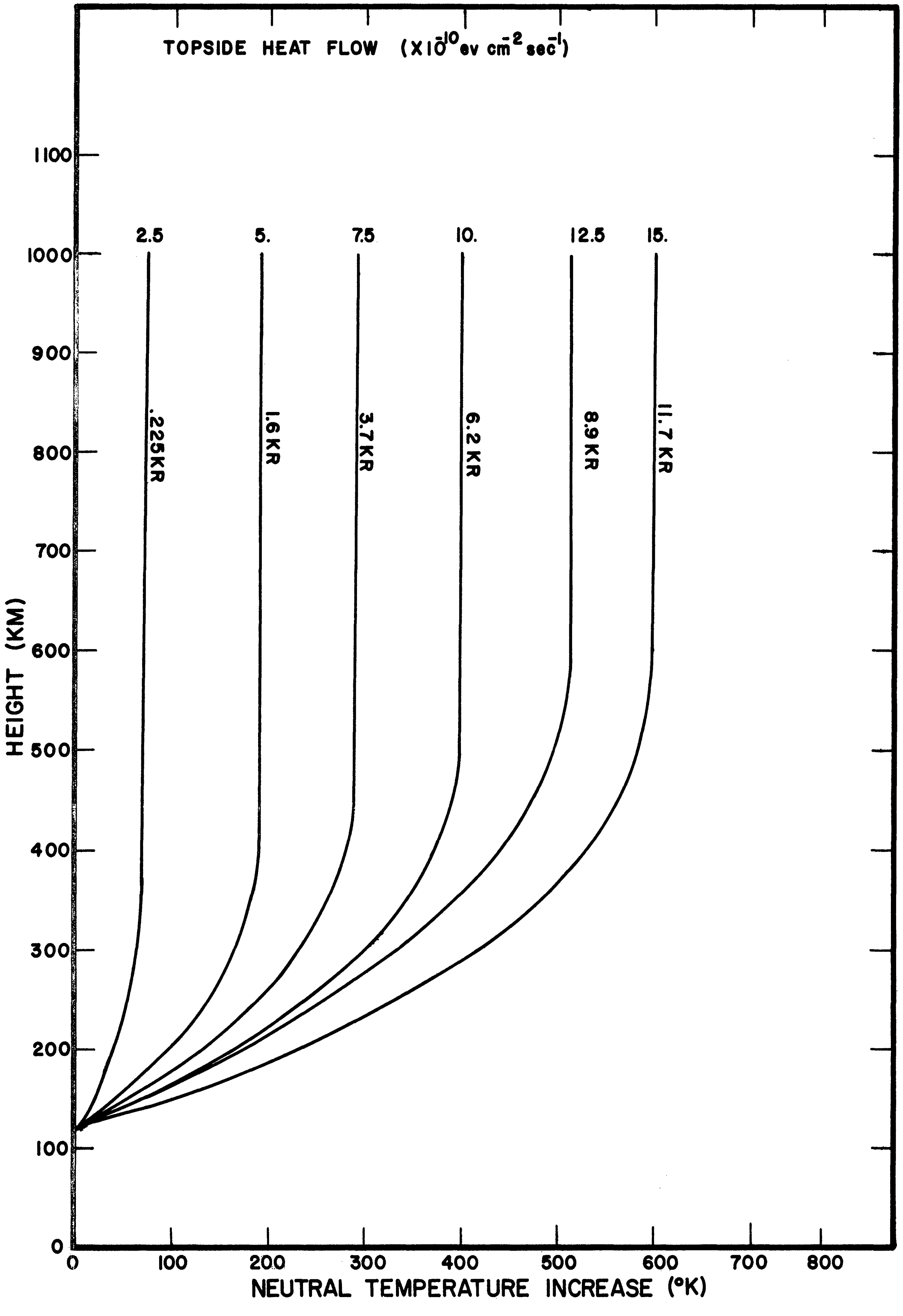

Fig. 15. Neutral temperature increase height profiles for SAR-arcs corresponding to case (1) conditions.

SAR-arc and compare it to a doppler profile obtained outside of that region. However, before this large neutral gas temperature increase can be accepted, the magnitude of the three neglected terms in the heat conduction equation must be investigated.

5.2.1 63μ RADIATION LOSS FROM THE FINE STRUCTURE OF ATOMIC OXYGEN

Bates (1951) has investigated the 63μ radiation loss process as a cooling mechanism in the thermosphere and has shown that it can be expressed as,

$$L^*(z,T_n) = 5.8\times 10^{-7} n(O) \left\{ \frac{3W_1\, EXP(-\frac{\epsilon_1}{k^* T_n})}{W_2 + W_1\, EXP(-\frac{\epsilon_1}{k^* T_n}) + W_0\, EXP(-\frac{\epsilon_0}{k^* T_n})} \right\} \tag{5-8}$$

where w_0, w_1, and w_2 are the statistical weights of the ground state of atomic oxygen, ϵ_0 and ϵ_1 are the energies of the excited states, k^* the Boltzmann constant, and T_n is the neutral gas temperature at a height z. The 63μ energy loss occurring from the basic thermospheric structure was first calculated and then compared to the energy loss from the perturbed atmosphere caused by heating within the SAR-arc. The difference was found to be negligible over all altitudes. The calculation was based on the assumption that the levels in the fine structure of the ground state of atomic oxygen are populated with an equilibrium statistical distribution which should be valid for heating by thermal F-region electrons. It is seen from equation (5-8) that the 63μ radiational loss increases at lower neutral gas temperatures and becomes most effective near the mesopause where low temperatures and a high concentration of atomic oxygen exist. Therefore, in the F-region where the neutral gas temperature is high and the atomic oxygen concentration is low by comparison, this term can be neglected from the thermodynamic energy equation. This conclusion is also verified by the calculations of Harris and Priester (1962), Lagos and Mahoney (1967), and Dickinson, Lagos, and Newell (1968).

5.2.2 TIME CONSTANTS FOR NEUTRAL HEATING WITHIN THE SAR-ARC.

The SAR-arc has been established as being persistent and stable with a time constant of 10 hours or more. Therefore, except for the initial formation phase of the SAR-arc, steady state conditions should rapidly be met. The electron gas in the ionosphere reacts rapidly to an energy source and gives rise to a uniformly distributed heat source in the neutral gas. The neutral gas reacts most rapidly to the heating in the upper atmosphere where the heat capacity of the neutral gas is low. At lower altitudes, the temperature does not increase as fast because the heat capacity is greater and therefore, the temperature increase is first apparent in the upper thermosphere and then progresses downward with time. Fig. 16 shows the relationship of the neutral temperature increase to the height of the lower boundary which is used in the solution to the steady state one-dimensional heat conduction equation. The temperature of the lower boundary is held fixed and the neutral heating above that altitude goes directly into raising the neutral gas temperature. Therefore, by showing a progression of steady state solutions as the lower boundary decreases in height, the time influence of the initial phase of the SAR-arc development may be appreciated. Some indication of the time for conduction to establish steady state conditions may be gained by calculating the time, Δt, that it takes a vertical column through the arc to reach a steady state temperature. This time is calculated by assuming that all of the heat locally deposited above a given lower altitude, z_o, goes directly into raising the neutral gas temperature from the basic thermospheric temperature profile $T_B(z)$ to the profile determined by the solution to the steady state neutral heat conduction equation with a lower boundary at z_o,

$$\Delta t = \int_{z_o}^{\infty} C_p \Delta T_n(z')\, dz' \Big/ \int_{z_o}^{\infty} Q(y, z')\, dz' \qquad (5\text{-}9)$$

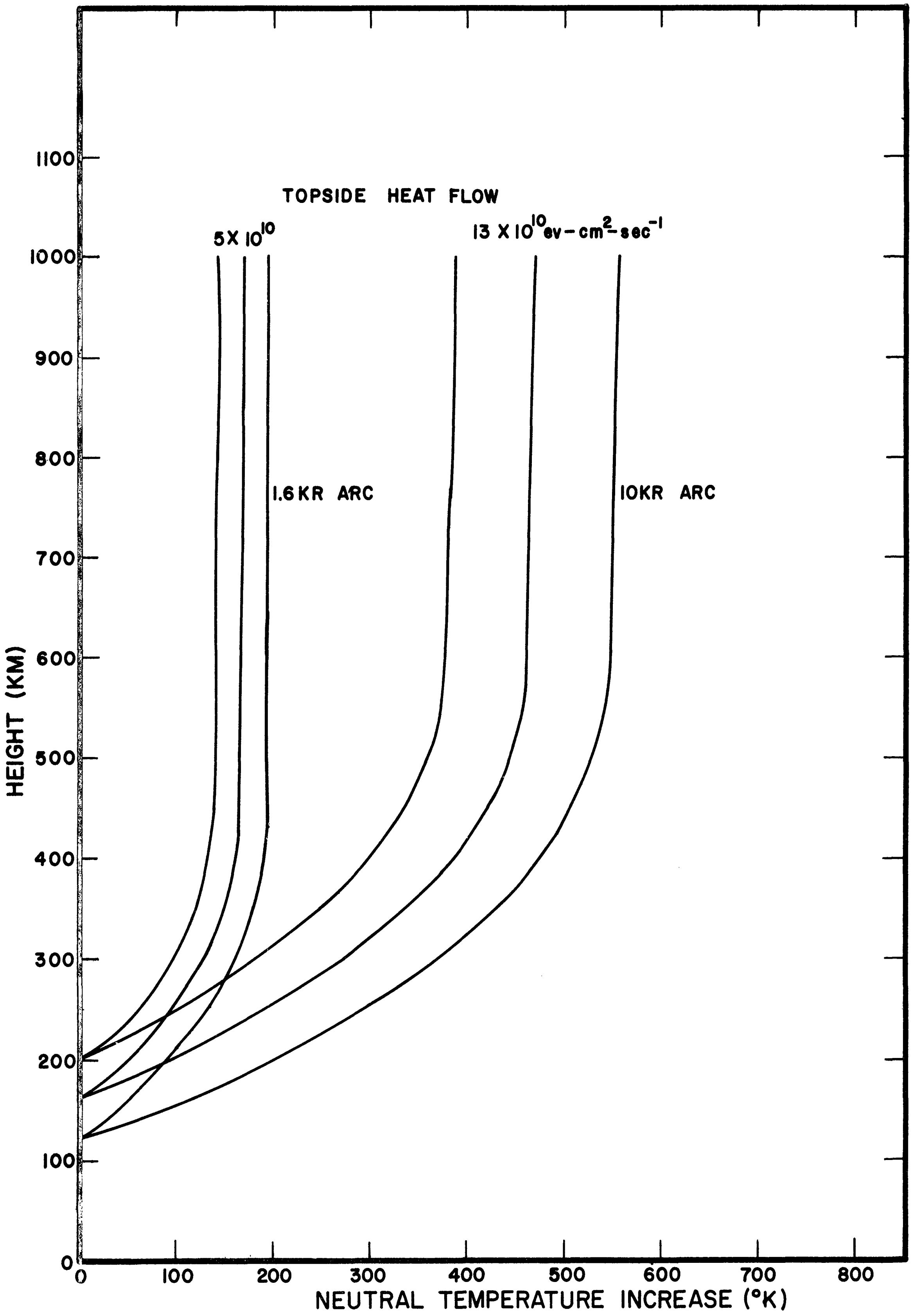

Fig. 16. Neutral temperature increase based on a solution to the one-dimensional neutral heat conduction equation and using various lower boundaries; case (1) conditions.

Here ΔT_n is the temperature increase at a given altitude due to neutral heating (as shown in Fig. 15), Q(y, z) is the volume rate of neutral heating, given in Fig. 8, and C_p is the specific heat at constant pressure. The value of C_p is obtained from Kauzmann (1966) and is

$$C_p = \left\{ \left[3.5 + \left(\frac{3337.}{T_n} \right)^2 EXP\left(- \frac{3337.}{T_n} \right) \right] n(N_2) + \left[3.5 + \left(\frac{2228.}{T_n} \right)^2 \cdot EXP\left(- \frac{2228.}{T_n} \right) \right] n(O_2) + 2.5\, n(O) + 2.5\, n(He) \right\} k^* \qquad (5\text{-}10)$$

where n(X) is the number density of species X, and k^* is the Boltzmann constant. The second term in the equation for molecular nitrogen and molecular oxygen is due to the excitation of the various vibrational levels of the molecules. Fig. 17 gives an indication of the time required for the atmosphere at that altitude to reach a steady state. At 200 km steady state conditions are met after 2 hours and after 10 hours, the time constant of the SAR-arc, steady state conditions exist down to a height of 140 km. Therefore, the lower boundary condition for the neutral heat conduction equation can be specified as $\Delta T_n = 0$ at 120 km. The steady state solution to the neutral heat conduction equation is considered to be valid for the later stages of the arc by assuming a constant heat flow into the ionosphere from the magnetosphere during the lifetime of the SAR-arc. The upper thermosphere is seen to respond rapidly to the neutral heating and because the SAR-arc is stable and persistent for 10 hours or more, the time dependent terms in the neutral heat conduction equation can be neglected. Lagos and Mahoney (1967) have numerically solved the one-dimensional time dependent neutral heat conduction equation and have shown that the neutral temperature in the lower thermosphere does not vary with the diurnal heating of the upper atmosphere. However, the upper thermosphere does respond and this is consistent with the time constants shown in Fig. 17.

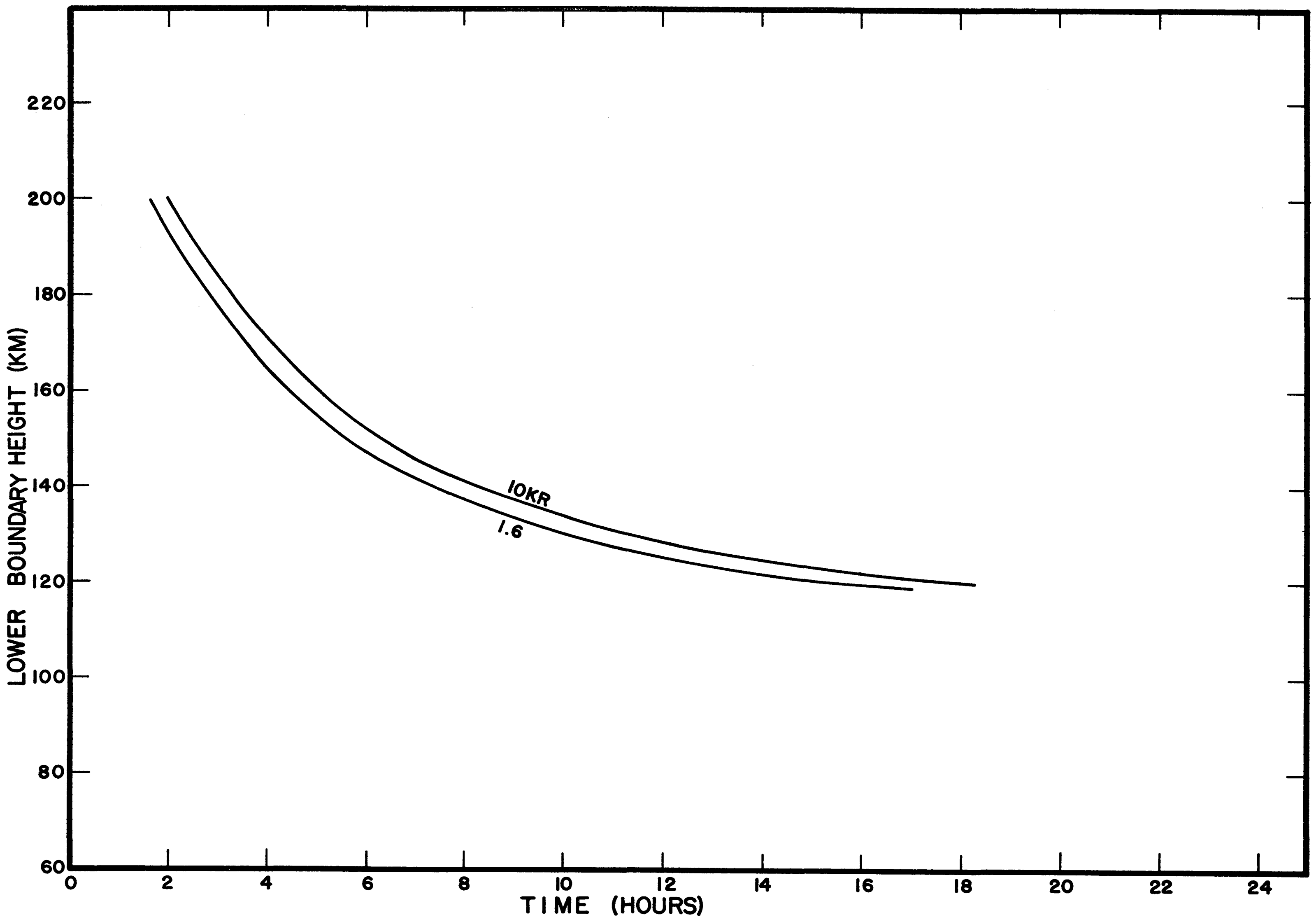

Fig. 17. Time for heat to be conducted in the neutral gas to various lower boundaries.

5.2.3 HORIZONTAL HEAT CONDUCTION IN THE SAR-ARC

Horizontal heat conduction was neglected in order to obtain a solution to the one-dimensional neutral heat conduction equation and evaluate the magnitude of the 63μ radiational loss and time dependent terms in that equation. It was shown in the previous sections that these two terms can be neglected for the case of the SAR-arc and now the question of horizontal heat conduction is examined. The curves for the neutral gas temperature increase, shown in Fig. 15, are used to construct the two-dimensional contours of the temperature increase within the SAR-arc in a manner similar to that described in Chapter 4. This is possible because the neutral heating height profiles, shown in Fig. 8, all generally peak at the same altitude and the profiles all have a constant shape. The normalized contours of the neutral temperature increase are shown in Fig. 18 and the peak temperature increase is shown as a function of arc intensity in the lower right corner of the figure. For a 10 KR SAR-arc the peak neutral gas temperature increase is near 500°K in the arc center at a height of 600 km. The figure indicates that a considerable amount of horizontal conduction exists because of the large horizontal temperature gradient and high thermal conductivity in the arc. Because the atmosphere is in diffusive equilibrium, the temperature pattern causes a large pressure gradient which in turn requires a large atmospheric response. Before the question of the atmospheric response is considered, a solution to the steady state two-dimensional neutral heat conduction equation is presented to show the magnitude and pattern of the neutral gas temperature increase due to conduction alone.

5.3 STEADY STATE TWO-DIMENSIONAL HEAT CONDUCTION EQUATION

The one-dimensional solution to the neutral heat conduction equation has been valuable in examing the importance of the 63μ radiation and

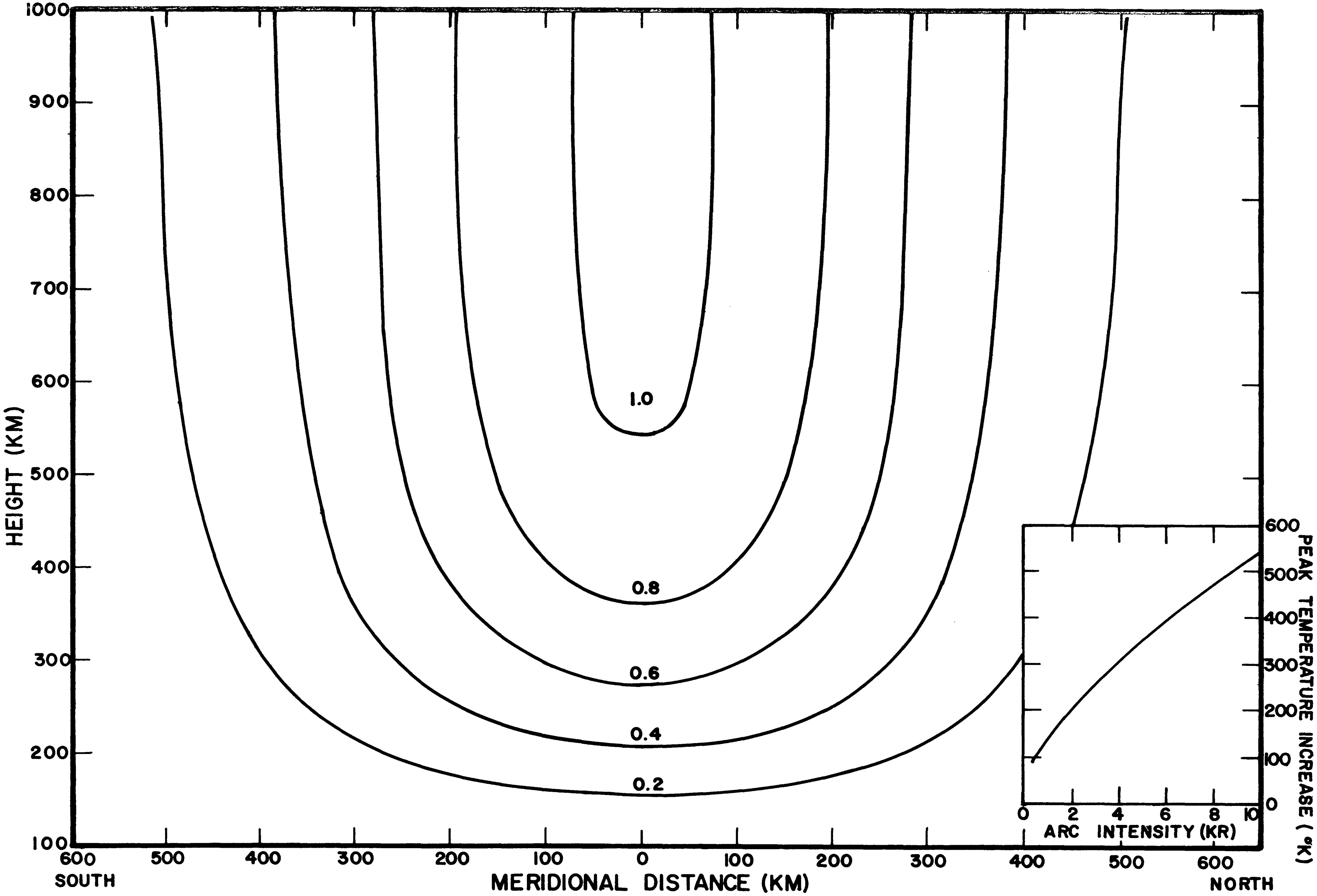

Fig. 18. Normalized contours of neutral temperature increase in a SAR-arc and based upon a solution to the one-dimensional neutral heat conduction equation at various meridional distances.

the conduction time constants, however, the neutral gas temperature increase was large and indicated considerable lateral heat conduction especially at high altitudes where conduction is most effective. Lateral conduction transports heat away from the center of the SAR-arc and lowers the peak temperature increase. Therefore, in this section the two-dimensional steady state neutral heat conduction equation is solved for the neutral heating values of the SAR-arc model given in Fig. 14 as the only heat source.

The heat conduction equation (5-3) can now be written as

$$\frac{\partial}{\partial y}\left(K_n \frac{\partial T_n}{\partial y}\right) + \frac{\partial}{\partial z}\left(K_n \frac{\partial T_n}{\partial z}\right) = -\left[Q(y,z) + Q_o(z)\right] \tag{5-11}$$

where Q(y, z) is the neutral heating function, given in Fig. 14, and $Q_o(z)$ again represents the heating necessary to establish the basic thermospheric structure. The thermal conductivity will have the same form as equation (5-4),

$$K_n = k T_n^{1/2} \tag{5-12}$$

however, it is assumed that k is now a constant over the altitude range under consideration. As the composition ratios of the various neutral constituents change, k will vary slightly, however, an average value of the coefficient is used here and this assumption should not change the results significantly. Equation (5-11) is now written as

$$\frac{\partial}{\partial y}\left(\frac{\partial T_n^{3/2}}{\partial y}\right) + \frac{\partial}{\partial z}\left(\frac{\partial T_n^{3/2}}{\partial z}\right) = -\frac{3}{2k}\left[Q(y,z) + Q_o(z)\right] \tag{5-13}$$

Now let

$$T_n^{3/2}(y,z) = T_B^{3/2}(z) + \phi(y,z) \tag{5-14}$$

where $T_B(z)$ is the basic thermospheric temperature profile established by the heating function, $Q_o(z)$, and $\varphi(y, z)$ is a term which is related to the temperature departure from the basic temperature profile due to neutral heating within the SAR-arc. The actual change in the neutral gas temperature is

$$\Delta T_n(y,z) = \left[T_B^{3/2}(z) + \varphi(y,z) \right]^{2/3} - T_B(z) \tag{5-15}$$

Now by subtracting the superimposed equation establishing the basic thermospheric temperature profile

$$\frac{\partial^2 T_B^{3/2}(z)}{\partial z} = -\frac{3}{2k} Q_0(z) \tag{5-16}$$

the heat conduction equation for neutral heating within the SAR-arc becomes,

$$\nabla^2 \varphi(y,z) = -\frac{3}{2k} Q(y,z) \tag{5-17}$$

where ∇^2 is the Laplacian. Equation (5-16) is not of interest because the basic temperature profile, $T_B(z)$ is assumed to already exist. Equation (5-17) gives the two-dimensional pattern of the temperature increase due to SAR-arc heating. The vertical boundary conditions for equation (5-17) require that no heat flows out of the top of the atmosphere and the temperature is held fixed at the lower boundary, 120 km. The lateral boundary conditions require that at great distances from the arc center a boundary is encountered at both the northern and southern extremities where no lateral heat flow occurs. Thus, the steady state two-dimensional neutral heat conduction equation reduces to the following boundary value problem,

$$\nabla^2 \varphi(y,z) = -\frac{3}{2k} Q(y,z) \tag{5-18}$$

with boundary conditions

$$\begin{aligned} \varphi &= 0 & \text{at} \quad & z = z_o \\ \frac{\partial \varphi}{\partial z} &= 0 & \text{as} \quad & z \longrightarrow \infty \\ \frac{\partial \varphi}{\partial y} &= 0 & \text{as} \quad & y \longrightarrow \pm \infty \end{aligned} \tag{5-19}$$

The details of the solution to equation (5-18) with boundary condition (5-19) are presented in Appendix C. Use is made of the fact that the neutral heating contours for the model SAR-arc, shown in Fig. 14, closely approximate ellipses and, therefore, can be related to a similar problem in potential theory. The neutral gas temperature is held constant over the lower boundary by placing symmetrical image ellipses opposite each other across the lower boundary so that the heating contribution from one is cancelled by the cooling contribution from the image at the boundary. The image ellipses also act as a dipole at large distances from the SAR-arc center thereby satisfying the remaining boundary conditions. The increase in the neutral temperature, caused by heating within the SAR-arc, is obtained by considering a thin elliptical shell of neutral heating and calculating the contribution that the shell and its image made toward the neutral gas temperature increase. The incremental gas temperature increase is then integrated over all elliptical shells giving the total neutral gas temperature increase within the SAR-arc. The analytic expressions representing the temperature increase are given in equations C-17 through C-19.

The increase in the neutral gas temperature caused by the heating shown in Fig. 14 for the two-dimensional model of the SAR-arc, was calculated according to the method outlined in Appendix C and Fig. 19 shows the results. Because of the linearity of the problem, the temperature increase is normalized and the peak temperature rise is related to the SAR-arc peak intensity indicated in Fig. 14. When comparing these results to those obtained from

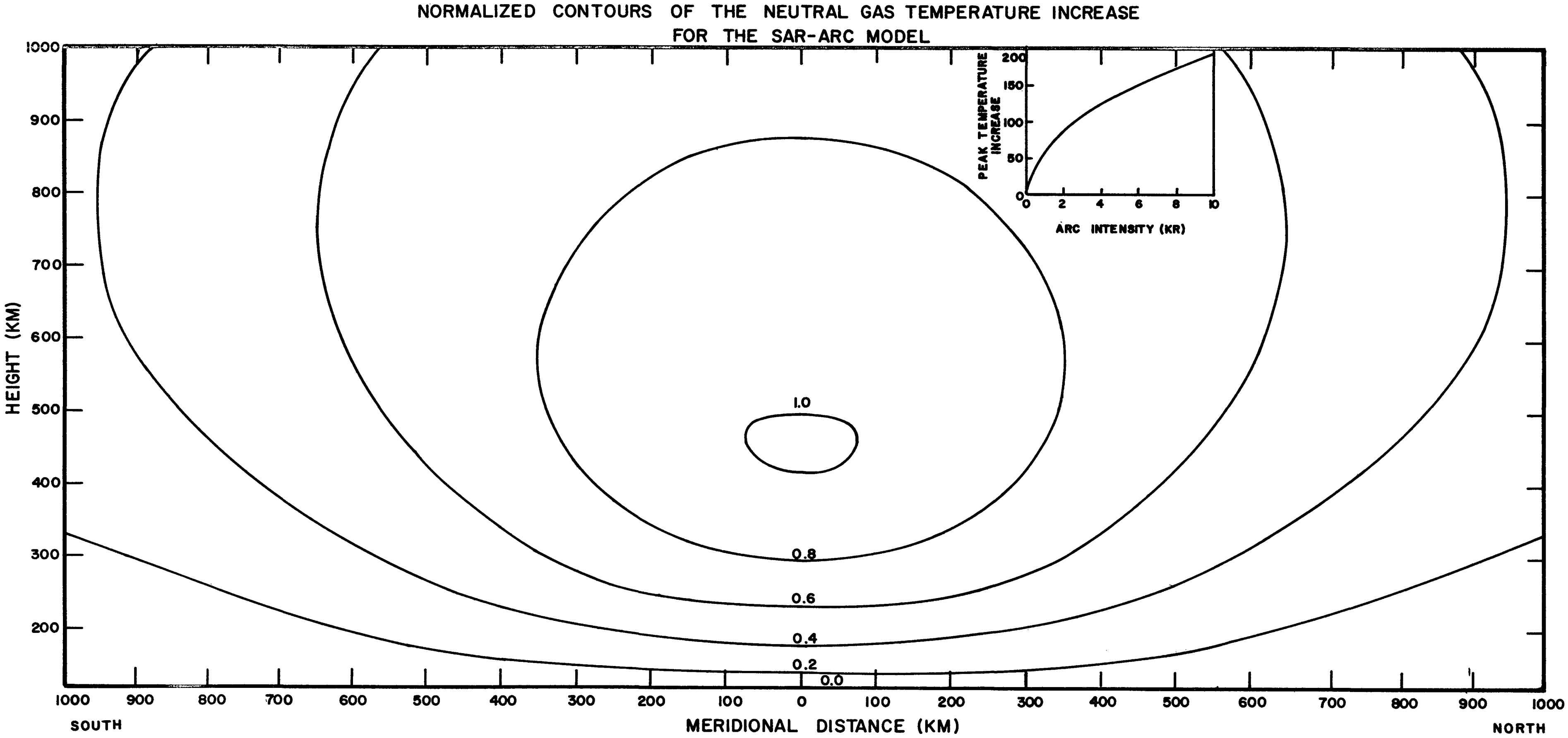

Fig. 19. Normalized contours of the neutral gas temperature increase for the SAR-arc model based upon a solution to the two-dimensional neutral heat conduction equation.

the one-dimensional solution, shown in Fig. 18, it is apparent that lateral heat conduction plays an important role in transferring heat out of the SAR-arc region and for a 10 KR SAR-arc the neutral gas temperature increase is reduced from 550°K to 200°K. It is also evident that conduction is very effective in the upper thermosphere spreading the heat beyond the outer edges of the SAR-arc, which is defined by the enhanced 6300 Å radiation, and reducing the peak temperature increase. Thermal conduction is not so effective in the lower thermosphere causing the heat to be more locally confined. In general instead of having a localized high temperature core in the immediate vicinity of the observed SAR-arc, the heat distribution over a broader region causes a much lower temperature increase in the SAR-arc region.

The results presented in this chapter are based upon the assumption that heat conduction is the dominant process in the thermosphere and therefore the other heat transport terms in the thermodynamic equation could be neglected. However, it was shown that the neutral gas temperature increase within the SAR-arc is large and also forms large temperature gradients. The large temperature variations cause pressure gradients to develop, which in turn set the neutral atmosphere in motion. As a result, the solutions presented in this chapter are an upper bound on the temperature increase within a SAR-arc. When motion is considered, part of the energy raising the neutral gas temperature is used to drive the neutral atmosphere. In the next chapter, the combined equations of motion, continuity, and thermodynamics are considered and an approximate solution is obtained which not only establishes the neutral gas temperature increase but also gives the atmospheric response caused by neutral heating within the two-dimensional model of the SAR-arc.

VI. ATMOSPHERIC RESPONSE TO A SAR-ARC

The results described previously have shown that when thermal conduction is considered as the only heat transport mechanism, the neutral gas temperature within the SAR-arc increases significantly. The temperature pattern for the two-dimensional SAR-arc model also shows the existence of large lateral temperature gradients within the arc region. Because the neutral atmosphere is in diffusive equilibrium, the increased temperature causes a pressure gradient, which then sets the atmosphere in motion. In this chapter, the atmospheric response to the neutral heating within the SAR-arc is investigated and the effect of this response upon the arc dynamics is discussed. The equations of motion, continuity, and thermodynamics governing the neutral gas motion in the SAR-arc region are formulated and the solutions to two special cases and an approximate solution to the full set of equations are presented. The first case considered is a lower bound to the circulation pattern and is obtained by neglecting thermal conduction and calculating the motion generated by the adiabatic expansion of the atmosphere without allowing the neutral gas temperature to increase. The second case represents an upper bound, and utilizes the temperature pattern which was obtained by considering thermal conduction alone in order to derive the pressure pattern for which the winds are solved. An approximate solution to the full set of equations, governing the atmospheric response within the SAR-arc region, is then constructed from the solutions of the two special cases. Finally, the ionospheric effects caused by the winds and the heating of the whole upper atmosphere by SAR-arcs during times of magnetic storms are discussed.

6.1 EQUATIONS GOVERNING THE ATMOSPHERIC RESPONSE

Problems dealing with the dynamics of the neutral gas in the thermosphere have received considerable attention recently, with particular emphasis on the motion generated by the diurnal bulge of atmospheric density. Some of the early work on the problem of neutral air movements in the upper atmosphere is due to King (1964), King-Hele (1964), Hines (1965), and Newell (1966). More recently Kohl and King (1967), Geisler (1966, 1967) and Lindzen (1966, 1967) have all examined the worldwide movements of the neutral gas in the thermosphere which are caused by the diurnal heat source. The diurnal pressure gradients driving the neutral atmosphere were derived from the thermospheric models of Jacchia (1964) and Harris and Priester (1962) and the magnitude of the calculated winds was large, of the order of hundreds of meters/sec, and was shown to be influenced by the viscous, Coriolis, pressure, inertial, and ion drag forces. Lagos (1967) has performed a scale analysis of the equations governing the planetary tidal motions in the thermosphere and found that the adiabatic heating and cooling terms in the thermodynamic equation are of the same order as the main terms considered in these hydrodynamic equations. Dickinson, Lagos, and Newell (1968) and Dickinson and Geisler (1968) considered these important terms when they calculated the atmospheric response to the diurnal pressure gradients determined from the thermospheric models of Jacchia (1965a, 1965b), and Lagos and Mahoney (1967). Their results show that the adiabatic heating and cooling by vertical winds, which are caused by the positive and negative divergence of the horizontal motion, have a very important influence on the motion of the neutral gas and also act as a heat source in the thermosphere. In fact, the computed adiabatic heating and cooling by vertical motion agrees in amplitude and phase with the so-called "second heat source" required in the Harris and Priester (1962) computations.

Observations which would allow the determination of the pressure gradients existing within the SAR-arc are not available at this time. Therefore, it is necessary to start with the neutral heat input into a SAR-arc and solve for the pressure gradient, temperature increase, and winds from the basic equations which govern the neutral gas motion in the thermosphere. This approach has been considered by Volland (1967), Lagos (1967), and Dickinson, Lagos, and Newell (1968) in solving for the response of the neutral atmosphere to the diurnal heating of the thermosphere.

The general equations of momentum, mass, and energy conservation relative to a rotating system in an x, y, and z Cartesian coordinate system are obtained from the Navier-Stokes equations (c. f. Schlichting, 1962) extended to take into account the Coriolis force and ion drag (Lagos, 1967) and may be written as

$$\rho \frac{d\vec{V}}{dt} + 2\rho\Omega\vec{k} \times \vec{V} = -\text{grad}\, p - \rho\vec{g} + (\vec{D} + \vec{E})\rho \qquad (6\text{-}1)$$

$$\frac{\partial\rho}{\partial t} + \text{div}(\rho\vec{V}) = 0 \qquad (6\text{-}2)$$

$$C_p \frac{dT_n}{dt} - \frac{dp}{dt} = \text{div}(K_n\, \text{grad}\, T_n) + \Phi + Q' \qquad (6\text{-}3)$$

$$p = \rho R T_n \qquad (6\text{-}4)$$

where R = the gas constant

ρ = density

$\vec{V}$ = velocity = $u\vec{i} + v\vec{j} + w\vec{k}$ ($\vec{i}$, $\vec{j}$, and $\vec{k}$ are in the east, north, and upward direction respectively)

u = zonal component of motion

v = meridional component of motion

w = vertical component of motion

Ω = the rate of rotation of the earth

p = pressure

$\vec{g}$ = acceleration of gravity

$\vec{D}$ = ion drag force

$\vec{E}$ = viscous drag force

C_p = specific heat at constant pressure, (equation 5-10)

T_n = neutral gas temperature

K_n = thermal conductivity of the neutral gas, (equation 5-4)

Φ = viscous dissipation function

Q' = non-adiabatic heating rate

Equation (6-1) is the equation of momentum, (6-2) is the equation of continuity, (6-3) is the thermodynamic equation, and (6-4) is the ideal gas equation of state. These equations are based upon the assumption of a continuous fluid and apply up to an altitude of 600-700 km, where the mean free path between neutral particle collisions approaches the atmospheric scale height. Above this altitude the hydrodynamic concept breaks down and the equations are no longer valid.

These equations are now reduced to a form which is appropriate to the SAR-arc. It was shown, in Chapter 5, that thermal equilibrium is rapidly approached in the SAR-arc because the arc is persistent and stable and the conduction time constant is short compared to the lifetime of the arc. Therefore, except for the initial SAR-arc formation phase, steady state conditions are assumed to exist and the time dependent terms in equations (6-1) through (6-4) are neglected. It was also discussed, in Chapter 5, that the SAR-arc appears as a belt of neutral heating existing at mid-latitudes and extending around the earth in an approximate east-west direction. As a result, all derivatives in the x direction can be neglected. The non linear acceleration terms in the equations of motion, representing a transport of momentum by fluid motion, are also neglected. These terms will be important if the magnitude of the winds calculated from the linear set of equations exceeds 100 M sec $^{-1}$ (Kohl and King, 1967).

In addition, because the vertical velocities are generally small the vertical equation of motion will reduce to the normal diffusive equilibrium equation in the thermosphere. With these assumptions equations (6-1) through (6-4) are written as

$$-fv = \left(D_x + E_x\right) \tag{6-6}$$

$$fu = -\frac{1}{\rho}\frac{\partial p}{\partial y} + \left(D_y + E_y\right) \tag{6-7}$$

$$p(y,z) = \sum_i p_i(z_0)\, EXP\left[-\int_{z_0}^{z} \frac{m_i g(z')}{k^* T_n(y,z)}\, dz'\right] \tag{6-8}$$

$$\frac{\partial(\rho v)}{\partial y} + \frac{\partial(\rho w)}{\partial z} = 0 \tag{6-9}$$

$$C_p v \frac{\partial T_n}{\partial y} + w\left(C_p \frac{\partial T_n}{\partial z} + \rho g\right) = \frac{\partial}{\partial y}\left(K_n \frac{\partial T_n}{\partial y}\right) + \frac{\partial}{\partial z}\left(K_n \frac{\partial T_n}{\partial z}\right) + Q' \tag{6-10}$$

where the neutral gas thermal conductivity is given by equation (5-4), f is the Coriolis parameter ($2\Omega \sin \theta$), θ is the geographic latitude, $D_{x,y}$ and $E_{x,y}$ represent the x and y components of the ion drag and viscous force respectively, m_i is the mass of the i^{th} species of the neutral gas, k^* is the Boltzmann constant and $p_i(z_o)$ is the partial pressure of the i^{th} atmospheric species at the lower boundary which is assumed to be a constant.

There are two main retarding forces acting on the air movements in the thermosphere at F-region heights and these are the frictional drag of ions and a viscous drag resulting from a decrease of density with altitude. The ion drag force arises because the ions cannot be easily moved by mechanical forces in directions perpendicular to the earth's magnetic field. The ion drag term is assumed to take the form (Rishbeth, Megill, and Cahn, 1965; Geisler, 1966, 1967; Kohl and King, 1967; Bramley, 1967; Lindzen, 1967),

$$\vec{D} = \frac{\rho_i}{\rho_n} \nu_i \left(\vec{V}_i - \vec{V}_n \right) \tag{6-11}$$

where $\vec{V}_n$ is the velocity of the neutral gas, $\vec{V}_i$ is the velocity of the ion gas, ν_i is the ion-neutral collision frequency, ρ_i is the ion density, and ρ_n is the neutral density. It is assumed here that no movement of the ion gas perpendicular to the geomagnetic field lines is possible, which is equivalent to taking the ion gyro frequency to be infinitely large compared to the ion-neutral collision frequency ν_i. Bramley (1967) has shown that this assumption is valid above 150 km, but breaks down for altitudes lower than 150 km. The ionization can, however, be forced by the neutral gas to move along the geomagnetic field line, and it is assumed that the ions will travel at a velocity equal to the component of the wind velocity along the direction of the geomagnetic field. Also over the range of altitude where ion drag is significant, atomic oxygen is the major neutral constituent and atomic oxygen ions are the major ionic constituent. As a consequence ρ_i/ρ_n may be replaced by N_i/N_n, the concentration ratio of ions to neutrals. Now the x and y components of the ion drag force can be written as

$$D_x = -N_i \left(\frac{\nu_i}{N_n} \right) u = -\lambda \cdot u$$

$$D_y = -N_i \left(\frac{\nu_i}{N_n} \right) \cdot \sin^2 I \cdot v = -\lambda \cdot \sin^2 I \cdot v \tag{6-12}$$

where I is the magnetic dip angle and λ is an ion drag parameter. The quantity (ν_i/N_n) is the ratio of the ion-neutral particle collision frequency to the neutral particle concentration and is very nearly a constant over the altitude range of interest. It has the value $7\text{x}10^{-10}\text{cm}^3\text{sec}^{-1}$ (Dalgarno, 1964). The viscous drag of an atmosphere in motion is determined by the product of the kinematic viscosity of the fluid and the divergence of the velocity gradient and is expressed as

$$\vec{E} = \frac{\mu}{\rho} \nabla^2 \vec{V} \tag{6-13}$$

where V is the velocity vector and ∇^2 is the Laplacian. The kinematic viscosity μ/ρ increases exponentially with altitude and becomes very important in the upper thermosphere. Viscosity tends to inhibit curvature in the velocity profile, and it is useful in defining an upper boundary condition to the equations of motion. At high altitudes the viscous drag force is very large, and the derivative of the velocity will be a constant and that constant must be zero or the neutral gas velocity will increase indefinitely with altitude.

The lateral viscous drag component, due to a variation of the velocity gradient in the y-direction, is neglected for simplicity; the magnitude of this term should be quite small in comparison with the vertical component. Equation (6-13) now becomes

$$E_x = \frac{\mu}{\rho} \frac{\partial^2 u}{\partial z^2}$$

$$E_y = \frac{\mu}{\rho} \frac{\partial^2 v}{\partial z^2} \tag{6-14}$$

where it is assumed that μ is a slowly varying function of z and because atomic oxygen is the major atmospheric constituent in the SAR-arc region, it has the value $3.34 \times 10^{-6}\ T_n^{0.61}$ gm cm^{-1}sec^{-1} (Dalgarno and Smith, 1962).

With these assumptions the equations governing the atmospheric motion caused by heating within the SAR-arc become,

$$\frac{\mu}{\rho} \frac{\partial^2 u}{\partial z^2} + f v - \lambda u = 0 \tag{6-15}$$

$$\frac{\mu}{\rho} \frac{\partial^2 v}{\partial z^2} - f u - \lambda \sin^2 I\, v = \frac{1}{\rho} \frac{\partial p}{\partial y} \tag{6-16}$$

$$\frac{\partial}{\partial y}(\rho v) + \frac{\partial}{\partial z}(\rho w) = 0 \qquad (6\text{-}17)$$

$$P(y,z) = \sum_{i} p_i(z_0)\, \mathrm{Exp}\left[-\int_{z_0}^{z} \frac{m_i\, g(z')}{k^* T_n(y,z')}\, dz'\right] \qquad (6\text{-}18)$$

$$-\frac{2}{3} k \nabla^2 T_n^{3/2} + C_p v \frac{\partial T_n}{\partial y} + w\left(C_p \frac{\partial T_n}{\partial z} + g\rho\right) = Q(y,z) \qquad (6\text{-}19)$$

where λ is a parameter defined in equation (6-12). The boundary conditions for the SAR-arc problem are

(1) The zonal, u, and the meridional, v, components of the wind at the lower boundary are zero. Lindzen (1967) has shown that even if there exists a nonzero velocity at the lower boundary, its effect on the solution becomes small within a few kilometers above that boundary.

(2) The temperature, $T_n(120)$, and pressure, $P_i(120)$, are both constant values at the lower boundary.

(3) The upper boundary conditions are that the fluxes of momentum, heat, and mass vanish in the limit as $z \to \infty$;

$$\frac{\partial u}{\partial z} \longrightarrow 0, \quad \frac{\partial v}{\partial z} \longrightarrow 0, \quad \frac{\partial T_n}{\partial z} \longrightarrow 0, \text{ and } \rho w \longrightarrow 0$$

(4) The lateral boundary conditions require a vanishing lateral heat flux at distances large from the SAR-arc center;

$$\partial T_n / \partial y \longrightarrow 0 \quad \text{as} \quad y \longrightarrow \pm \infty$$

The solution to this set of equations and boundary conditions gives the pressure gradient, temperature pattern, and winds for the neutral atmosphere in the arc region. The set of equations were linearized, however, no closed form solution was found. Even when the vertical height coordinate was changed into log of pressure coordinates, no advantage was apparent and a closed form solution was still not possible. Therefore, the basic set of equations were left in Cartesian coordinates to make use of the analytic solution to the neutral heat conduction equation presented in Appendix C and construct an approximate solution to the set of equations. Two special solutions to the basic set of equations are first presented which give an upper and lower bound to the circulation pattern and magnitude of the winds. These two solutions are then used to construct the approximate solution.

6.2 DIRECT ATMOSPHERIC RESPONSE TO NEUTRAL HEATING

Thermal conduction in the neutral gas is neglected in this first "limiting solution" and the neutral SAR-arc heating is considered to directly generate the atmospheric wind system without causing the neutral gas temperature to increase. It is assumed that the entire thermosphere has the properties which are defined by the atmospheric model, described in Appendix A, with a basic thermospheric temperature profile, $T_B(z)$. With this assumption, all derivatives of the atmospheric properties in the x and y direction vanish. The vertical motion is driven by the adiabatic heating and cooling term in the thermodynamic equation, and it is determined from equation (6-19) by neglecting terms (a) and (b) and solving for w directly to give

$$w = \frac{Q(y,z)}{\left[C_p(z)\frac{\partial T_B(z)}{\partial z} + \rho(z) g(z)\right]} \tag{6-20}$$

where Q(y, z) is the two-dimensional neutral heating function given in Fig. 14 for the SAR-arc model. As was shown in Chapter 5, term (a) gives the thermal conduction for only the perturbation neutral heating caused by the SAR-arc and is zero in this case because a neutral gas temperature increase is not allowed. This vertical wind is generated as an atmospheric response to local neutral heating within the SAR-arc. It transports the heated gas upward to lower pressures and it is adiabatically cooled in the process. Equation (6-20), therefore, represents a balance between the rate at which the neutral gas is locally heated and the rate by which the heated gas is adiabatically cooled in order to maintain a constant basic vertical temperature profile, $T_B(z)$. Equation (6-17) can be neglected here, because the vertical pressure gradient is determined by the neutral model atmosphere. The meridional velocity, v, caused by the divergence of the vertical mass flow is determined by integrating the continuity equation (6-17) which gives

$$v(y) = \frac{1}{\rho(z)} \int_0^y \frac{d[\rho(z)\, w(y', z)]}{dz}\, dy' \qquad (6\text{-}21)$$

The limits of integration are determined by assuming that the meridional velocity is zero at the center, because of the symmetry of the neutral heating function about the SAR-arc center, and that the meridional wind flows away from the arc center on both sides of the arc. The zonal wind, u, caused by the coriolis force acting on the meridional wind, is small and it is determined by a numerical solution to equation (6-15). In solving equation (6-15) it is also assumed that the model ionosphere has no horizontal variation.

This solution gives an indication of the importance of the adiabatic heating and cooling term in the thermodynamic equation for generating direct atmospheric motion in the thermosphere. It is not a closed solution and the calculated circulation pattern does not close. However, it is shown in a later section that the atmospheric motion, generated by this mechanism, is applicable to the lower thermosphere where the adiabatic heating and cooling term is the dominant term in the thermodynamic equation (Lagos, 1967). The normalized vertical winds which are caused by the neutral heating function of the two-dimensional SAR-arc model, are shown in Fig. 20 and the peak value of the vertical wind is shown in the upper right corner as a function of SAR-arc intensity. The vertical wind contours are seen to be symmetrical about the arc center and the upward directed vertical

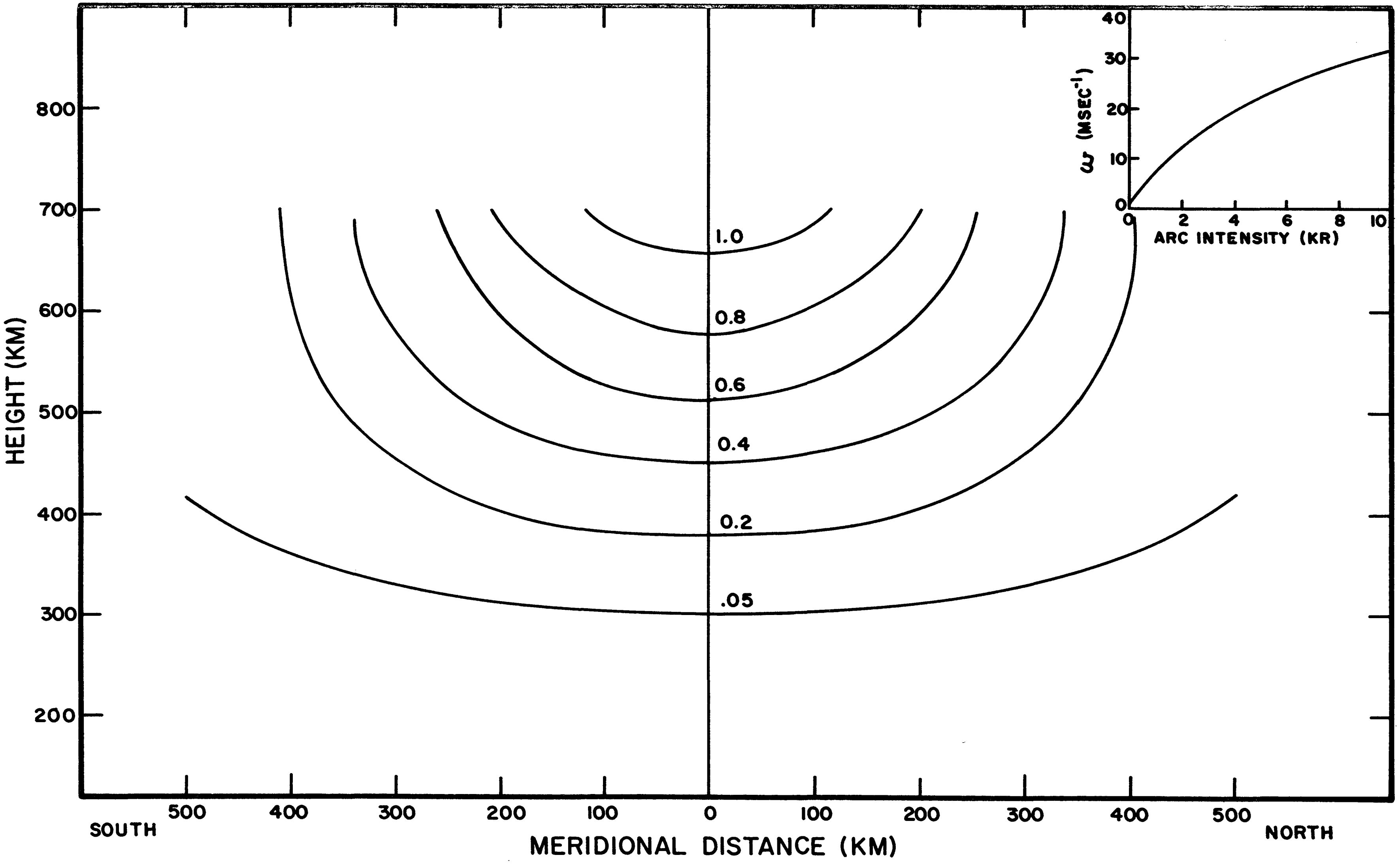

Fig. 20. Normalized vertical winds for the direct atmospheric expansion to neutral heating within the SAR-arc region.

winds increase with altitude, indicating a decreasing effectiveness of the adiabatic cooling term in the upper thermosphere. The normalized meridional and zonal winds are shown in Fig. 21 with the peak values plotted as a function of SAR-arc intensity in the upper right corner. From these two figures, the general cellular overturning of the atmosphere is quite evident even though the circulation pattern does not close on itself, because the complete set of equations governing the atmospheric motion in the SAR-arc region was not solved. In the lower thermosphere, the meridional winds are flowing toward the SAR-arc center, and above 350 km the direction reverses and the winds flow away from the arc region. The zonal wind contours have approximately the same shape as the meridional wind contours and therefore the same figure is used to represent both cases. In the upper thermosphere weak westerlies flow in the region north of the arc and easterlies are present on the southern side. Below 250 km the direction of these winds reverse; however, they have an almost negligibly small magnitude. It is interesting to note, at this time, that the meridional and zonal winds both go to zero at 350 km; this fact will be used, in a later section, as a boundary condition for an approximate solution to the equations governing the neutral gas motion in the SAR-arc region. The motion generated in this case is seen to have the form of a large thermal cell where the circulation pattern develops in such a way that the local heating within the SAR-arc is removed by adiabatic expansion of the heated gas through vertical motion.

6.3 ATMOSPHERIC RESPONSE TO THE SAR-ARC TEMPERATURE DISTRIBUTION DETERMINED BY THERMAL CONDUCTION ALONE

The magnitude and direction of the wind system caused by the pressure gradients determined from the two-dimensional SAR-arc temperature pattern, shown in Fig. 19, is calculated in the second "limiting solution" to be discussed in this section. Thermal conduction is assumed to be the dominant heat

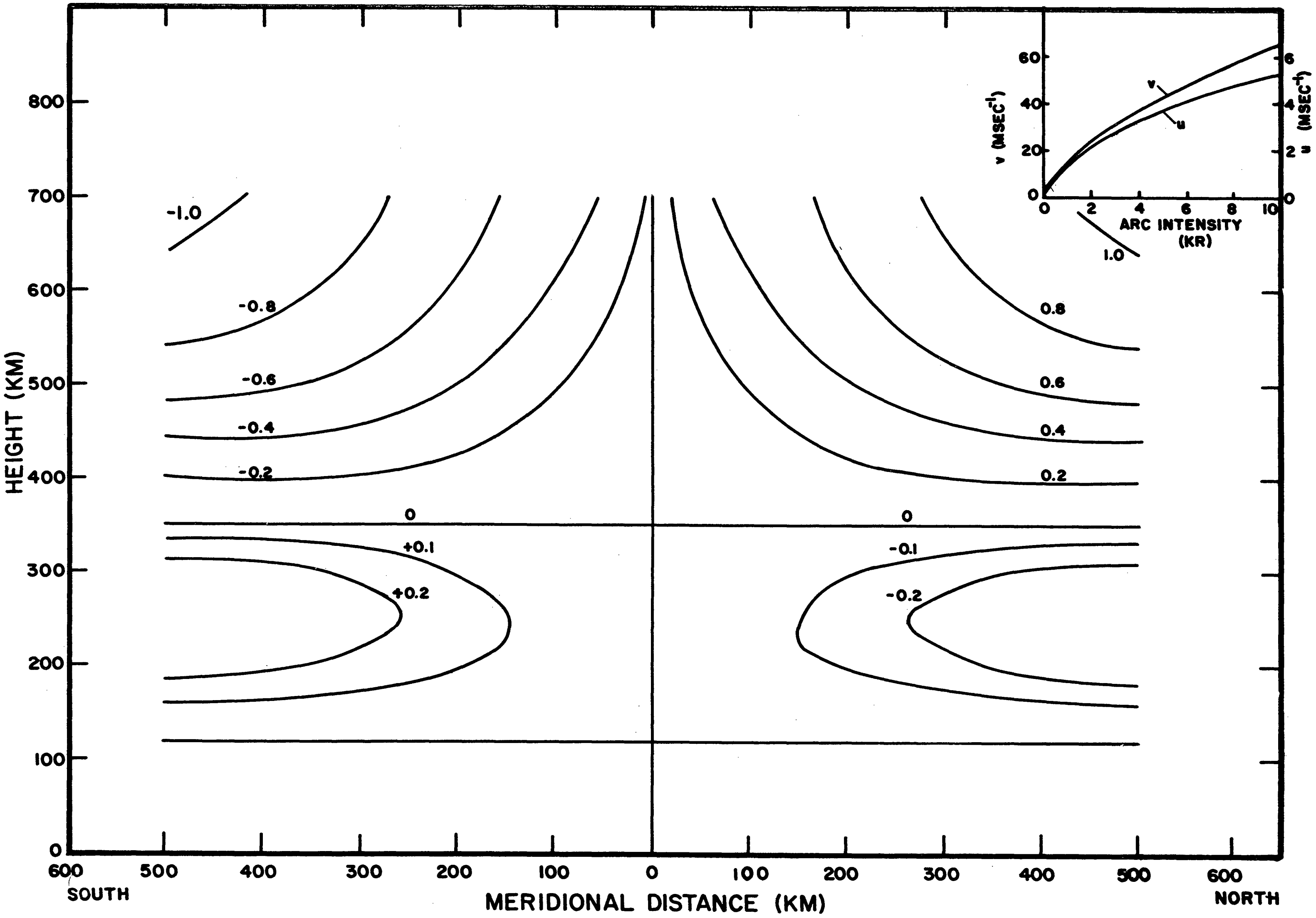

Fig. 21. Normalized zonal and meridional winds for the direct atmospheric expansion to neutral heating within the SAR-arc region.

transport process acting in the thermosphere. Therefore, the meridional heat transport term and the adiabatic heating and cooling term in the thermodynamic equation (6-19) are neglected and the neutral gas temperature pattern is determined from the solution to the two-dimensional neutral heat conduction equation, presented in Chapter 5. The consistency of this assumption is important for it affects the validity of the solution and it will be discussed later in this section.

Because the thermosphere is in diffusive equilibrium, the neutral temperature increase within the SAR-arc will cause a large thermal expansion of the atmosphere resulting in a density bulge. The pressure gradient caused by this density bulge provides the driving force for the neutral atmosphere and it can be determined by differentiating equation (6-18) to give

$$\frac{\partial p(y,z)}{\partial y} = \sum_{i} p_i(z_0)\, Exp\left[-\int_{z_0}^{z} \frac{m_i g\, dz'}{k^* T_n(y,z')}\right] \int_{z_0}^{z} \frac{m_i g}{k^* T_n^2(y,z')} \frac{\partial T_n(y,z')}{\partial y}\, dz' \qquad (6\text{-}22)$$

where $T_n(y, z)$ is the temperature pattern given by equation (C-20) and the meridional temperature gradient is determined by differentiating this same equation. The pressure force, $\frac{1}{\rho}\frac{\partial p(y,z)}{\partial y}$, is now substituted into the equation of motion and the equations are solved for the zonal and meridional components of the wind. Equations (6-15) and (6-16) are easily solved in complex form. Let $W = u + iv$, then by multiplying equation (6-16) by i, the imaginary constant, and adding this equation to equation (6-15), the equations of motion reduce to

$$\frac{\mu}{\rho}\frac{d^2 W}{dz^2} - (\lambda + if)W = i\frac{1}{\rho}\frac{\partial p(y,z)}{\partial y} \qquad (6\text{-}23)$$

The lower boundary condition for this equation is that $W = 0$ at 120 km where the pressure gradient vanishes. The upper boundary condition requires that $\frac{dW}{dz} \rightarrow 0$ as $z \rightarrow \infty$ due to the influence of viscosity. Equation (6-23) was written as a finite difference equation and solved through the use of a recursion relationship giving the u and v components of the wind directly from the real and imaginary parts of W respectively.

Once the u and v components of the wind are obtained, the vertical winds caused by a mass divergence of the meridional winds are calculated from the continuity equation as

$$w = \frac{1}{\rho(z)} \int_{z}^{\infty} \frac{\partial(\rho v)}{\partial y}\, dz' \qquad (6\text{-}24)$$

where it is assumed that the vertical mass flow at the top of the atmosphere is zero.

Now that all of the unknowns in equations (6-15) to (6-19) have been determined, the magnitudes of these terms is used to calculate the neglected meridional heat transport and adiabatic heating and cooling terms in the thermodynamic equation. The agreement between the solution, outlined here, and the true solution to the full set of equations governing the neutral gas motion within the SAR-arc depends upon the magnitude of the neglected terms. If they are negligibly small, the true solution should lie close to the one presented here. However, if these terms are very large, then the true solution is probably closer to the previous case considered and a new approach to solve these equations must be attempted.

The normalized zonal and meridional winds for the model SAR-arc are shown in Figs. 22 and 23 with the peak values of the wind plotted as a function of the arc intensity in the upper right corner. The resulting wind pattern is a steady state balance between the viscous drag, ion drag, coriolis, and pressure forces. Because the neutral heating contours are ellipses, there is a symmetry

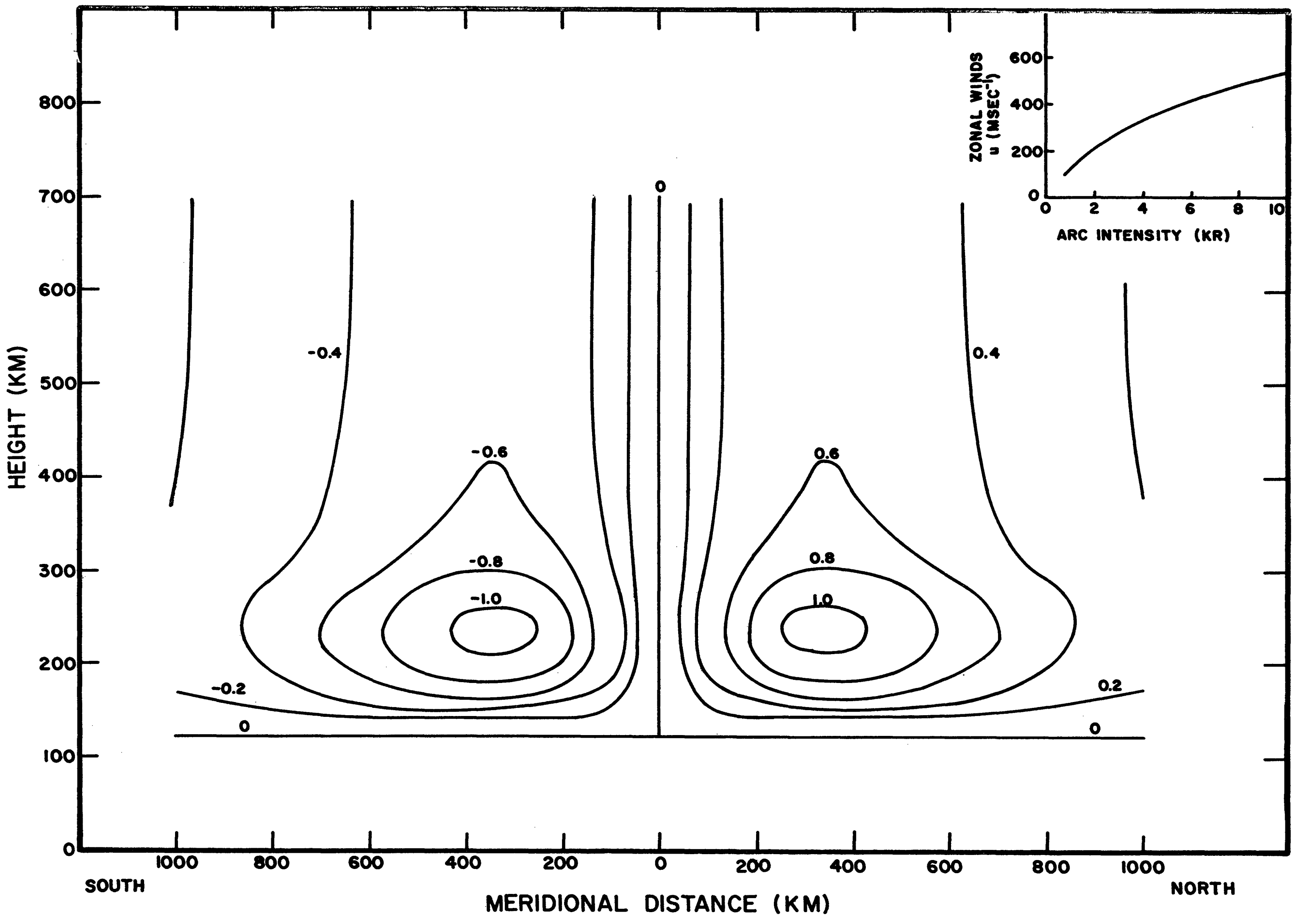

Fig. 22. Normalized zonal winds for the SAR-arc temperature pattern determined by considering thermal conduction alone.

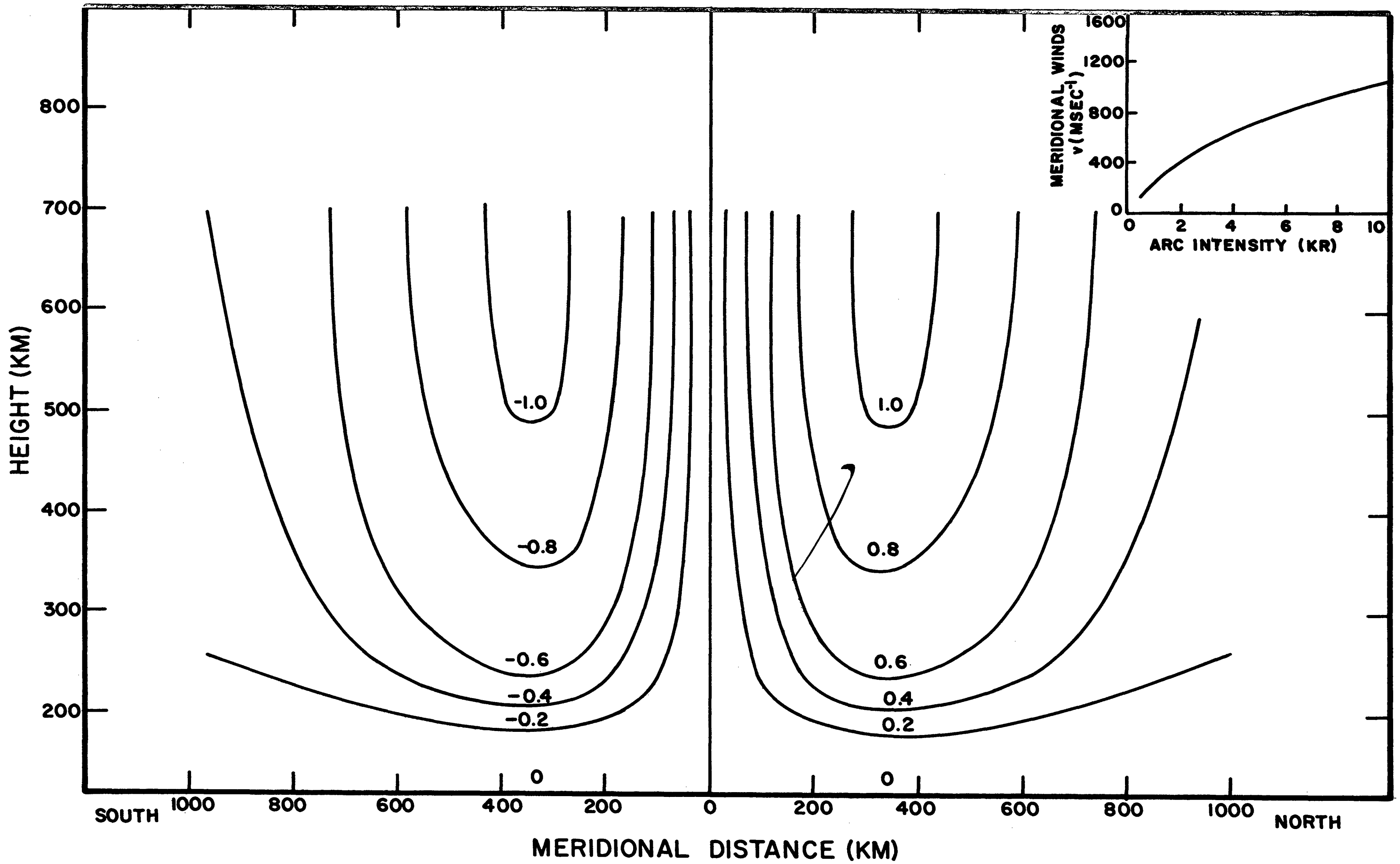

Fig. 23. Normalized meridional winds for the SAR-arc temperature pattern determined by considering thermal conduction alone.

in both the temperature and circulation pattern about the SAR-arc center. These winds increase away from the arc center and reach a maximum velocity at a meridional distance of about 300 km. Beyond this distance the meridional winds slowly decrease. On the south side of the arc center, a symmetrical northerly wind is present. The large westerly and easterly jets existing just below the ionosphere where the ion drag term is small reveal a near geostrophic balance in the lower thermosphere. However, at higher altitudes the ion drag term becomes important and the character of the wind changes from a geostrophic balance to a counter gradient flow. Thus, the total wind vector is seen to rotate in a counter-clockwise direction with increasing altitude in both regions, north and south of the SAR-arc center.

The normalized vertical winds are presented in Fig. 24 and reveal a cellular overturning with upward directed velocities over a 600 km meridional distance section in the center of the arc and downward directed velocities elsewhere. The magnitude of all wind components is very large indicating a violent circulation pattern generated by the assumed temperature distribution, which was determined by thermal conduction alone. When these winds are substituted into the neglected meridional heat transport and adiabatic heating and cooling terms in the thermodynamic equation, the calculated magnitude of these terms is enormous; especially in the lower thermosphere where the effectiveness of these terms is most pronounced.

The results of this section show that the neutral gas temperature increase, due to a local heat source, cannot be determined by solving the neutral gas heat conduction equation alone, but it can only be determined by a solution to the full set of equations governing the atmospheric motion in the thermosphere. The pressure gradients, determined from a conduction solution for the temperature

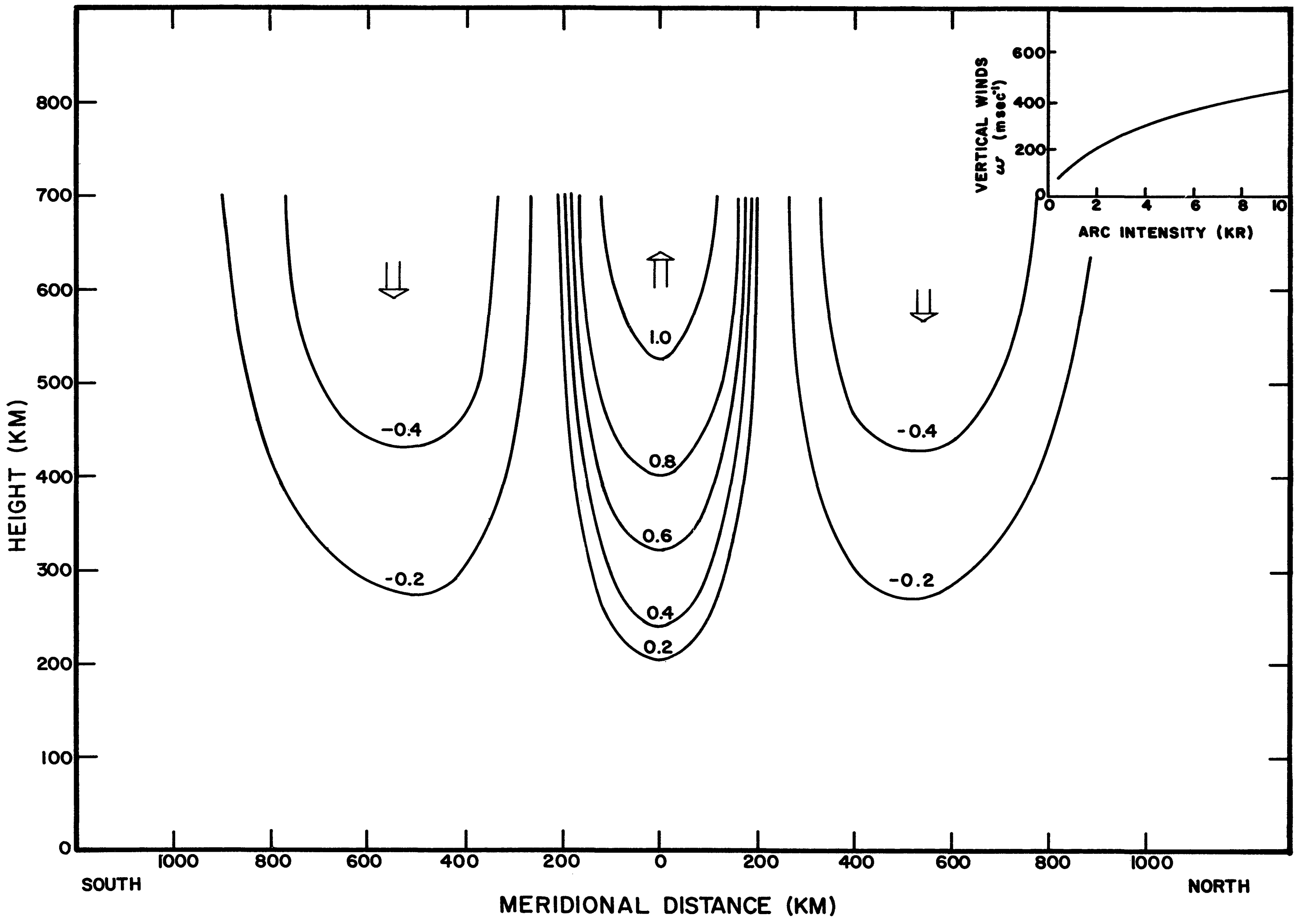

Fig. 24. Normalized vertical winds for the SAR-arc temperature pattern determined by considering thermal conduction alone.

pattern, are too large, indicating that the adiabatic heating and cooling term must act in such a way that the pressure driving force and neutral gas temperature increase are both reduced so as to effect an appropriate balance between all terms in the equations governing the atmospheric motion.

6.4 AN APPROXIMATE SOLUTION FOR THE ATMOSPHERIC RESPONSE WITHIN A SAR-ARC

In the previous sections, the atmospheric response due to direct motion, caused by the adiabatic expansion term in the thermodynamic equation, and the motion caused by the pressure gradients, associated with the temperature pattern determined by considering thermal conduction alone, was investigated and the differences between the two cases were large. As a result, it is necessary to more effectively bracket the actual solution of the equations governing the atmospheric response in order to determine the magnitude of the winds and neutral temperature increase caused by heating within the SAR-arc. The scale analysis performed by Lagos (1967) and Dickinson, Lagos, and Newell (1968) defines approximate height regions where the conduction and adiabatic heating and cooling terms dominate the thermodynamic equation. Below approximately 300km, depending upon the atmospheric model used, the adiabatic terms dominate whereas above that height thermal conduction is considered to be more important. It appears then, that the true solution must be a combination of the two cases discussed in the previous sections, where the direct motion caused by the adiabatic expansion of the atmosphere is representative of the motion in the upper thermosphere. If these two solutions could be connected in a consistent manner then an approximate solution giving a more adequate representation of the true wind and temperature pattern would be obtained.

The approximate solution to the full set of equations governing the atmospheric response within the SAR-arc region is therefore obtained by considering two separate regions (one below 350 km where the adiabatic heating and cooling is important and the other above 350 km where thermal conduction is important) in the following manner:

(1) In the lower thermosphere, below 350 km, the neutral heating rate is decreasing rapidly with decreasing altitude. It is assumed that this neutral heating goes directly into generating the atmospheric motion through the adiabatic heating and cooling term in the thermodynamic equation. Thermal conduction in the lower thermosphere is neglected and no neutral gas temperature increase occurs. The magnitude and direction of the winds are determined for the region below 350 km by the procedure outlined in section 6.2 and are calculated for the heating function shown in Fig. 14. It was shown in section 6.2 that by using these approximations the zonal and meridional components of the wind go to zero at a height of approximately 350 km. This result can be conveniently used as a boundary condition for the solution of the problem above this altitude. Another boundary condition considered later, concerns the magnitude of the vertical winds at 350 km and a meridional cross section of the wind at this boundary is shown in Fig. 27 for the lower model.

(2) In the upper thermosphere, above 350 km, it is assumed that thermal conduction is the dominant term in the thermodynamic equation and that the neutral gas temperature increase is obtained by a solution to the neutral heat conduction equation. The atmospheric motion is driven by the pressure gradients determined from this temperature pattern and it is calculated in the manner which was described in section 6.3. The lower boundary conditions for the winds are obtained from the lower level solution, where it

was shown that the zonal and meridional components of the wind go to zero at 350 km.

(3) The neutral heating function $\overline{Q}(y, z)$ which is the heat source driving the atmosphere in the upper region is adjusted using a trial and error procedure, in such a way, that the solution has the following properties:

   (a) The vertical winds across the lower boundary at 350 km closely match the vertical winds calculated in (1).

   (b) The total integrated neutral heat input for the assumed heating function is nearly equal to the actual integrated neutral heat function for the upper levels of the SAR-arc model shown in Fig. 14.

   (c) The effective heating function $\overset{*}{\overline{Q}}(y, z)$ defined by the sum of the assumed neutral heat input, $\overline{Q}(y, z)$, and the heating and cooling resulting from the adiabatic terms in the thermodynamic equation, must closely approximate the SAR-arc neutral heat input function $Q(y, z)$ shown in Fig. 14.

The effective neutral heating function is the actual heat input function for which the wind solution determined by the procedure being described applies. The closeness of the effective neutral heating function to the true SAR-arc neutral heating function indicates the closeness of the resulting wind and temperature pattern to the true solution.

The normalized meridional winds and neutral gas temperature increase contours for the SAR-arc model are shown in Fig. 25. This solution was obtained by the trial and error procedure and it satisfies all of the requirements which were outlined above. The neutral gas temperature increase obtained in this manner is considerably reduced over the temperature increase which was obtained when thermal conduction was considered alone. The meridional winds are generally weak when compared to the diurnal

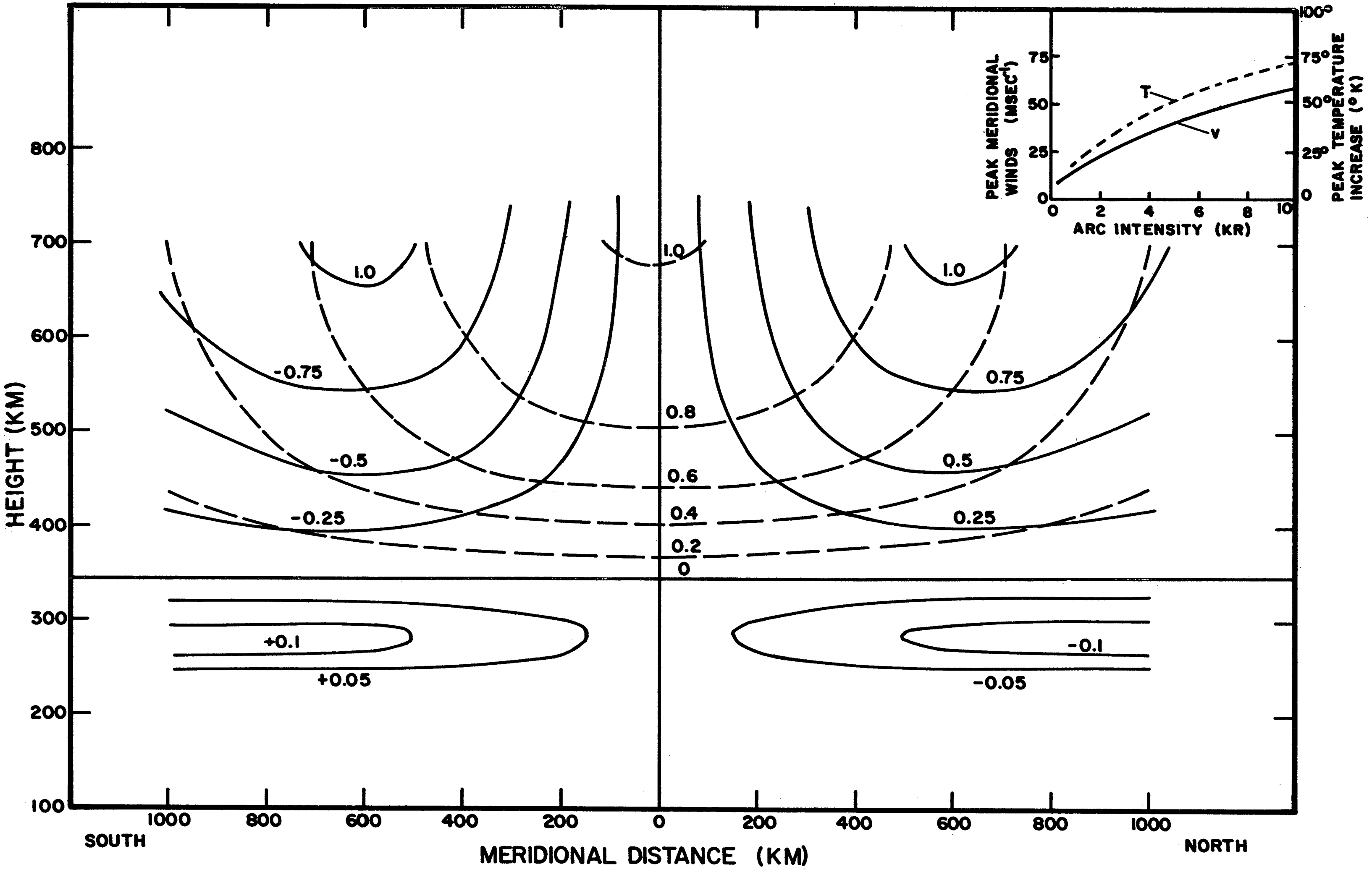

Fig. 25. Normalized temperature increase and meridional wind contours for the approximate solution to the set of equations governing the atmospheric response in the SAR-arc region.

winds in the upper F-region and they exhibit the cellular overturning which was evident in the preceding sections. There is no neutral temperature increase below 350 km and at 400 km where the bulk of the 6300 Å radiation of the SAR-arc is emitted, the neutral gas temperature increase is small. Therefore, a ground based interferometer, making doppler temperature measurements within the SAR-arc and in the airglow region outside the SAR-arc, would detect only a small temperature increase if it is within the temperature resolution of the instrument. In the low thermosphere, the divergence of the vertical motion within the SAR-arc thermal cell causes a meridional wind to flow into the SAR-arc and preserve mass continuity. Above 350 km, the meridional winds flow out and away from the arc center. In the absence of any diurnal winds, the meridional winds in the upper thermosphere are southerly to the north of the arc center and northerly on the south side reaching a maximum velocity high in the thermosphere at approximately 300 km north and south of the arc center.

The vertical winds caused by the SAR-arc are shown in Fig. 26 where a cellular overturning is evident with warm air rising in the SAR-arc region and the surrounding air settling downward. This large thermal cell distributes the neutral heating of the SAR-arc by atmospheric motion, preventing an abnormally high temperature perturbation to exist in the SAR-arc region. The vertical winds at the intermediate boundary, 350 km, separating the two layers are shown for the models representing each layer in Fig. 27. The calculated winds agree reasonably well within 800 km of the arc center. But beyond the SAR-arc center the vertical winds obtained from the solution to the upper level are negative indicating a

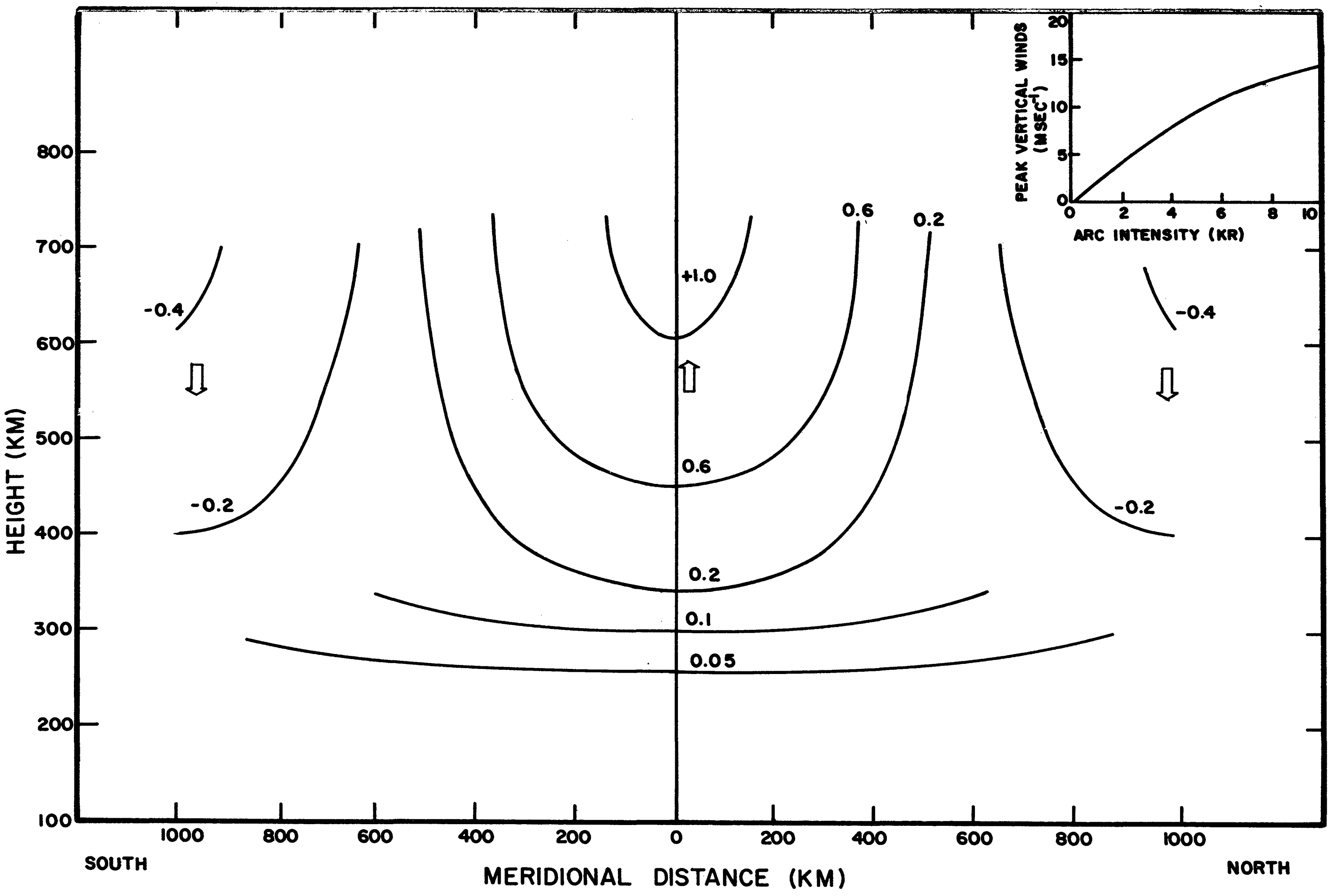

Fig. 26. Normalized vertical wind contours for the approximate solution to the set of equations governing the atmospheric response in the SAR-arc region.

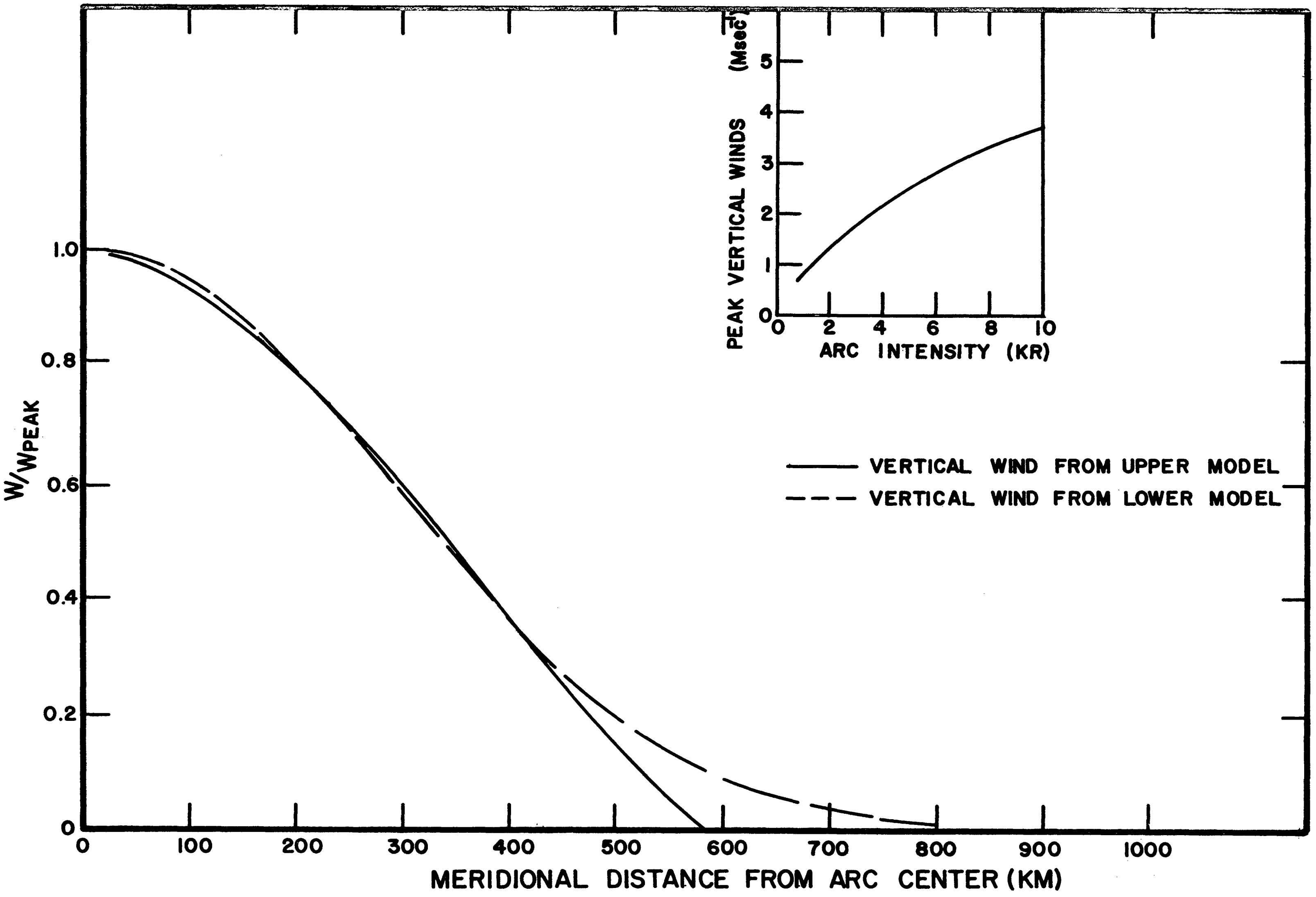

Fig. 27. Normalized vertical winds at 350km, the matching boundary for the upper and lower models.

downward transport and they do not match the vertical winds from the lower level where only positive vertical winds are possible because of the nature of the solution. The solution obtained by this procedure does not give a closed circulation pattern; however, it should give a good representation over a 1200 km meridional span near the SAR-arc center. The downward vertical velocities obtained in the wings of the arc are considered to more closely approximate the actual case. This matching of the vertical winds at the 350 km separating boundary satisfies the requirement 3(a). The estimated neutral heating function for this solution $\overline{Q}(y, z)$ was an elongated ellipse having a peak value at 440 km, a $1/e$ width of 100 km, and a ratio of semi-major to semi-minor axes of 8. The integrated value of this function and the heating function used in the lower model is nearly equal to the integrated heat input for the SAR-arc model, $Q(y, z)$, which satisfies requirement 3(b).

The effective heating function $\overline{Q}^{*}(y, z)$ which is defined by condition 3(c) and is shown in Fig. 28 represents the actual heating function which drives the circulation pattern shown in these figures. This heating function should be compared to the SAR-arc neutral heating function which is shown in Fig. 14. The closeness of the solution is represented by the closeness of the fit between the two heating functions and in view of the trial and error process involved the solution obtained is believed to be a reasonable approximation to the SAR-arc problem. The contours of the effective neutral heating function are slightly more elongated than the SAR-arc neutral heating function and this is due to the nature of the approximating function. In the wings the contours between the two models do not match; however in the SAR-arc central region a reasonable fit is realized.

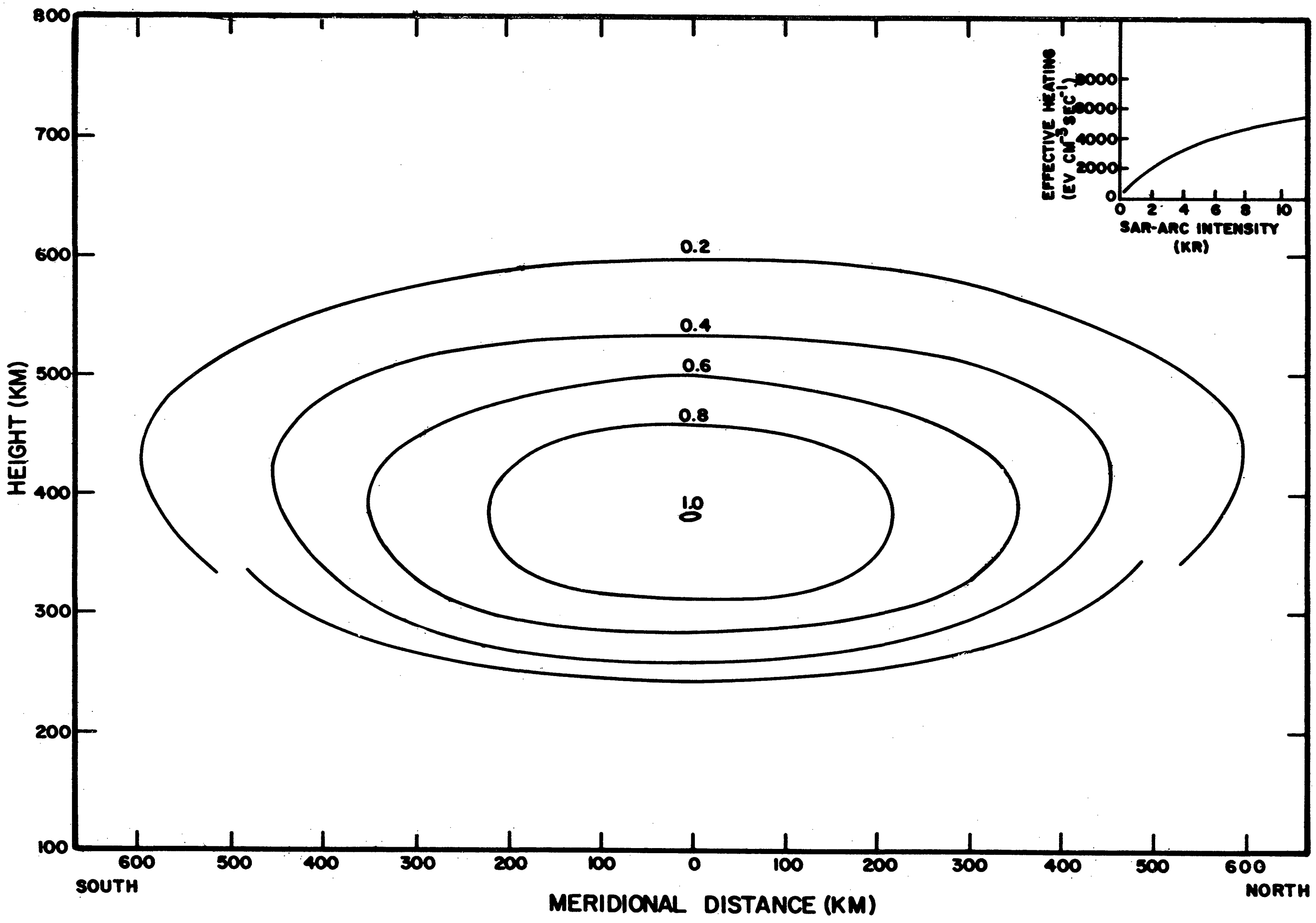

Fig. 28. Normalized effective heating function $\overline{Q}^{*}(y, z)$ for the approximate solution to the set of equations governing the atmospheric response in the SAR-arc model.

6.5 IONOSPHERIC EFFECTS

The SAR-arc neutral heating was shown to cause neutral winds in addition to increasing the temperature of the neutral gas. The wind pattern is represented by a large thermal cell with air rising in the SAR-arc and flowing outward from the arc center. These winds will influence the ionosphere because of the ion drag term existing between the neutral and ionized components of the atmosphere. The ionization is forced by the neutral gas to move along the geomagnetic field lines at a velocity equal to the component of the wind velocity along the direction of the geomagnetic field. Thus, in the region to the north of the SAR-arc center a southerly meridional wind will force ionization downward into the lower ionosphere where enhanced recombination could cause an electron density depression. To the south of the SAR-arc center a northerly meridional wind will force ionization upward along the geomagnetic field lines into the upper ionosphere. In addition to the meridional winds the vertical winds will also influence ionospheric movements. Within the SAR-arc vertical winds will cause an upward movement of the ionosphere whereas in the wings of the arc the flow will be downward because of the cellular overturning of the circulation pattern. To the north of the arc center, the downward vertical velocities will reinforce the southerly meridional winds pumping ionization lower into the ionosphere. South of the arc center, the downward vertical velocities will tend to oppose the upward flow of ionization caused by a northerly meridional wind. The magnitude of the winds in the calculated circulation pattern are low and they were calculated without considering the influence of the diurnal winds which have been calculated to be of the order of hundreds of meters per second (Geisler, 1967; Kohl and King, 1967; Dickinson, Lagos, and Newell, 1968). Therefore, it is not clear whether these ionospheric effects can be caused by the winds generated by the

SAR-arc alone; however, the observational evidence for the September 28/29, 1967 SAR-arc (discussed in Chapter 8) tends to support the predicted ionospheric effects. Thus, it appears that besides the ionospheric effects caused by electron heating within the SAR-arc, the neutral winds generated by the arc will have an important influence on the surrounding ionosphere.

6.6 ATMOSPHERIC HEATING DURING MAGNETIC STORMS

The heating of the upper atmosphere in mid-latitudes during times of geomagnetic storms has been related by Jacchia and Slowey (1963, 1964) to the intensity a_p of the storm and the results are shown as curve (1) in Fig. 29. The SAR-arc intensity is also related to a_p in Fig. 3 and the results of the previous sections are now used to determine the contribution of the SAR-arc to the observed atmospheric heating. Several curves are plotted in Fig. 29 representing the neutral gas temperature increase as a function of SAR-arc intensity for various models. Curve (2) represents the peak neutral gas temperature increase within the SAR-arc region which was obtained from the solution of the two-dimensional neutral heat conduction equation. Curve (3) is the peak neutral gas temperature increase which is obtained from the approximate solution to the set of hydrodynamic equations governing the motion within the SAR-arc region. These two cases represent the peak heating in a narrow region within the arc and do not apply to the whole thermosphere for which the results of Jacchia and Slowey (1963) are applicable.

Curve (4) shows the neutral gas temperature increase for the whole hemisphere when the total energy transferred to the neutral gas from the SAR-arc, during its lifetime of about 10 hours, is used as the only energy source to raise the temperature. It was shown in Chapter 5 that the lower boundary to which the neutral heating is apparent during the lifetime of the SAR-arc is 140 km.

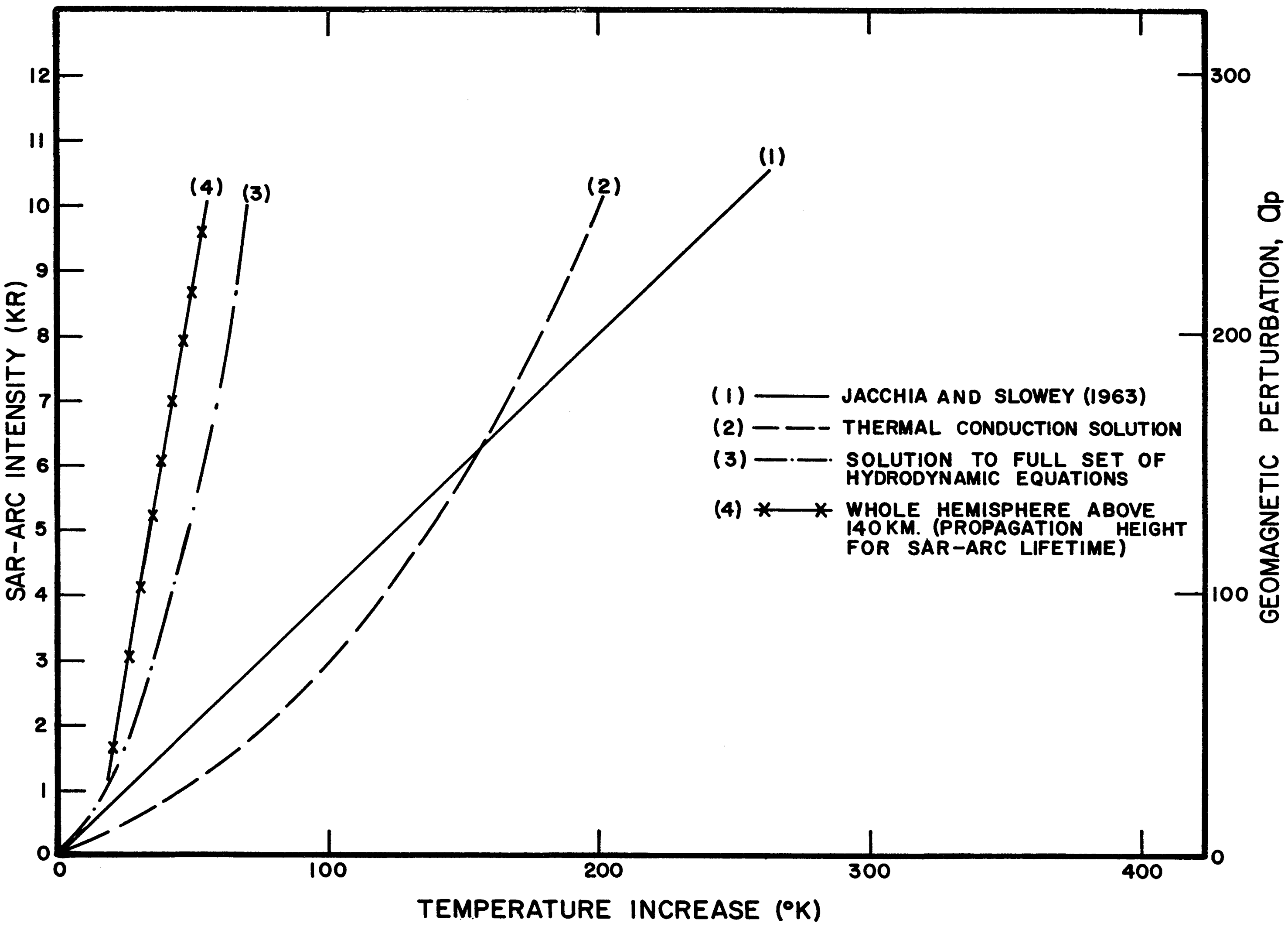

Fig. 29. A comparison of the atmospheric heating caused by various SAR-arc models to the heating determined from satellite drag measurements (Jacchia and Slowey, 1963).

Therefore, curve (4) is the temperature increase of the whole hemisphere above 140 km caused by heating within the arc. The magnitude of the atmospheric heating caused by the SAR-arc is much lower than that determined from the satellite drag measurements. This indicates that the atmospheric heating observed during geomagnetic storms is primarily caused by an energy source other than the SAR-arc.

VII. THE AIRGLOW OBSERVATORY

A general purpose airglow observatory has been constructed at the University of Michigan in order to study the SAR-arcs, low latitude aurora, twilight glow, normal nightglow, pre-dawn enhancement, and other optical features in the night sky. In this thesis, the instruments of the airglow observatory have been primarily used to study the SAR-arc.

Most of the SAR-arc observations made in the United States during the last solar cycle maximum were obtained from western geophysical observatories and few or no observations were made from stations east of the Rocky Mountains. It is seen, from the zones of SAR-arc occurrence shown in Fig. 1, that Michigan lies in the northern part of the zone of occurrence crossing the United States, and is in a position for measurement to be made over the eastern portion of the country. It also has a favorable location for viewing the arc because most arcs would be detected away from the auroral background in the north and it would stand out distinctly against the normal airglow background in the south.

Two optical measurements are of interest: (1) measurements of the intensity of the various emission lines in the SAR-arc and normal nightglow, and (2) doppler temperature measurements of the 6300 Å atomic oxygen emission line within the arc region and normal nightglow. These measurements are important for determining the state of the upper atmosphere during quiet and disturbed conditions. The 6300 Å doppler temperature in the normal nightglow has been shown by Roble, Hays, and Nagy (1968) to be a measure of the neutral exospheric temperature. The night portion of the diurnal variation of the exospheric temperature can therefore be monitored by observing the 6300 Å doppler temperatures in the normal nightglow. These results then provide another means of determining the exospheric temperature variations and they can be compared to temperatures derived from satellite drag measurements. (cf. Biondi and Feibelman, 1968). The neutral atmospheric heating within the SAR-arc and the exospheric temperature variations during a magnetic storm can also be obtained from 6300 Å doppler temperature measurements. Because the temperature of the upper atmosphere is such a significant parameter, the measurements of the atomic oxygen temperature from doppler broadening of the 6300 Å red line should add significantly to our understanding of the SAR-arc and indeed the whole upper atmosphere.

7.1 SELECTION OF INSTRUMENTS TO ACCOMPLISH MEASUREMENTS

An interference filter photometer was selected for the measurement of the intensity of the various emission lines in the nightglow. This instrument is a proven intensity monitor which has been used by many geophysical observatories since the IGY. It is a versatile instrument which uses the appropriate narrow band interference filter to separate the emission line from the night sky spectrum. The details of the measurement and the actual instrument are presented in section 7.3.

The 6300 Å emission line originates in the F-region of the ionosphere and has a doppler line shape with a half width proportional to the square root of the neutral gas temperature,

$$S = 7.16 \times 10^{-7} \lambda_o \sqrt{\frac{T_n}{M}} \qquad (7\text{-}1)$$

where s is the full width of the doppler line at half intensity points, λ_o is the wavelength of the emission line, T_n is the neutral gas temperature, and M is the molecular weight of the emitting atom. An instrument with a high resolution is necessary to measure the 6300 Å line profile because an exospheric temperature of 1000°K has a doppler half width of only .035 Å. The instrument must also have a great light gathering power because the normal 6300 Å emission in the night sky is generally weak; of the order of 10 to 100 Rayleighs in the nightglow. There are four types of instruments which could be considered for making the doppler temperature measurement: (1) a prism spectrometer, (2) a grating spectrometer, (3) a Michelson interferometer, and (4) a Fabry-Perot interferometer. Jacquinot (1954) has compared the prism, grating, and Fabry-Perot spectrometers at a given resolution and the same effective area. He found that the grating spectrometer will always have a greater light gathering power than a prism spectrometer, and a Fabry-Perot spectrometer will have as much as 30 to 400 times the light gathering power of either instrument. For this reason the Fabry-Perot spectrometer is a superior instrument even for low resolution where good light gathering power is important.

In the visible region of the spectrum Hunten, et. at. (1967) have shown that the Fabry-Perot interferometer and Michelson interferometer have about equal capabilities for measurements on the nightglow. If only a few spectral elements are to be examined the Fabry-Perot is easier to use; however, for a large number of spectral elements the Michelson becomes increasingly advantageous. Hillard and Shepherd (1966a) have modified the basic Michelson interferometer in such a manner that the light gathering power is greatly increased. This wide angle Michelson interferometer (WAMI) has been constructed and measurements were made on faint aurora and even nightglow (Hillard and Shepherd, 1966b). It can have a field of view as large as 5° as compared to the 0.2° field of view of the Fabry-Perot interferometer, resulting in a greater light gathering power at a given resolution. The instrument, however, operates at a single optical path and relates the visibility of a source having an assumed gaussian profile to the doppler width, or temperature, of the source.

The 6300 Å emission line is embedded in a region of the nightglow spectrum where there exists a number of strong hydroxyl lines belonging to the 5-0 and 9-3 transitions in the Meinel OH bands. (Chamberlain and Smith, 1959; Broadfoot and Kendall, 1968). These background emission lines are strong enough to distort the interferogram sufficiently so that a doppler temperature measurement of a gaussian line within this background is very difficult. The interferometer must perform a long optical scan in order to sort out the background emission lines and at optical wavelengths alignment problems become critical. In view of these difficulties, the Fabry-Perot interferometer is selected as the instrument to perform the 6300 Å doppler temperature measurements.

7.2 FABRY-PEROT INTERFEROMETER

The use of a Fabry-Perot interferometer for measuring the temperature of the upper atmosphere from the doppler profiles of the forbidden transition lines of atomic oxygen is well known and measurements have been made by many investigators. Most of the measurements have been made on the more intense 5577 Å oxygen line, but doppler temperatures of the 6300 Å atomic oxygen red line have been determined by Turgeon and Shepherd (1962) in the aurora, and by Wark (1960), Jarrett, Hoey, and Paffrath (1964), Jarrett and Hoey (1966), Hernandez (1967), and Biondi and Feibelman (1968) in the nightglow, all using the Fabry-Perot interferometer for the measurement of the line profile.

7.2.1 BASIC PRINCIPLES OF THE FABRY-PEROT INTERFEROMETER

The basic theory of the Fabry-Perot interferometer is given in many optical textbooks (i.e. Born and Wolf, 1965; Tolansky, 1955; Jenkins and White, 1950). Because there are many different types of Fabry-Perot interferometers and each can be used in a different way, only the details of the theory, as it applies to the instrument which has been constructed at the airglow observatory are presented.

A simplified schematic of the Fabry-Perot interferometer is shown in Fig. 30. The main component of the instrument is the high quality quartz etalon plates with plane surfaces carefully polished flat to a very small fraction of a wavelength. The two inner faces are coated with partially transmitting coatings of high reflectance. The coated surfaces are set adjacent to each other and are maintained at a fixed spacing by a precision spacer. The two surfaces are adjusted to precise parallelism for the production of Haidinger fringes. When a beam of light is incident upon the etalon plates, there are multiple reflections between the two coated surfaces and a series of beams of diminishing amplitude emerge from the etalon. For each member of the transmitted set of waves, the variable part of the phase of the wave function differs from that of the preceding member by an amount which corresponds to a double traversal of the plate spacing. This phase difference can be expressed as

$$\delta = 4\pi\mu t \lambda_0^{-1} \cos\theta \tag{7-2}$$

where t is the spacing between the plates, μ is the index of refraction of the medium between the plates, θ is the incident angle, and λ_0 is the wavelength of the incident radiation. The radiation emerging from the Fabry-Perot etalon plates is collected by an objective lens and brought to a focus where a set of narrow bright fringes of equal inclination is formed in the focal plane. In the photoelectric method of recording the Fabry-Perot fringes the interference fringes are imaged by the objective lens onto a plate containing a circular

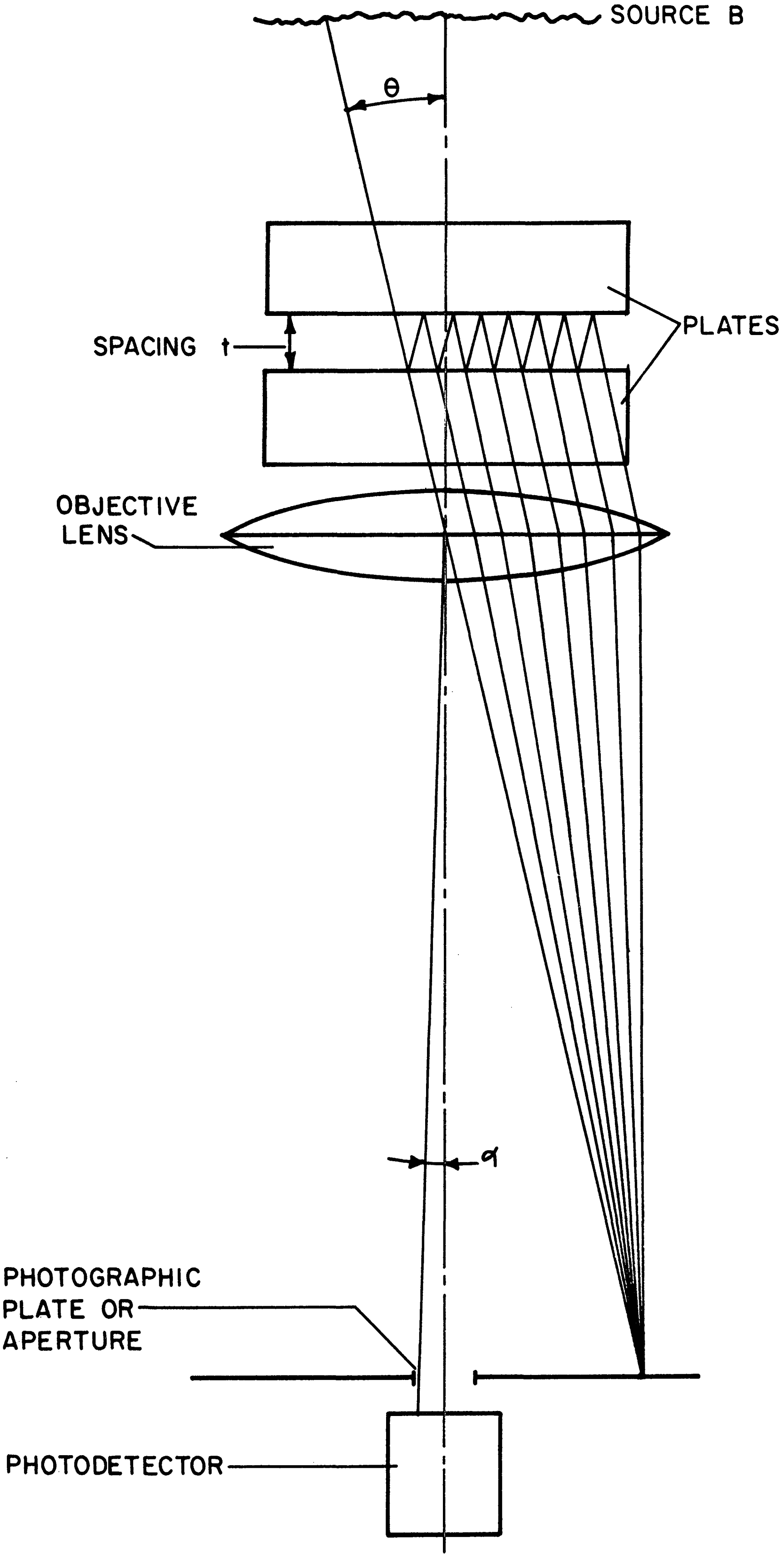

Fig. 30. Simplified schematic diagram of a Fabry-Perot interferometer.

aperture which is adjusted to coincide with the center of the fringes and pass a portion of the central spot to a detecting photomultiplier. The order of interference at the center of the fringe pattern is defined as $m = \delta/(2\pi)$ or

$$m = 2\mu t \lambda_0^{-1} \cos\theta \tag{7-3}$$

In a multiple beam interferometer the constructive interference of a great number of waves is very critical. When m has an integral value, constructive interference of the collected waves occurs, producing a bright spot on the aperture axis; and if m has a half-integral value, destructive interference results. Therefore, the photomultiplier output is proportional to the intensity of radiation having a wavelength given by the condition for constructive interference at the center of the fringe pattern. This wavelength can be scanned by varying one of the three parameters given in equation (7-2). A discussion of the scanning system for the instrument constructed at the University of Michigan Airglow Observatory is given in section 7.2.4.

7.2.2 IDEAL INSTRUMENT

The resolving properties of the Fabry-Perot interferometer are completely determined by the representation which it gives of a perfectly monochromatic spectral line. If the total luminance of the source line $B(\sigma)$, given by the integral of $B(\sigma)$ over all wavenumbers, is localized in frequency of zero width, ($B(\sigma) = \bar{\alpha}\,\delta(\sigma - \sigma_0)$, $\delta(\;)$ being the Dirac function and $\bar{\alpha}$ a constant), the representation of this line by the Fabry-Perot interferometer is spread out over a small domain of frequency according to a function $Y(\sigma) = W(\sigma - \sigma_0)$; this is the definition of the instrument function of the Fabry-Perot interferometer. If the Fabry-Perot interferometer is now illuminated by radiation having a spectral density $G(\sigma)$, the instrument yields a spectrum, $Y(\sigma)$, which differs from the real spectrum, $G(\sigma)$, by

$$Y(\sigma) = \int_0^\infty W(\sigma - \sigma_0)\, G(\sigma_0)\, d\sigma_0 \tag{7-4}$$

$Y(\sigma)$ is the convolution of the source function by the instrumental function and can be written as $Y(\sigma) = W(\sigma) * G(\sigma)$. $Y(\sigma)$ resembles more and more closely $G(\sigma)$ as the "width" w of W becomes smaller in comparison with the width of $G(\sigma)$ (Nilson and Shepherd, 1961). Two monochromatic lines are resolved when their wavenumber separation $\sigma_2 - \sigma_1$ is greater than a certain value $\delta\sigma$, which is of the order of the width w of W. The effective limit of resolution is $\delta\sigma$, and the resolving power of the Fabry-Perot interferometer is defined as $\mathcal{R} = \sigma / \delta\sigma$, where $\delta\sigma$ must take into account all of the characteristics of the instrument contributing to the width w which is described below.

Another important parameter of the Fabry-Perot interferometer is its luminosity. The light gathering power, U, is proportional to the product of the area of the cross section of the outgoing beam and the solid angle Ω^* associated with the resolving power of the Fabry-Perot interferometer. The product of the two parameters $U\mathcal{R}$ is generally a constant for the Fabry-Perot interferometer (Chabbal, 1953; Jacquinot, 1960) and depends upon the dimensions and physical properties of the instrument. Thus, for a given instrument, if one attempts to increase the resolving power of the instrument, it will be done at a loss of light gathering power and a compromise must be made between the two for a specific application.

If it is assumed that the Fabry-Perot etalon plates are perfectly plane and parallel and the width of the aperture in the focal plane of the lens, shown in Fig. 30, is negligible, then all of the interfering rays have the optical retardation given by equation (7-2). Also, if the reflecting power of the coatings deposited on the etalon plates is equal to unity, then all of the reflected waves would have the same amplitude and, their number being infinite, the interference should be destructive for all wavenumbers except when m in equation (7-2) is an integral value. Under these ideal conditions the instrument function of the Fabry-Perot interferometer is represented by a series of infinitely sharp peaks, (or a Dirac comb).

$$W(\sigma) = \sum_{0}^{\infty} \delta(\sigma - \sigma_M) \tag{7-5}$$

where σ_m is the wavelength for constructive interference; m is integral. The fringe peaks are separated by the interval

$$\Delta\sigma = \left(2\mu t \cos\theta\right)^{-1} \tag{7-6}$$

which is called the free spectral range of the instrument. Under normal conditions the reflective power of the coatings is less than unity and in this case the instrument function is the well known Airy Function, (cf. Born and Wolf, 1965 for a complete derivation of this function)

$$A(x) = \frac{\tau_A (1-R)^2}{(1 - 2R\cos x + R^2)} \tag{7-7}$$

where τ_A is a transmission coefficient that includes the effects of absorption and/or scattering of the reflective coatings, and R is the reflectivity of the coated etalon plates. The variable x is related to the phase difference between the various waves emerging from the etalon plates and it is defined as (cf. Hernandez, 1966).

$$x = 4\pi\mu t (\sigma - \sigma_0)\cos\theta \tag{7-8}$$

where σ and σ_0 are the wavenumbers of the incident radiation and a reference respectively. Each peak now has a half width at half-height

$a = \Delta\sigma/(2N_R)$; $N_R = \pi\sqrt{R/(1-R)}$ being a reflective finesse that depends only on the reflectivity of the plates (Chabbal, 1953). The transmission, τ_A, has a maximum value

$$\tau_A = \left(\frac{T}{1-R}\right)^2 = \left(1 - \frac{A}{1-R}\right)^2 \tag{7-9}$$

and it differs from unity only because the coatings have an absorption coefficient $A = 1 - T - R$. T here is the transmission of the etalon plate coatings. The spacing between the peaks of the Airy function is again given by equation (7-6).

7.2.3 INSTRUMENTAL BROADENING

Chabbal (1953) has examined the various broadening functions contributing to the instrument function of the Fabry-Perot interferometer in considerable detail. Beside the broadening by the reflective coating, due to the reflectivity having a value less than unity, there is also a broadening due to etalon surface imperfections and finite aperture size.

7.2.3.1 SURFACE IMPERFECTIONS

The Fabry-Perot etalon plates should be perfectly flat and parallel for the highest resolution. In practice, these conditions are difficult to obtain for there will be some imperfections due to polishing of the etalon plates. The most common imperfections are due to randomly distributed micro-defects and a slight spherical curvature in the etalon plates. Chabbal (1953) has shown that the microscopic flatness imperfections of the plates can be expressed by a gaussian function and the spherical curvature, as well as adjustment errors of the plates, can be expressed as a square or step function.

If the etalon plates have microscopic defects, with a gaussian distribution and a mean shift of the defects of the order of λ / n^*, then a surface defect function D_g is associated with the fringe broadening caused by this source. Chabbal (1953) has shown that this defect function is a gaussian with a half-width at half height of $d_g = \Delta\sigma/(2N_{D_g})$, where N_{D_g} is a coefficient of finesse of the same nature as N_R, and equal to $n^* /4.7$. Hernandez (1966) has expressed this function as

$$D_g = \frac{1}{\sqrt{\pi} D} \, \mathrm{EXP}\left(-x^2/D^2\right) \tag{7-10}$$

where $D = 2\pi \, d_g / (\Delta\sigma \sqrt{\ln 2})$, and x is related to the phase difference given by equation (7-8). The expression given in equation (7-10) has been normalized to unit area.

Chabbal (1953) has also shown that if the etalon plates have a spherical curvature of sagitta λ / m^*, the surface function D_f is a rectangular, or step, function with a half-width at half-height of $d_f = \Delta\sigma/(2N_{D_f})$, where the coefficient N_{D_f} is a spherical defect finesse having a value of $m^*/2$. Hernandez (1966) has expressed this function as

$$D_f = \frac{\Delta\sigma}{4\pi d_f} \, \Pi(x) \tag{7-11}$$

where

$$\Pi(x) = \begin{cases} 1 & 2\pi d_f (\Delta\sigma)^{-1} > |x| \\ 1/2 \quad \text{when} & 2\pi d_f (\Delta\sigma)^{-1} = |x| \\ 0 & 2\pi d_f (\Delta\sigma)^{-1} < |x| \end{cases} \tag{7-12}$$

with d_f as the half-width at half-height of the step function. Another possible surface defect is that of sinusoidal roughness discussed by Hill (1963); however, this defect is not presented here. The various broadening functions are shown graphically in Fig. 31.

7.2.3.2 BROADENING BY A FINITE APERTURE

Up to now an infinitely small circular aperture has been considered; of course in practice a finite aperture is employed to permit light to be transmitted through the aperture to the photomultiplier. The finite aperture causes a further broadening of the fringe profile and this broadening can be represented by a square function. Hernandez (1966) has expressed this function in units of phase difference, x, as

$$F(x) = \frac{\Delta\sigma}{4\pi f}\,\Pi'(x) \tag{7-13}$$

where

$$\Pi'(x) = \begin{cases} 1 & \\ 1/2 & \text{when} \\ 0 & \end{cases} \begin{array}{l} 2\pi f(\Delta\sigma)^{-1} > |x| \\ 2\pi f(\Delta\sigma)^{-1} = |x| \\ 2\pi f(\Delta\sigma)^{-1} < |x| \end{array} \tag{7-14}$$

where f now represents the half-width at half-height of the aperture function.

The aperture function, unlike the Airy function and defect function, has its width f independent of plate spacing t. Because of this, a true finesse cannot be assigned to it, but it is sometimes useful to think of a finesse $N_f = \frac{\Delta\sigma}{f}$ which is valid for only a given plate spacing. Most

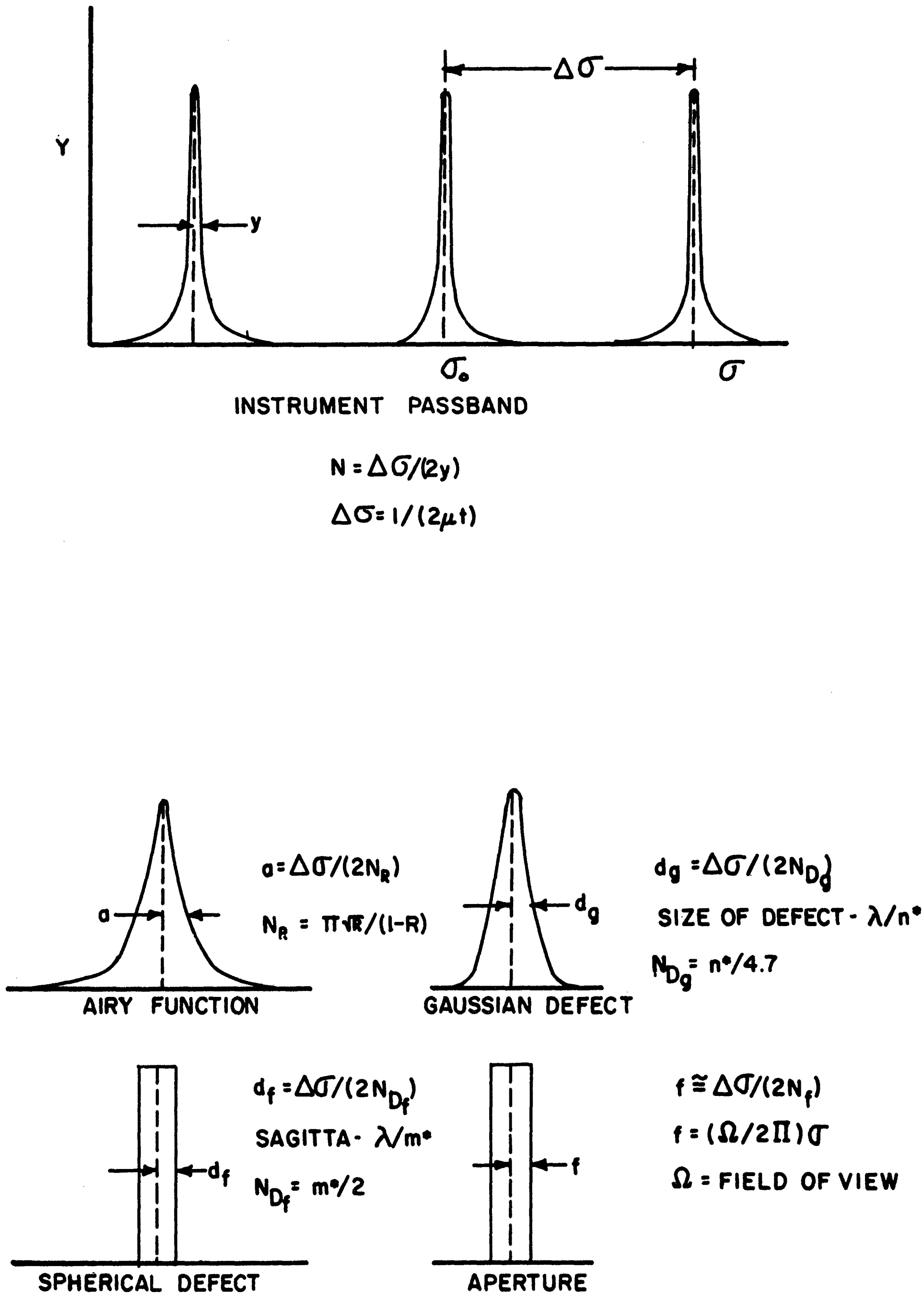

FUNCTIONS DETERMINING FABRY-PEROT PASSBAND

Fig. 31. Various broadening functions of the Fabry-Perot interferometer.

high resolution work is usually done at a fixed spacing and therefore it serves as a convenient parameter.

7.2.4 ANALYTIC REPRESENTATION OF THE INSTRUMENT FUNCTION

Chabbal (1953) has shown that the recorded signal from a photoelectric Fabry-Perot interferometer can be expressed by a convolution of the following functions: (a) the source spectral density, (b) the Airy function representing the coated etalon plates, (c) a gaussian function representing the microscopic flatness imperfections, (d) a step function representing the spherical curvature of the Fabry-Perot etalon plates, and (e) a step function representing the finite size of the circular exploring aperture. The recorded signal can now be expressed as

$$Y = G * A * D_g * D_f * F \qquad (7\text{-}15)$$

where the star represents the convolution. The source function G represents the 6300 Å doppler line profile of atomic oxygen in the nightglow and it is plotted in Fig. 32 as a function of wavenumber from the central peak, σ_0, for various temperatures. The normalized gaussian distribution has been related to the variable x by Hernandez (1966) and is

$$G(x) = \frac{1}{\sqrt{\pi}\, G_0} \, EXP\left(-x^2/G_0^2\right) \qquad (7\text{-}16)$$

where $G_0 = 2\pi g/(\Delta\sigma\sqrt{\ln 2})$ and g is the half-width at half height of the doppler profile. It is related to the temperature of the emitting source by

$$g = 3.58 \times 10^{-7} \sigma_0 \sqrt{\frac{T_n}{M}} \qquad (7\text{-}17)$$

where σ_o is the emission wavenumber, T_n is the temperature, and M is the molecular weight of the emitting species.

Hernandez (1966) has normalized the Airy function given in equation (7-6) to unit area for one period which is written as

$$A(x) = \frac{(1-R^2)}{2\pi(1-2R\cdot\cos X + R^2)} \tag{7-18}$$

The Fourier series expansion of equation (7-18), given by Krebs and Sauer (1953) is:

$$A(x) = \frac{1}{2\pi}\left[1 + 2\sum_{n=1}^{\infty} R^n \cos(nx)\right] \tag{7-19}$$

Hernandez (1966), taking advantage of the work of Chabbal (1953), Bayer-Helms (1963), and Ballik (1966), obtained an analytic convolution of the various functions representing the Fabry-Perot interferometer, and the recorded function is expressed as,

$$Y(x) = \frac{1}{2\pi}\left\{1 + 2\sum_{n=1}^{\infty} R^n \mathrm{EXP}\left[\frac{n^2}{4}(G^2+D^2)\right] \mathrm{SINC}\left(\frac{2nd_f}{\Delta\sigma}\right) \cdot \mathrm{SINC}\left(\frac{2nf}{\Delta\sigma}\right)\cos(nx)\right\} \tag{7-20}$$

where sinc $\beta = (\sin\pi\beta)/(\pi\beta)$. Equation (7-20) represents the shape of the output profile of the Fabry-Perot interferometer. All the functions that were convolved together to give the output profile have been normalized to unit area; therefore in accordance with the theory of convolutions the area of the final expression is also unity. This means that, if a line of unit brightness and arbitrary width is measured with the interferometer, the output profile is broadened and its maximum height decreases in order to maintain the unit area restriction. In determining line profiles, the broadening property of the Fabry-Perot interferometer is important and Hernandez (1966) normalizes the output profile to unity at its peak height and expresses the normalized output as,

$$\psi(x) = \left\{ 1 + 2 \sum_{n=1}^{\infty} R^n \mathrm{EXP}\left[\frac{n^2}{4} (G^2 + D^2) \right] \mathrm{SINC}\left(\frac{2nd_f}{\Delta\bar{\sigma}} \right) \mathrm{SINC}\left(\frac{2nf}{\Delta\bar{\sigma}} \right) \cos(nx) \right\} \left\{ 1 + 2 \sum_{n=1}^{\infty} R^n \mathrm{EXP}\left[\frac{n^2}{4} (G^2 + D^2) \right] \mathrm{SINC}\left(\frac{2nd_f}{\Delta\bar{\sigma}} \right) \mathrm{SINC}\left(\frac{2nf}{\Delta\bar{\sigma}} \right) \right\}^{-1} \tag{7-21}$$

This function predicting the output profile of the Fabry-Perot interferometer is used in the design of the instrument for the Michigan Airglow Observatory.

7.2.5 METHOD OF SCANNING

Shepherd (1967) has discussed three methods of scanning the Fabry-Perot interferometer which are: (a) refractive index scanning, by varying μ, (b) mechanical scanning, by varying t, and (c) spatial scanning, by varying θ.

The index of refraction of a gas is related to its density through the Dale and Gladstone Law

$$\mu = 1 + h\rho \tag{7-22}$$

where h is a constant for a small wavelength scan. A wavelength scan can be accomplished by changing the pressure of the medium between the plates at a constant temperature because the density is related to the pressure and temperature through the ideal gas law. Therefore, for pressure scanning, equation (7-3) can be differentiated and with use of the Dale and Gladstone law, the wavelength change for a given pressure interval becomes,

$$\frac{d\lambda}{dp} = \frac{\lambda}{\mu}\frac{d\mu}{dp} \tag{7-23}$$

where p is the pressure of the gas. The wavelength region scanned is independent of the order of interference. This scanning method is usually used for high resolution work, and for typical values of dp and $d\mu/dp$, a reasonable scanning range is 1 Å.

Mechanical scanning involves the variation of the distance between the plates by mechanical means. From equation (7-3) the scanning rate is

$$\frac{d\lambda}{dt} = \frac{\lambda}{t} \tag{7-24}$$

The scanning range will increase as t decreases and because the inter-order separation, $\Delta\lambda$, is $\lambda^2/2\mu t$; equation (7-24) becomes

$$\frac{d\lambda}{dt} = \frac{2\mu\,\Delta\lambda}{\lambda} \tag{7-25}$$

indicating that the scanning range is a fixed fraction of the interorder separation, independent of the plate spacing. This method of scanning is best suited for low resolution studies where a greater scanning range is desired.

Spatial scanning is accomplished by a variation of the angle of incidence falling upon the aperture, giving approximately

$$\lambda = \lambda_0 - \frac{\lambda_0 \theta'^2}{2\mu^2} \tag{7-26}$$

This type of scanning is accomplished by using an annular aperture, which is expanded in such a manner that its area is held constant, giving a spectral element of constant width (Shepherd, et. al., 1965). The main difficulty with spatial scanning is mechanical, because of the problems involved with constructing a set of very small apertures of equal area in order to scan in discreet steps and yet have enough spectral elements to derive the high resolution required for doppler temperature measurements.

The discussion in this section clearly indicates that pressure scanning is required for the high resolution which is necessary for making doppler temperature measurements in the nightglow.

7.2.6 INSTRUMENT DESIGN

The low intensity of the 6300 Å emission line in the nightglow made it necessary to order a set of large diameter Fabry-Perot etalon plates to ensure good light gathering power at high resolution. The 6" diameter etalon plates were ordered from Optical Works Ltd. in England and they were the largest etalon plates available at that time. The 6" diameter plates were received in August 1967 and had a measured flatness of $\lambda/180$ over 5-1/4" of the central diameter of the plates.

The free spectral range of the Fabry-Perot interferometer was shown to be determined by the plate spacing, $\Delta\sigma = 1/(2\mu t \cos\theta)$. For a photoelectrically scanned interferometer the angle θ is very small and the index of refraction of the medium between the plates is of the order of unity. Therefore, the free spectral range is approximately given by $\Delta\sigma \simeq \frac{1}{2t}$. The free spectral range has been selected so that the measured line profile falls within this range and does not allow an interorder overlap. The doppler line shape of the 6300 Å emission line is shown in Fig. 32 and if it is assumed that the exospheric temperature will not exceed 2500° K, the free spectral range should be at least 0.360 cm^{-1}. A free spectral range of 0.5 cm^{-1} was selected for the 6300 Å emission line based on the

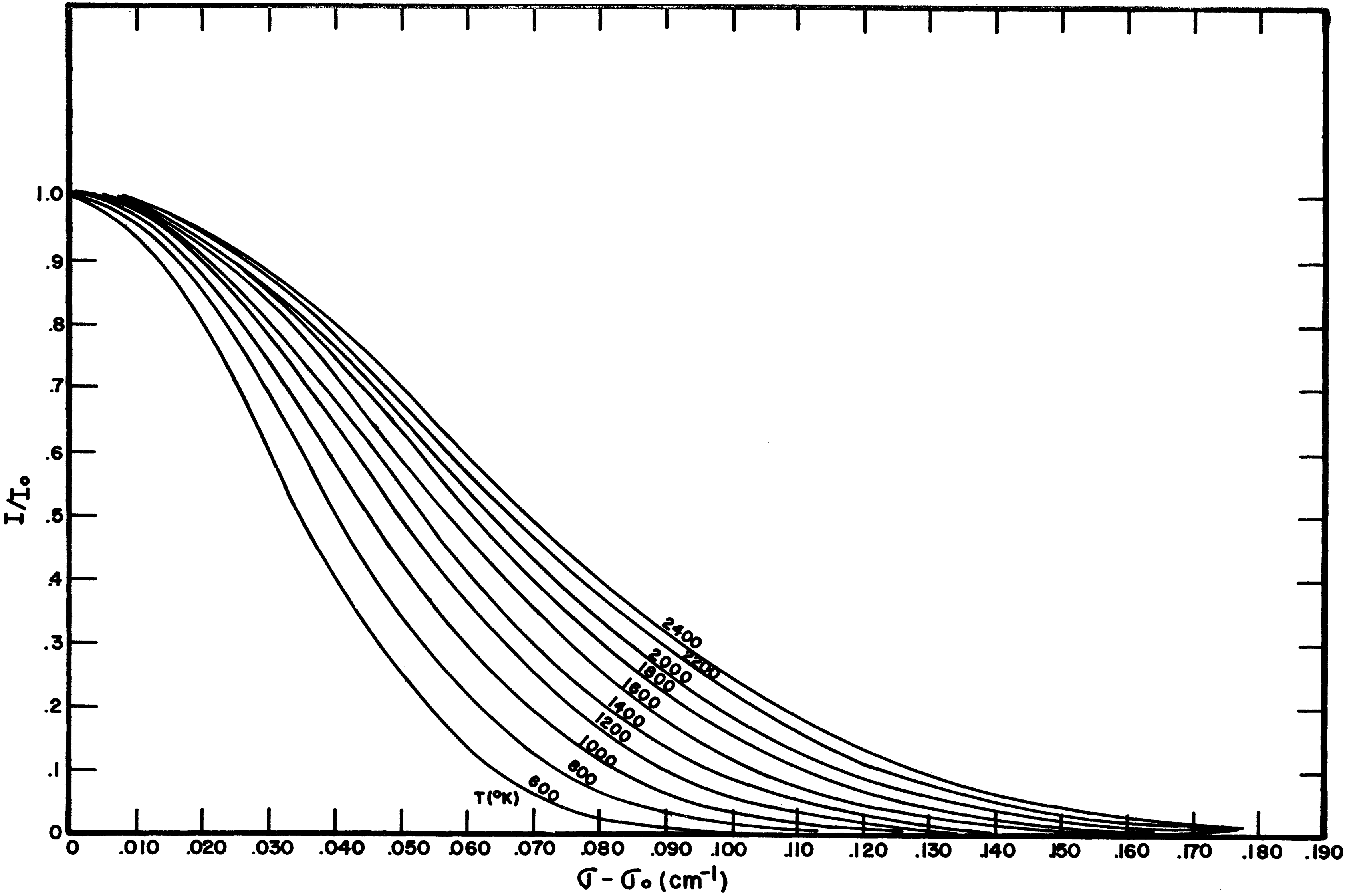

Fig. 32. Doppler line profiles of the 6300Å OI radiation at various temperatures.

a priori estimate of the instrument broadening and the need to determine a zero reference line between the fringe peaks. This free spectral range is obtained with a 1 cm thick spacer which was also ordered from Optical Works Ltd. The spacer was specifically machined for our set of etalon plates and consisted of three raised 1/8" diameter supports with rounded ends on a ring of quartz. The supports were polished flat to $\lambda/10$ of the desired spacing. As will be discussed later, the free spectral range appears to be appropriate for the 6300 Å atomic oxygen emission line in the thermosphere, because the fringe is broad enough to detect a small variation in the line width and yet there is enough distance between the peaks to determine the zero reference line.

The etalon plates had to be coated in order to obtain the highly reflective surfaces necessary for high resolution measurements. The value of the transmission factor τ_A and the value of the reflective finesse N_R depend upon the properties of the coatings. The coatings should have a high value of τ_A at a given reflective finesse and Jacquinot (1960) shows that this condition is best attained with the use of multilayer dielectric coatings instead of the metallic coatings, such as aluminum or silver. The multilayer dielectric coatings consist of a small number of material layers of alternate high and low index of refraction which when deposited upon etalon plates result in a high reflective power if the optical thickness of the layers is $\lambda/4$. In the visible region, ZnS is most often used as the high index material and cryolite as the low index material. According to Chabbal (1953), 5 alternate layers of ZnS and cryolite give a reflectivity of 0.87, 7 alternate layers give 0.95, and 9 alternate layers give 0.98. This corresponds to reflective finesse, N_R of 23, 60, and 180 respectively. Chabbal (1953) has also shown that one obtains maximum luminosity at a given resolution when $N_R \simeq N_D$, where N_D is the limiting defect finesse determined by the surface conditions of the etalon plates. Although the etalon plates had a measured flatness of $\lambda/180$, it was not certain that the multilayer dielectric coatings could be applied with that flatness. The coatings, for the large etalon plates, are especially difficult to apply and there was the possibility that the limiting defect finesse of the uncoated etalon plates would be degraded by a nonuniform application of the multilayer dielectric coatings. Therefore, there appeared to be no great advantage to applying a highly reflective coating which would give a reflective finesse greatly exceeding the limiting defect finesse. This would only result in a departure from the maximum luminosity condition and not increase the resolving power of the instrument. As a result, 5 alternate layers of ZnS and cryolite were applied over 5-1/4" of the central diameter of the plates leaving the outer edges uncoated where the spacer ring would be placed. These coatings result in a reflectivity of 0.87 which gives a reflective finesse of 23.

There is another reason for selecting 5 alternate layers of ZnS and cryolite. The transmitted maximum of the fringe pattern of the Fabry-Perot interferometer has the same brightness as the source, degraded only by the transmissivity of the instrument, regardless of the reflectivity. However, the integrated quantity of the light in the fringe is reduced in accordance with the reflectivity, thus affecting the total incident energy which is transmitted to the photodetector. This is based upon the assumption that the aperture width is adjusted in such a manner that its finesse is of the same order as the defect finesse and reflective finesse (Chabbal, 1953). Because the 6300 Å emission line is weak, a trade-off can be made between the resolution and energy transmitted to the photodetector.

Calculations shown in Fig. 34 indicate that 5 alternate layers of ZnS and cryolite transmit sufficient energy to make 6300 Å nightglow doppler temperature measurements possible. If 7 layers are used, less energy is transmitted making the measurements more difficult.

The reflective finesse of the etalon plates is now established $N_R = 23$, and although the defect finesse of the plates having the applied coatings is not known, it can initially be assumed that $N_R = N_D$. The actual value of N_D is determined from measurements discussed later in the chapter. For maximum intensity at a given resolution, mainly established by the properties of the etalon plates, the ratio of the half-width at half-height of the aperture to the Airy functions should lie within the range $0.9 < f/a < 1.5$. The maximum intensity is actually obtained for $f/a = 1.15$, but the maximum is flat and good performance is obtained over the range indicated (Chabbal, 1953). According to this condition the aperture finesse, for the free spectral range established by the fixed 1 cm spacing, should be approximately $N_F = 20$. From the geometry of the Fabry-Perot interferometer the half-width at half-height of the aperture function, f, becomes

$$f = \frac{\sigma \alpha^2}{4} \tag{7-27}$$

where σ is the wavenumber and α is the angle subtended by the aperture from the etalon plates, shown in Fig. 30, and can be expressed as

$$\alpha = \frac{d}{2F} \tag{7-28}$$

where d is the diameter of the aperture, and F is the focal length of the objective lens. Now solving these equations for d, the diameter of the aperture, one obtains

$$d = 4F\sqrt{\frac{f}{\sigma}} \tag{7-29}$$

In order to keep the aperture at a reasonable size and prevent diffraction effects, a 6" diameter corrected achromat with a 48" focal length, (121.9 cm), was selected for the objective lens. The diameter of the aperture was calculated from equation (7-29) and for an aperture finesse, N_F of about 20, the aperture should be 0.17" diameter (0.43 cm). This now establishes the field of view of the instrument, Ω, which is

$$\Omega = \frac{2\pi f}{\nabla} \tag{7-30}$$

For the parameters given, the field of view of the Fabry-Perot interferometer is 0.2° which extends approximately 1.3 km at an altitude of 400 km.

The fringe pattern formed in the focal plane of the objective lens has the following diameters for the first three fringes: $D_o = 0.$ (fringe peak on the central axis), $D_1 = 0.764''$ (1.94 cm), $D_2 = 1.08''$ (2.74 cm), and $D_3 \doteq 1.33''$ (3.37 cm).

The main parameters of the Fabry-Perot interferometer have been defined and although the plate defect function is not known, it is still possible to make a reasonable estimate of this parameter and calculate the instrument performance. Once the instrument is operational, then the true value of this parameter can be determined and used in the data reduction procedure. Therefore by using the established instrumental parameters and equation (7-21), the performance of the designed instrument was calculated. In Fig. 33 the normalized output profiles of the Fabry-Perot interferometer are shown for a range of doppler temperatures. This figure shows the broadened profile of the 6300 Å doppler line presented in Fig. 32 for a range of temperatures. Clearly the resulting figure satisfies the requirements set forth in this chapter and allows for additional broadening should the measured defect function be larger than

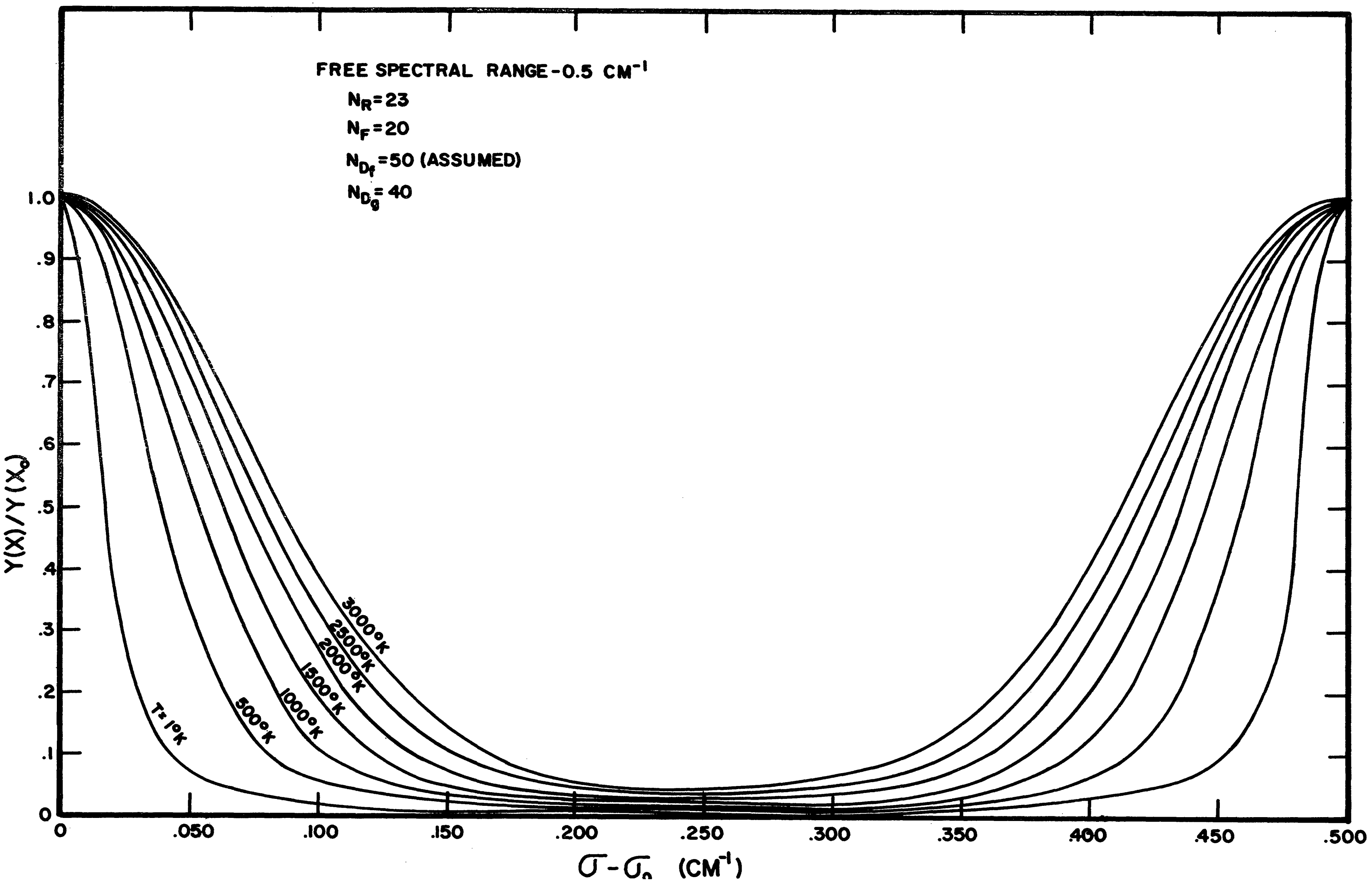

Fig. 33. Predicted 6300Å fringe profiles for the Fabry-Perot interferometer.

estimated. Fig. 34 shows the calculated signal intensities for a 100 Rayleigh 6300 Å emission line. It is assumed that the S-20 photomultiplier efficiency is 5% and the output is normalized to 100% transmission for the glass surfaces and interference filter. The signal level is shown to be quite low and pulse counting techniques are required. Even for a SAR-arc of 10 KR, the number of electrons/sec will be about 10 KHz, well within the range for current pulse counting instruments.

The line intensity is defined as the integral of the doppler curve; therefore the peak value is greater for low temperatures and the profile at high temperatures is broader having a lower peak value. These signal calculations provided the basis upon which the Fabry-Perot interferometer was built and the electronics selected.

The normal nightglow spectrum consists of many background emission lines which must be separated in order to isolate the 6300 Å emission line. Therefore, the Fabry-Perot interferometer must be used with a narrow band interference filter, acting as a pre-monchromator, separating the unwanted orders from the signal. The interference filter has to be narrow enough to reduce the number of nearby OH emission lines and the amount of continuum contaminating the signal. For this instrument, a 2" diameter 4.2Å half-width interference filter peaked at 6302 Å was selected to isolate the 6300 Å emission line. The filter was peaked slightly to the red of the 6300 Å emission line because the peak normally shifts to shorter wavelengths with age.

The instrument described here was built for the Michigan Airglow Observatory. The details of the system including a description of the mechanical layout, electronic system, auxiliary components, adjustment

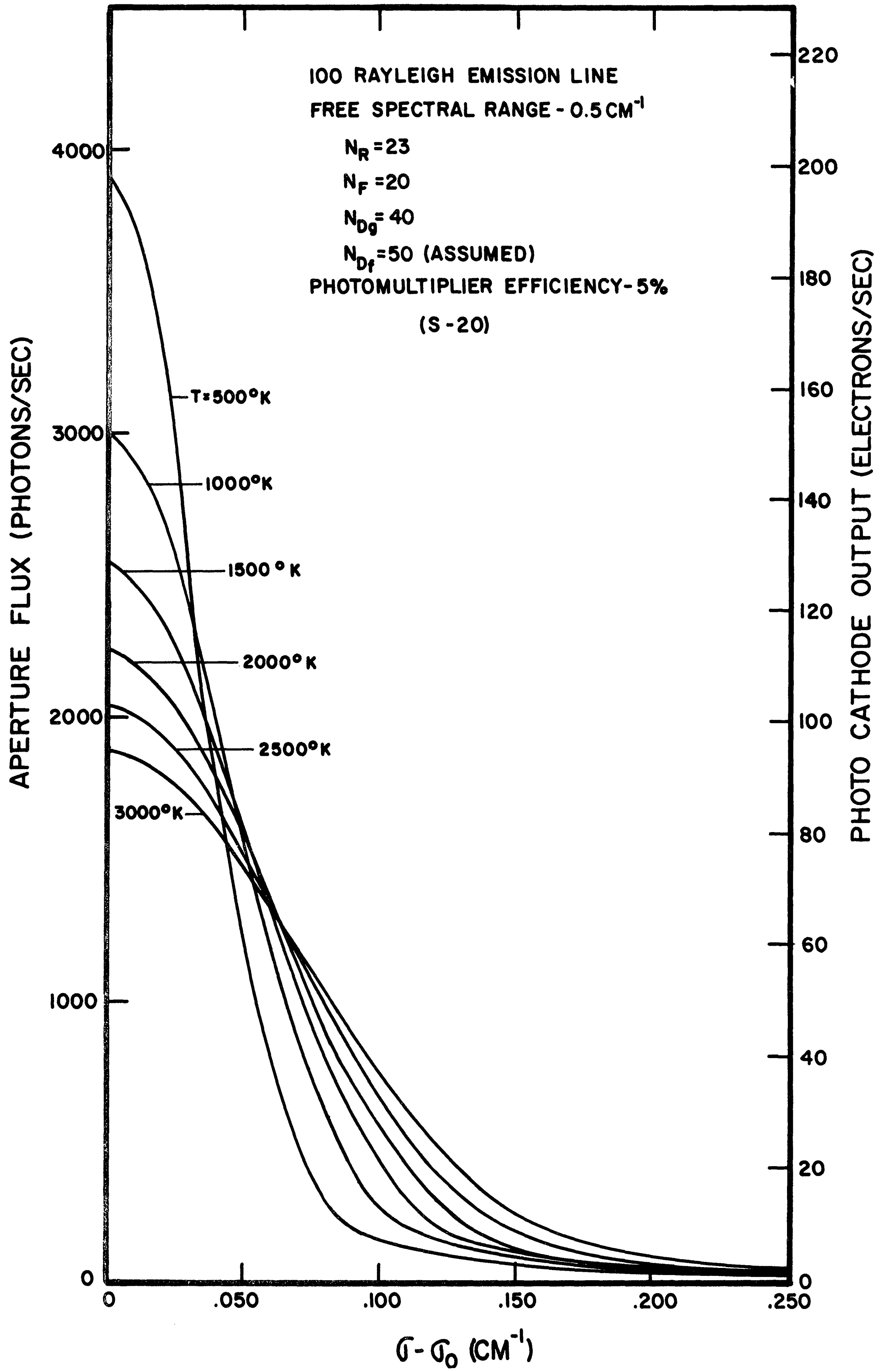

Fig. 34. Predicted signal level and fringe profile of the Fabry-Perot interferometer for a 100 Rayleigh 6300Å emission line at various temperatures.

and operating procedures are presented in Appendix D. In the next section the operational performance of the Fabry-Perot interferometer is described.

7.2.7 OPERATIONAL PERFORMANCE

The Fabry-Perot interferometer was installed in the trailer-van of the University of Michigan Airglow Observatory in June 1968 and numerous tests were performed on the instrument in order to determine the instrument function. The first test involved the determination of the instrument function for a small spot on the etalon plates. A disk with a small central aperture was placed over the Fabry-Perot etalon allowing the light from He-Ne 6328 Å laser source to be transmitted through the etalon and focused on the photomultiplier. The instrument function of the interferometer determined in this manner consists of the broadening functions due to the reflective properties of the plates, the surface roughness defects, and the aperture function. The plate defect due to curvature is not present because only a very small portion of the etalon plates is used. The fringe profile which was recorded by the photomultiplier is shown in Fig. 35. The instrument finesse determined from this curve is approximately 14 assuming that the source profile is a delta function. The aperture function is known because the aperture was precisely machined to 11/64" diameter in order to obtain an aperture finesse of 19.6. The surface defect finesse is about 40 and the reflective finesse is 23. When these parameters are used to calculate the fringe profile from equation (7-21), the overall instrument finesse is also approximately 14 in apparent agreement with the measuredfringes. It was observed, when the etalon was adjusted, that the fringes appeared to grow when the eye was moved from the center of the plates to the outer edges. This effect indicated a departure

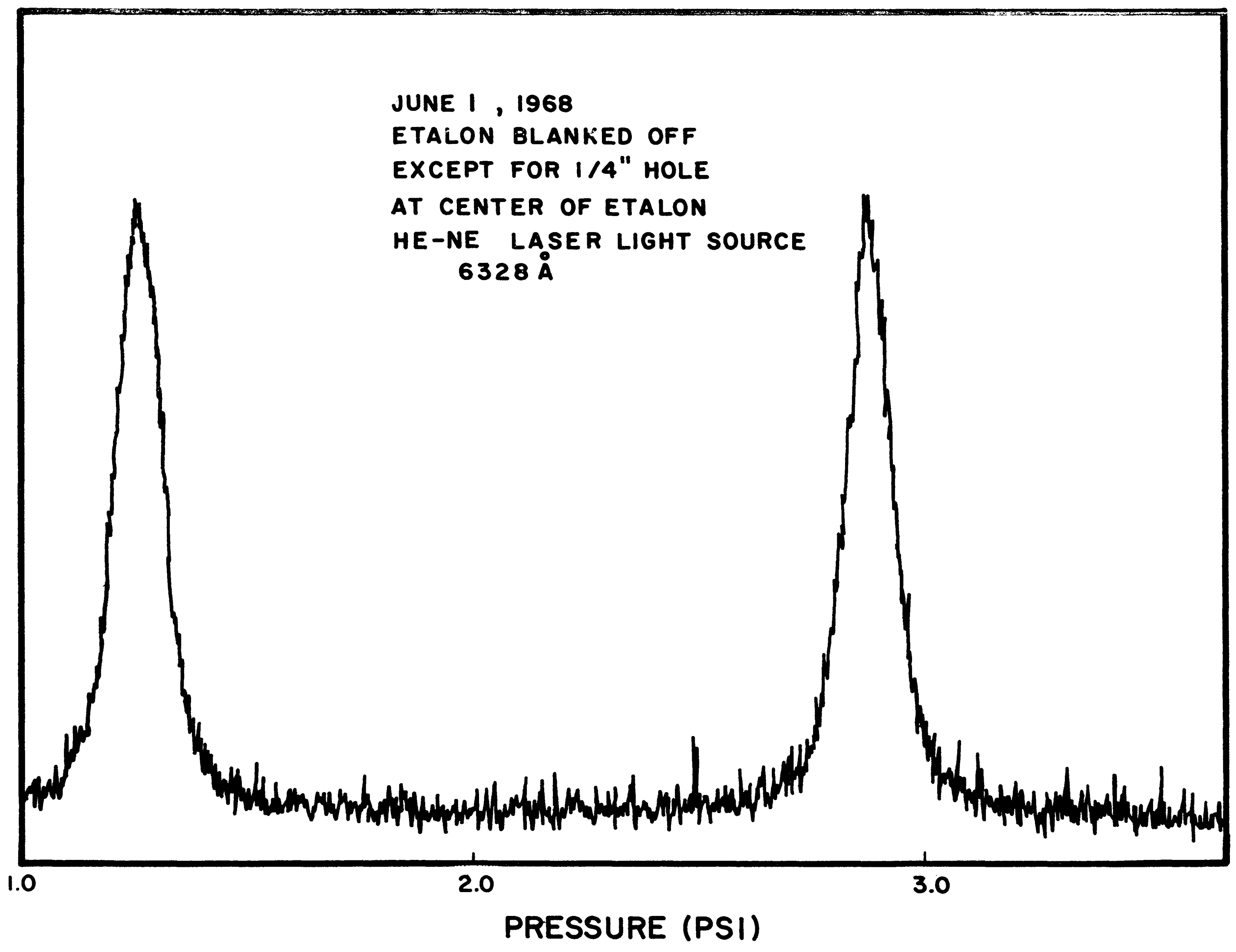

Fig. 35. Measured 6328Å He-Ne laser fringe profile for a small central spot of the etalon plates.

from perfect parallelism and was attributed to a spherical defect due to either a sagging of the plates caused by their own weight, or a non-uniform application of the dielectric coatings. This effect was studied by moving the circular hole in the disk over the etalon to various radial distances, recording the fringe profile obtained at that position, and determining the amount of frequency shift between the peak fringes. Fig. 36 shows the fringe profiles which were obtained when the aperture was located at the center of the plates, at a 1" and a 2" radius from the center, and also when the whole etalon was exposed. The fringes at the center and also at the other radii are narrow and of the same shape as the profile shown in Fig. 35. There is, however, a noticeable shift in the peak frequency for the various fringes as the aperture was moved to the different radii over the etalon plates. When the whole etalon is exposed to the light, the resulting fringe encompasses all of the component fringes. The frequency shift of the fringes indicates a spherical defect with a saggitta of 1.55×10^{-6} cm. According to Chabbal (1953) the spherical defect function is a square function and for this saggitta the half-width at half-height is 0.012 cm^{-1} which corresponds to a defect finesse, N_{D_f}, of 20.3 for this instrument.

The overall operating parameters of the Fabry-Perot interferometer have now been determined and are summarized in Table III. Also the calculated normalized fringe profiles for the Fabry-Perot interferometer with these parameters are shown in Fig. 37.

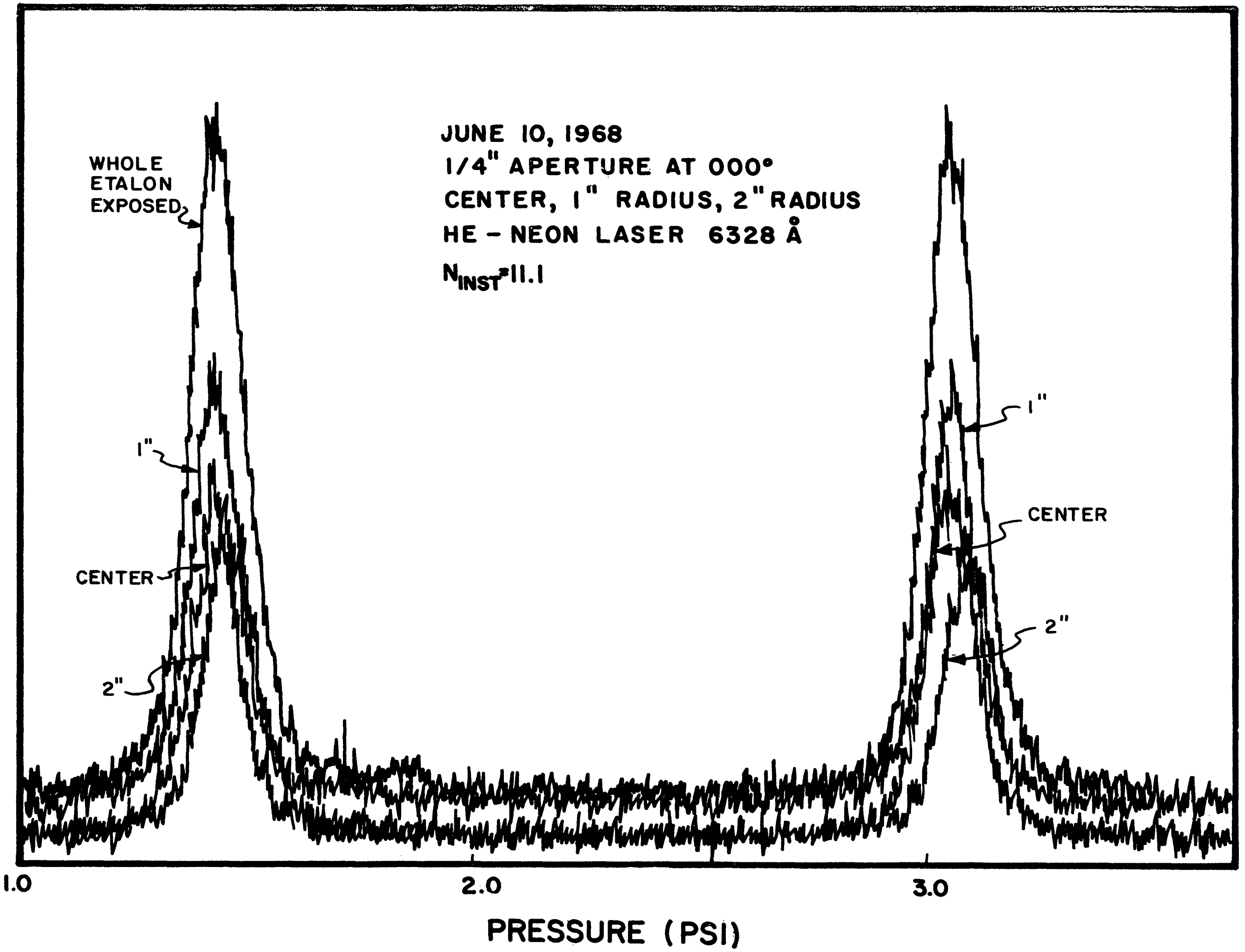

Fig. 36. Measured 6328 Å He-Ne laser fringe profiles for the entire etalon plates and for a 1/4" aperture located at the center of the etalon plates, and at 1" and 2" radii from the center.

TABLE III

OPERATING PARAMETERS OF THE FABRY-PEROT INTERFEROMETER

1. Etalon plates	
effective diameter	5-1/4"
flatness	λ /180
roughness defect, N_{D_g}	40
reflective coatings	5 alternate layers of ZnS and cryolite
reflectivity	0.87 at 6300 Å
reflective finesse, N_R	23
spherical defect finesse, N_{D_f}	20.3
saggitta	1.55×10^{-6} cm
spacing, t	1 cm
2. Objective lens	48" (achromat)
diameter	6"
3. Aperture	
diameter	11/64"
finesse	19.6
4. Instrument field of view	0.2°
5. Interference filter	
diameter	2"
half-width	4.2 Å
peak transmission	45%
peak wavelength	6302 Å
6. Photomultiplier (ITT-FW-130)	
quantum efficiency at 6300 Å	5%
photocathode surface	S-20
effective aperture	1/10"
dark count (cooled to -15°C)	1-2 counts/sec.
(uncooled)	80-90 counts/sec.
7. Resolving power	350,000
8. Operating order	31,700
9. Free spectral range	.198 Å (0.5 cm^{-1})
10. Scanning gas	(Dry Nitrogen)
11. Pressure change for 1 order	1.72 psi
12. Overall instrument finesse	11

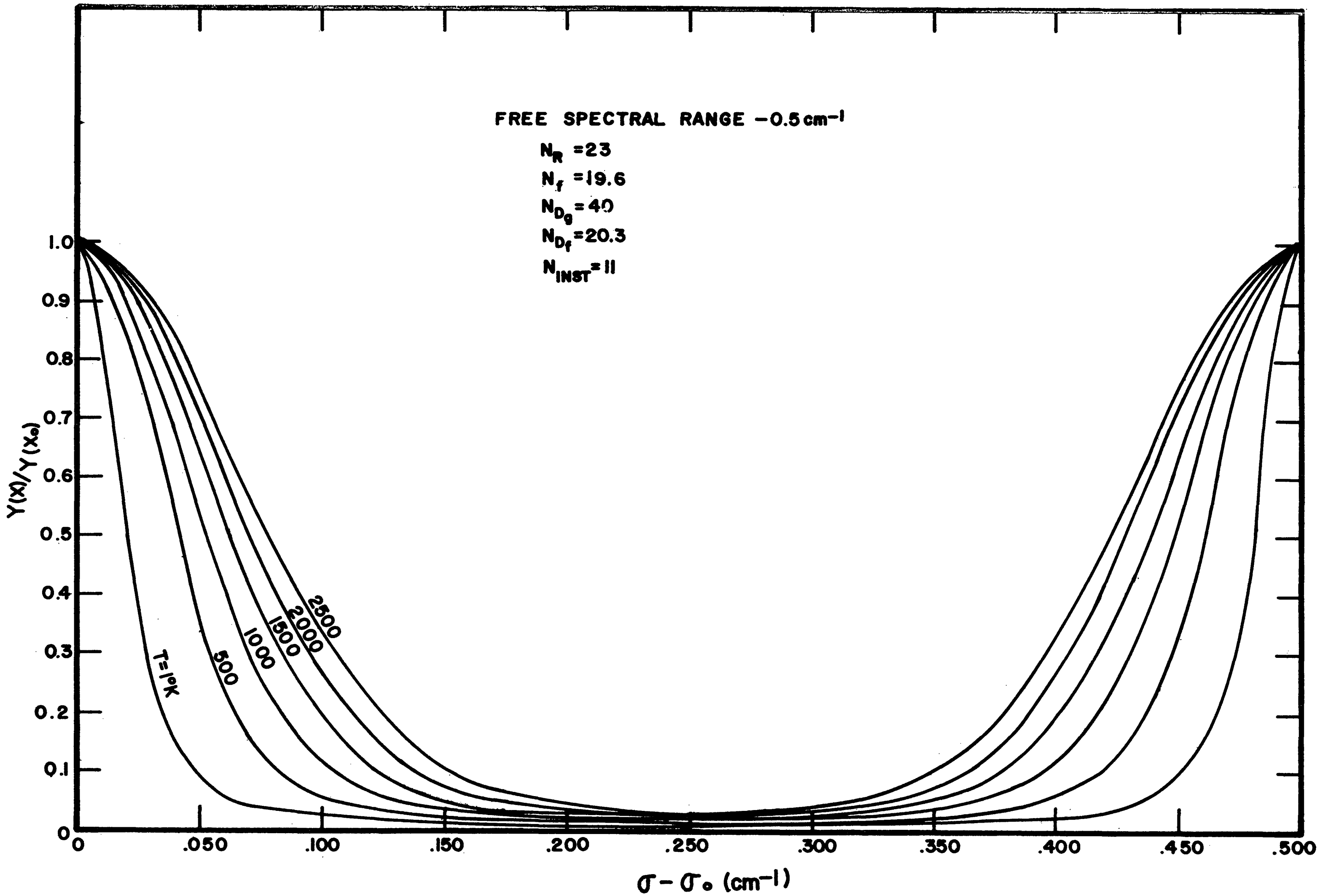

Fig. 37. Calculated 6300Å fringe profiles for the designed Fabry-Perot interferometer having the experimentally determined broadening function parameters.

Some of the parameters listed in the table were based upon the assumption that the He -Neon laser operating at 6328 Å provides a very narrow line source. The laser operates at a single mode; however it is not temperature compensated and may actually be slightly broader. Such a broadening would result in a slightly greater instrument finesse than the measured value of 11. The actual manner in which the laser is used is discussed in Appendix D. Measurements were also carried out with a single isotope mercury 198 line source where the line shape and width are known and the finesse measurements are in essential agreement with the results obtained from the laser. The mercury line source is, however, at a wavelength of 5461 Å which is relatively far from the 6300 Å red line and therefore corrections to certain broadening functions must be applied to obtain an instrument finesse at 6300 Å.

7.2.8 6300 Å NIGHTGLOW MEASUREMENTS

In this section several fringe profiles are presented showing the performance of the instrument on the night sky. The instrument was first used to make observations of the 6300 Å emission line in the twilight where the intensity of the line is relatively strong and Fig. 38 shows a typical twilight fringe. The x-axis is a measure of the etalon pressure which is directly proportional to the scanning wavelength and the y-axis gives the number of counts from the photomultiplier. A relatively fast scan is used in order to avoid intensity changes which occur in twilight and the signal to noise ratio can be improved by adding fringes through their Fourier transforms, as will be described in the next section. The peak signal shows a counting rate of 40 counts per second and the fluctuations in the signal are due to the normal statistical fluctuation of the photomultiplier which is proportional to the square root of the signal. These high

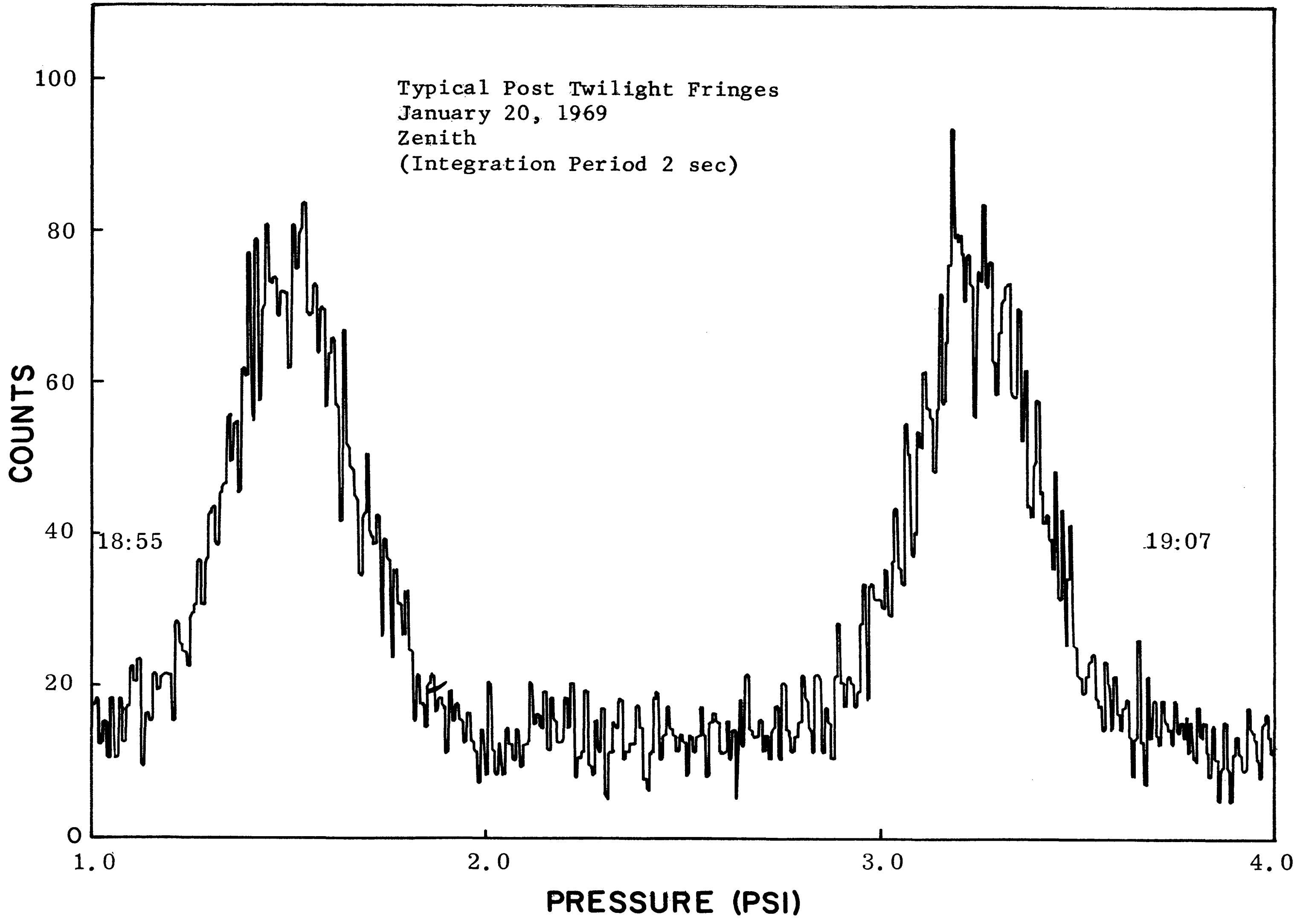

Fig. 38. Typical 6300Å post twilight fringe profiles obtained on January 20, 1969.

frequency variations are eliminated in the data reduction program in a manner which is described in the next section. Fig. 39 shows a nightglow signal in the early morning hours when the 6300 Å intensity is very low. A long integration time is required to obtain an acceptable signal to noise ratio. The peak signal shows a count rate of about 5 counts/sec compared to a background of 1.4 counts per second. These fringe profiles indicate that it is possible to monitor the diurnal variation of the doppler temperature for the normal 6300 Å nightglow emission (Roble, Hays, and Nagy, 1968).

Two other fringe profiles are presented here in order to show a range of operating conditions and also for comparison purposes. The first is a fringe obtained on Oct. 31/Nov. 1, 1968 SAR-arc and it is shown in Fig. 40. The fringe peak shows a count rate of about 50 counts/sec whereas in the normal nightglow, at the time the fringe was taken, the count rate would be about 10 counts/sec. The fourth fringe, shown in Fig. 41 was taken in an aurora which occurred over Ann Arbor, Michigan, on the night of Nov. 1/2, 1968. This fringe was taken at the same local time as the fringe on the SAR-arc and it indicates a peak count rate of 600 counts $\sec^{-1}$ indicating an auroral feature of about 6-8 KR. These curves show the intensity range for which doppler temperature measurements are made with this Fabry-Perot interferometer.

7.2.9 DATA REDUCTION PROCEDURE

In section 7.2.7 the measured line profile of the Fabry-Perot interferometer was shown to consist of a multiple convolution of various broadening functions. In order to retrieve the true line profile of the 6300 Å emission line a deconvolution of the interferometer instrument function is necessary. Several authors (Chabbal, 1953; Turgeon and Shepherd,

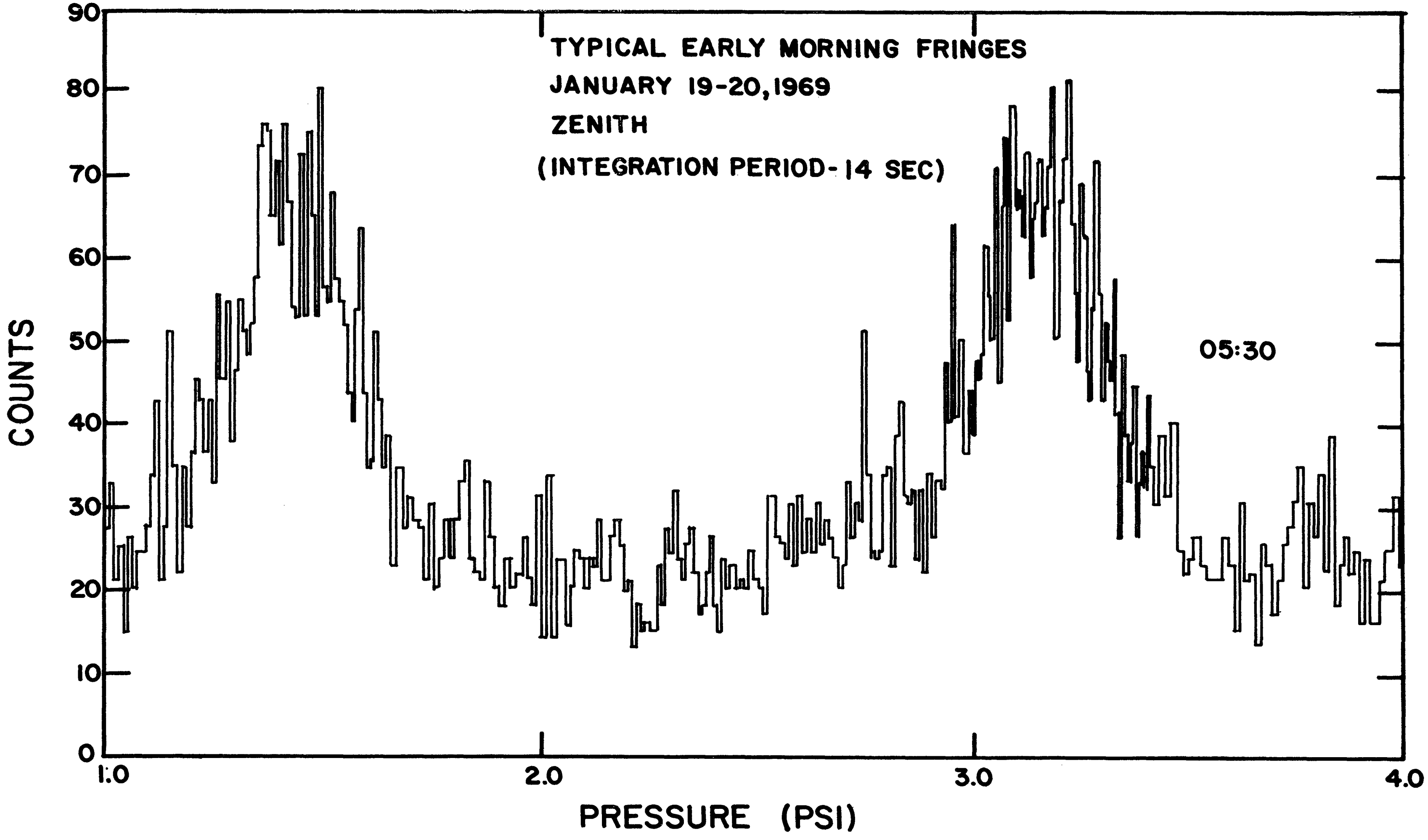

Fig. 39. Typical 6300Å nightglow fringe profiles obtained on January 21, 1969.

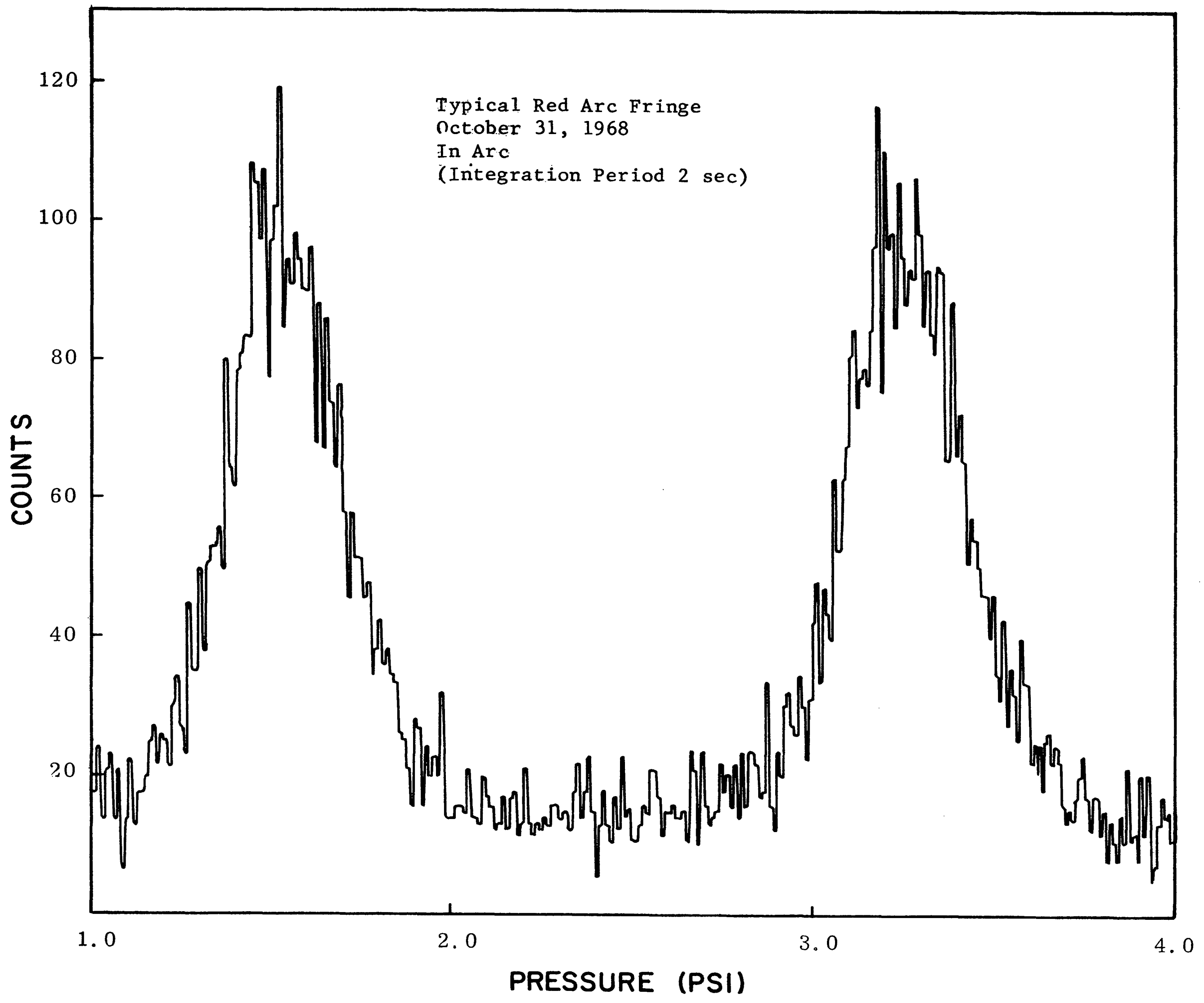

Fig. 40. Typical 6300Å SAR-arc fringe profiles obtained within the SAR-arc region on October 31, 1968.

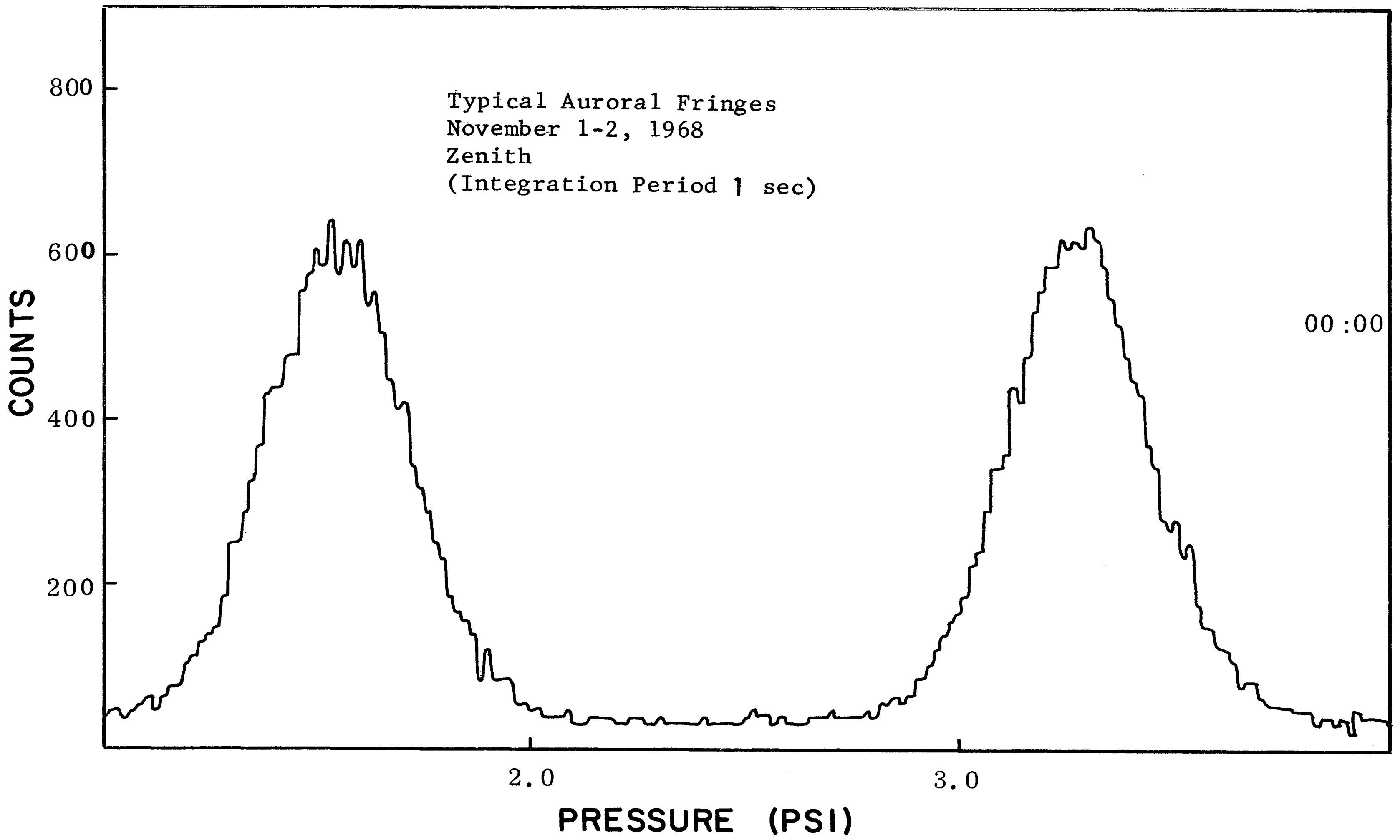

Fig. 41. Typical 6300Å auroral fringe profiles measured on the low latitude aurora of November 1/2, 1968.

1962; Hernandez, 1966; Larson and Andrew, 1967; and Shepherd, 1967) have presented methods for retrieving the emission line profile from the measured signal; however, these techniques generally work best with noise free, or smoothed, data. It can be seen from the figures presented in section 7.2.8, that the intensity of the signal is very weak resulting in a spectrum which contains a certain amount of noise due to the statistical fluctuations of the photomultiplier. This noise is proportional to the square root of the signal count rate and for very weak signals, as would exist in the nightglow, the noise can become an appreciable part of the signal level. However, this noise is of a very high frequency and can be removed by a filtering process leaving only the fundamental frequencies which contribute to the fringe profile. The filtering is accomplished by taking the finite Fourier transform over a free spectral range. The Fourier cosine transform of the fringe profile $\tilde{Y}_{cm}$, for wavenumber m, is obtained by holding all parameters constant and varying the index of refraction of the gas so as to give a wavelength scan over one free spectral range (from fringe peak to fringe peak); this can be written as

$$\tilde{Y}_{cm} = \int_{x_1}^{x_2} \cos(mx)\, Y(x)\, dx \qquad (7-31)$$

where x_1 and x_2 are the optical paths for a change of the index of refraction over a free spectral range μ_1, μ_2; Y(x) is given in equation (7-20) and the rest of the parameters are defined in section 7.2.7.

The equipment operation sequence, described in Appendix D, shows that the etalon pressure, which is directly proportional to the index of refraction of the gas and hence the scanning wavelength, is linearly varied and the number of electron counts from the photomultiplier is recorded for a given pre-set time. At the end of a sampling time Δ t, the pressure has changed by an amount δp, (where $\delta p/\Delta t$ = constant) and the counter records Y(p) counts per second. The Fourier cosine transform of the fringe profile is now calculated with respect to pressure to give

$$\tilde{Y}_{cm} = \int_0^{\Delta p} \cos\left[4\pi t(\sigma-\sigma_0)\cos\theta\cdot mkp\right] Y(p)\,\frac{2\pi}{\Delta p}\,dp \tag{7-32}$$

where Δp is the pressure change over a free spectral range. This equation is integrated over one small pressure step, δp, and then summed over all pressure steps for one free spectral range resulting in the expression

$$\tilde{Y}_{cm} = -\frac{1}{m}\sum_{i}^{i_{max}} Y_i(p_i)\left[2\sin\left(\frac{2\pi m p_i}{\Delta p}\right)\sin^2\left(\frac{\pi m\delta p}{\Delta p}\right) + \cos\left(\frac{2\pi m p_i}{\Delta p}\right)\sin\left(\frac{2\pi m}{\Delta p}\delta p\right)\right] \tag{7-33}$$

where $\delta p = p_i - p_{i-1}$ is the pressure difference for the i^{th} step, and $Y_i(p_i)$ is the total count at the end of the time for a pressure change δp. Thus, every recorded point is used in the determination of the Fourier components of the fringe. The Fourier cosine transform requires that the fringe be calculated from fringe peak to fringe peak over one free spectral range. This requirement is removed by also considering the Fourier sine transform. It is then possible to begin the transform calculation at any point on the fringe profile as long as the total number of points considered include a free spectral range. The Fourier sine transform can be written as

$$\tilde{Y}_{sm} = \frac{1}{m}\sum_{i}^{i_{max}} Y_i(p_i)\left[2\cos\left(\frac{2\pi m p_i}{\Delta p}\right)\sin^2\left(\frac{\pi m\delta p}{\Delta p}\right) - \sin\left(\frac{2\pi m p_i}{\Delta p}\right)\sin\left(\frac{2\pi m\delta p}{\Delta p}\right)\right] \tag{7-34}$$

Now the total Fourier transform of the data becomes,

$$\tilde{Y}_M = \sqrt{\tilde{Y}_{CM}^2 + \tilde{Y}_{Sm}^2} \tag{7-35}$$

By considering only about the first ten of the transform components, the high frequency noise superimposed on the fringe profile is filtered out leaving only the terms directly contributing to the fringe profile. The analytic representation of the fringe profile determined by Hernandez (1966) is given in equation (7-20) and can be written as

$$Y(x) = I_o \left\{ A_o + \sum_{n=1}^{\infty} A_n \, EXP\left(-n^2 G^2/4\right) \cos(nx) \right\} \tag{7-36}$$

where

$$A_o = \frac{1}{2\pi}$$

$$A_n = \frac{1}{\pi} R^n \cdot EXP\left(\frac{n^2 D^2}{4}\right) SINC\left(\frac{2n d_f}{\Delta\sigma}\right) SINC\left(\frac{2nf}{\Delta\sigma}\right)$$

The measured profile can be expressed as

$$Y^*(x) = \sum_{m=1}^{\infty} \tilde{Y}_m \cos(mx) + C \tag{7-37}$$

where C is the background level of the signal and is equivalent to the constant $I_o A_o$ term in equation (7-36). The temperature is now obtained in a least square sense by minimizing

$$\langle \delta y^2 \rangle = \int_{-\Delta x/2}^{\Delta x/2} \left[Y(x) - Y^*(x) \right]^2 dx \tag{7-38}$$

where Δx represents the free spectral range in units of optical path. Utilizing equations (7-36) and (7-37) one obtains for the integral

$$\langle \delta Y^2 \rangle = \sum_{m=1}^{M} \tilde{Y}_m^2 - \left[\sum_{m=1}^{M} A_m \tilde{Y}_m \, \mathrm{Exp}(-n^2 \gamma T_n/4) \right] \left[\sum_{m=1}^{M} A_m^2 \, \mathrm{Exp}(-n^2 \gamma T_n/4) \right]^{-1} \qquad (7\text{-}39)$$

where $\gamma = \left(\frac{5.12 \times 10^{-6} \pi}{\ln 2} \right) \frac{\sigma_o^2}{M}$. Because all terms except T_n are constant in equation (7-39), the doppler temperature is obtained by varying T_n in such a manner that $\langle \delta Y^2 \rangle$ is minimized. The T_n corresponding to the minimum is the doppler temperature in a least square sense. The time required to invert a temperature profile, using an IBM 360/67, is very short, approximately 2 seconds.

Although a complete error analysis utilizing the technique has not been completed, the points determined from the calculated fringe profile, equation (7-20), were randomly scattered with an approximate noise distribution similar to that shown in the figures of the fringe profile, and the technique was able to retrieve the original temperature within a band of ± 40°K. This is a preliminary estimate, however, and more analysis is required to adequately determine the error bands of the measurement. As shown in the figures presented in the previous section, two fringes are normally obtained for one scan and therefore the signal to noise ratio can be increased by adding the Fourier transforms of the two fringes before the temperature is obtained from the least square fit. In this manner the accuracy of the temperature is improved; in fact, as many scans as are desirable can be added together to improve the signal to noise ratio and obtain an average temperature for the period.

7.3 AIRGLOW PHOTOMETER

A detailed description of the airglow photometer is given in Appendix D. Basically, it is of the turret type designed by Purdy, Megill, and

Roach (1961) where a lower turret wheel positions a narrow band interference filter over a telescope and the upper turret wheel alternately positions: (a) a blank disk for a dark reference reading, (b) a standard light reference source, and (c) an access hole for a reading of the night sky, over the telescope and interference filter. These three readings are sufficient to determine the signal from the night sky in Rayleighs. Normally, an emission line filter passband is of the order of 15 to 30 Å and therefore the signal entering the photometer consists of (a) the emission line (b) an underlying continuum background, and (c) light from any nearby contaminating emission lines. The intensity of emission lines is obtained by appropriately subtracting the continuum from the signal. The continuum is determined from a separate filter which has a passband in a region which is near the emission line and also is in a region which is relatively free of other airglow emissions. If there are other lines near the emission line of interest, this method is not the best for measuring the intensity of that line.

7.3.1 FILTER SELECTION

The 5577 Å and 6300 Å emission lines were selected as the lines to be studied with the airglow photometer. The airglow spectrum in the region of interest, from 5400 Å to 6400 Å, has been given by Broadfoot and Kendall (1968). Their spectrum shows that the 5577 Å emission line is free from contaminating nightglow emission lines; however, the 6300 Å emission line lies within some relatively weak OH lines belonging to the 9-3 and 5-1 vibrational transitions in the Meinel bands (Chamberlain and Smith, 1959). The OH lines should generally be constant through the night and a predetermined constant may be subtracted from the signal to account for the contamination from these lines. The nightglow spectrum near 5400 Å and

6100 Å are free of strong emission lines and are in a good region to monitor the continuum.

Four interference filters were ordered for the airglow photometer; 5400 Å and 6100 Å interference filters both with a 30 Å half-width for monitoring the continuum, and 5577 Å and 6300 Å interference filters both with 15 Å half-widths for measuring the intensity of the atomic oxygen emission lines. There are other contaminating features which must be considered if the airglow measurements are being made near populated areas. The 5571 Å mercury line lies close to the atomic oxygen green line and a weak 6304 Å neon line lies close to the red line of atomic oxygen and each may contribute to the photometer signal.

7.3.2 DATA REDUCTION PROCEDURE

When the photometer is in normal operation three readings are made with each interference filter: the dark count of the photomultiplier tube, the calibration signal from the standard light source, and the sky reading. These readings from both the emission line filter and the continuum filter are then sufficient to retrieve the intensity of the nightglow emission line. Consider the 6300 Å emission line and the 6100 Å continuum filter combination for the determination of the intensity of the atomic oxygen red line. The calibration signal of the continuum filter, S_{CC}, can be written as

$$S_{cc} = S_D + A\Omega_1 \int_0^\infty c(\lambda)\, T(\lambda)\, P(\lambda)\, d\lambda \tag{7-40}$$

where S_D is the photomultiplier dark count signal, A is the photometer collecting area, Ω_1 is the photometer field of view, λ is the wavelength, c (λ) is the standard light spectral characteristics, shown in Fig. 74, T (λ) is the filter transmission function, and P (λ) is the photomultiplier spectral response for an S-20 photomultiplier. The night sky signal from the continuum filter, S_{cs}, is

$$S_{cs} = S_D + A\Omega_1 \int_0^\infty E_c(\lambda) T(\lambda) P(\lambda) d\lambda \tag{7-41}$$

where $E_c(\lambda)$ is the spectral intensity of the nightglow continuum. The photomultiplier spectral response $P(\lambda)$ is considered to be a constant $\bar{P}$ over the narrow passband of the filter. By assuming that the continuum spectral intensity is constant over the filter passband, $\bar{E}_c$, equations (7-40) and (7-41) can be solved directly to yield the total continuum signal under the filter passband.

$$\bar{E}_c = \frac{(S_{cs} - S_D)}{(S_{cc} - S_D)} \bar{C}_c \tag{7-42}$$

where

$$\bar{C}_c = \int_0^\infty C(\lambda) T(\lambda) d\lambda \Big/ \int_0^\infty T(\lambda) d\lambda$$

This value is divided by the effective width of the filter to obtain the continuum background in R/Å.

Now for the emission line filter the calibration signal, S_{sc} becomes

$$S_{sc} = S_D + A\Omega_1 \int_0^\infty C(\lambda) T_1(\lambda) P(\lambda) d\lambda \tag{7-43}$$

where $T_1(\lambda)$ is the emission line filter transmission function. The sky signal from the emission line filter, S_{ss}, can be written as

$$S_{ss} = S_D + A\Omega_1 \left\{ E(\lambda_0) T_1(\lambda_0) P(\lambda_0) + \int_0^\infty E_c(\lambda) T_1(\lambda) P(\lambda) d\lambda \right\} \tag{7-44}$$

where it is assumed that the 6300 Å emission line profile is narrow enough to be transmitted through the filter at essentially one wavelength, thus acting as a delta function. Again noting that the photomultiplier spectral response $P(\lambda)$ and the continuum spectral intensity $E_c(\lambda)$ are constant over the spectral region of interest, then the emission line intensity comes directly from equations (7-42), (7-43), and (7-44) as

$$E(\lambda_0) = \left\{ \frac{(S_{ss} - S_D)}{(S_{sc} - S_D)} - \frac{(S_{cs} - S_D)}{(S_{cc} - S_D)} \, \frac{\bar{C}_c}{\bar{C}_s} \right\} \frac{\int_0^\infty c(\lambda) T_1(\lambda) \, d\lambda}{T_1(\lambda)} \tag{7-45}$$

where $\bar{C}_s$ is defined in the same manner as $\bar{C}_c$ except for using $T_1(\lambda)$ instead of $T(\lambda)$. $\bar{C}_c$ and $\bar{C}_s$ are the mean values of the standard light spectral characteristics over the wavelength region of the continuum and emission line filters respectively. From the spectral characteristics of the filter transmission function and the standard light shown in Fig. 74, the integrals may be evaluated for each filter and then used as constant factors in the data reduction program. The source and filter characteristics do, however, change with time (Blifford, 1966) and should be re-calibrated every 6 months.

After the uncorrected signal is obtained the data is reduced in accordance with the method described by Cruz, et. al. (1965) where corrections are made for scattering, attenuation, and the Van Rhijn effect for both the 5577 Å and 6300 Å emission line.

VIII. RESULTS OF OBSERVATIONS

In this chapter the data and analysis of three SAR-arcs are presented: (1) The SAR-arc of October 30/31, 1968, (2) the SAR-arc of October 31/ November 1, 1968, both observed from the airglow observatory at Ann Arbor, Michigan, and (3) the SAR-arc of September 28/29, 1967, which was photometrically observed from the ground (Hoch, Marovich, and Clark, 1968) at the same time that the Alouette I and II satellites passed over the arc (Norton and Findlay, 1969). The results of the observations are discussed and compared to the theoretical model of the SAR-arc which was presented in the previous chapters.

8.1 THE SAR-ARC OF OCTOBER 30/31, 1968

A large geomagnetic storm, as revealed by the increased magnetic index, K_p, plotted in Fig. 42, began at about 0000 UT on October 31, 1968, and both the Fabry-Perot interferometer and the airglow photometer were making nightglow measurements at that time. The early evening records gave some indication of a SAR-arc type enhancement at an approximate zenith angle of 30^o north of the geophysical observatory; however, it was not possible to resolve the feature completely because of some clouds in the area. No measurements were made from 0200 UT to 0545 UT because of cloudy conditions, but a general clearing occurred near 0600 UT and a small 100 R SAR-arc was observed from Ann Arbor at a zenith angle of approximately 50^o south in the meridian plane. The photometer mirror system was performing a north-south vertical circle scan and the SAR-arc appeared as a distinct enhancement of the 6300 Å emission at 50^oS which was superimposed upon the normal Van Rhijn intensity variation. At the same time, there was a noticeable increase in the 6300 Å emission line in the north which was probably related

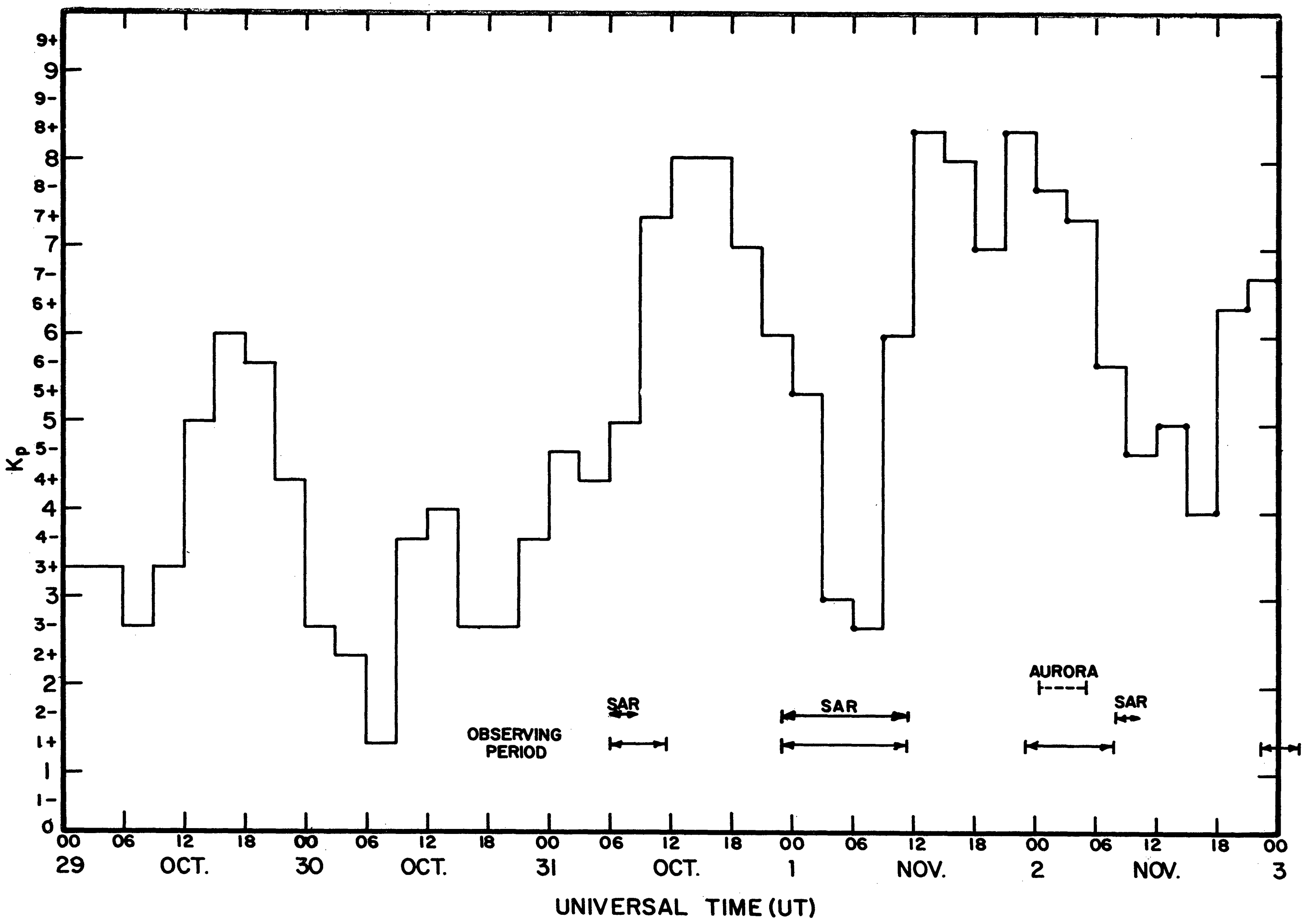

Fig. 42. The magnetic index K_p as a function of time for the disturbed period October 30-November 2, 1968.

to auroral activity. No enhancement, in the SAR-arc region, was evident from either the 5577 Å or 6100 Å photometer scans. The arc moved slowly southward 5 to 10 degrees and persisted until 0715 UT when it disappeared.. At 0837 UT the 6300 Å emission again increased in the north;however, the SAR-arc did not reappear. A few 6300 Å doppler temperature measurements were made at various times during the night and the results are shown in Fig. 53. The doppler temperatures appeared to remain constant during the night. The important temperature measurement made within the SAR-arc region is doubtful because of several small clouds drifting past the interferometer field of view during the scan. It is interesting to note in Fig. 42, that the SAR-arc persisted at a time when the K_p index was increasing and dissappeared even though K_p continued to increase during the night.

8.2 THE SAR-ARC OF OCTOBER 31/NOVEMBER 1, 1968

The magnetic storm which started on the night of October 30/31, 1968, continued during the next day, reaching a K_p value of 8 near 1200 UT on October 31, as shown in Fig. 42. The storm then decreased in intensity and a SAR-arc was detected south of Ann Arbor shortly after sunset and it persisted throughout the night. Measurements with both the Fabry-Perot interferometer and airglow photometer were made on the SAR-arc and the results are presented in the next sections.

8.2.1 AIRGLOW PHOTOMETER MEASUREMENTS

The airglow photometer, performing a vertical circle scan at an azimuth angle of 005°, first detected the SAR-arc at 2345 UT on October 31, 1968, slightly to the south of the airglow observatory. At 0030 UT the SAR-arc was clearly defined to be at a zenith angle of 15° and a true azimuth angle of 190°. Between 0000 and 0300 UT on November 1, the SAR-arc moved southward with a speed of about 40 m sec^{-1} when the speed is calculated at 400 km, the assumed SAR-arc height. The arc settled at a zenith angle near 60°S and remained at that position until 0800 UT at which time the arc began moving southward again at a speed of approximately 40 m sec^{-1}. The position of the SAR-arc in the meridian plane is shown in Fig. 43 as a function of time.

Vertical circle surveys were performed after the initial location of the SAR-arc in order to define the horizontal position and extent of the arc. The mirror scanning system was first positioned in azimuth and maintained at that position while a vertical circle scan was performed, going from +80° zenith angle in the north through the zenith to -80° zenith angle in the south. The mirror was then positioned to a new azimuth angle, usually 20° from the previous position, and the scan was repeated. A typical scan pattern using the 6300 Å filter in the airglow photometer is shown in Fig. 44. The SAR-arc appears as a distinct enhancement superimposed on the normal Van Rhijn intensity increase near the horizon. When the azimuth angle is 115°, corresponding to a near east-west scan, no noticeable enhancement is present because the scan is almost parallel to the arc. However, as the azimuth angle increases, so that the zenith scans begin crossing the arc, the peak 6300 Å emission appears at different zenith angles and these angles are used to determine the geographical alignment of the SAR-arc relative to the observatory. The sky conditions during the entire night of October 31/November 1 were clear;however, a near full moon was present in the southern sky until about 0730 UT. The moon's presence is evident in Fig. 45 where an identical scan is presented for the 6100 Å continuum filter. The increased intensity in the southern sky is caused by the moon;however, the sharp intensity enhancement evident in the 6300 Å filter scan is not apparent in this figure. A similar scan with the 5577Å green line filter, shown in Fig. 46, also exhibits the normal

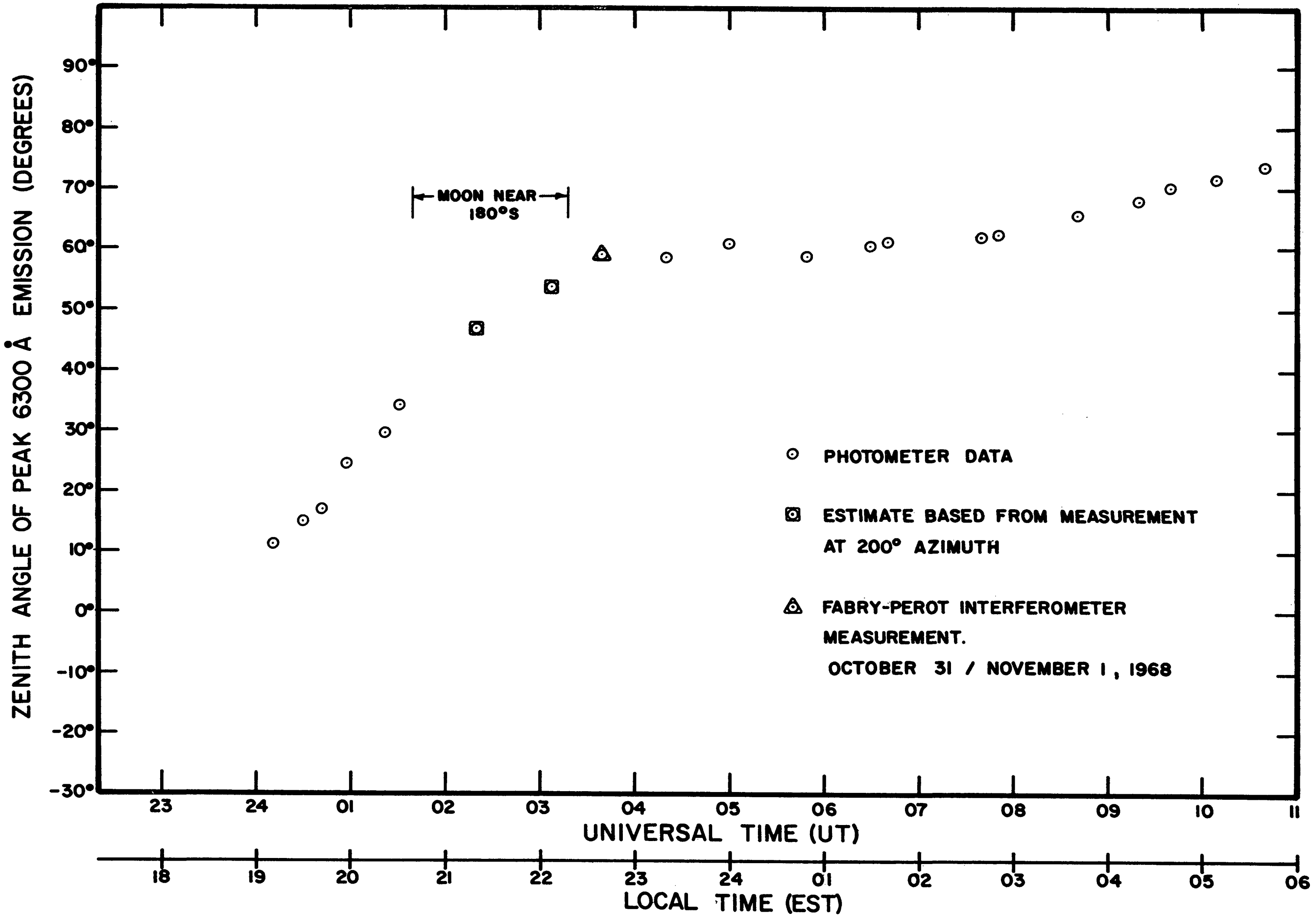

Fig. 43. Zenith angle of the peak 6300Å intensity in the meridian plane of the airglow observatory as a function of time during the night of October 31/November 1, 1968.

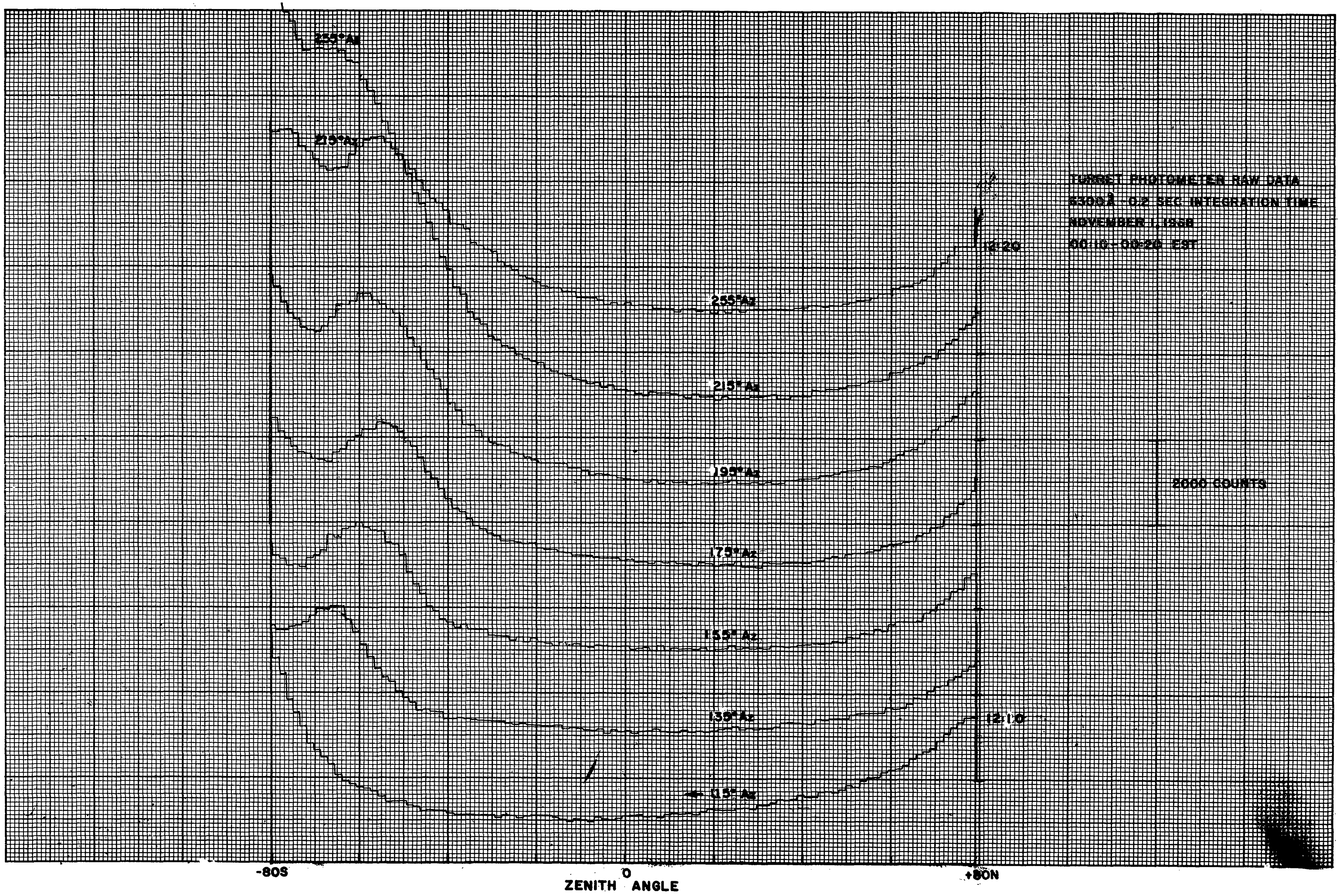

Fig. 44. 6300Å vertical circle scans with the turret photometer at 00:10 - 00:20 EST on November 1, 1968.

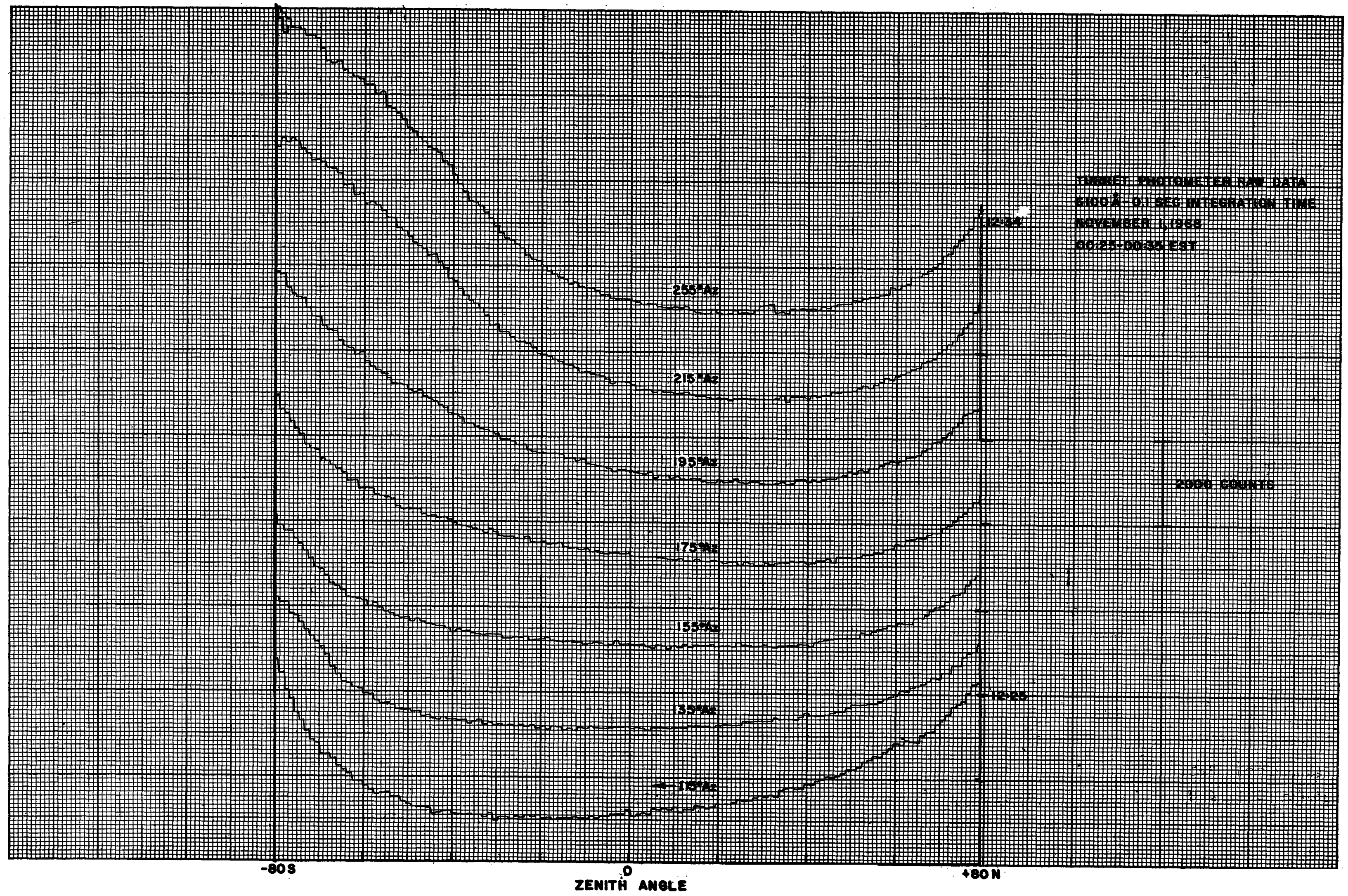

Fig. 45. 6100Å vertical circle scans with the turret photometer at 00:25 - 00:35 EST on November 1, 1968.

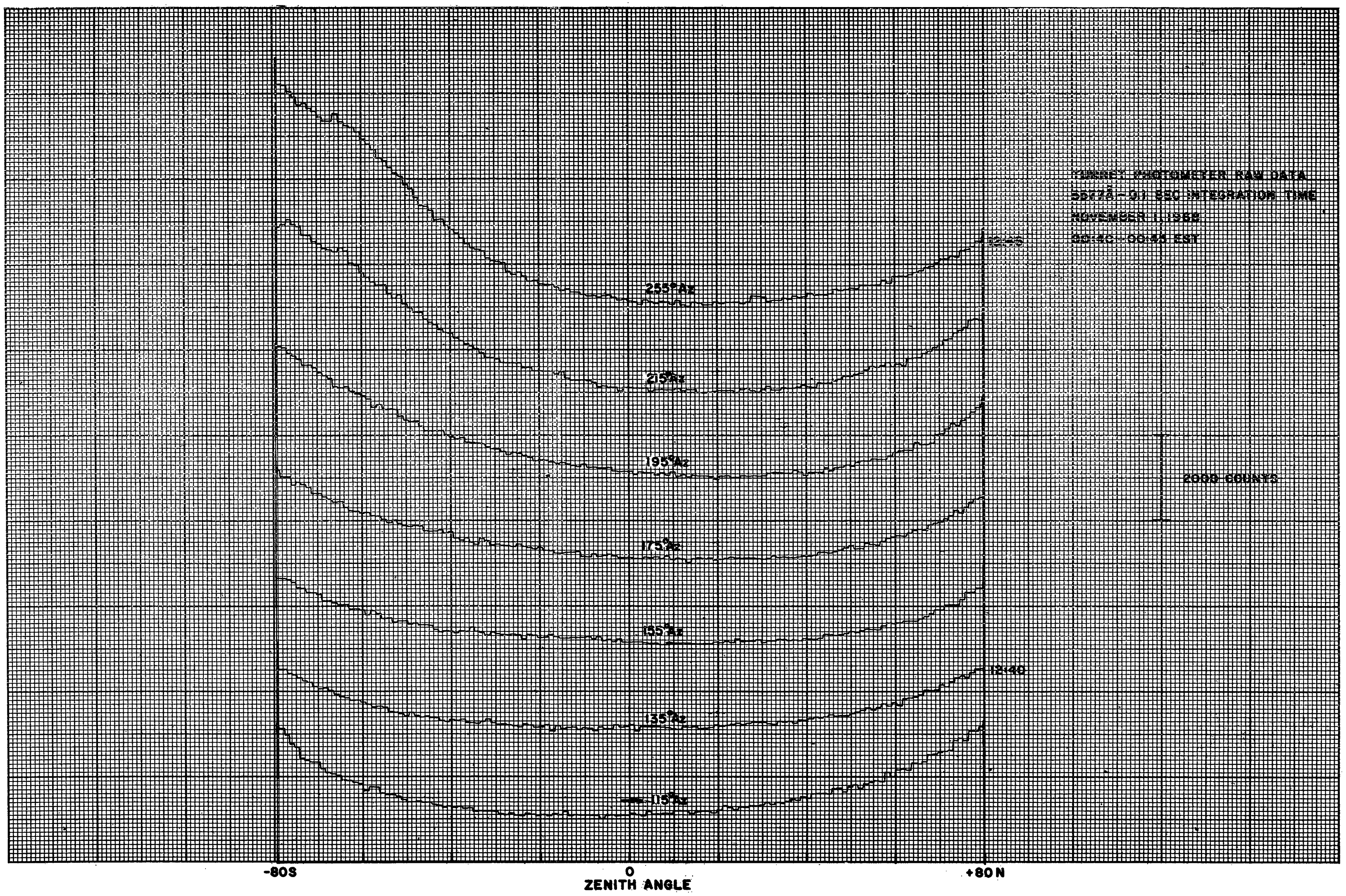

Fig. 46. 5577Å vertical circle scans with the turret photometer at 00:40-00:45 EST on November 1, 1968.

VanRhijn intensity variation with zenith angle and a brighter southern sky because of the moon, but the sharp intensity enhancement present in the 6300 Å scan is absent at this wavelength. These results clearly indicate a region of predominantly 6300 Å enhancement which cannot be attributed to the presence of clouds because an intensity enhancement on the 6100 and 5577 Å filter scans would also be evident. Scans of this type, using the 5400 Å, 5577Å, 6100Å, and 6300 Å filters in the turret photometer, were made throughout the night and only the 6300 Å scans showed the characteristic enhancement revealing the presence of a SAR-arc. The horizontal extent of the SAR-arc relative to the airglow observatory at Ann Arbor was determined from these figures and the results are shown in Fig. 47, where the peak 6300 Å intensity position is located on an auroral plotting map at various times. In order to position the arc on the map, the height of the peak emission was assumed to be 400 km which is consistent with the theoretical calculations and the results of numerous observations (Roach and Roach, 1963; Rees, 1963; Hoch, Marovich, and Clark, 1968). The SAR-arc is seen to lie approximately along constant L-shells, although there appears to be a slight departure from true alignment. This departure is also evident in the data of Hoch, Marovich, and Clark (1968) for the SAR-arc of September 28/29, 1967. The SAR-arc lies across the eastern U. S. and the whole arc progressed southward throughout the night. The arc moved southward at a time when K_p was decreasing and even moved further south when K_p began to increase again toward the early morning hours. The SAR-arc position, as determined by Marovich (1969) from Fritz Peak at 0950 UT, is shown as a dotted line, and when it is considered together with the arc positions determined by the Airglow Station at Ann Arbor, the SAR-arc is seen to extend across the entire U. S.

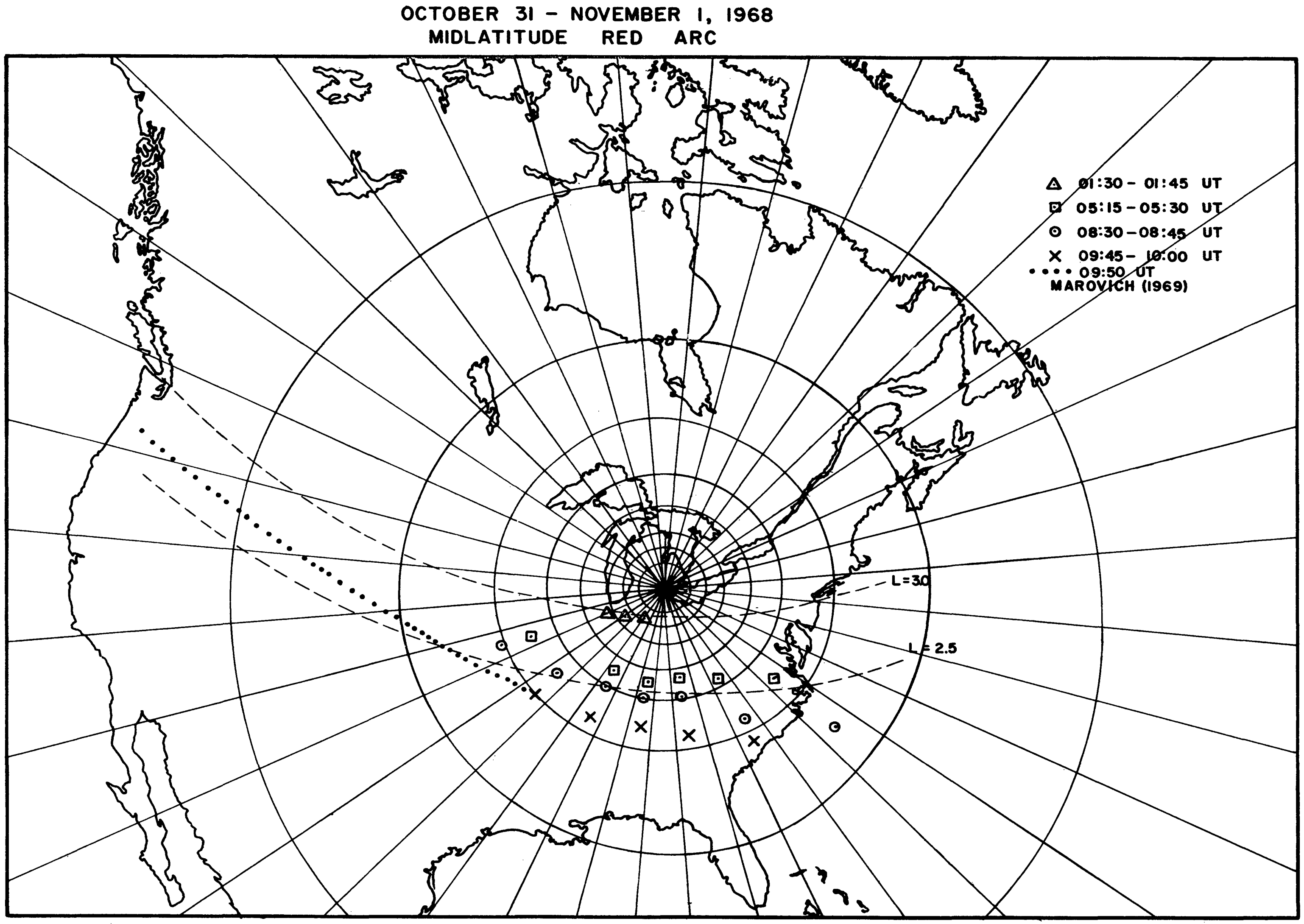

Fig. 47. Geographic position of the SAR-arc of October 31/November 1, 1968 determined from the airglow observatory; the dotted line indicates the position of the SAR-arc at 0950 UT determined from Fritz Peak, Colorado (Marovich, 1969).

Figs. 48, 49, 50, and 51 give the reduced photometer data for various vertical circle scans corresponding to the 4 SAR-arc positions shown in Fig. 47. The absolute magnitude of the intensity shown in these figures is in doubt for a typical autumn haze existed in the Ann Arbor area and scattered moonlight provided some signal contamination. The intensity of the SAR-arc appears to have varied throughout the night, ranging from 100 R to 600 R, and there also appears to have been some intensity variations along the length of the arc. The intensity was about 300 R at 0130 UT and increased until it reached a maximum of about 600 R near 0515 UT. The intensity then decreased to 300 R at 0830 UT, and shortly before dawn at 0945 UT it was about 100 R or less and low on the southern horizon. It is not clear to what extent the signal was attenuated by the hazy conditions existing near the southern horizon. In the early part of the evening there is also evidence of an enhancement in the north which is probably due to auroral background, although no visual sighting of an aurora was made during the night. The general airglow background appeared to have been slightly enhanced from normal conditions in the early evening but it decayed to about 100 R at 0515 UT and then remained nearly constant for the remainder of the night.

8.2.2 FABRY-PEROT INTERFEROMETER MEASUREMENTS

The Fabry-Perot interferometer was also in operation during the night and it was primarily devoted to making doppler temperature measurements. The doppler temperature measurements were, at times, interrupted in order to use the Fabry-Perot interferometer as an extremely narrow interference filter and perform a zenith scan. The interferometer was positioned and maintained on the 6300 Å fringe peak while the mirror scanning system operated in a north-south vertical circle scan crossing the SAR-arc region. The results of the scan are shown in Fig. 52 where the enhanced 6300 Å

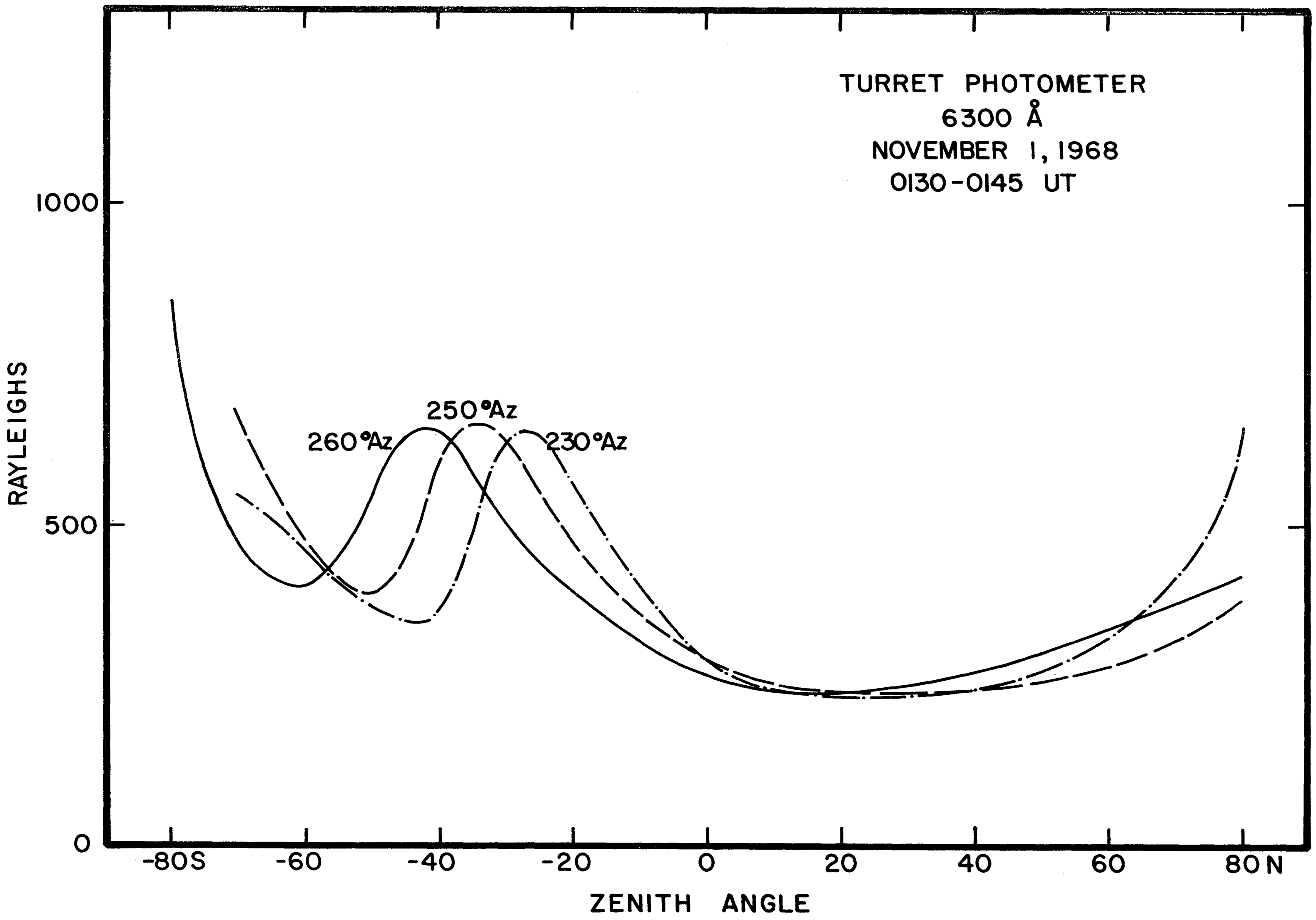

Fig. 48. Reduced 6300 Å vertical circle scan data of the turret photometer at 0130 - 0145 UT, November 1, 1968.

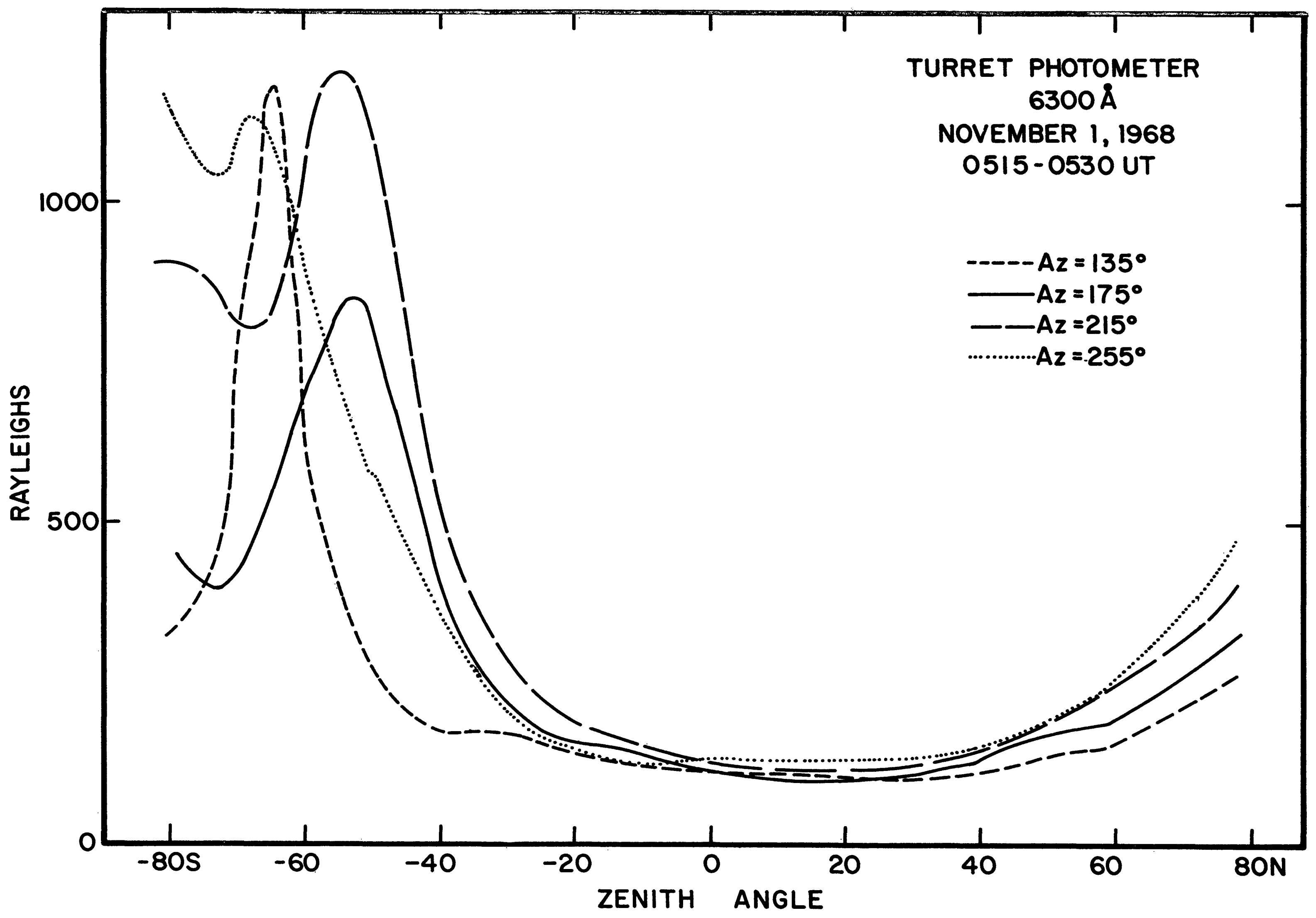

Fig. 49. Reduced 6300Å vertical circle scan data of the turret photometer at 0515 - 0530 UT, November 1, 1968.

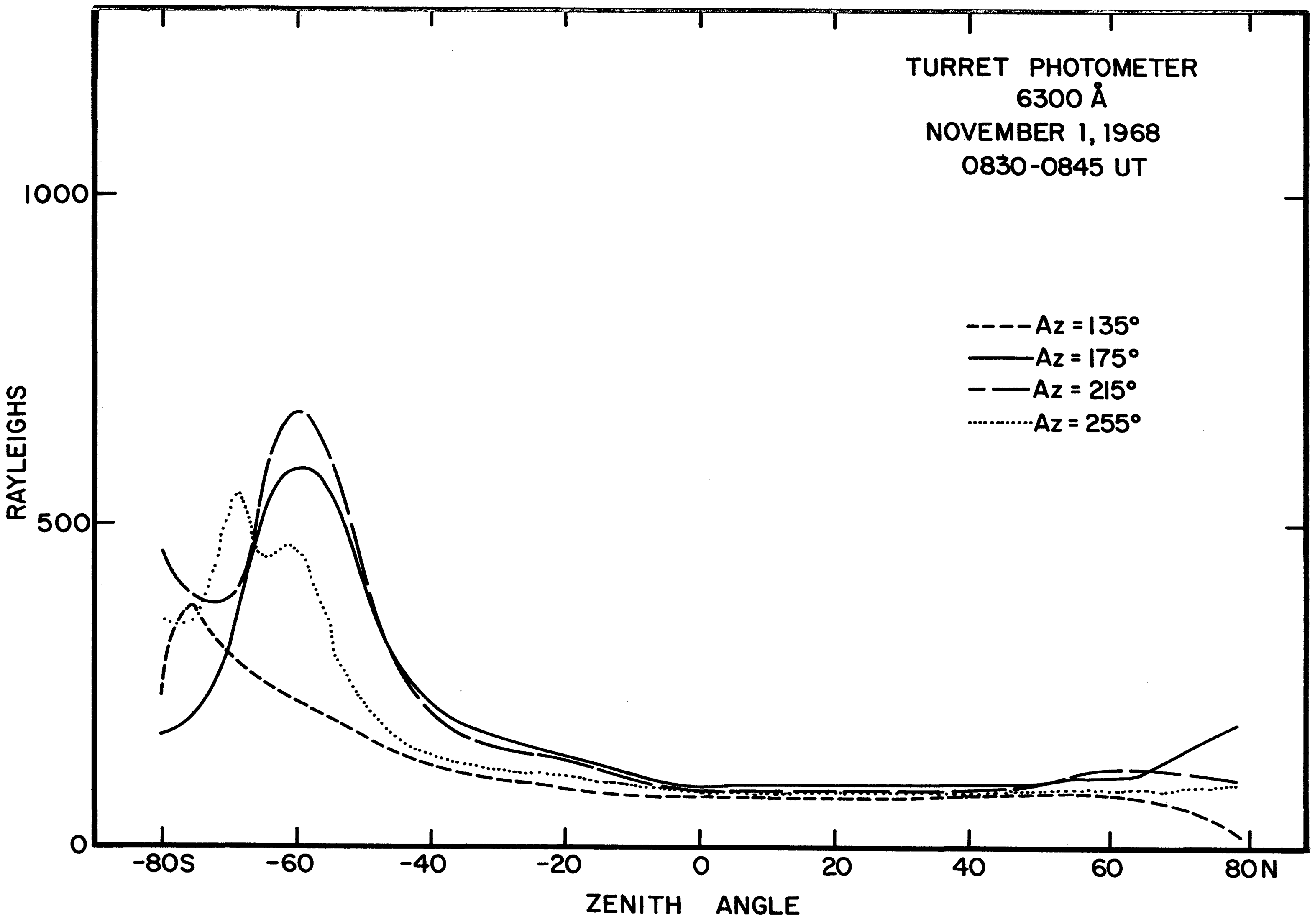

Fig. 50. Reduced 6300 Å vertical circle scan data of the turret photometer at 0830 - 0845 UT, November 1, 1968.

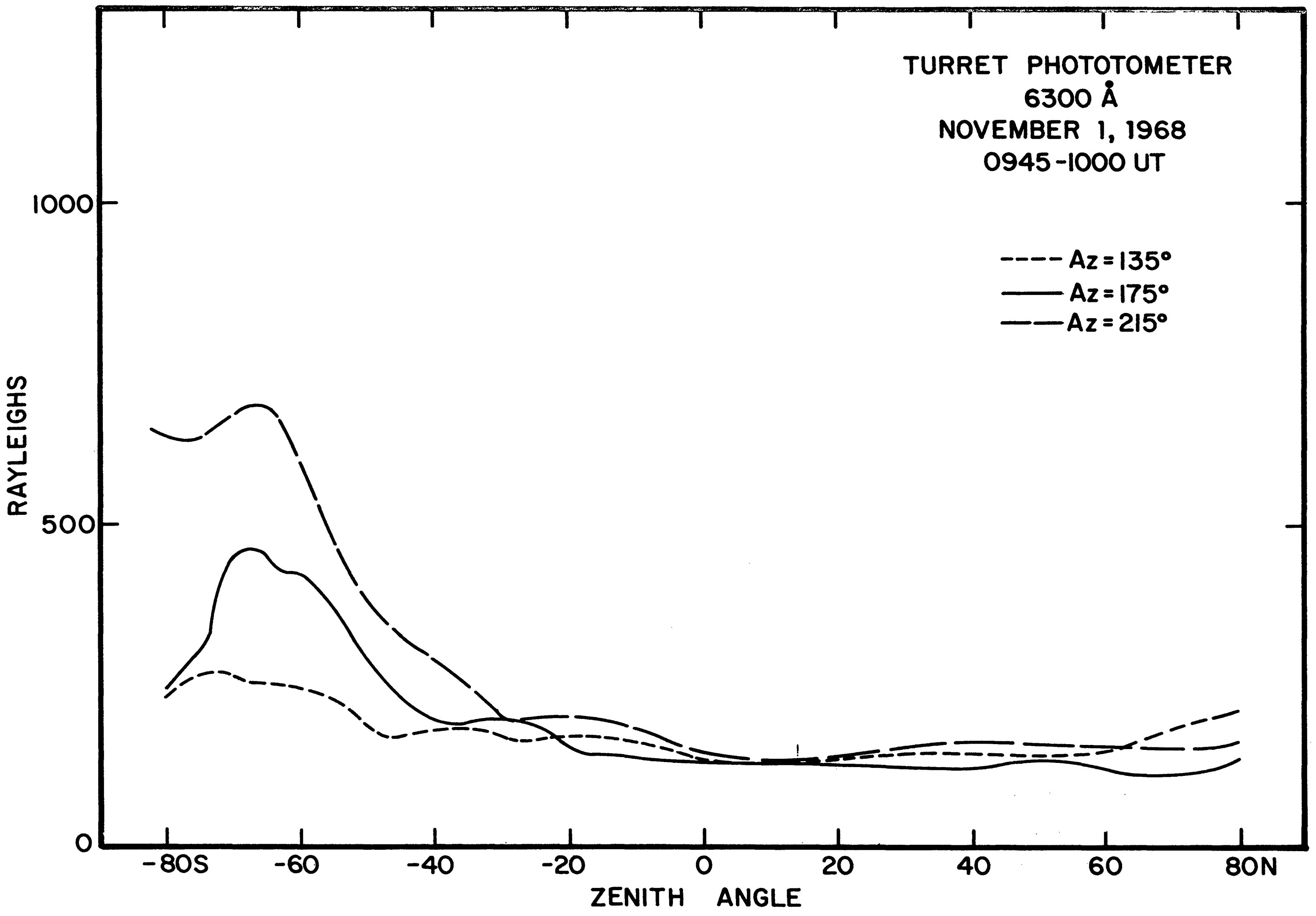

Fig. 51. Reduced 6300Å vertical circle scan data of the turret photometer at 0945-1000 UT, November 1, 1968.

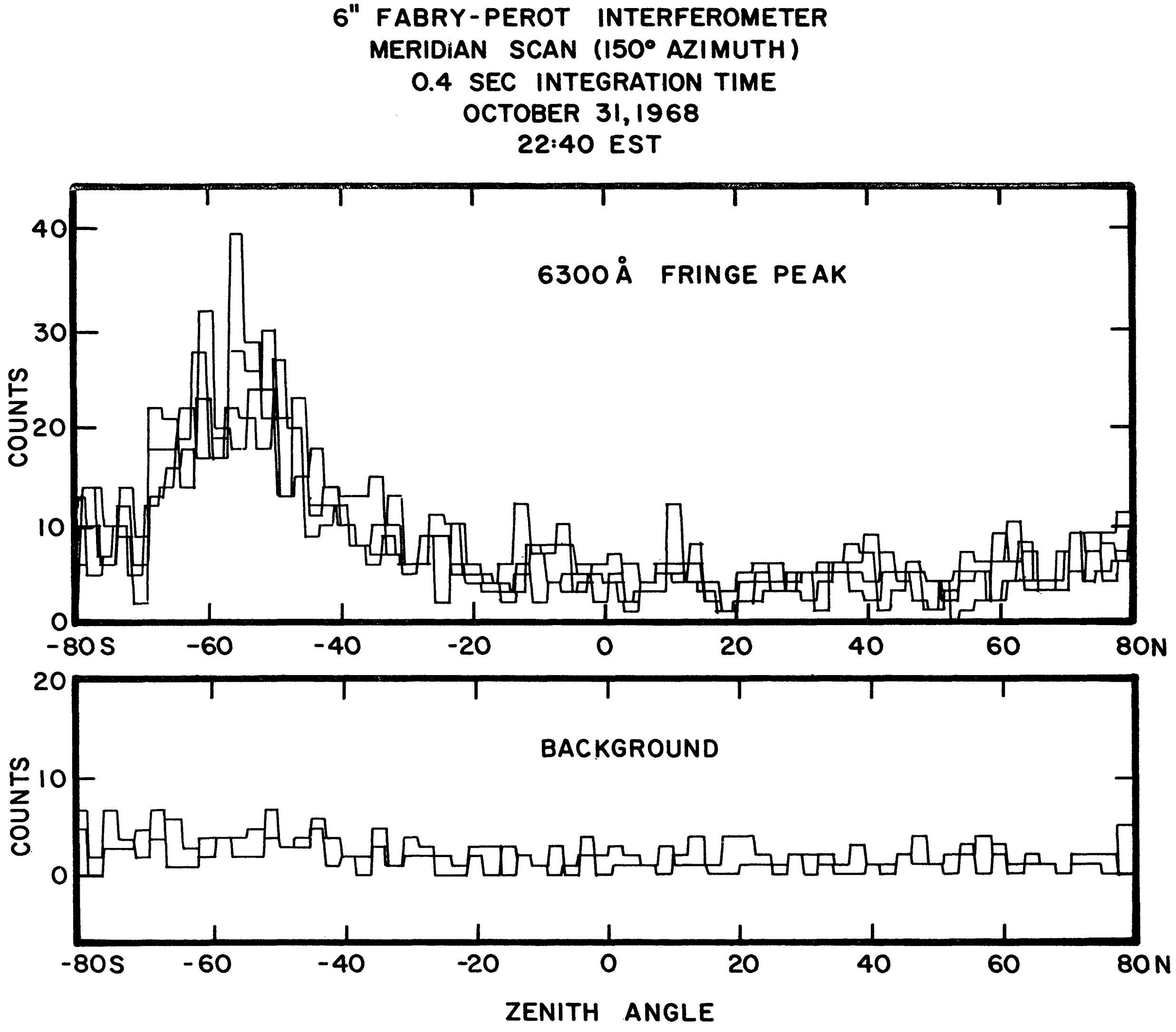

Fig. 52. 6" Fabry-Perot interferometer vertical circle scan at 0340 UT, October 31, 1968.

emission of the SAR-arc clearly stands out. After the scan was completed, the interferometer was moved 0.1 Å off of the fringe peak, beyond the wings of the doppler emission line, in order to measure the nearby background. A vertical circle scan of the interferometer in this position revealed no noticeable enhancement of the background near 6300 Å where the SAR-arc was present. The same measurement was also performed using the 5577 Å green line filter in the interferometer and the results show no major enhancement of the green line or its background in the SAR-arc region, verifying that the major emission of the SAR-arc is the 6300 Å radiation of atomic oxygen.

The main purpose of the interferometer was, however, to measure the doppler temperature within and outside of the SAR-arc region and to monitor the exospheric temperature variation during the magnetic storm. A typical SAR-arc fringe is shown in Fig. 40 and, as discussed in Chapter 7, it was considerably enhanced over the normal nightglow fringe. The fringe profile obtained within the SAR-arc was examined and when the instrument function was de-convolved from the measured fringe, the temperature of the resulting 6300 Å doppler broadened emission line was obtained.

The results of the doppler temperature measurements for the two nights during which SAR-arcs occurred are summarized in Fig. 53. The crosses on the figure are the doppler temperatures determined for the previous night, October 30/31, and they indicate that the exospheric temperature, shortly after sunset, was about 1000°K and appeared to remain constant during the night as the magnetic storm intensity increased. The magnetic storm continued during the day, as shown in Fig. 42, reaching a peak K_p value of 8 and then began to decrease. At the time of local sunset on Oct. 31/ Nov. 1, K_p was 6 and it decreased to about 4 toward sunrise on Nov. 1. Shortly after

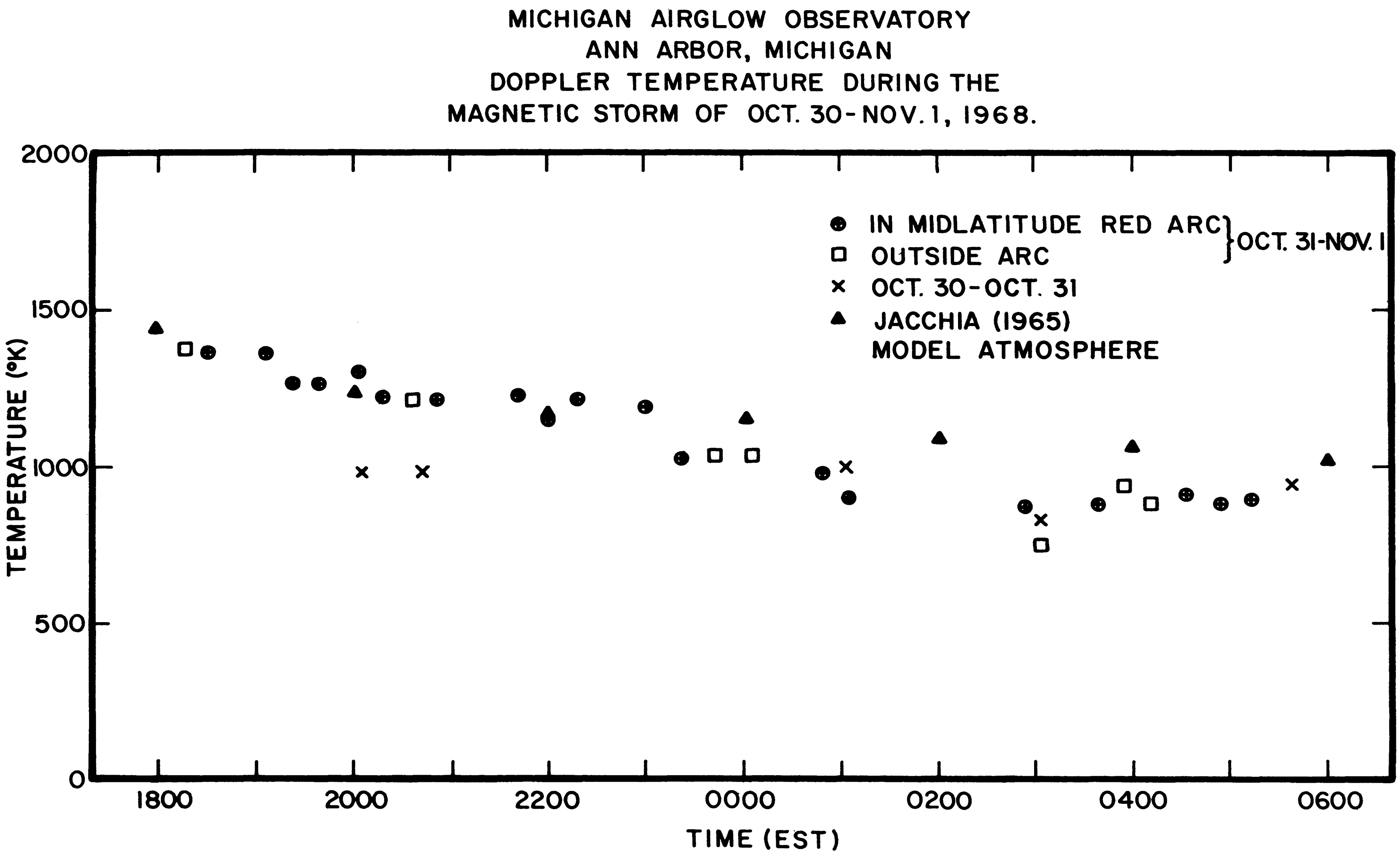

Fig. 53. 6300 Å doppler temperature measurements during the magnetic storm of October 30- November 1, 1968.

sunset at 2300 UT, the measured doppler temperature was near 1400°K, considerably enhanced from the night before and in general agreement with the exospheric temperature predicted by the Jacchia (1965b) model. The doppler temperatures show a general exospheric temperature decay during the night until about 0700 UT, and after that time the temperature remained nearly constant at 950°K. The exospheric temperature predicted by the Jacchia (1965b) model shows a slower decay with time and a greater temperature in the early morning hours.

Doppler temperature measurements were made inside and outside of the SAR-arc region in order to investigate the role of neutral heating within the SAR-arc. The results show no measurable temperature difference between the measurements obtained within the SAR-arc region to the measurements made away from the arc. The doppler temperatures measured within the SAR-arc are assigned to an effective altitude of 400 km where the maximum 6300 Å emission occurs. Those made outside of the SAR-arc apply to the 250-300 km region where the normal 6300 Å nightglow exists (Roble, Hays, and Nagy, 1968). There does not appear to be any noticeable difference between the two measurements, indicating that the region between 250-400 km is nearly isothermal and the neutral gas temperature increase within the SAR-arc is below the estimated ± 75°K error limits of the instrument.

8.2.3 DISCUSSION OF RESULTS AND COMPARISON TO THEORY

In this section, the main results of the measurements are discussed and wherever applicable they will be compared to the theory. The main points are:

(1) The results of the photometer and Fabry-Perot interferometer vertical circle scans show that the SAR-arc is indeed predominantly 6300Å radiation with no noticeable enhancement of the other major emission lines or

continuum background within the SAR-arc region. The absence of a 5577Å enhancement within the SAR-arc region indicates that the arc was not caused by an increased rate of dissociative recombination in the F-region nor by a flux of electrons with energy higher than 15 ev. (see Chapter 3).

(2) The SAR-arc was seen to extend across the eastern portion of the U.S. and it was aligned approximately along constant L-shells; however, the arc appeared to be slightly tilted with respect to the quiet L-shells.

(3) The SAR-arc on the night of October 30/31, 1968, occurred at a time when K_p was increasing and apparently disappeared even though K_p continued to increase during the night.

(4) The SAR-arc on the night of October 31/November 1, 1968, was detected when K_p was 6 and it persisted while K_p decreased during the night.

(5) The SAR-arc was first detected at 2345 UT approximately 15° south of the airglow observatory and the arc moved rapidly southward at a speed of approximately 40 m sec^{-1} until 0330 UT. From 0330 to 0730 UT the arc remained stationary at a zenith angle of 60° south of the observatory, but at 0730 the arc began to move southward again at a speed of about 40 m sec.

(6) There appears to have been intensity variations along the horizontal extent of the SAR-arc which are probably due to variations of the structure of the arc or due to an attenuation of the signal caused by the hazy sky conditions. The intensity also varied in time from near 300 R at 0130 UT increasing to 600R at 0515UT and then decaying throughout the remainder of the night until it was of the order of 50-100 R at 0945UT shortly before sunrise. The SAR-arc intensities here are only approximate because the signal was probably contaminated by scattered moonlight

and attenuated by the hazy sky conditions.

(7) The calculated normalized signal of a photometer performing a north-south vertical circle scan and crossing a model SAR-arc which is aligned in an east-west direction is shown in Fig. 54. The 6300Å intensity cross section of the arc used in this calculation is shown in Fig. 2 and the numbers given on each curve represent the zenith angle of the peak SAR-arc intensity from the observing station. The calculations were performed for the airglow photometer in use, which has a 5° circular field of view, and the intensity variation within the field of view during the scan was also taken into consideration. The shape of the normalized curves and the shape of the observed zenith scan curves, shown in Fig. 48, are similar, indicating that the SAR-arc intensity structure is localized, forming a narrow arc across the southern sky and probably with 6300 Å intensity contours similar to those shown in Fig. 2.

(8) The doppler temperatures measured within the SAR-arc region, when compared to the doppler temperatures outside of the arc, reveal no noticeable neutral gas temperature increase. The lack of a significant neutral gas temperature increase is consistent with the thermal conduction model of the SAR-arc which predicts a temperature increase of about 30°K for a 600 R SAR-arc when considering thermal conduction alone, and about 10°K for a 600 R SAR-arc based upon the dynamic model of the arc.

In Chapter 3, it was shown that the electric field hypothesis for the excitation of a SAR-arc required very large ion temperatures in the 200-400 km height interval. Ion temperatures of the order of 6000°K were required for a 600 R SAR-arc and because of the large ion-neutral collision frequency the neutral gas temperature was expected to increase

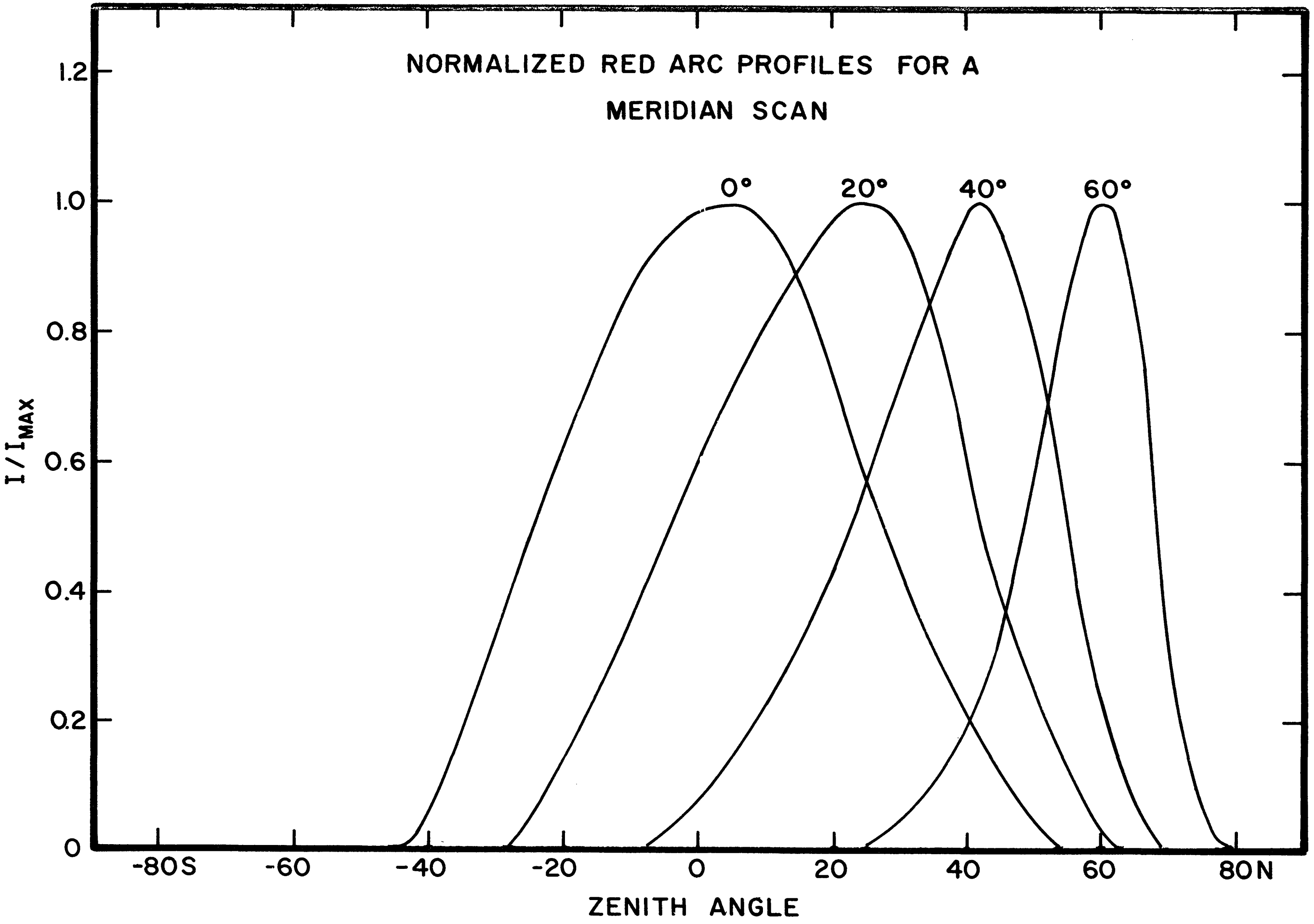

Fig. 54. Normalized meridian scans on a model SAR-arc located at various zenith angles and having the 6300 Å isophotal contours determined by Tohmatsu and Roach (1962).

significantly (Walker and Rees, 1968). No neutral gas temperature increase was detected within the SAR-arc, and it is doubtful that the electric field hypothesis is the excitation mechanism of the SAR-arc.

(9) Doppler temperature measurements were made at 5° zenith angle steps across the SAR-arc and no noticeable temperature gradient was evident.

(10) The exospheric temperature was seen to remain nearly constant during the night of October 30/31, 1968, as the magnetic storm increased in intensity. On the following night, October 31/ November 1, 1968, the exospheric temperature was considerably enhanced. It decreased from 1400°K shortly after sunset to about 950°K before dawn. The temperature decay, however, appears to be at a faster rate than the exospheric temperature variations predicted by the Jacchia (1965b) model.

The results presented in this section are consistent with the thermal conduction model of the SAR-arc and are also in apparent agreement with the theoretical model of the SAR-arc which was presented in the previous sections.

8. 3 THE SAR-ARC OF SEPTEMBER 28/29, 1967

A SAR-arc was observed on the night of September 28/29, 1967, from airglow observatories at Fritz Peak, Colorado, and Richland, Washington (Hoch, Marovich, and Clark, 1968). At the same time that the SAR-arc was being observed from the ground, the Alouette I and II satellites passed over the SAR-arc region. (Norton and Findlay, 1969). The data obtained from these two sources are used to theoretically calculate the SAR-arc structure according to the thermal conduction model and to compare the results of the calculations with the observed properties of the SAR-arc.

8.3.1 OBSERVED PROPERTIES OF THE SEPTEMBER 28/29, 1967 SAR-ARC

The SAR-arc was photometrically observed to have the following properties:

(1) The SAR-arc was aligned approximately along constant L-shells and was observed to extend from 90°W longitude to 140°W, a distance of approximately 4500 km.

(2) The average intensity of the SAR-arc was 150 R and the maximum intensity was 300R. It was observed that at any given time the intensity along the length of the arc was nonuniform, varying by about a factor of 2. There were also sluggish temporal variations of about the same magnitude and apparently not correlated from place to place along the arc.

(3) The width of the arc at half-intensity points was approximately 160 km in the north-south direction.

(4) The SAR-arc moved southward during the night and reached its most southerly position approximately 2° south of the Fritz Peak zenith at 1050 UT and then reversed its direction and drifted northward about 100km by 1125UT.

The Alouette I satellite was in a near circular orbit at the time of the SAR-arc and made two approximately north-south passes over the arc at an altitude of 1000 km; one at about 0500UT near Fritz Peak and the second at 0700 UT just off the coast of California. The Alouette II satellite made one pass over the arc at 0900 UT in a south-north direction, passing close to Fritz Peak at an altitude of 1800 km. Both satellites had swept frequency topside sounders on board and the Alouette II satellite also had an electron temperature and density probe. The results of the observations have been given by Norton and Findlay (1969) and only the main points of interest will be summarized here:

(1) The electron temperature and electron density measured by the Alouette II satellite while passing over the SAR-arc region at an altitude of 1800 km are shown in Fig. 55 as a function of the L-shell parameter. The position of the SAR-arc is located at an approximate L-shell value of 2.3 which is in a region where a considerable enhancement of the electron temperature is observed at 1800 km. North of that position, the electron temperature decreases slightly but a secondary peak is present at an L-shell of 2.8. An electron density depression to the north of the SAR-arc is apparent in the electron density readings at the satellite and the depression is also observed by the topside sounder to extend downward to the F2 peak.

(2) The electron density height profiles deduced from the Alouette I & II topside sounder data are shown in Fig. 56. The bottom side of the electron density profile was matched to the model ionosphere presented in Chapter 4. In the region of the observed SAR-arc (L=2.3) there is considerably more ionization than to the north of the arc where an electron density depression exists. The approximate form of the electron density contours for a cross section through the SAR-arc region has been constructed from this satellite data and it is shown in Fig. 57. There appears to be two distinct density depressions at L=2.8, one below 1000 km, and one above 1000 km. At 1000 km the electron density does not appear to vary greatly over the cross section.

(3) In both Alouette I satellite passes, which were separated by a distance of several hundred km, the electron density at the peak of the F2 layer shows a sharp depression in density in the same range of L values as the position of the SAR-arc. Fig. 56 shows that the depression was observed near Fritz Peak and 4 hours later when Alouette II passed over the same region, the electron density depression was still evident

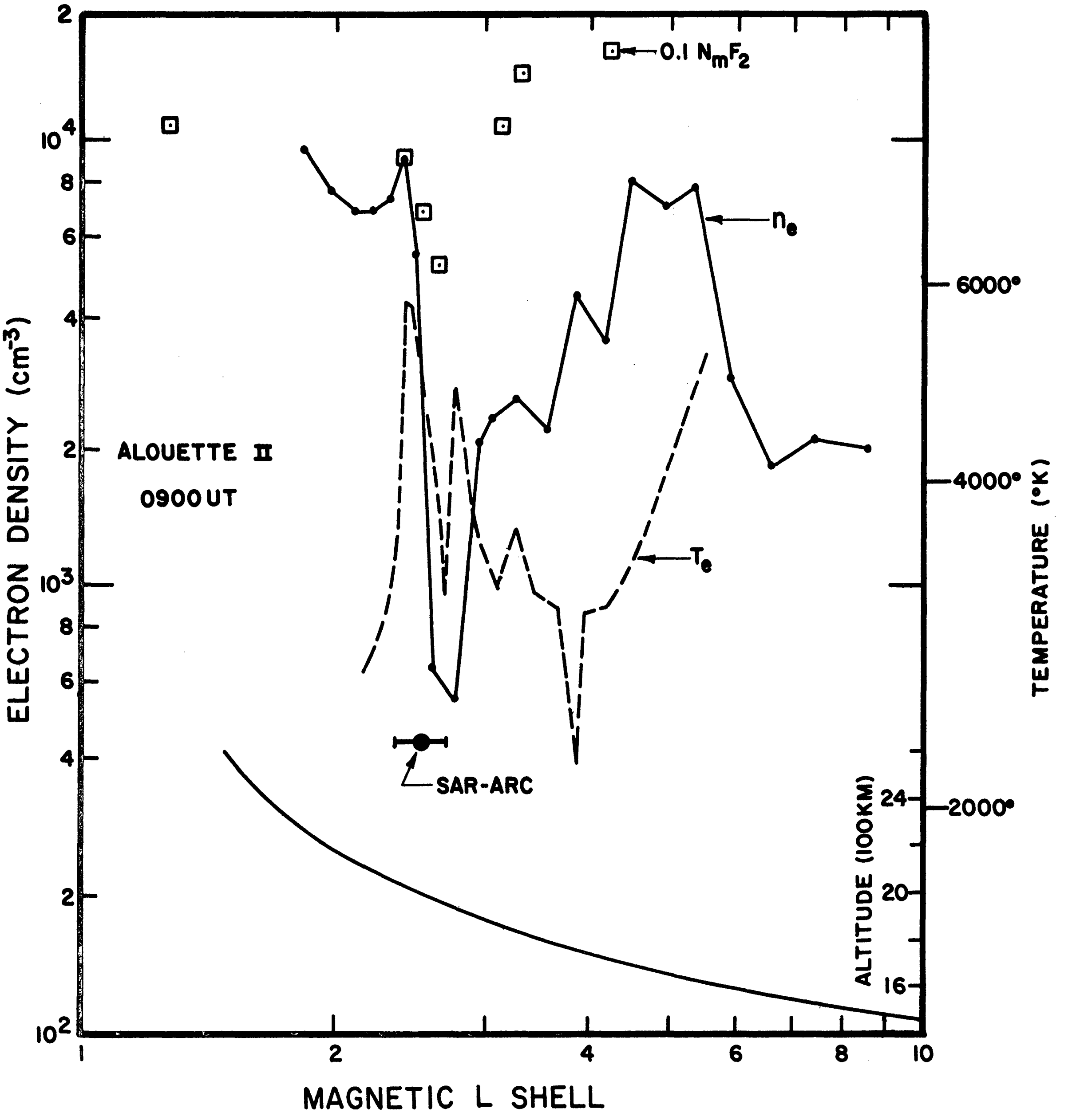

Fig. 55. Electron density and temperature as a function of the magnetic L-value determined by the Alouette II satellite in a pass over the SAR-arc of September 28/29, 1967. (Norton and Findlay, 1969).

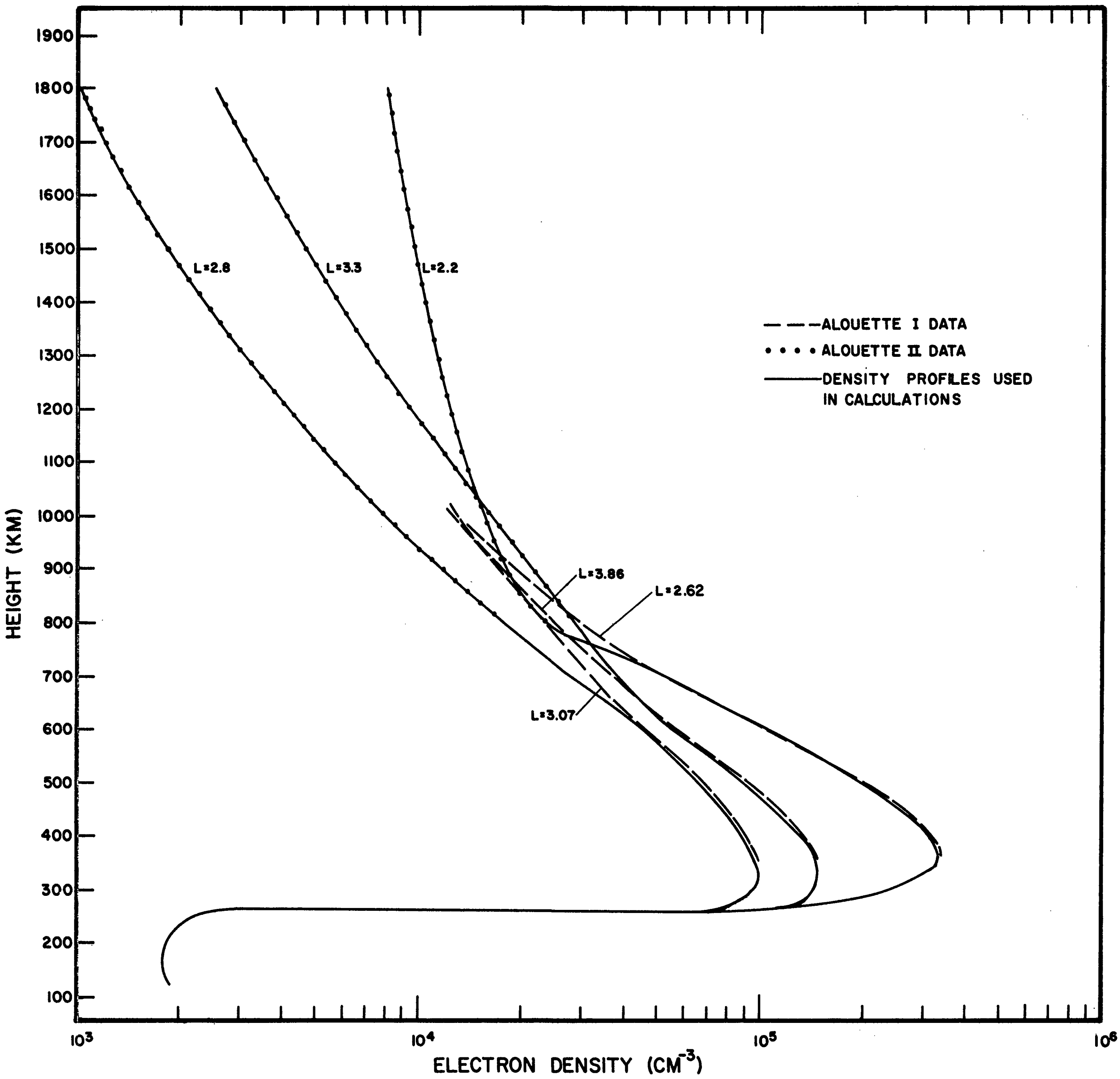

Fig. 56. Electron density height profiles for the SAR-arc of September 28/29, 1967. The topside data for the Alouette I and II satellites is from Norton and Findlay (1969).

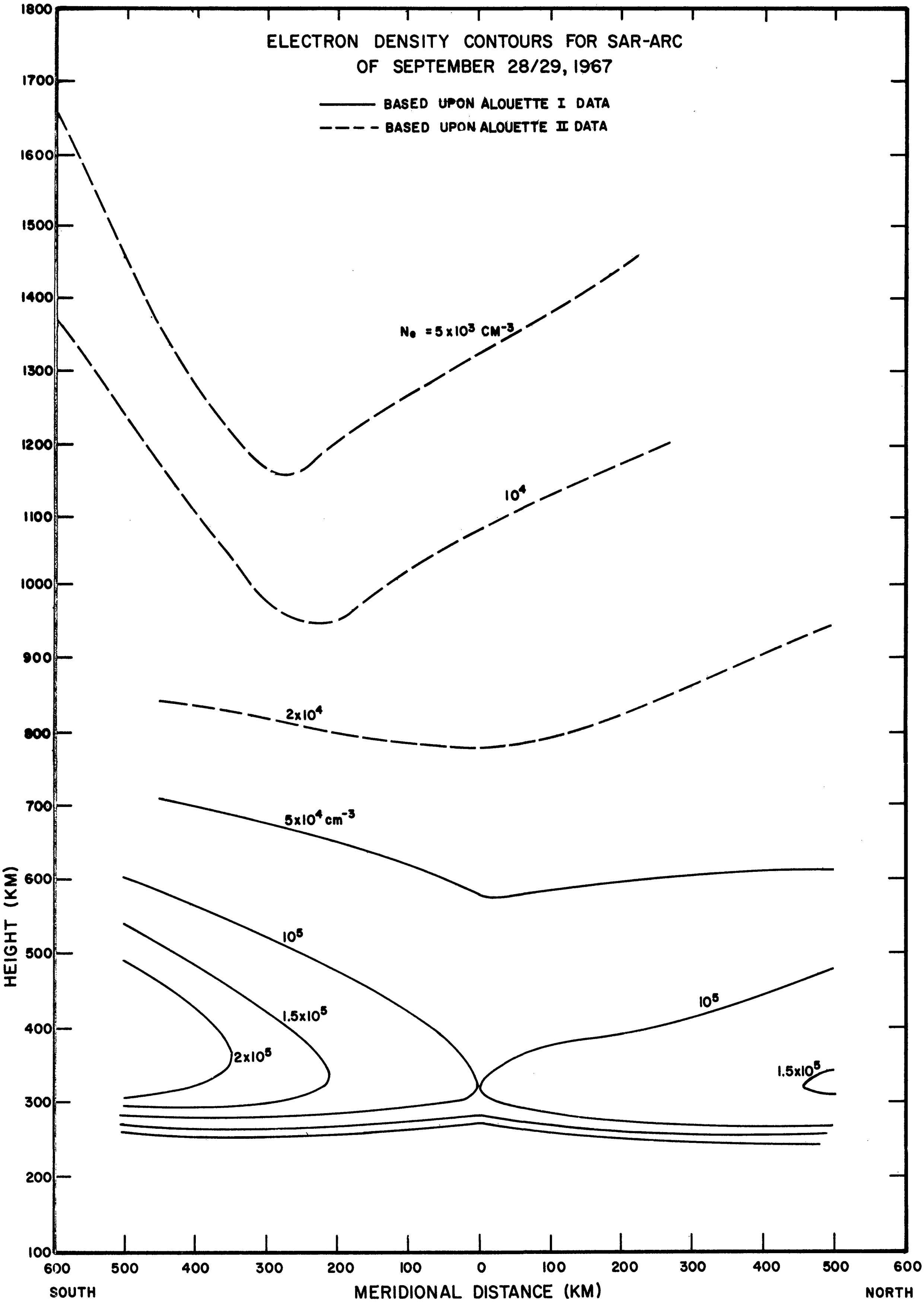

Fig. 57. Electron density contours for the SAR-arc of September 28/29, 1967 based upon the Alouette I and II satellite data of Norton and Findley (1969).

although it appears to have moved slightly southward.

(4) The SAR-arc appears to have been centered on the equatorward edge of the density depression.

The data obtained from the satellites passing over the SAR-arc are now used to theoretically calculate the shape of the SAR-arc and to compare the results with the photometric properties of the arc determined from the ground based observatories.

8.3.2 THEORETICAL CALCULATION OF THE SAR-ARC

The electron density profile necessary to carry out the calculations is available for any meridional distance and the electron temperature is specified at 1800 km by the Alouette II data shown in Fig. 55. The model neutral atmosphere is assumed to be the analytic model, described in Chapter 4, with an exospheric temperature of 1100°K. With these input parameters, the electron heat conduction equation was solved on a trial and error basis by varying the topside heat flow rate at 1800 km in such a manner that the computed electron temperature at 1800 km matched the observed 1800 km electron temperature at the satellite. For conditions along the $L=2.8$ shell, a topside heat flow rate of 10^{10} ev cm^{-2} sec^{-1} results in an electron temperature of 4885°K at 1800 km which is very close to the observed value. In a similar manner for other positions along the north-south cross section of the region, the topside heat flow rate is determined such that the computed electron temperature at 1800 km equals the observed temperature. For an L-shell, $L=2.2$, a topside heat flow of 2.25×10^{10} ev $cm^{-2} sec^{-1}$ gives an electron temperature near the observed 6000°K and for the L-shell, $L=3.3$, a topside heat flow rate of 5×10^{9} ev $cm^{-2} sec^{-1}$ results in an electron temperature of 3800°K. The entire electron temperature profile, along with the integrated 6300 Å volume emission rate, is shown in Fig. 58. Several other profiles are

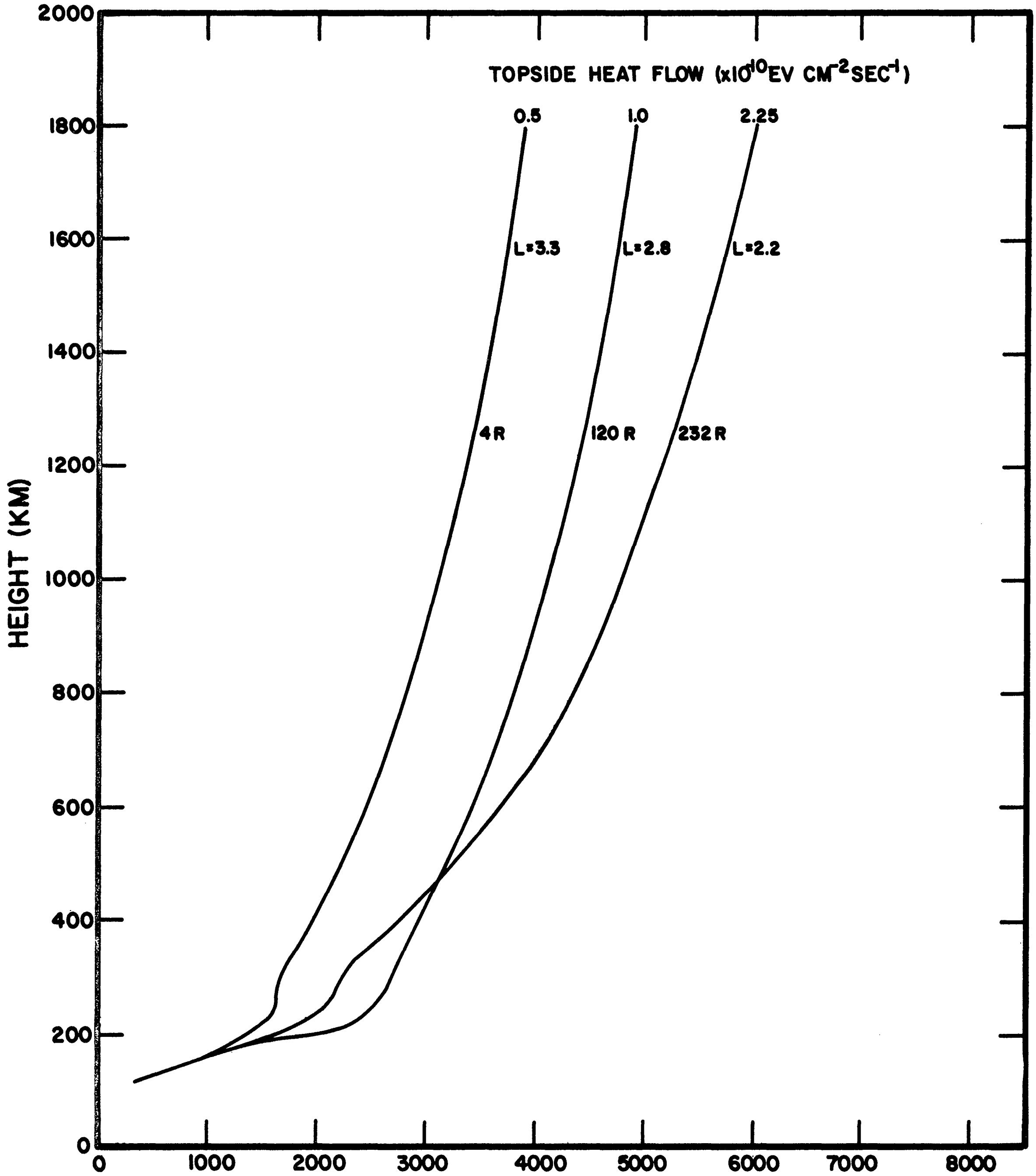

Fig. 58. Calculated electron temperature height profiles for the SAR-arc of September 28/29, 1967.

determined at various meridional distances and the results are presented as two-dimensional contours of electron temperature and 6300Å volume emission rate in Fig. 59. There are two distinct peaks in the electron temperature, one at an L-shell of 2.2 and the other at 2.8. These regions have an enhanced electron temperature profile existing down into the ionosphere where the atomic oxygen in the F-region of the ionosphere is excited by electron impact to form two distinct regions of enhanced 6300 Å emission. The satellite electron temperature between these two L-shells is low and the lower electron temperatures existing along the L-shell will result in a decreased 6300 Å emission rate. Thus for this particular arc there should exist two enhanced 6300 Å emission regions with the more intense region of 230 Rayleighs in the south having a peak volume emission rate near 400 km and a meridional extent of a couple of hundred km which agrees well with the observed data of Hoch, Marovich, and Clark, (1968). The northern arc has an intensity of 130 Rayleighs, a much smaller lateral extent, and a lower peak in the volume emission rate which occurs near 320 km. The photometric data of Hoch, Marovich, and Clark (1968) do not reveal a double arc-like structure; however, the intensity of the northern arc may perhaps be blended in the general background region of the main southern arc. The neutral heating contours for this particular SAR-arc are shown in Fig. 60, giving two distinct regions of localized heating in the vicinity of the two arcs. Although it is not possible to solve for the neutral gas temperature increase and the atmospheric winds directly from the theory presented in the previous chapters, it is possible to make certain qualitative statements regarding the expected temperature and wind pattern. A solution to the one-dimensional neutral heat conduction equation at various meridional positions along the cross section indicates that the gas temperature within the SAR-arc region is about 75°K greater than to the north of the arc. When

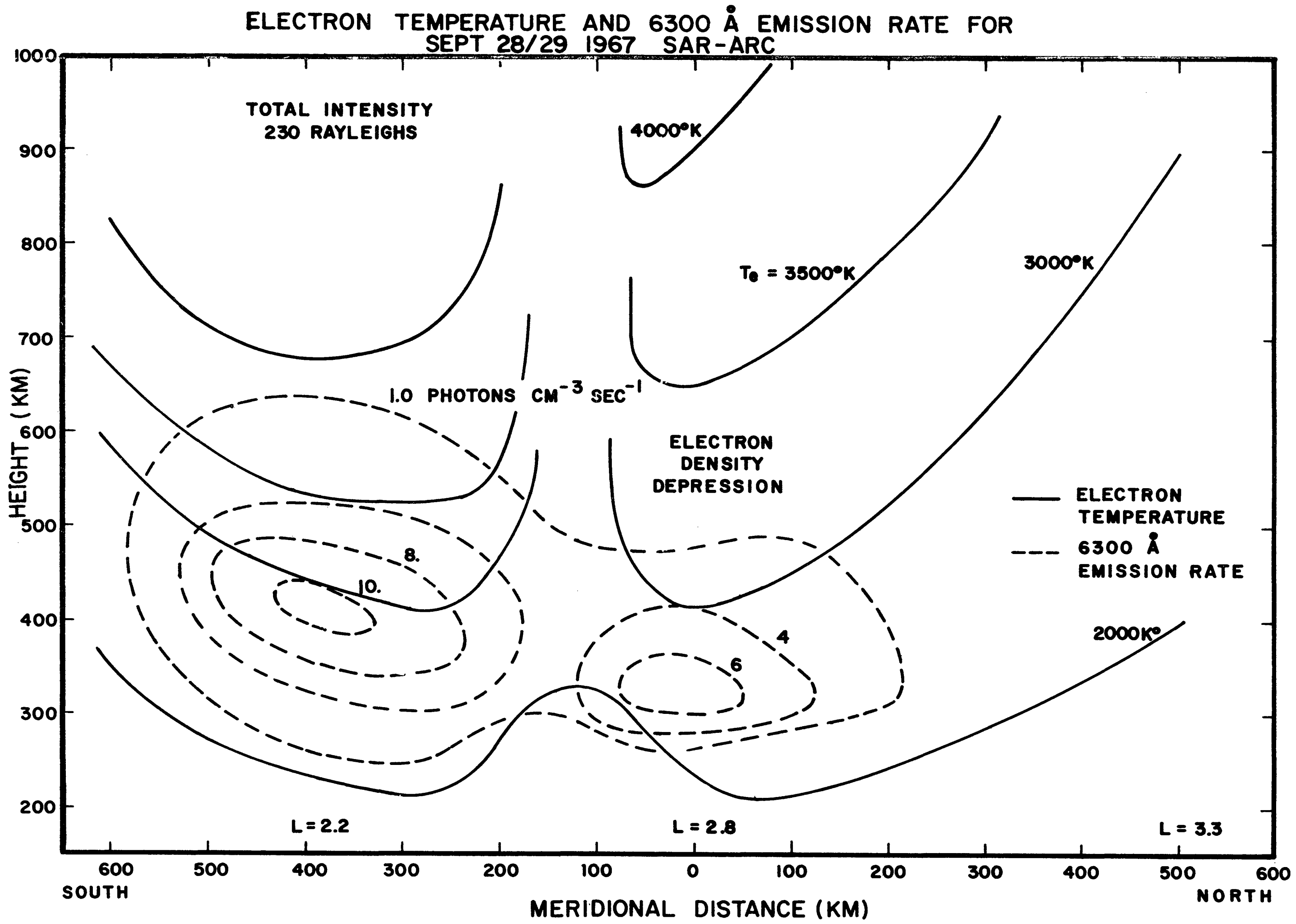

Fig. 59. Calculated contours of electron temperature and 6300Å volume emission rate for the SAR-arc of September 28/29, 1967.

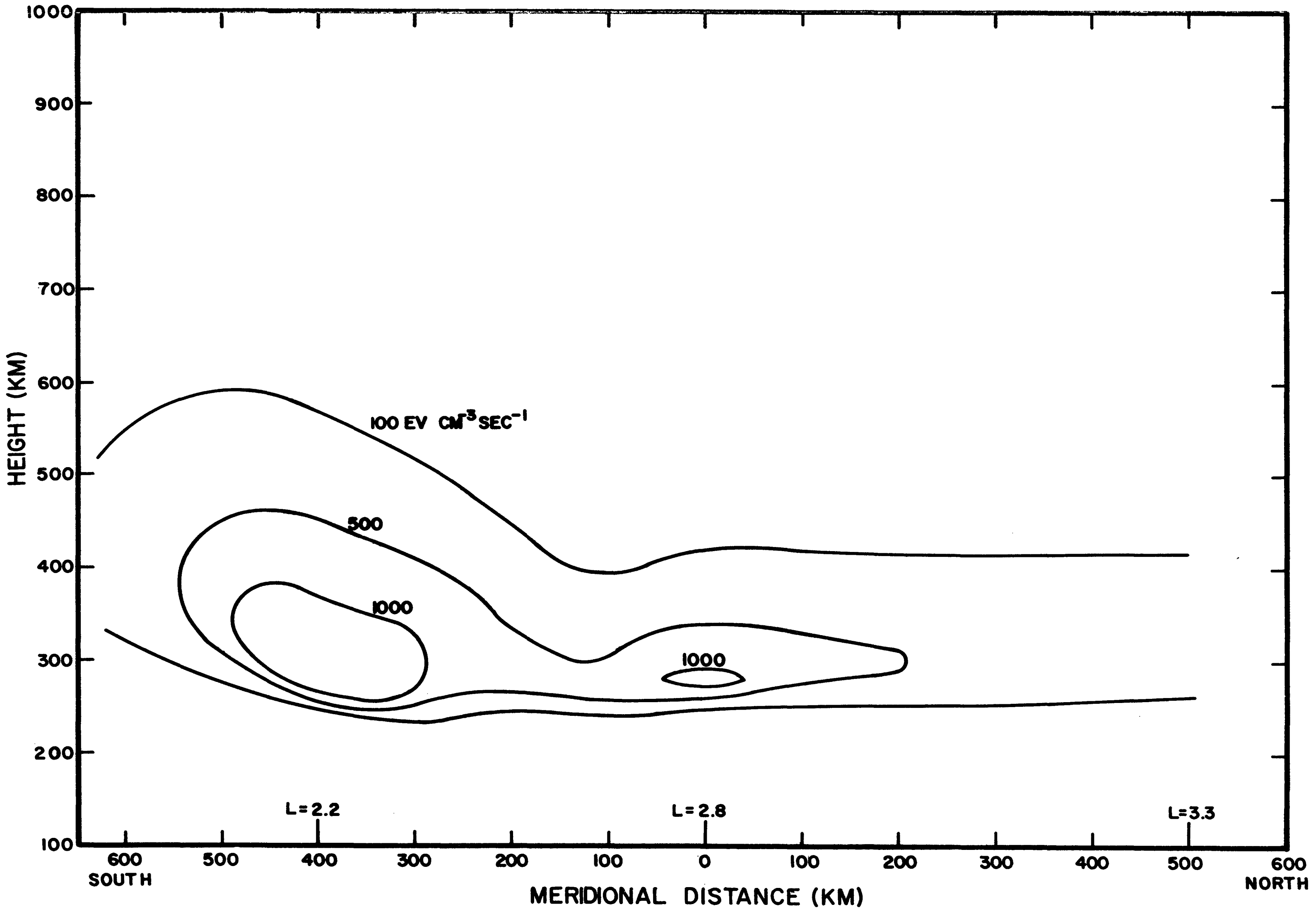

Fig. 60. Calculated neutral heating contours for the SAR-arc of September 28/29, 1967.

adiabatic cooling and lateral thermal conduction are both considered, the magnitude of the neutral gas temperature increase will be smaller; however, a temperature gradient decreasing to the north will still exist. The pressure gradient caused by this temperature pattern will cause a southerly meridional wind to flow on the north side of the arc. The meridional wind, reinforced by the vertical winds due to a general cellular overturning, may force ionization down along the geomagnetic field lines to the north of the SAR-arc center where an enhanced recombination may give rise to an electron density depression. The general trend is consistent with the observed data, although it is not clear whether the winds caused by the SAR-arc are of sufficient magnitude to overcome the normal diurnal winds, which have been calculated to be of the order of hundreds of meters $\sec^{-1}$ (Geisler, 1967; King and Kohl, 1967; Dickinson, Lagos, and Newell, 1968).

8.3.3 COMPARISON WITH THEORY

The results reveal that the calculated SAR-arc closely resembles the observed arc. The peak intensity is calculated to be 230R, well within the observed 100-300 R range. The height of the peak 6300 Å intensity is 400 km and the calculated width of the arc is about 200 km, both in reasonable agreement with the observed data. The secondary arc was not reported by Hoch, Marovich, and Clark (1968) but it is possible that the secondary arc was obscured or it was blended into the main SAR-arc.

The electron density contours shown in Fig. 57 indicate that an electron density depression existed above 1000 km and also below 1000 km; however, the conditions were generally undisturbed at 1000 km. It is conceivable that the undisturbed 1000 km surface is a dividing line separating two different physical processes causing the depression in their respective regions. The SAR-arc appears on the equatorward side of both electron density depressions. If the SAR-arc is indeed the sink for the energy of the particles causing the main phase decrease in a magnetic storm, D_{st}(Cole, 1965), then the position of the SAR-arc reveals the position of the ring current in the magnetosphere because the two are connected by the geomagnetic field lines. The magnetospheric ring current probably forms on the outermost surface of the sphere containing the closed geomagnetic field lines. Therefore the field lines which lie poleward of the SAR-arc would be swept back into the geomagnetic tail where they could conceivably be broken. If they are broken, then a polar wind of the type discussed by Banks and Holzer (1968) and Axford (1968) could cause the plasma contained in the field tube to flow outward into interplanetary space. Such a flow would cause an electron density depression in the region just to the north of the SAR-arc in the upper ionosphere. Under normal conditions the field tubes existing at mid-latitudes are closed and only the field lines in the polar region are swept back into the tail. However, at times of geomagnetic disturbances the surface separating the closed and open field lines may be forced radially inward to L shells which correspond to mid-latitudes, sweeping normally closed field lines into the tail where they are opened, allowing a polar wind to reduce the electron density within the field tube. If the storm is strong enough, its position would be revealed by the presence of a SAR-arc. The region just to the north of the SAR-arc would lie along a field tube which was recently opened in the geomagnetic tail and the polar wind would begin to empty the tube. If the time constant for plasma depletion within the tube is sufficiently short, then an electron density depression would exist to the north of the SAR-arc and the height to which it would be apparent is dependent upon the time constant at that given altitude. Therefore, if the 1000 km surface, shown in Fig. 57, is the limit of the plasma depletion caused by the polar wind, it then accounts for the electron density depression existing to the north of the SAR-arc at high altitudes. However, at lower altitudes the time constant of plasma depletion by the polar wind may be sufficiently long, so that the electron density depression must be attributed to another cause. This cause could conceivably be due to enhanced recombination caused by neutral winds forcing ionization down along the geomagnetic field lines north of the SAR-arc region. Thus, two different types of winds causing the electron density depression may be associated with the SAR-arc, the polar wind in upper ionosphere, and the neutral thermospheric wind in F-region. This question may be resolved as the satellite data for the October 31/November 1, 1968, SAR-arc becomes available.

IX. CONCLUSIONS

The thermal conduction hypothesis of Cole (1965) was shown to be the most likely cause for the excitation of the SAR-arc. The theoretical and experimental results are consistent with the suggestion by Cole (1965) that the arc is excited by hot F-region electrons, which are heated by energy conducted down from the magnetosphere. The bulk of the energy flowing into the SAR-arc was shown to be transferred to the neutral gas through elastic and inelastic collisions of electrons and ions with the neutral particles. The neutral gas temperature increase caused by heating within the arc cannot be determined from solutions to the one or two-dimensional neutral heat conduction equations. Thermal conduction in the neutral gas was shown to be the dominant energy transport process in the upper thermosphere; however, adiabatic heating and cooling are most important in the lower thermosphere. The winds generated by the pressure gradients associated with the temperature pattern, determined from the heat conduction equation, were very large and did not in themselves balance the hydrodynamic equations governing the atmospheric response in the SAR-arc region. The approximate solution to these equations which was obtained shows that the neutral atmosphere responds to the heating within the SAR-arc in such a manner as to establish a circulation pattern which does not allow a significant increase in the neutral gas temperature to develop. The calculated neutral gas temperature increase within the SAR-arc of October 31/November 1, 1968, which was of the order of 500 R, shows no significant atmospheric heating within the arc itself. However, the doppler temperature measurements indicate that a large general thermospheric heating occurred during the geomagnetic storm, which does not appear to be caused by the SAR-arc alone but is probably associated with a more general atmospheric heating process.

The lack of any significant atmospheric heating within the SAR-arc region does not completely rule out electric fields as the excitation source. Walker and Rees (1968) have shown that if electric fields are exciting a SAR-arc to an intensity equivalent to that of the October 31/ November 1, 1968, arc, the ion temperature must be as high as 5000 - 6000°K. A steady state ion temperature of this magnitude results in a significant neutral heating; however, the neutral atmosphere is capable of responding in such a manner as to prevent a significant local temperature anamoly. Therefore, although the electric field hypothesis is unlikely, it is still necessary to measure the ion temperature directly within the SAR-arc to completely evaluate the role of electric fields as an excitation source for the SAR-arc.

The experimental results obtained on the SAR-arc of October 31/ November 1, 1968, cannot rule out the soft electron flux either. The results of the Fabry-Perot meridian scans and the photometer scans show that the 6300 Å emission line is the major feature of the arc, indicating that if the SAR-arc is indeed excited by a soft electron flux, the initial energy of the incoming particles should be of the order of 15 ev or less to excite the red line of atomic oxygen and not the other emission lines normally present in the aurora (Walker and Rees, 1968).

The other main experimental results of the observed SAR-arcs can be summarized as:

(1) The SAR-arc of October 30/31, 1968, occurred at a time when the K_p index was increasing and it apparently disappeared even though the K_p index continued to rise.

(2) The SAR-arc of October 31/November 1, 1968, was observed for a period of 12 hours and was stable, and extended across the entire United States slightly tilted with respect to the lines of constant L-shell.

(3) The intensity of the SAR-arc was of the order of 500-600 R near 0000UT at a time when K_p had a value of 3-4 which is in agreement with the data given in Fig. 3 (Roach and Roach, 1963).

(4) The measured exospheric temperature during the geomagnetic storm was shown to be in general agreement with the calculated temperatures of the Jacchia (1965) model; however, the exospheric temperature was seen to decay at a rate faster than the prediction.

The calculations made with the Alouette I and II satellite data show that the calculated and observed properties of the September 28/29, 1967, SAR-arc are in good agreement, adding considerable support to the thermal conduction hypothesis as the cause of the SAR-arc. The predicted ionospheric variations caused by the neutral winds in the SAR-arc model are also evident in the satellite data for this SAR-arc. The satellite data from only one SAR-arc has been analyzed and therefore the agreement may be fortuitous. Nevertheless, the theoretical model presented in this thesis clearly shows a significant coupling between the neutral and ionized components of the atmosphere and the need for considering atmospheric dynamics when one is attempting to study complex phenomena in the upper atmosphere.

X. SUGGESTIONS FOR FUTURE RESEARCH

Several geophysical satellites were in orbit at the time of the October 31/November 1, 1968 SAR-arc and an attempt should be made to gather all of the ground based and satellite data which will become available. These data can then be used to examine the world wide properties of the SAR-arc and determine the consistency of the theoretical SAR-arc model developed in this thesis.

The continued acquisition of ground based and satellite data is desirable in order to study various phases of SAR-arc development and the relationship of the arc to the magnetospheric processes.

A numerical time-dependent atmospheric model should be developed to determine the atmospheric response to an arbitrary neutral heating function. Such a model will also allow the initial phase of SAR-arc formation to be studied.

Finally, the relationship of the SAR-arc to open and closed magnetic field lines should be investigated in order to evaluate the role of the polar wind in causing the observed plasma depletion north of the SAR-arc in the upper thermosphere.

REFERENCES

Axford, W. I., "The Polar Wind and the Terrestrial Helium Budget", *J. Geophys. Res. 73,* 6855, 1968.

Ballik, E. A., "The Response of Scanning Fabry-Perot Interferometers to Atomic Transition Profiles", *Appl. Opt. 5,* 170, 1966.

Banks, P., "Electron Thermal Conductivity in the Ionosphere", *Earth and Planetary Science Letters 1,* 151, 1966a.

Banks, P., "Collision Frequencies and Energy Transfer-Electrons", *Planet. Space Sci. 14,* 1085, 1966b.

Banks, P., "Collision Frequencies and Energy Transfer-Ions", *Planet. Space Sci. 14,* 1105, 1966c.

Banks, P., "Ion Temperature in the Upper Atmosphere", *J. Geophys. Res. 72,* 3365, 1967a.

Banks, P., "The Temperature Coupling of Ions in the Ionosphere", *Planet. Space Sci. 15,* 77, 1967b.

Banks, P., Holzer, T. E., "The Polar Wind", *J. Geophys. Res. 73,* 6846, 1968.

Barbier, D., "L'activite ' aurorale aux basses latitudes", *Annls. Geophys. 14,* 334, 1958.

Barbier, D., "L'arc Auroral Stable", *Annls. Geophys. 16,* 544, 1960.

Bates, D. R., "The Temperature of the Upper Atmosphere", *Proc. Royal Soc. London B64,* 805, 1951.

Bates, D. R., "Some Problems Concerning the Terrestrial Atmosphere above about the 100-km Level", *Proc. Royal Soc. London A253,* 451, 1959.

Bayer-Helms, F., "Analyse von Linienprofilen. III", *Z. Angew. Physik, 15,* 330, 1963.

Biondi, M. A., Feibelman, W. A., "Twilight and Nightglow Spectral Line Shapes of Oxygen λ 6300 and λ 5577 Radiation", *Planet. Space Sci. 16,* 431, 1968.

Blacker, H. V., Gadsden, M., "On the Calibration of Airglow Photometers", *Planet. Space Sci. 14,* 921, 1966.

Blifford, I. H., "Factors Affecting the Performance of Commercial Interference Filters", *Appl. Opt. 5,* 105, 1966.

Born, M., Wolf, E., *Principles of Optics,* Third Edition, Pergamon Press, New York, 1965.

Bramley, E. N., "The Effects of Ion Drag and of Plasma Forces on Neutral Winds in the F-region", *J. Atmos. Terr. Phys. 29,* 1317, 1967.

Broadfoot, A. L., Kendall, K. R., "The Airglow Spectrum, 3100-10,000 Å", *J. Geophys. Res. 73,* 426, 1968.

Carleton, N. P., Roach, J. R., "Spectrographic Observations of a Mid-Latitude Red Auroral Arc", *J. Geophys. Res. 70,* 1262, 1965.

Chabbal, R., "Recherche des Meilleures Conditions D'Utilisation D'UN Spectromètre Photoelectrique Fabry-Perot", *J. Rech. Centre Nat. Rech. Sci. Lab.,* Bellevue, Paris *24,* 138, 1953.

Chamberlain, J.W., Smith, C. A., "On the Excitation Rates and Intensities of OH in the Airglow", *J. Geophys. Res. 64,* 611, 1959.

Cole, K. D., "On the Depletion of Ionization in the Outer Magnetosphere during Magnetic Disturbances", *J. Geophys. Res. 69,* 3595, 1964.

Cole, K. D., "Stable Auroral Red Arcs, Sinks for Energy of D_{st} Main Phase", *J. Geophys. Res. 70,* 1689, 1965.

Cole, K. D., "The D_{st} Main Phase and Certain Associated Phenomena", *Physics of Geomagnetic Phenomena,* Vol. II, Academic Press, New York, 1967.

Cruz, J. E., Davies, R., Droppleman, L. K., Marovich, E., Megill, L. R., Rees, M. H., Reisbeck, L., Roach, F. E., "Data Reduction for Stable Auroral Red Arcs Observed at Rapid City, South Dakota", *NBS Tech. Note* No. 308, 1965.

Dalgarno, A., "Corpuscular Radiation in the Upper Atmosphere", *Annls. Geophys. 20,* 65, 1964.

Dalgarno, A., Deggs, T. P., "Electron Cooling in the Upper Atmosphere", *Planet. Space Sci. 16,* 125, 1968.

Dalgarno, A., McElroy, M. B., Walker, J. C. G., "The Diurnal Variation of Ionospheric Temperatures", *Planet. Space Sci. 15,* 331, 1967.

Dalgarno, A., McElroy, M. B., Rees, M. H., Walker, J. C. G., "The Effect of Oxygen Cooling on Ionospheric Electron Temperatures", *Planet. Space Sci. 16,* 1371, 1968.

Dalgarno, A., Smith, F. J., "The Thermal Conductivity and Viscosity of Atomic Oxygen", *Planet. Space Sci. 9,* 1, 1962.

Dalgarno, A., Walker, J. C. G., "The Red Line of Atomic Oxygen in the Day Airglow", *J. Atmos. Sci. 21,* 463, 1964.

Da Rosa, A. V., "The Theoretical Time-Dependent Thermal Behavior of the Ionospheric Electron Gas", *J. Geophys. Res. 17,* 4107, 1966.

Dickinson, R. E., Geisler, J. E., "Vertical Motion Field in the Middle Thermosphere from Satellite Drag Densities", Mon. Wea. Rev. 96, 606, 1968.

Dickinson, R. E., Lagos, C. P., Newell, R. E., "Dynamics of the Neutral Gas in the Thermosphere for Small Rossby Number Motions", J. Geophys. Res. 73, 4299, 1968.

Donahue, T. M., "The Problem of Atomic Hydrogen", Annls. Geophys. 22, 175, 1966.

Geisler, J. E., "Atmospheric Winds in the Middle Latitude F-region", J. Atmos. Terr. Phys. 28, 703, 1966.

Geisler, J. E., "A Numerical Study of the Wind System in the Middle Thermosphere", J. Atmos. Terr. Phys. 29, 1469, 1967.

Geisler, J. E., Bowhill, S. A., "Exchange of Energy Between the Ionosphere and the Protonosphere", J. Atmos. Terr. Phys. 27, 119, 1965.

Harris, I., Priester, W., "Time-Dependent Structure of the Upper Atmosphere", J. Atmos. Sci. 19, 286, 1962.

Hays, P. B., Walker, J. C. G., "Doppler Profiles of the 5577 Å Airglow", Planet. Space Sci. 14, 1331, 1966.

Hernandez, G., "Analytic Description of a Fabry-Perot Photoelectric Spectrometer", App. Opt. 5, 1745, 1966.

Hernandez, G., Private Communication, 1967.

Hill, R. M., "Some Fringe-Broadening Defects in a Fabry-Perot Etalon", Opt. Acta. 10, 141, 1963.

Hilliard, R. L., Shepherd, G. G., "Wide-Angle Michelson Interferometer for Measuring Doppler Line Widths", J. Opt. Soc. Amer. 56, 362, 1966a.

Hilliard, R. L., Shepherd, G. G., "Upper Atmospheric Temperatures from Doppler Line Widths - IV. A Detailed Study Using the OI 5577 Å Auroral and Nightglow Emission", Planet. Space Sci. 14, 383, 1966b.

Hines, C. O., "Comments on the Rotational Speed of the Upper Atmosphere Determined from Changes in Satellite Orbits by D. G. King-Hele", Planet. Space Sci. 13, 169, 1965.

Hoch, R. J., Marovich, E., Clark, K. C., "Reappearance of a Stable Auroral Red Arc at Midlatitudes", J. Geophys. Res. 73, 4213, 1968.

Holmes, J. C., Johnson, C. Y., Young, J. M., "Ionospheric Chemistry", Space Res. V (Ed. D. G. King-Hele, P. Muller, and G. Righini), 756, North-Holland, Amsterdam, 1965.

Hunten, D. M., McElroy, M. B., "Quenching of Metastable States of Atomic Oxygen by Molecular Oxygen and Nitrogen", *Rev. Geophys. 4,* 303, 1966.

Hunten, D. M., Rundle, H. N., Shepherd, G. G., Vallance-Jones, A., "Optical Upper Atmospheric Investigations at the University of Saskatchewan", *Appl. Opt. 6,* 1609, 1967.

Jacchia, L. G., "Static Diffusion Models of the Upper Atmosphere with Empirical Temperature Profiles", *Smithsonian Astrophys. Obs. Spec. Rept. 170,* 1964.

Jacchia, L. G., "The Temperature above the Thermopause", *Space Res. V,* North-Holland, Amsterdam, 1152, 1965a.

Jacchia, L. G., "Static Diffusion Models of the Upper Atmosphere with Empirical Temperature Profiles", *Smithsonian Contributions* to *Astrophys. 8,* No. 9, 1965b.

Jacchia, L. G., Slowey, J., "An Analysis of the Atmospheric Drag of the Explorer 9 Satellite from Precisely Reduced Photographic Observations", *Smithsonian Astrophys. Obs. Spec. Rept. 125,* 1963.

Jacchia, L. G., Slowey, J., "Atmospheric Heating in the Auroral Zones: A Preliminary Analysis of the Atmospheric Drag of the Injun 3 Satellite", *J. Geophys. Res. 69,* 905, 1964.

Jacquinot, P., "The Luminosity of Spectrometers with Prisms, Gratings, or Fabry-Perot Etalons", *J. Opt. Soc. Amer. 44,* 761, 1954.

Jacquinot, P., "New Developments in Interference Spectroscopy", *Rept. Progr. Phys. 23,* 267, 1960.

Jarrett, A. H., Hoey, M. J., Paffrath, L., "Observations of the 6300 Å OI Emission of the Nightglow with a Pressure Scanning Fabry-Perot Interferometer", *Planet. Space Sci. 12,* 591, 1964.

Jarrett, A. H., Hoey, M. J., "Observations of the 6300 Å OI Nightglow Emission", *J. Atmos. Terr. Phys. 28,* 175, 1966.

Jenkins, F. A., White, H. E., *Fundamentals of Optics,* Second Edition, McGraw-Hill Book Company, Inc., New York, 1950.

Kauzmann, W., *Kinetic Theory of Gases,* Benjamin Press, New York, 1966.

King, G. A. M., "The Dissociation of Oxygen and High Level Circulation in the Atmosphere", *J. Atmos. Sci. 21,* 231, 1964.

King, G. A. M., Roach, F. E., "Relationship Between Red Auroral Arcs and Ionospheric Recombination", *J. Res. NBS 65D, 129,* 1961.

King-Hele, D. G., "The Rotational Speed of the Upper Atmosphere Determined from Changes in Satellite Orbits", *Planet. Space Sci. 12,* 835, 1964.

Kohl, H., King, J. W., "Atmospheric Winds Between 100 and 700 km and Their Effects on the Ionosphere", J. Atmos. Terr. Phys. 29, 1045, 1967.

Krebs, K., Sauer, A., "Über die Intensitätsverteilung von Spektrallinien im Perot-Fabry-Interferometer", Annls. Physik 13, 359, 1953.

Kulkarni, P. V., Sanders, C. L., "Use of a Radioactivated Light Source for the Absolute Calibration of Two-Colour Night Airglow Photometers", Planet. Space Sci. 12, 189, 1964.

Lagos, C. P., "On the Dynamics of the Thermosphere", Rept. No. 20, Department of Meteorology, M.I.T., 134 pp., 1967.

Lagos, C. P., Mahoney, J. R., "Numerical Studies of Seasonal and Latitudinal Variability in a Model Thermosphere", J. Atmos. Sci. 24, 88, 1967.

Larson, H. P., Andrew, K. L., "A Least-Squares Deconvolution Technique for the Photoelectric Fabry-Perot Spectrometer", Appl. Opt. 6, 1701, 1967.

Lindzen, R. S., "Crude Estimate for the Zonal Velocity Associated with the Diurnal Temperature Oscillation in the Thermosphere", J. Geophys. Res. 71, 865, 1966.

Lindzen, R. S., "Reconsideration of Diurnal Velocity Oscillation in the Thermosphere", J. Geophys. Res. 72, 1591, 1967.

MacMillan, W. D., The Theory of the Potential, First Edition Dover Publications, Inc., New York, 1958.

Marovich, E., Roach, F. E., "Distribution of Latitude of Red Arcs", J. Geophys. Res. 68, 1885, 1963.

Marovich, E., "Fritz Peak Observations of Stable Auroral Red Arcs, Summary 1955-1965," ESSA Tech, Rept. IER 16-ITSA 16, 68 pp, 1966.

Marovich, E., Private Communication, 1969.

McGrath, W. D., McGravey, J. J., "The Production, Deactivation and Chemical Reactions of $O(^1D)$ Atoms", Planet. Space Sci. 17, 427, 1967.

Megill, L. R., Carleton, N. P., "Excitation by Local Electric Fields in the Aurora and Airglow", J. Geophys. Res. 69, 101, 1964.

Megill, L. R., Rees, M. H., Droppleman, L. K., "Electric Fields in the Ionosphere and the Excitation of the Red Lines of Atomic Oxygen", Planet. Space Sci. 11, 45, 1963.

Megill, L. R., Van Zandt, T., "Heating of the Neutral Atmosphere During Magnetic Storms", Trans. A. G. U. 45, 355, 1964.

Moore, J. G., Odencrantz, F. K., "The Height and Geographical Position of the Red Auroral Arc of April 1-2, 1960", J. Geophys. Res. 66, 2101, 1961.

Nagy, A. F., Walker, J. C. G., "Direct Measurements Bearing on the Question of Nighttime Heating Mechanism in the Ionosphere", Planet. Space Sci. 15, 95, 1967.

Newell, R. E., "Thermospheric Energetics and a Possible Explanation of Some Observations of Geomagnetic Disturbances and Radio Aurorae", Nature, London, 211, 700, 1966.

Nilson, J. A., "A Fabry-Perot Spectrometer for Auroral Observations", M. S. Thesis, University of Saskatchewan, Saskatoon, Saskatchewan, 1960.

Nilson, J. A., Shepherd, G. G., "Upper Atmospheric Temperatures from Doppler Line Widths - I. Some Preliminary Measurements on OI 5577 Å in Aurora", Planet. Space Sci. 5, 299, 1961.

Norton, R. B., Findlay, J. A., "Electron Density and Temperature in the Vicinity of a Middle Latitude Red Arc", J. Geophys. Res. (submitted to), 1969.

Parker, E. N., "Dynamics of the Geomagnetic Storm", Space Sci. Rev., 1, 62, 1962.

Peterson, V. L., Van Zandt, T. E., Norton, R. B., "F-Region Nightglow Emissions of Atomic Oxygen, 1, Theory", J. Geophys. Res., 71, 2255, 1966.

Purdy, C. M., Megill, L. R., Roach, F. E., "A New Airglow Photometer", J. Res. NBS 65C, 4, 213, 1961.

Reed, E. I., Blamont, J. E., "OGO-4 Observations of the September 1967 M-arc", Transactions, A.G.U., 49, 641, 1968.

Rees, M. H., "Excitation of High Altitude Red Auroral Arcs", Planet. Space Sci. 8, 59, 1961.

Rees, M. H., "On the Excitation of Subvisual OI $\lambda\lambda$ 6300-6364 Arcs at Middle Latitudes", Planet. Space Sci. 8, 198, 1962.

Rees, M. H., "A Method for Determining the Height and Geographical Position of an Auroral Arc from One Observing Station", J. Geophys. Res. 68, 175, 1963.

Rees, M. H., Akasofu, S. J., "On the Association Between Subvisual Red Arcs and the D_{st}(H) Decrease", Planet. Space Sci. 11, 105, 1963.

Rees, M. H., Walker, J. C. G., "Ion and Electron Heating by Auroral Electric Fields", Annls. Geophys. 24, 193, 1968.

Rees, M. H., Walker, J. C. G., Dalgarno, A., "Auroral Excitation of the Forbidden Lines of Atomic Oxygen", Planet. Space Sci. 15, 1097, 1967.

Rishbeth, H., Megill, L. R., Cahn, J. H., "The Effect of Ion-Drag on the Neutral Air in the Ionospheric F-Region", *Annls. Geophys.* *21,* 235, 1965.

Roach, F. E., Barbier, D., Duncan, R. A., "Observation of a 6300 Å arc in France The United States, and Australia", *Annls. Geophys.* *18,* 390, 1962.

Roach, F. E., Marovich, E., "A Monochromatic Low-Latitude Aurora", *J. Res. NBS 63D,* 297, 1959.

Roach, F. E., Marovich, E., "Aurora of October 22/23, 1958, at Rapid City, South Dakota", *J. Res. NBS 64D,* 205, 1960.

Roach, F. E., Moore, J. G., Bruner, E. C., Cronin, H., Silverman, S. M., "The Height of Maximum Luminosity in an Auroral Arc", *J. Geophys. Res.* *65,* 3575, 1960.

Roach, F. E., Roach, J. R., "Stable 6300 Å Auroral Arcs in Mid-Latitudes", *Planet. Space Sci.* *11,* 523, 1963.

Roble, R. G., Hays, P. B., Nagy, A. F., "Calculated [OI] 6300 Å Nightglow Doppler Temperatures for Solar Cycle Minimum", *Planet. Space Sci.* *16,* 1109, 1968.

Schlichting, H., *Boundary Layer Theory,* Fourth Edition, McGraw-Hill Book Co., Inc. New York, 1960.

Serbu, G. P., "Results from the IMP-1 Retarding Potential Analyzer", Goddard Space Flight Center, NASA Publ. X-615-64-109, 1964.

Shepherd, G. G., "Applications of the Fabry-Perot Spectrometer to Upper Atmospheric Spectroscopy", Colloque sur les Methodes Nouvelles Spectroscopie Instrumentale, *J. Phys.* *28,* 301, 1967.

Shepherd, G. G., Lake, C. W., Miiler, J. R., Cogger, L. L., "A Spatial Spectral Scanning Technique for the Fabry-Perot Spectrometer", *Appl. Opt.* *4,* 267, 1965.

Spitzer, L. Jr., *Physics of Fully Ionized Gases,* Second Edition, Interscience Publishers, New York, 1965.

Taylor, H. A., Brace, L. H., Brinton, H. C., Smith, C. R., "Direct Measurement of Helium and Hydrogen Ion Concentration and Total Ion Density to an Altitude of 940 km", *J. Geophys. Res.* *68,* 5339, 1963.

Tohmatsu, T., Roach, F. E., "The Morphology of Mid-Latitude 6300 Angstrom Arcs", *J. Geophys. Res.* *67,* 1817, 1962.

Tolansky, S., *An Introduction to Interferometry,* Longmans, London, 1955.

Turgeon, E. C., "Auroral and Airglow Temperatures from Doppler Line-Widths", M. S. Thesis, University of Saskatchewan, Saskatoon, Saskatchewan, 1961.

Turgeon, E. C., Shephard, G. G., "Upper Atmospheric Temperatures from Doppler Line Widths - II. Measurements on the OI 5577 and OI 6300 Å lines in Aurora", Planet. Space Sci. 9, 925, 1962.

Volland, H., "A Two-Dimensional Dynamic Model of the Diurnal Variation of the Thermosphere, Part 1. Theory", J. Atmos. Sci. 23, 799, 1966.

Walker, J. C. G., "Analytic Representation of Upper Atmosphere Densities Based on Jacchia's Static Diffusion Models", J. Atmos. Sci. 22, 462, 1965.

Walker, J. C. G., Rees, M. H., "Excitation of Stable Auroral Red Arcs at Sub-Auroral Latitudes", Planet. Space Sci. 16, 915, 1968.

Wark, D. Q., "Doppler Widths of the Atomic Oxygen Lines in the Airglow", Ap. J. 131, 491, 1960.

Appendix A

SOLUTION TO THE HEAT CONDUCTION EQUATION FOR THE IONOSPHERIC ELECTRON GAS

The heat conduction equation for the electron gas in the ionosphere is

$$-\frac{d}{dz}\left[K_e(z,T_e)\frac{dT_e}{dz}\right] = Q_e(z) - L(z,T_e) \qquad (4.1)$$

Here T_e is the electron temperature, z is the altitude, K_e is the thermal conductivity of the electron gas, $Q_e(z)$ is the local heating at height z, and $L(z, T_e)$ represents the energy loss rate for the electrons. In the thermal conduction model of the SAR-arc there is no local heating of the electron gas, but heat from the magnetosphere is assumed to be conducted along the geomagnetic field lines into the ionosphere. Considering the various electron loss terms in the ionosphere, the electron gas heat conduction equation appropriate to a SAR-arc becomes,

$$\frac{d}{dz}\left[K_e(z,T_e)\frac{dT_e}{dz}\right] = L(N_2) + L(O_2) + L(O) + L(H)$$

$$+ L(He) + L(He^+) + L(H^+) + L(O_2^+) + L(NO^+) + L(O^+) \qquad (A.1)$$

Here L ( ) represents the loss rate due to the elastic and inelastic collisions of electrons with ions and neutrals (ev $cm^{-3} sec^{-1}$). The expression for each loss rate appearing in the equation is presented below.

A-1 THERMAL CONDUCTIVITY

The electron thermal conductivity for a completely ionized gas is proportional to the electron temperature raised to the 5/2 power (Spitzer, 1965) and is

$$K_{ee}(z, T_e) = 7.7 \times 10^{5}\, T_e^{5/2}(z)\, \mathrm{SIN}^2 I \quad (\mathrm{ev\ cm^{-1} sec^{-1} deg^{-1}}) \tag{A.2}$$

Where I is the geomagnetic dip angle. The electron gas thermal conductivity in the ionosphere is, however, affected by the presence of neutral particles and Dalgarno, McElroy, and Walker (1967) accounted for this presence by considering the thermal conductivity of the electron gas to be represented by a harmonic mean between the two components.

$$\frac{1}{K_e} = \frac{1}{K_{ee}} + \frac{1}{K_{en}} \tag{A.3}$$

where K_{en} is the conductivity due to collisions of electrons with the neutral particles and is

$$K_{en}(z, T_e) = 3.2 \times 10^{7} \frac{T_e(z)\, n_e(z)}{\nu_{en}(z, T_e)}\, \mathrm{SIN}^2 I \tag{A.4}$$

Here $n_e(z)$ is the electron density at height z, and ν_{en} is the electron-neutral collision frequency

$$\nu_{en}(z, T_e) = 1.7 \times 10^{-11} n(N_2)\, T_e(z) + 3.8 \times 10^{-10} n(O_2) \cdot T_e^{1/2}(z) + 1.4 \times 10^{-10} n(O)\, T_e^{1/2}(z) \quad (\mathrm{sec^{-1}}) \tag{A.5}$$

where n(x)is the number density of species x at height z. The electron gas thermal conductivity adopted here becomes

$$K_e(z,T_e) = 7.7\times10^{5}\, T_e^{5/2}(z)\, \mathrm{SIN}^2 I \Big\{ 1 + 3.22\times10^{4} \Big(T_e^{2}(z) / n_e(z) \Big) \cdot \Big[1.26\times10^{-17}\, T_e^{1/2}(z)\, n(N_2) + 2.82\times10^{-16}\, n(O_2) + 1.02\times10^{-16}\, n(O) \Big] \Big\}^{-1} \qquad \text{(A. 6)}$$

A-2 LOSS RATES

Taking the loss rates in the order presented in equation (A. 1), $L(N_2)$ is the loss rate due to collisions of electrons with nitrogen molecules and is (Dalgarno, McElroy, and Walker, 1967)

$$L(N_2) = 1.3\times10^{-4}\, n_e\, n(N_2) \Big[\Big[\Big\{ 7.6\times10^{-16}\, T_e + \frac{2.0\times10^{-10}}{T_e^{1/2}} \Big\} (T_e - T_n) + \Big(1. - \mathrm{EXP}\Big[3200. \Big(\frac{1}{T_e} - \frac{1}{T_n} \Big) \Big]\Big] \Big) A \Big]$$

(A. 7)

where T_n is the temperature of the neutral gas and n_e is the electron density. The first term represents the loss due to elastic collisions of electrons with molecular nitrogen, the second term is the loss due to the excitation of the rotational bands of N_2 by the thermal electrons, and the third term is the loss due to the excitation of the vibrational bands of N_2 by the thermal electrons. The variable A in equation (A. 7) takes the form

$$A = \begin{cases} 5.715 \times 10^{-8} \, \mathrm{Exp}(-3352.6/T_e) \, ; & T_e < 1000^\circ K \\ 2.0 \times 10^{-7} \, \mathrm{EXP}(-4605.2/T_e) \, ; & 1000^\circ K \leq T_e \leq 2000^\circ K \\ 2.53 \times 10^{-6} \, T_e^{1/2} \, \mathrm{EXP}(-17620./T_e) \, ; & T_e > 2000^\circ K \end{cases} \tag{A.8}$$

$L(O_2)$ is the loss rate due to elastic collisions of electrons with molecular oxygen (Banks, 1966b)

$$L(O_2) = 1.21 \times 10^{-18} n_e n(O_2) \left[1. + 3.6 \times 10^{-2} T_e^{1/2} \right] T_e^{1/2} (T_e - T_n) \tag{A.9}$$

L(H) is the loss rate due to elastic collisions of electrons with atomic hydrogen (Banks, 1966b)

$$L(H) = 9.63 \times 10^{-16} n_e n(H) \left[1. - 1.35 \times 10^{-4} T_e \right] T_e^{1/2} (T_e - T_n) \tag{A.10}$$

L(He) is the loss rate due to elastic collisions of electrons with helium atoms. (Banks, 1966b)

$$L(He) = 2.46 \times 10^{-17} n_e n(He) T_e^{1/2} (T_e - T_n) \tag{A.11}$$

L(O) is the loss rate due to elastic and inelastic collisions of electrons with atomic oxygen and includes (a) elastic collisions of electrons with atomic oxygen, (b) a loss to the excitation of atomic oxygen to the ^1D state and (c) a loss to the excitation of the fine structure levels of the ground state of atomic oxygen. The following expressions are used for these processes:

$L_e(O)$ is the loss rate due to elastic collisions of electrons with atomic oxygen (Banks, 1966b)

$$L_e(O) = 3.74 \times 10^{-18} n_e n(O) T_e^{1/2} (T_e - T_n) \qquad \text{(A.12)}$$

$L(O(^1D))$ is the loss rate due to the excitation of atomic oxygen to the (^1D) state by collisions with thermal electrons (Rees, Walker, and Dalgarno, 1967).

$$L(O(^1D)) = 5.45 \times 10^{-11} n(O) n_e T_e^{1/2} EXP(-2.27 \times 10^4/T_e)$$
$$\Big[0.406 + 0.357 \times 10^{-4} T_e - EXP(-1.37 \times 10^4/T_e)(0.33$$
$$+ 0.183 \times 10^{-4} T_e) - EXP(-2.97 \times 10^4/T_e) \cdot (0.456$$
$$+ 0.174 \times 10^{-4} T_e)\Big] \qquad \text{(A.13)}$$

$L(O(^3P))$ is the loss rate due to the excitation of the fine structure levels of the ground state of atomic oxygen by thermal electrons (Dalgarno and Deggs, 1968; Dalgarno, McElroy, Rees, and Walker, 1968)

$$L(O(^3P)) = 3.0 \times 10^{10} n_e n(O) \Big[T_e^{1/2} (5. + 3. EXP($$
$$-.02/[8.63 \times 10^{-5} T_n]) + EXP(-.028/[8.63 \times 10^{-5}$$
$$T_n])\Big]^{-1} \Big\{ (4.75 \times 10^{-21} T_e + 6.28 \times 10^{-17}) .02 \Big[8.63 \times 10^{-5}$$

$$T_e \, \mathrm{Exp}(-.02/[8.63\times10^{-5} T_e]) - 8.63\times10^{-5} \, \mathrm{Exp}(-.02/$$

$$[8.63\times10^{-5} T_n])] + (2.3\times10^{-21} T_e + 1.16\times10^{-17}) \, .028$$

$$[8.63\times10^{-5} \, T_e \, \mathrm{Exp}(-.028/[8.63\times10^{-5} T_e])$$

$$- 8.63\times10^{-5} T_e \, \mathrm{Exp}(-.028/[8.63\times10^{-5} T_n])] + ($$

$$3.\times10^{-21} T_e + 2.2\times10^{-17}) \, .008 \, [8.63\times10^{-5} \, T_e$$

$$\mathrm{Exp}(-.008/[8.63\times10^{-5} T_e]) - 8.63\times10^{-5} T_e \, \mathrm{Exp}($$

$$-.008/[8.63\times10^{-5} T_n])] \, \mathrm{Exp}(-.02/[8.63\times10^{-5} T_n])\Big\} \tag{A.14}$$

The loss rates due to coulomb collisions between the thermal electrons and the various ions are obtained from Banks(1966b).

$$L(O^+) = 4.8\times10^{-7} n_e \, n(O^+) [T_e - T_i(O^+)] \, T_e^{-3/2}$$

$$L(He^+) = 1.9\times10^{-6} n_e \, n(He^+) [T_e - T_i(He^+)] \, T_e^{-3/2}$$

$$L(H^+) = 7.7\times10^{-6} n_e \, n(H^+) [T_e - T_i(H^+)] \, T_e^{-3/2}$$

$$L(O_2^+) = 2.4\times10^{-7} n_e\, n(O_2^+)\left[T_e - T_i(O_2^+)\right] T_e^{-3/2}$$

$$L(NO^+) = 2.56\times10^{-7} n_e\, n(NO^+)\left[T_e - T_i(NO^+)\right] T_e^{-3/2}$$

(A.15)

where $T_i(X^+)$ is the ion temperature of ion X^+.

When equations (A. 6) through (A. 15) are inserted into equation (A. 1), the heat conduction equation for the electron gas is obtained. Before this equation can be solved, however, the neutral temperature, neutral density, ion density, and electron density altitude profiles must be specified.

A-3 MODEL ATMOSPHERE

The neutral gas temperature and neutral density profiles are obtained from the analytic model atmosphere given by Bates (1959), as modified by Walker (1964).The neutral gas temperature is analytically represented by

$$T_B(z) = T_\infty - (T_\infty - T_{120})\, EXP(-\sigma\, \xi)$$

(A. 16)

where T_∞ is the exospheric temperature, T_{120} is the temperature of the neutral gas at 120 km, ξ is the geopotential altitude ($\xi = (z-120)(R_e+120)/(R_e+z).$), z is the altitude under consideration, and R_e is the radius of the earth. $\sigma = \left[S+1/(R_e+120)\right]$ where S is an analytic function of T_∞ used by Jacchia (1964).

$$S = 0.0291\, EXP\left\{-\left[(T_\infty - 800)/(750. + 1.722\times10^{-4}\left[T_\infty - 800\right]^2)\right]^2/2.\right\}$$

(A. 17)

Jacchia (1964) gives analytic expressions for T_∞ which take into consideration the solar cycle, short period solar activity, semi-annual, diurnal, and geomagnetic activity variations of atmospheric density. The expressions for T_∞ and S have been determined so that the temperature profile yields atmospheric densities in agreement with satellite drag data when the diffusive equilibrium equation for N_2, O_2, O, and He are integrated numerically using a single set of boundary conditions. Walker (1964) has made a modification to Jacchia's equations so that the diffusive equilibrium equation can be integrated exactly to give an analytic expression for the number density profiles

$$n(i,z) = n(i,120)\left[\frac{1-(T_\infty - T_{120})/T_\infty}{1-\left[(T_\infty - T_{120})/T_\infty\right]\mathrm{Exp}(-\sigma\xi)}\right]^{1+\alpha+\gamma'} \cdot \mathrm{Exp}(-\sigma\gamma'\xi) \qquad \text{(A.18)}$$

n(i, z) is the number density of the i^{th} species at altitude z, n(i/120) is the number density at the lower boundary, α is the thermal diffusion coefficient (equal to -0.4 for He and zero for N_2, O_2, and O) and $\gamma' = \frac{m_i g_{120}}{k^* T_\infty \sigma}$, where m_i is the molecular mass of constituent i, k^* is the Boltzmann constant, and g_{120} is the acceleration of gravity at 120km. The number density of atomic hydrogen used in the calculations is not obtained from equation (A.18) but was obtained from the work of Donahue (1966).

A-4 ION TEMPERATURE

The expressions for the loss rate due to coulomb collisions between electrons and ions require a value of the ion temperature; equation (A.17). It is assumed that all ion species have the same ion temperature throughout the ionosphere and that thermal conduction in the ion gas can be neglected. It appears from the calculations of Banks (1967a, 1967b) that the effect of ion conductivity is not important below 600 km. Therefore, the ion temperature is obtained by a balance between the rate at which the ions are heated in elastic collisions with the ambient electrons, L(e) $(T_e - T_i)$, and the rate at which the ions cool in elastic collisions with the neutrals, L(n) $(T_i - T_n)$. Equating these two rates and solving for T_i gives:

$$T_i = \frac{L(n)T_n + L(e)T_e}{L(n) + L(e)} \qquad (A.19)$$

where

$$L(e) = \frac{7.7 \times 10^{-6} n_e}{T_e^{3/2}} \sum_i \frac{n(i)}{A_i} \qquad (A.20)$$

and A_i is the ion mass unit in a.m.u. L(n) is the loss rate of ions to the various neutrals due to polarization interaction and resonance charge exchange processes. L(n) can be represented by the sum of the following individual loss processes:

$$\begin{aligned} L(n) = \Big[& L(O^+, N_2) + L(O^+, O_2) + L(O^+, He) + L(O^+, H) + L(He^+, N_2) \\ & + L(He^+, O_2) + L(He^+, O) + L(He^+, H) + L(H^+, N_2) + L(H^+, O_2) \\ & + L(H^+, He) + L(H^+, O) + L(NO^+, O_2) + L(NO^+, N_2) + L(NO^+, O) \\ & + L(O_2^+, N_2) + L(O_2^+, O) \Big] + \Big\{ L(O, O^+) + L(H, H^+) + L(O_2, O_2^+) \\ & + L(He, He^+) \Big\} \end{aligned} \qquad (A.21)$$

where the square bracketed terms are losses due to polarization interaction and the curly bracketed terms are due to resonance charge exchange. The expressions for these loss terms are obtained from Banks (1966c) and are listed in Table IV. Since it was known a priori that the ion temperature would depart relatively little from the neutral gas temperature in the lower altitudes, where the neutral density is higher and the loss mechanism more effective, it was assumed that the non-linear term $(T_i+T_n)^{1/2}$ in the resonance charge exchange loss rate could be approximated by $\sqrt{2T_n}$. This would lead to an error of less than 10% even in the most intense SAR-arc considered. A solution to the electron heat conduction equation therefore, yields an electron temperature height profile.

A-5 6300 Å VOLUME EMISSION RATE OF O(^{1}D)

The volume emission profile for the 6300 Å radiation of the O(^{1}D) atomic oxygen red line is obtained from the loss rate term L(O(^{1}D)), due to thermal excitation of the oxygen atom in the ground state to the ^{1}D state by electron impact. Once the oxygen atom is in the ^{1}D state it has a radiative half-life of approximately 110 seconds and a red photon is emitted unless it is collisionally deactivated. Therefore, the volume emission rate depends upon these two terms and can be expressed as

$$E_\lambda = \frac{A_\lambda}{A_D} \frac{L(O(^1D))}{\left(1+\frac{S_D n(N_2)}{A_D}\right) 1.96} \quad \text{(photons cm}^{-3}\text{sec}^{-1}) \qquad \text{(A. 22)}$$

where A_D and A_λ are the corresponding Einstein level and transition coefficients for O(^{1}D) (0.0091 sec^{-1}), and 6300 Å red line (.0069 sec^{-1}) respectively, and $S_D = 5\times10^{-11}$ cm^{3}sec^{-1} is the collisional deactivation coefficient due to quenching by N_2. (Hunten and McElroy, 1966;

TABLE IV
ENERGY LOSS RATES DUE TO COLLISIONS OF IONS WITH NEUTRALS

(Banks, 1966 C)

Ion Mixture	Energy Loss Rate $(10^{-14}\text{ev cm}^{-3}\text{sec}^{-1})$
O^+-N_2	$6.6n(O^+)n(N_2)(T_i-T_n)$
O^+-O_2	$5.8n(O^+)n(O_2)(T_i-T_n)$
O^+-He	$2.8n(O^+)n(He)(T_i-T_n)$
O^+-O	$0.21n(O^+)n(O)(T_i+T_n)^{\frac{1}{2}}(T_i-T_n)$
O^+-H	$0.36n(O^+)\,n(H)T_n^{\frac{1}{2}}(T_i-T_n)$
He^+-N_2	$5.3n(He^+)n(N_2)(T_i-T_n)$
He^+-O_2	$4.5n(He^+)n(O_2)(T_i-T_n)$
He^+-O	$5.8n(He^+)n(O)(T_i-T_n)$
He^+-H	$10.0n(He^+)n(H)(T_i-T_n)$
He^+-He	$0.4n(He^+)n(He)(T_i+T_n)^{\frac{1}{2}}(T_i-T_n)$
H^+-N_2	$3.1n(H^+)n(N_2)(T_i-T_n)$
H^+-O_2	$2.8n(H^+)n(O_2)(T_i-T_n)$
H^+-He	$5.5n(H^+)n(He)(T_i-T_n)$
H^+-H	$1.4n(H^+)n(H)(T_i+T_n)^{\frac{1}{2}}(T_i-T_n)$
H^+-O	$0.40n(H^+)n(O)T_n^{\frac{1}{2}}(T_i-T_n)$
NO^+-O_2	$5.45n(NO^+)n(O_2)(T_i-T_n)$
NO^+-N_2	$5.916n(NO^+)n(N_2)(T_i-T_n)$
NO^+-O	$4.5n(NO^+)n(O)(T_i-T_n)$
$O_2^+-N_2$	$5.807n(O_2^+)n(N_2)(T_i-T_n)$
O_2^+-O	$4.358n(O_2^+)n(O)(T_i-T_n)$
$O_2^+-O_2$	$0.14n(O_2^+)n(O_2)(T_i+T_n)(T_i-T_n)$

McGrath and McGarvey, 1967). The volume emission rate profile can, therefore, be easily obtained once $L(O(^1D))$ is known from the solution of the electron heat conduction equation.

A-6 NEUTRAL HEATING

The neutral particles are an energy sink for the heated electrons and ions. Energy is transferred into the neutral gas through the following processes:

(1) polarization interaction and resonance charge exchange encounters between the ions and neturals $L(N)$, (2) elastic electron-neutral particle collisions; $L(O_2)$, $L(He)$, $L(H)$, $L(O)$, $[L(N_2)-L(N_{2\nu})]$ where the last term allows a total radiation loss of the vibrationally excited bands of molecular nitrogen, (3) fine structure cooling of the ground state of atomic oxygen is negligible over the altitude under consideration), and (4) collisional quenching of $O(^1D)$ atoms by molecular nitrogen $L(O(^1D))*q$. Here q represents the fraction of the $O(^1D)$ atoms quenched. Therefore, the amount of heat going into the neutral gas due to the cooling of the electrons and ions is expressed as

$$H(z, T_e) = L(n)\left[T_i - T_n\right] + L(O_2) + L(He) + L(H) + L_e(O) + L\left(O(^3P)\right) + \left[L(N_2) - L(N_{2\nu})\right] + L\left(O(^1D)\right)\cdot q \tag{A.23}$$

A-7 METHOD OF SOLUTION

The ion and electron density profiles must also be specified in order to solve the electron gas heat conduction equation. These profiles appropriate to conditions within a SAR-arc, are presented in Chapter 4 where a discussion of the results is given.

Equation A-1 was solved by a Runge-Kutta technique. The equation was first re-written as

$$\frac{d}{dz}\left(\frac{2}{7}K_e'(z)\frac{dT_e^{7/2}}{dz}\right)=\sum L(z,T_e) \qquad (A.24)$$

where $K_e(z, T_e) = K_e'(z)T_e^{5/2}$. Separating equation A. 24 into two first order equations gives

$$2/7\, K_e'(z)\frac{dT_e^{7/2}}{dz} = y \qquad (A.25)$$

and

$$\frac{dy}{dz} = \sum L(z,T_e)$$

These equations were solved by a trial and error technique for the electron temperature profile by specifying a given heat flow into the ionosphere at 1000 km as one boundary condition and setting the electron temperature equal to the neutral gas temperature at 120 km as the other. The scheme used to solve the equations is to assume a temperature at the upper boundary and by integrating equation (A. 25) a new temperature is found at the next lower altitude step. Then with this new temperature equation (A. 25) is integrated again to find the temperature at the next lower step. This process is then repeated by integrating to lower altitudes and, if the initial temperature is properly chosen, the last integrated temperature should match the neutral gas temperature at the lower boundary. In practice, if the initial value of the assumed electron temperature at 1000 km is too low, the electron temperature profile crosses the neutral temperature profile at an altitude higher than the lower boundary and proceeds to high negative values. If the electron temperature is chosen too high then the electron temperature profile might follow the true solution for a while, but explode to high electron temperature values before reaching the lower boundary. By continually bracketing the estimated temperature at 1000 km the integration proceeds deeper and deeper into the atmosphere until the lower boundary is finally reached; with further bracketing of the electron temperature at 1000 km the lower boundary condition is eventually satisfied. Using this approach an electron temperature profile can be obtained in less than 60 seconds on an IBM 360 computer. Height profiles of ion temperature, volume emission rate of 6300 Å radiation, neutral heating, heat flow rate, and loss rates for the various atmospheric constituents are also obtained from the computer program.

A listing of the computer program used to solve the electron gas heat conduction equation is given in Table V.

Table V

Listing of the Computer Program Used to Solve the Electron Gas Heat Conduction Equation

```
$LIST -A
      SUBROUTINE MAIN
C       THIS IS A DOUBLE PRECISION PROGRAM
C       THIS PROGRAM SOLVES THE ELECTRON HEAT CONDUCTION EQUATION IN
C       THE IONOSPHERE USING A RUNGE-KUTTA TECHNIQUE
      IMPLICIT REAL*8(A-H,O-Z),INTEGER(I-N)
      DIMENSION X(100),YZ(100),YYZ(100),XZ(100),YLASZ(100),EOS1(100),
     1EOS1V(100),EOS2(100),EOS1D(100),EOS3(100),EOS4(100),EOS5(100),
     2EOS6(100),EOS7(100),EOS8(100),TLOS(100),ZNQT(100),ZNQ(100)
      COMMON G,HE(100),C1,C2,Y(100),YLAST(100),TOPHF,TL,DELTA,Y11,
     1RG(100),YY(100),DELTY,Y1,Y0,PRMT(5),YX(2),YYX(2),AUX(8,2),XION(5),
     2XLN,TN,XLOSS,XLOO,XL1,XL2,O1D,XL3,XL4,XL5,XL6,XL7,RGLOW,TINF,
     3TZERO,XNO(4),HTION(100),EHY(100),YOE,ENE(100),Y1F,DELS,OI(100),
     4HEI(100),HYI(100),OOI(100),XNOI(100),BETA,ALT(100),Q(100),Q1,
     5XN(6),TLOWL,THI,C4,STSZ,IPT,MQX,IQSWT,MX,LKIM,
     6N,NN,INDX,INDXX,JF
      NAMELIST/ZZM/ XII,N,TOPHF,Y1,Y0,TGES,TZERO,IQSWT,TINF,YOE,Y1F,
     1XNO,BETA,HEO,ALTO,DELS,DELQS,MX,MQX,LKIM,ENE,Q,EHY,HTION,OOI,
     2XNOI,OI,HEI,HYI,Q1,BRAC,ISTP,STSZ
      READ(5,ZZM)
      IJ=1
      G=0.
      XI=3.1415926/XII
      Y11=Y1
      ISW=0
      TLL=0.
      TLR=0.
      DO 125 I=1,N
      Y(I)=0.
  125 YLAST(I)=0.
      C1=2./7.
      C2=7.7E5*C1*DSIN(XI)*DSIN(XI)
      DO 100 I=1,MX
  100 HE(I)=HEO+(I-1)*DELS
      DO 101 I=1,MQX
  101 ALT(I)=ALTO+(I-1)*DELQS
      N1=N-1
      NN=N
      DELTA=(Y1-Y0)/N1
      DELTY=-DELTA
      WRITE(6,105)
  105 FORMAT(7X,1HZ,14X,2HTN,13X,2HN2,13X,2HO2,13X,1HO,14X,2HHE,13X,1HH/
     11/)
      DO 103 I=1,N
      X(I) = Y1-DELTA*(I-1)
      CALL ATMMOD(X(I))
  103 WRITE(6,104)X(I),TN,XN(1),XN(2),XN(3),XN(4),XN(6)
  104 FORMAT(1H ,7E15.5)
      WRITE(6,195)
  195 FORMAT(7X,1HZ,14X,2HO+,13X,3HHE+,12X,2HH+,13X,3HO2+,12X,3HNO+,12
     1X,2HNE//)
```

```
      DO 196 I=1,N
      CALL EION(X(I))
  196 WRITE(6,197) X(I),XION(1),XION(2),XION(3),XION(4),XION(5),XN(5)
  197 FORMAT(1H ,7E15.5)
  203 CALL ATMMOD(Y0)
C       THIS IS THE BEGINNING OF THE SEARCH METHOD FOR THE UPPER
C       BOUNDARY TEMPERATURE WHICH SATISFIES THE EQUATION
      T=TN
      TLOWL=(T-300.)**3.5
      THI=1.E60
      TLEFT=T**3.5
      TL=TGES**3.5
      TL1=1.
      WRITE(6,106) Y0,T,TOPHF,TLEFT
 106  FORMAT(1X,'LOWER BOUND = ',E12.4,'TEMP = ',E12.4,'TOPHE = ',E12.4,
     1'TLEFT = ',E12.4//)
  281 LL=0
      ICALL=1
      I=1
 1065 CONTINUE
      IF(I.GT.30) GO TO 1075
      DO 107 I=1,30
      CALL RUNGE(TL,TOPHE)
      IF(IPT.EQ.1) GO TO 108
      IF(IPT.EQ.2) GO TO 109
      IF(IPT.EQ.3) GO TO 110
 108  TEMP=TL**C1
      WRITE(6,150) TEMP,INDX
 150  FORMAT(5X,'ESTIMATE TE = ',1E14.7,'DRIVES TE NEGATIVE AT STEP ',
     1I3)
      IF(ISW.GT.0) GO TO 161
      TLL=TL
      TL1=TL
      TLR=TL*3.
      TL=TL*3.
      GO TO 162
  161 TLL=TL
      TL1=TL
      TL=TL+(TLR-TL)/2.
 162  CONTINUE
      I=I+1
      GO TO 1065
 107  CONTINUE
 1075 CONTINUE
 109  TEMP=TL**C1
      WRITE(6,151) TEMP,INDX
 151  FORMAT(10X,'ESTIMATE TL = ',1E14.7,'EXPLODES TE AT STEP ',I3)
      TL1=TL
      TLR=TL
      TL=TLL+(TL-TLL)/2.
      GO TO 111
  110 TEMP=DABS(TL/TL1-1.)
      IF(TEMP.LT.1.E-6) GO TO 112
      IF(Y(N).EQ.YLAST(N)) GO TO 112
      IF(Y(N).EQ.TLEFT) GO TO 112
      IF(Y(N).GT.TLEFT) GO TO 113
      GO TO 114
 113  TLR=TL
      TL1=TL
      TL=TLL+(TL-TLL)/2.
```

```
      TEMP=TL1**C1
      WRITE(6,152) TEMP,Y(N)
  152 FORMAT(10X,'ESTIMATE OF TL = ',1E14.7,'YIELDS TE = ',1E14.7,'TOO H
     1IGH')
      GO TO 111
  114 TLL=TL
      TL1=TL
      TL=((TLR-TL)/2.)+TL
      TEMP=TL1**C1
      WRITE(6,153) TEMP,Y(N)
  153 FORMAT(5X,'ESTIMATE OF TL = ',1E14.7,'YIELDS TE = ',1E14.7,'TOO LO
     1W')
  111 IF(LL.EQ.20) GO TO 116
      LL=LL+1
      GO TO 117
  116 WRITE(6,155)
  155 FORMAT(5X,'WE DID IT 30 TIMES THAT IS ENOUGH')
      GO TO 112
  117 DO 118 I=1,N
  118 YLAST(I) = Y(I)
      ICALL=2
      CALL RUNGE(TL,TOPHF)
      IF(IPT.EQ.1) GO TO 119
      GO TO 120
  119 TLL=TL
      TL1=TL
      TL=TL+(TLR-TL)/2.
      TEMP=TL1**C1
      WRITE(6,150) TEMP,INDX
      GO TO 111
  120 IF(IPT.EQ.2) GO TO 109
      IF(IPT.EQ.3) GO TO 110
  112 CONTINUE
C       THIS IS THE BEGINNING OF THE SECOND ITERATION
      DO 200 I=1,N
      IM=(IJ-1)+I
      YZ(IM) = Y(I)**C1
      YLASZ(IM)=YLAST(I)**C1
      YYZ(IM)=YY(I)
  200 XZ(IM) = X(I)
      IF(ISTP.EQ.1) GO TO 201
      IF(ISW.EQ.1) GO TO 201
      ISW=ISW+1
      IJ=(Y11-3.E7) /DELTA+1.0001
      TGES=YZ(IJ)
      TOPHF=YYZ(IJ)
      Y1=3.E7
      N=1.8E7/DELTA+1.00001
      TLL=0.
      TLR=0.
      DO 202 I=1,N
      X(I) =3.E7-DELTA*(I-1)
      Y(I) = 0.
      YY(I) = 0.
  202 YLAST(I) = 0.
      TLL=(TGES-BRAC)**(1./C1)
      TLR=(TGES+BRAC)**(1./C1)
      TL=TGES**3.5
      TL1=1.
      GO TO 281
```

```
  201 CONTINUE
C       THIS IS THE BEGINNING OF THE EXTRAPOLATION TO THE LOWER
C       BOUNDARY
      YZ(NN) = TZERO
      YZ(NN-1) = YZ(NN)+(YZ(NN-2)-YZ(NN))/(XZ(NN-2)-XZ(NN))*(XZ(NN-1)-
     1XZ(NN))
      CALL ATMMOD(XZ(NN-1))
      CALL FION(XZ(NN-1))
      C4=XZ(NN-1)
      YYZ(NN-1)=COND(YZ(NN-1))*((YZ(NN-2))**3.5-(YZ(NN))**3.5)/(XZ(NN-2)
     1-XZ(NN))
      CALL ATMMOD(XZ(NN))
      CALL EION(XZ(NN))
      C4=XZ(NN)
      YYZ(NN)=COND(YZ(NN))*((YZ(NN-1))**3.5-(YZ(NN))**3.5)/(XZ(NN-1)-
     1XZ(NN))
      WRITE(6,156)
  156 FORMAT(7X,1HZ,14X,2HTE,13X,4HCOND,11X,4HTION,11X,5HRGLOW,10X,
     14HQDIV,11X,5HHEATF,10X,5HNHEAT//)
      DO 205 I=1,NN
      CALL ATMMOD(XZ(I))
      CALL FION(XZ(I))
      C4=XZ(I)
      CALL LOSS(YZ(I))
      TEMP=XLOSS
      EOS1(I)=XL1
      EOS1V(I)=XLOO
      EOS2(I)=XL2
      EOS1D(I)=O1D
      EOS3(I)=XL3
      EOS4(I) = XL4
      EOS5(I) = XL5
      EOS6(I)=XL6
      EOS7(I)=XL7
      TIP=TII(YZ(I))
      EOS8(I)=XLN*(TIP-TN)
      TLOS(I)=XL1+XL2+XL3+XL4+XL5+XL6+XL7
      RG(I)=RGLOW
      RR=RGLOW*1.96
      ZNQT(I)=-TEMP+SOURC(C4)
      ZNQ(I)=EOS1(I)-EOS1V(I)+EOS2(I)+EOS4(I)+EOS6(I)+EOS7(I)+EOS8(I)+
     1EOS3(I)-RR
      UUU=3.5*COND(YZ(I))*YZ(I)**2.5
      FLO=-YYZ(I)
  205 WRITE(6,157)XZ(I),YZ(I),UUU,TIP,RG(I),TEMP,FLO,ZNQ(I)
  157 FORMAT(1H ,8E15.6)
      WRITE(6,158)
  158 FORMAT(5X,1HZ,10X,3HLN2,8X,4HLN2V,7X,3HLO2,8X,3HO1D,8X,2HLO,9X,
     13HLHE,8X,4HLION,7X,3HO3P,8X,5HLHION,6X,8HLOSS I-N//)
      DO 206 I=1,NN
  206 WRITE(6,159) XZ(I),EOS1(I),EOS1V(I),EOS2(I),EOS1D(I),EOS3(I),
     1EOS4(I),EOS5(I),EOS6(I),EOS7(I),EOS8(I)
  159 FORMAT(1H ,11E11.4)
      TRAYC=SIMPS(N1)*1.E-6
      WRITE(6,160) TRAYC
  160 FORMAT(10X,'TOTAL RAYLEIGHS = ',1E15.6)
      CALL EXIT
      RETURN
      ENTRY FUDGEL
      GO TO (108,119),ICALL
```

```
      ENTRY FUDGEH
      GO TO (109,120),ICALL
      END
      REAL FUNCTION TII*8(QQ)
C       THIS SUBROUTINE CALCULATES THE ION TEMPERATURE
      IMPLICIT REAL*8(A-H,O-Z),INTEGER(I-N)
      COMMON G,HE(100),C1,C2,Y(100),YLAST(100),TOPHF,TL,DELTA,Y11,
     1RG(100),YY(100),DELTY,Y1,YO,PRMT(5),YX(2),YYX(2),AUX(8,2),XION(5),
     2XLN,TN,XLOSS,XLOO,XL1,XL2,O1D,XL3,XL4,XL5,XL6,XL7,RGLOW,TINF,
     3TZERO,XNO(4),HTION(100),EHY(100),YOE,ENE(100),Y1E,DELS,OI(100),
     4HEI(100),HYI(100),OOI(100),XNOI(100),BETA,ALT(100),Q(100),Q1,
     4XN(6),TLOWL,THI,C4,STSZ,IPT,MQX,IQSWT,MX,LKIM,
     6N,NN,INDX,INDXX,JF
      XLE=(4.8E-7*XION(1)+1.9E-6*XION(2)+7.7E-6*XION(3)+2.566E-7*XION(4)
     1+2.406E-7*XION(5))*XN(5)/(QQ*DSQRT(QQ))
      XLN1=(6.6*XN(1)+5.8*XN(2)+2.8*XN(4)+.21*XN(3)*DSQRT(2.*TN))*
     1XION(1)
      XLN2=(5.3*XN(1)+4.5*XN(2)+5.8*XN(3)+10.*XN(6)+.4*XN(4)*
     1DSQRT(2.*TN))*XION(2)
      XLN3=(3.1*XN(1)+2.8*XN(2)+5.5*XN(4)+1.4*XN(6)*DSQRT(2.*TN))*XI
     1ON(3)
      XLN4=(5.807*XN(1)+4.358*XN(3)+.14*XN(2)*DSQRT(2.*TN))*XION(4)
      XLN5=(5.45*XN(2)+5.916*XN(1)+4.5*XN(3))*XION(5)
      XLN=(XLN1+XLN2+XLN3+XLN4+XLN5)*1.E-14
      TII=(XLN*TN+XLE*QQ)/(XLN+XLE)
      RETURN
      END
      REAL FUNCTION COND*8(QR)
C       THIS SUBROUTINE CALCULATES THE ELECTRON GAS THERMAL
C       CONDUCTIVITY
      IMPLICIT REAL*8(A-H,O-Z),INTEGER(I-N)
      COMMON G,HE(100),C1,C2,Y(100),YLAST(100),TOPHF,TL,DELTA,Y11,
     1RG(100),YY(100),DELTY,Y1,YO,PRMT(5),YX(2),YYX(2),AUX(8,2),XION(5),
     2XLN,TN,XLOSS,XLOO,XL1,XL2,O1D,XL3,XL4,XL5,XL6,XL7,RGLOW,TINF,
     3TZERO,XNO(4),HTION(100),EHY(100),YOE,ENE(100),Y1E,DELS,OI(100),
     4HEI(100),HYI(100),OOI(100),XNOI(100),BETA,ALT(100),Q(100),Q1,
     4XN(6),TLOWL,THI,C4,STSZ,IPT,MQX,IQSWT,MX,LKIM,
     6N,NN,INDX,INDXX,JF
      TEMP1=DSQRT(QR)
      UN=1.7E-11*XN(1)*QR+3.8E-10*XN(2)*TEMP1+1.4E-10*XN(3)*TEMP1
      W=41.8*XN(5)/(QR*TEMP1*UN)
      COND=C2*W/(1.+W)
      RETURN
      END
      SUBROUTINE LOSS(QQL)
C       THIS SUBROUTINE CALCULATES THE LOSS RATE OF ELECTRONS
C       INTERACTING WITH IONS AND NEUTRALS
      IMPLICIT REAL*8(A-H,O-Z),INTEGER(I-N)
      COMMON G,HE(100),C1,C2,Y(100),YLAST(100),TOPHF,TL,DELTA,Y11,
     1RG(100),YY(100),DELTY,Y1,YO,PRMT(5),YX(2),YYX(2),AUX(8,2),XION(5),
     2XLN,TN,XLOSS,XLOO,XL1,XL2,O1D,XL3,XL4,XL5,XL6,XL7,RGLOW,TINF,
     3TZERO,XNO(4),HTION(100),EHY(100),YOE,ENE(100),Y1F,DELS,OI(100),
     4HEI(100),HYI(100),OOI(100),XNOI(100),BETA,ALT(100),Q(100),Q1,
     4XN(6),TLOWL,THI,C4,STSZ,IPT,MQX,IQSWT,MX,LKIM,
     6N,NN,INDX,INDXX,JF
      SQTE=DSQRT(QQL)
      IF(QQL-2000.) 20,21,21
   21 XLO=2.53E-6*SQTE*DEXP(-17620./QQL)
      GO TO 26
   20 IF(QQL-1000.) 22,23,23
```

```
   22 XLO=5.7154E-8*DEXP(-3352.6/QQL)
      GO TO 26
   23 XLO=2.0E-7*DEXP(-4605.2/QQL)
   26 XLOO=XLO*(1.-DEXP(3200.*(1./QQL-1./TN)))
      XL1=(XLOO+(7.6E-16*QQL+2.E-10/SQTE)*(QQL-TN))*1.3E-4*XN(5)*XN(1)
      XL2=1.3E-4*XN(5)*XN(2)*(4.E-14*QQL-8.E-12)*(QQL-TN)
      O1D=1.07E-10*XN(5)*XN(3)*SQTE*DEXP(-2.27E4/QQL)*(.406+.357E-4*
     1QQL-DEXP(-1.37E4/QQL)*(.333+.183E-4*QQL)-DEXP(-2.97E4/QQL)*(.456
     2+.174E-4*QQL))
      RGLOW=O1D/(1.96*(1.32+4.338E-9*XN(1)))
      XL3=3.74E-18*XN(5)*XN(3)*SQTE*(QQL-TN)+O1D
      XL4=2.46E-17*XN(5)*XN(4)*SQTE*(QQL-TN)
      XL5=((QQL-TII(QQL))*XN(5)/(QQL*SQTE))*(4.8E-7*XION(1)+1.9E-6*
     1XION(2)+7.7E-6*XION(3)+2.566E-7*XION(4)+2.406E-7*XION(5))
      IF(QQL.GE.7400.) GO TO 24
      XL7=9.63E-16*XN(5)*XN(6)*(1.-1.35E-4*QQL)*SQTE*(QQL-TN)
      GO TO 25
   24 XL7=0.
   25 CONTINUE
      EXDN=(8.63E-5)*TN
      EXDE=(8.63E-5)*QQL
      A10=((4.7E-21)*QQL+6.82E-17)*.02*(8.63E-5*QQL*DEXP(-.02/EXDE
     1)-EXDE*DEXP(-.02/EXDN))
      B10=((2.3E-21)*QQL+1.16E-17)*.028*(EXDE*DEXP(-.028/EXDE)-EXDE*
     1DEXP(-.028/EXDN))
      C10=((3.E-21)*QQL+2.2E-17)*.008*(EXDE*DEXP(-.008/EXDE)-EXDE*
     1DEXP(-.008/EXDN))*DEXP(-.02/EXDN)
      XL6=(3.E10*XN(5)*XN(3)/(SQTE*(5.+3.*DEXP(-.02/EXDN)+DEXP(-.028/
     1EXDN))))*(A10+B10+C10)
      XLOS=XL1+XL2+XL3+XL4+XL5+XL6+XL7
      XLOSS=SOURC(C4)-XLOS
      RETURN
      END
      SUBROUTINE ATMMOD(QQM)
C        THIS SUBROUTINE GIVES A MODEL ATMOSHERE
      IMPLICIT REAL*8(A-H,O-Z),INTEGER(I-N)
      DIMENSION ALPHA(4),GAMMA(4)
      COMMON G,HE(100),C1,C2,Y(100),YLAST(100),TOPHE,T1,DELTA,Y11,
     1RG(100),YY(100),DELTY,Y1,Y0,PRMT(5),YX(2),YYX(2),AUX(8,2),XION(5),
     2XLN,TN,XLOSS,XLOO,XL1,XL2,O1D,XL3,XL4,XL5,XL6,XL7,RGLOW,TINF,
     3TZERO,XNO(4),HTION(100),EHY(100),YOE,ENE(100),Y1E,DELS,OI(100),
     4HEI(100),HYI(100),OOI(100),XNOI(100),BETA,ALT(100),Q(100),Q1,
     4XN(6),TLOWL,THI,C4,STSZ,IPT,MQX,IQSWT,MX,LKIM,
     6N,NN,INDX,INDXX,JF
      DATA ALPHA/3*0.,-.4/
      CA1=120.E5
      CA2=6476.77
      CA3=6356.77E5
      XPSI=(QQM-CA1)*CA2/(CA3+QQM)
      IF(G) 10,11,10
   11 W2=(TINF-800.)
      EX=W2/(750.+1.722E-4*W2*W2)
      ES=.0291*DEXP(-EX*EX/2.)+.00015
      G=ES*(TINF-TZERO)
   10 SIGMA=G/(TINF-TZERO)
      T2=-SIGMA*XPSI
      A=(TINF-TZERO)/TINF
      TN=TINF*(1.-A*DEXP(T2))
      T1=(1.-A)*TINF/TN
      W1=1.14/(SIGMA*TINF)
```

```
      GAMMA(1)=W1*28.
      GAMMA(2)=W1*32.
      GAMMA(3)=W1*16.
      GAMMA(4)=W1*4.
      DO 12 II=1,4
   12 XN(II)=XNO(II)*T1**(1.+ALPHA(II)+GAMMA(II))*DEXP(T2*GAMMA(II))
      DO 15 LKI=1,LKIM
      IF(QQM.GE.HTION(LKI).AND.QQM.LE.HTION(LKI+1)) GO TO 16
   15 CONTINUE
   16 XN(6)=EHY(LKI)+(EHY(LKI+1)-EHY(LKI))/(HTION(LKI+1)-HTION(LKI))
     1*(QQM-HTION(LKI))
      RETURN
      END
      SUBROUTINE EION(QMM)
C       THIS SUBROUTINE GIVES A MODEL IONOSPHERE ELECTRONS
C       AND IONS
      IMPLICIT REAL*8(A-H,O-Z),INTEGER(I-N)
      COMMON G,HE(100),C1,C2,Y(100),YLAST(100),TOPHF,TL,DELTA,Y11,
     1RG(100),YY(100),DELTY,Y1,Y0,PRMT(5),YX(2),YYX(2),AUX(8,2),XION(5),
     2XLN,TN,XLOSS,XLOO,XL1,XL2,O1D,XL3,XL4,XL5,XL6,XL7,RGLOW,TINF,
     3TZERO,XNO(4),HTION(100),EHY(100),YOE,ENE(100),Y1E,DELS,OI(100),
     4HEI(100),HYI(100),OOI(100),XNOI(100),BETA,ALT(100),Q(100),Q1,
     4XN(6),TLOWL,THI,C4,STSZ,IPT,MQX,IQSWT,MX,LKIM,
     6N,NN,INDX,INDXX,JF
      IF(QMM.GE.YOE) GO TO 30
      H2=(HE(2)-HE(1))/DLOG(ENE(2)/ENE(1))
      XN(5)=ENE(1)*DEXP((QMM-HE(1))/H2)
      GO TO 31
   30 IF(QMM-Y1E) 32,33,34
   33 XN(5)=ENE(MX)
      GO TO 31
   34 H1=6.1E3*BETA*TINF
      XN(5)=ENE(MX)*DEXP((HE(MX)-QMM)/H1)
      GO TO 31
   32 JJ=(QMM-YOE)/DELS+1.0001
      XN(5)=ENE(JJ)+(ENE(JJ+1)-ENE(JJ))/(HE(JJ+1)-HE(JJ))*(QMM-HE(JJ))
   31 CONTINUE
      DO 35 IF=1,MX
      IF(QMM.GE.HTION(IF).AND.QMM.LE.HTION(IF+1)) GO TO 36
   35 CONTINUE
   36 XION(1)=(OI(IF)+(OI(IF+1)-OI(IF))/(HTION(IF+1)-HTION(IF))*
     1(QMM-HTION(IF)))*XN(5)
      XION(2)=(HEI(IF)+(HEI(IF+1)-HEI(IF))/(HTION(IF+1)-HTION(IF))
     1*(QMM-HTION(IF)))*XN(5)
      XION(3)=(HYI(IF)+(HYI(IF+1)-HYI(IF))/(HTION(IF+1)-HTION(IF))*
     1(QMM-HTION(IF)))*XN(5)
      XION(4)=(OOI(IF)+(OOI(IF+1)-OOI(IF))/(HTION(IF+1)-HTION(IF))
     1*(QMM-HTION(IF)))*XN(5)
      XION(5)=(XNOI(IF)+(XNOI(IF+1)-XNOI(IF))/(HTION(IF+1)-HTION(IF))*
     1(QMM-HTION(IF)))*XN(5)
      RETURN
      END
      REAL FUNCTION SOURC*8(QQS)
C       THIS SUBROUTINE GIVES THE LOCAL HEAT INPUT TO THE ELECTRON
C       GAS
      IMPLICIT REAL*8(A-H,O-Z),INTEGER(I-N)
      COMMON G,HE(100),C1,C2,Y(100),YLAST(100),TOPHF,TL,DELTA,Y11,
     1RG(100),YY(100),DELTY,Y1,Y0,PRMT(5),YX(2),YYX(2),AUX(8,2),XION(5),
     2XLN,TN,XLOSS,XLOO,XL1,XL2,O1D,XL3,XL4,XL5,XL6,XL7,RGLOW,TINF,
     3TZERO,XNO(4),HTION(100),EHY(100),YOE,ENE(100),Y1E,DELS,OI(100),
```

```
     4HEI(100),HYI(100),OOI(100),XNOI(100),BETA,ALT(100),Q(100),Q1,
     4XN(6),TLOWL,THI,C4,STSZ,IPT,MQX,IQSWT,MX,LKIM,
     6N,NN,INDX,INDXX,JF
      IF(IQSWT.EQ.0) GO TO 45
      IF(QQS-ALT(1)) 46,47,48
   46 H2S=(ALT(2)-ALT(1))/DLOG(Q(2)/Q(1))
      SOURC=Q(1)*DEXP((QQS-ALT(1))/H2S)
      GO TO 50
   45 SOURC=0.
      GO TO 50
   47 SOURC=Q(1)
      GO TO 50
   48 IF(QQS-ALT(MQX)) 49,51,52
   52 H1S=6.1E3*Q1
      SOURC=Q(MQX)*DEXP((ALT(MQX)-QQS)/H1S)
      GO TO 50
   51 SOURC=Q(MQX)
      GO TO 50
   49 CONTINUE
      DO 53 IW=1,MQX
      IF(QQS.GE.ALT(IW).AND.QQS.LE.ALT(IW+1)) GO TO 54
   53 CONTINUE
   54 SSS=(Q(IW+1)-Q(IW))/(ALT(IW+1)-ALT(IW))
      SOURC=Q(IW)+SSS*(QQS-ALT(IW))
   50 RETURN
      END
      REAL FUNCTION SIMPS*8(N11)
C       THIS FUNCTION INTEGRATES THE 6300 A VOLUME EMISSION RATE
C       WITH RESPECT TO HEIGHT
      IMPLICIT REAL*8(A-H,O-Z),INTEGER(I-N)
      COMMON G,HE(100),C1,C2,Y(100),YLAST(100),TOPHE,TL,DELTA,Y11,
     1RG(100),YY(100),DELTY,Y1,Y0,PRMT(5),YX(2),YYX(2),AUX(8,2),XION(5),
     2XLN,TN,XLOSS,XL00,XL1,XL2,O1D,XL3,XL4,XL5,XL6,XL7,RGLOW,TINF,
     3TZERO,XNO(4),HTION(100),EHY(100),YOE,ENE(100),Y1E,DELS,OI(100),
     4HEI(100),HYI(100),OOI(100),XNOI(100),BETA,ALT(100),Q(100),Q1,
     4XN(6),TLOWL,THI,C4,STSZ,IPT,MQX,IQSWT,MX,LKIM,
     6N,NN,INDX,INDXX,JF
      SUM=0.
      DO 60 IW=1,N11
   60 SUM=SUM+((RG(IW+1)+RG(IW))/2.)*DELTA
      SIMPS=SUM
      RETURN
      END
      SUBROUTINE RUNGE(TPL,TOPH)
C       THIS SUBROUTINE SETS UP THE RUNGE-KUTTA SOLUTION
      IMPLICIT REAL*8(A-H,O-Z),INTEGER(I-N)
      COMMON G,HE(100),C1,C2,Y(100),YLAST(100),TOPHE,TL,DELTA,Y11,
     1RG(100),YY(100),DELTY,Y1,Y0,PRMT(5),YX(2),YYX(2),AUX(8,2),XION(5),
     2XLN,TN,XLOSS,XL00,XL1,XL2,O1D,XL3,XL4,XL5,XL6,XL7,RGLOW,TINF,
     3TZERO,XNO(4),HTION(100),EHY(100),YOE,ENE(100),Y1E,DELS,OI(100),
     4HEI(100),HYI(100),OOI(100),XNOI(100),BETA,ALT(100),Q(100),Q1,
     4XN(6),TLOWL,THI,C4,STSZ,IPT,MQX,IQSWT,MX,LKIM,
     6N,NN,INDX,INDXX,JF
      EXTERNAL FCT
      EXTERNAL OUTP
      PRMT(1)=Y1
      PRMT(2)=Y0
      PRMT(3)=DELTY/STSZ
      PRMT(4)=1.
      NDIM=2
```

```
      YX(1)=TPI
      YX(2)=TOPH
      YYX(1)=0.
      YYX(2)=0.
      INDX=0
      INDXX=0
      JF=0
      CALL DRKGS(PRMT,YX,YYX,NDIM,IHLF,FCT,OUTP,AUX)
      RETURN
      END
      SUBROUTINE FCT(X,X17,X18)
C       THIS FUNCTION CALCULATES TERMS IN THE DIFFERENTIAL
C       EQUATIONS
      IMPLICIT REAL*8(A-H,O-Z),INTEGER(I-N)
      DIMENSION X17(2),X18(2)
      COMMON G,HE(100),C1,C2,Y(100),YLAST(100),TOPHF,TL,DELTA,Y11,
     1RG(100),YY(100),DELTY,Y1,YO,PRMT(5),YX(2),YYX(2),AUX(8,2),XION(5),
     2XLN,TN,XLOSS,XLOO,XL1,XL2,O1D,XL3,XL4,XL5,XL6,XL7,RGLOW,TINF,
     3TZERO,XNO(4),HTION(100),EHY(100),YOE,ENE(100),Y1E,DELS,OI(100),
     4HEI(100),HYI(100),OOI(100),XNOI(100),BETA,ALT(100),O(100),O1,
     4XN(6),TLOWL,THI,C4,STSZ,IPT,MQX,IQSWT,MX,LKIM,
     6N,NN,INDX,INDXX,JF
      IF(X17(1).LE.TLOWL) GO TO 666
      IF(X17(1).GE.THI) GO TO 667
      GO TO 668
  666 IPT=1
      CALL FUDGEL
      GO TO 668
  667 IPT=2
      CALL FUDGEH
  668 CONTINUE
      CALL ATMMOD(X)
      CALL EION(X)
      C4=X
      TVE=X17(1)**C1
      CNDT=COND(TVE)
      X18(1)=X17(2)/CNDT
      CALL LOSS(TVE)
      X18(2)=-XLOSS
      IPT=3
      RETURN
      END
      SUBROUTINE OUTP(Z,ZW,ZZW,IHLF,NDIN,PRM)
C      THIS IS THE OUTPUT SUBROUTINE FOR THE RUNGE-KUTTA SYSTEM
      IMPLICIT REAL*8(A-H,O-Z),INTEGER(I-N)
      DIMENSION ZW(2),ZZW(2),PRM(5)
      COMMON G,HE(100),C1,C2,Y(100),YLAST(100),TOPHF,TL,DELTA,Y11,
     1RG(100),YY(100),DELTY,Y1,YO,PRMT(5),YX(2),YYX(2),AUX(8,2),XION(5),
     2XLN,TN,XLOSS,XLOO,XL1,XL2,O1D,XL3,XL4,XL5,XL6,XL7,RGLOW,TINF,
     3TZERO,XNO(4),HTION(100),EHY(100),YOE,ENE(100),Y1E,DELS,OI(100),
     4HEI(100),HYI(100),OOI(100),XNOI(100),BETA,ALT(100),Q(100),Q1,
     5XN(6),TLOWL,THI,C4,STSZ,IPT,MQX,IQSWT,MX,LKIM,
     6N,NN,INDX,INDXX,JF
      MF=STSZ+.00001
      INDXX=INDXX+1
      III=INDXX-1
      IPAR=III-JF*MF
      IF(IPAR.EQ.0) GO TO 28
      GO TO 29
   28 INDX=INDX+1
```

```
      Y(INDX)=ZW(1)
      YY(INDX)=ZW(2)
      JE=JE+1
   29 CONTINUE
      PRMT(5)=0.
      PRM(5)=PRMT(5)
      IPT=3
      RETURN
      END
END OF FILE
```

Appendix B

SAR-ARCS FOR VARIOUS IONOSPHERIC AND ATMOSPHERIC MODELS

The electron heat conduction equation was solved for each of the three cases described in Chapter 4 and the results are presented in this Appendix. These results are also compared to those of case (1) presented in Chapter 4.

B-1 Case (2)

In this case the analytic model atmosphere, described in Appendix A, having an exospheric temperature of 1061°K is used to represent the neutral atmosphere and the basic model ionosphere, described in Chapter 4 and shown in Fig. 5, is used to represent the ionospheric conditions within the SAR-arc. This case is examined for a two-fold purpose: (a) to compare the results obtained here with the results given by Walker and Rees (1968) and, (b) to study a SAR-arc with a low exospheric temperature which is typical of solar cycle minimum conditions. The effect of a lower exospheric temperature is to cause a reduced neutral gas scale height and thus a general lowering of the neutral atmosphere.

The electron temperature profiles obtained from a solution of the electron heat conduction equation, assuming various heat flows into the ionosphere, are presented in Fig. 61. The electron temperature profiles are similar to those in case (1), presented in Chapter 4, however, there are a few notable differences. In this case, the bulk of the atomic oxygen is present at lower altitudes, because of the reduced neutral gas scale height, and therefore, a high electron temperature is necessary at lower altitudes in order to excite the SAR-arc. In general, the whole topside ionosphere has a much higher electron temperature reflecting the reduced electron-neutral collision frequency at high levels. For example, at 400 km the electron temperature in case (2) is almost 1000°K greater than the electron temperature calculated for case (1). The electron temperature gradient in the topside ionosphere, down to a height of 400 km, is

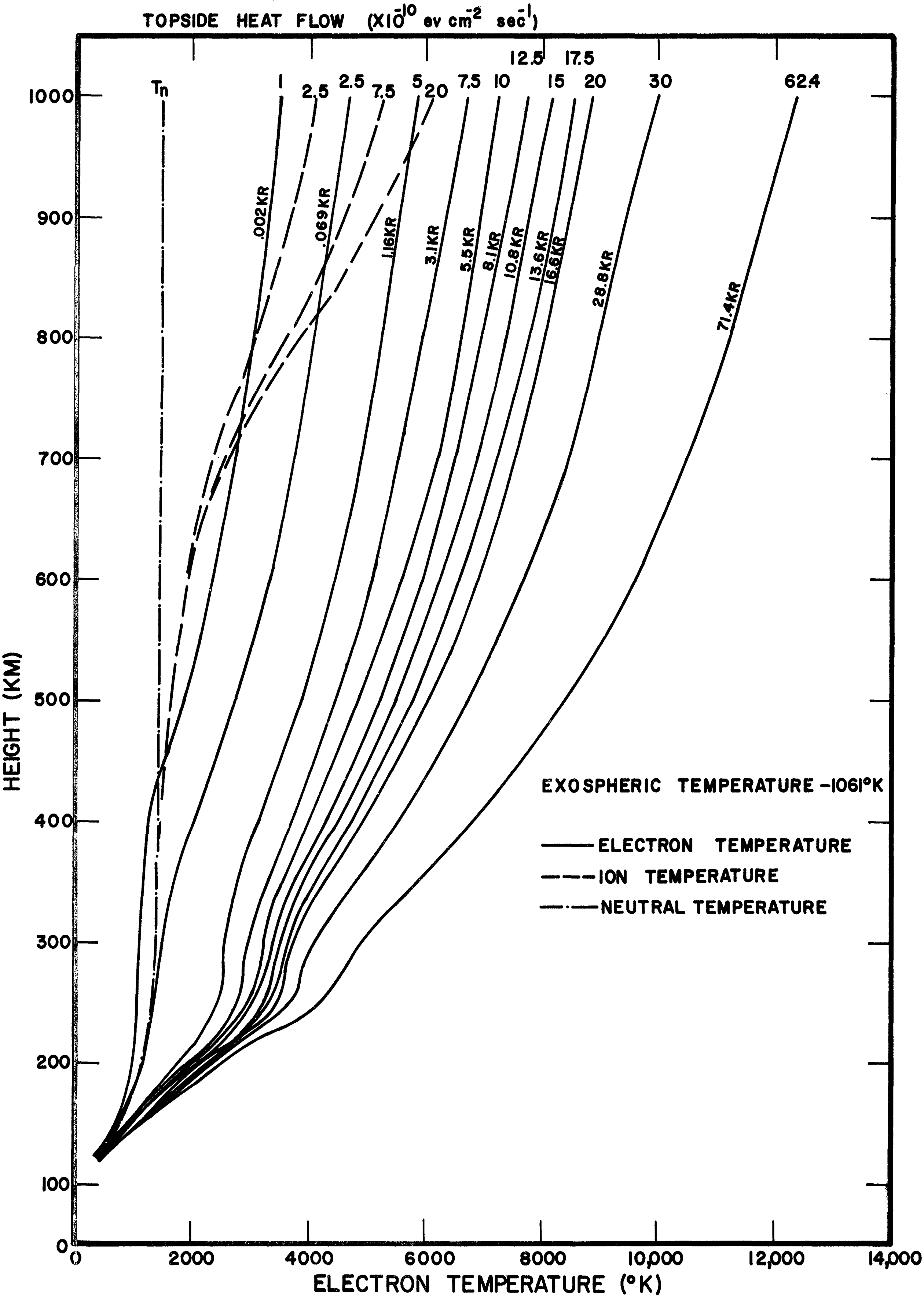

Fig. 61. Electron and ion temperature height profiles for SAR-arcs corresponding to case (2) conditions.

considerably less in case (2) however, below 400 km, the gradient becomes much steeper because of the rapidly increasing electron-neutral particle collision frequency in the lower atmosphere. These results also indicate that, for an equivalent topside heat flow rate, the SAR-arc intensity is lower than it is in case (1). The ion temperature profiles for this case are also shown in Fig. 61 and they are seen to be almost identical to those given in Chapter 4 for case (1) conditions. The 6300 Å volume emission rate profile is shown in Fig. 62. Because of the low exospheric temperature, resulting in a reduced neutral gas scale height, the peak volume emission rate occurs lower, 380 km, as compared to the 480 km peak existing in case (1). In addition, the shape of the intensity profile is sharper, decreasing more rapidly with height than in case (1) and reflecting the atomic oxygen re-distribution to lower altitudes. The peak of the 6300 Å volume emission rate is seen to progress to lower altitudes as the SAR-arc intensity increases, however beyond an intensity of about 2 KR the peak height remains nearly constant. Fig. 63 shows the neutral heating due to energy transfer from the electron and ion gas to the neutrals within the SAR-arc. The maximum neutral heating is seen to occur at a lower altitude than the peak volume emission rate. The maximum neutral heating occurs at high altitudes for the faint SAR-arcs, and it progresses downward as the arc intensity increases however, beyond an arc intensity of 2 KR the height remains constant and the relative shape of the height profiles are similar.

B-2 Case (3)

In this case, the basic electron density profile used in the two previous cases is increased by a factor of three at all altitudes in order to determine the influence of electron density on the excitation rate of the arc. The exospheric temperature, in this case, is 1500°K and these conditions may be considered to approximate the atmospheric conditions for a daytime SAR-arc. Fig. 64 shows the electron temperature profiles for the same range of topside heat flow

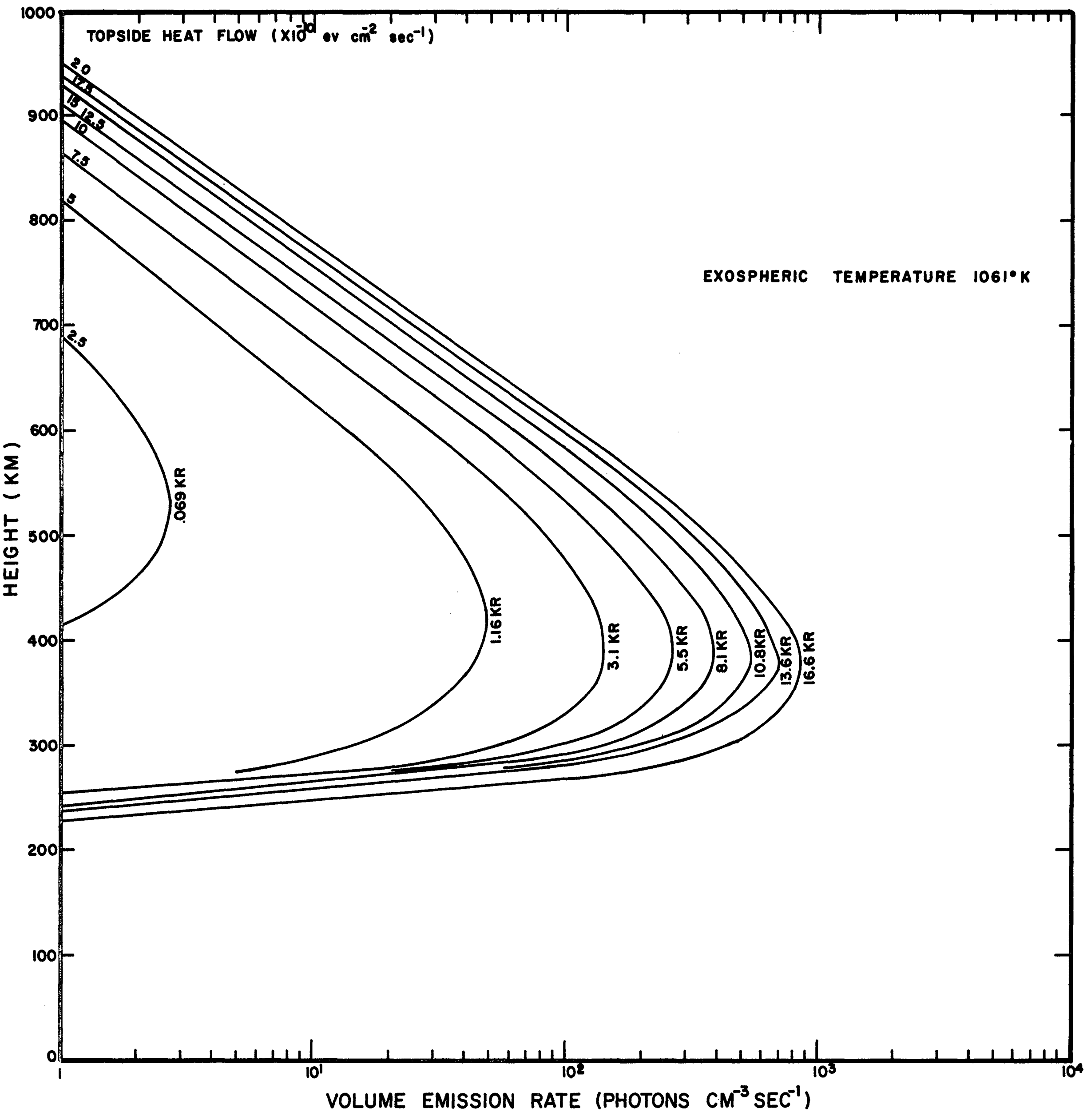

Fig. 62. 6300Å volume emission rate height profiles for SAR-arcs corresponding to case (2) conditions.

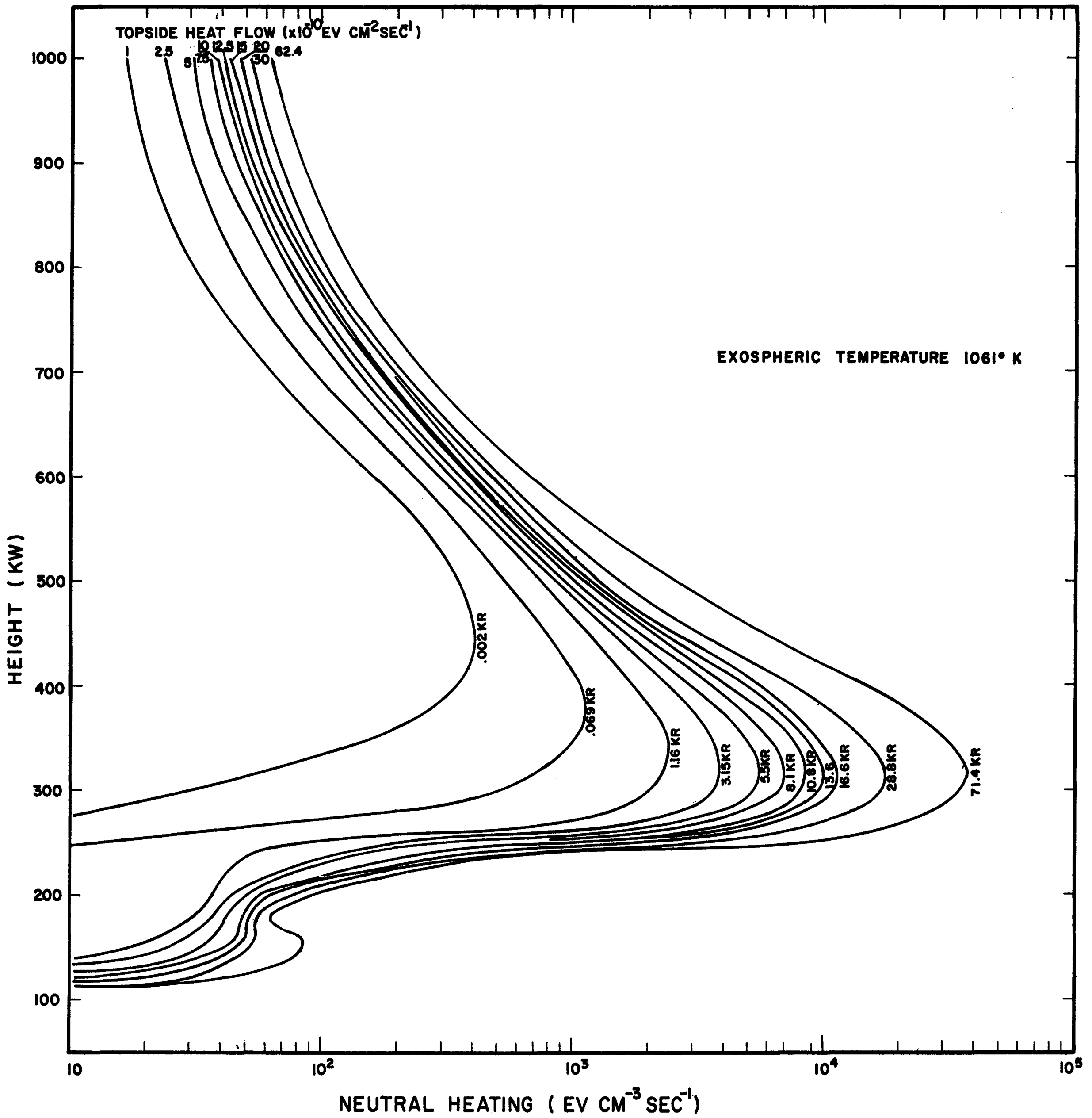

Fig. 63. Neutral heating rate height profiles for SAR-arcs corresponding to case (2) conditions.

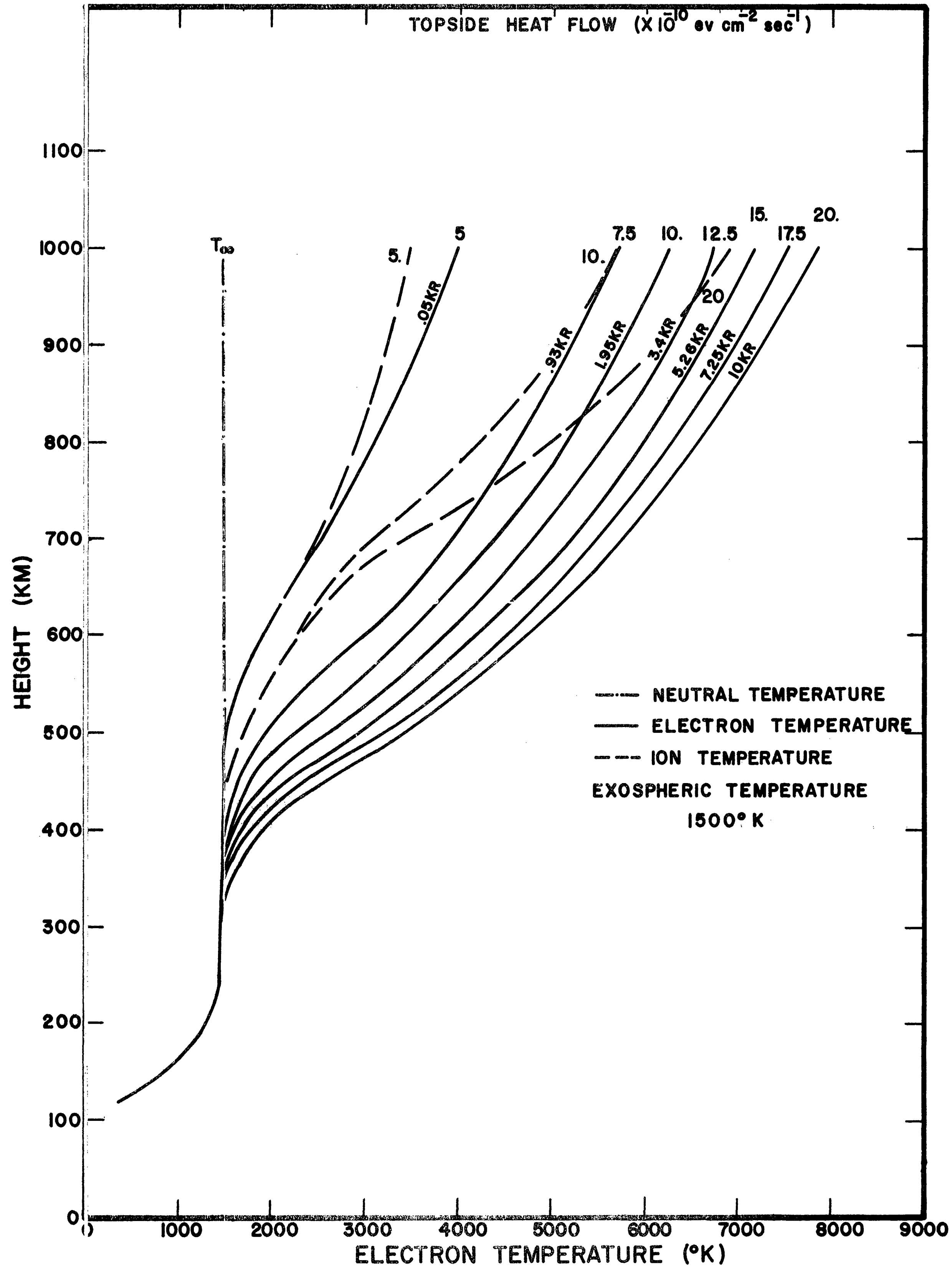

Fig. 64. Electron and ion temperature height profiles for SAR-arcs corresponding to case (3) conditions.

inputs as is used in the two previous cases. It is seen from these figures that the heat flow required from the magnetosphere to excite a SAR-arc to a given intensity is much greater than for the previous two cases. Also, because of the high electron densities, the electron temperature will significantly depart from the neutral gas temperature only in the upper regions. At lower altitudes, the high ion-neutral and electron-neutral collision frequency effectively cools the electron gas and it is seen to approach the neutral gas temperature at a much higher altitude than in the previous two cases. However, the ambient topside electrons are still sufficiently hot and the atomic oxygen number density is also sufficiently great to excite the 6300 Å emission line and give rise to a high altitude SAR-arc. Because of the reduced atomic oxygen number density at high altitudes, the electron temperature in the topside F-region must be considerably greater in order to increase the electron-atomic oxygen collision frequency and effectively excite the available atomic oxygen species to the ^1D state. These calculations show that if higher electron densities are present, more heat flow from the magnetosphere is needed to excite a given arc. The 6300 Å volume emission rate height profile presented in Fig. 65, shows that the peak occurs at a much higher altitude than for the previous two cases, near 600 km, and generally decreases in altitude for the brighter arcs. The neutral heating profiles are shown in Fig. 66. It is seen that because the arc is excited high in the ionosphere the peak value of the neutral heating also occurs relatively high, near 480 km, and has a broad profile indicating an electron energy transfer to the neutral gas occurring over a large altitude region, different from the previous two cases.

B-3 Case (4)

In this case the electron density profile is adjusted to have a topside scale height three times less than the normal profile but yet has the same integrated column density as the profiles used in cases (1) and (2). The resulting electron

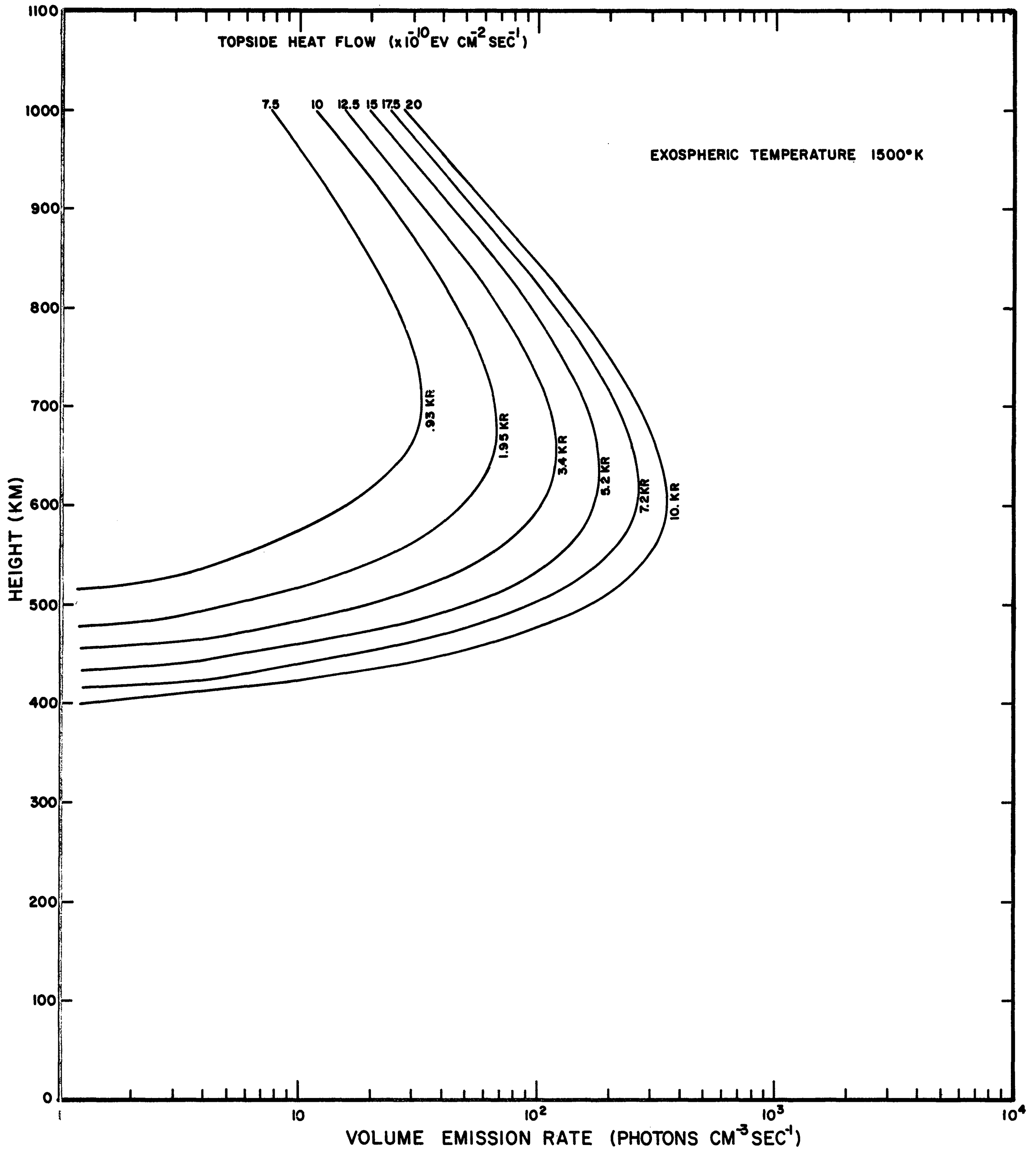

Fig. 65. 6300 Å volume emission rate height profiles for SAR-arcs corresponding to case (3) conditions.

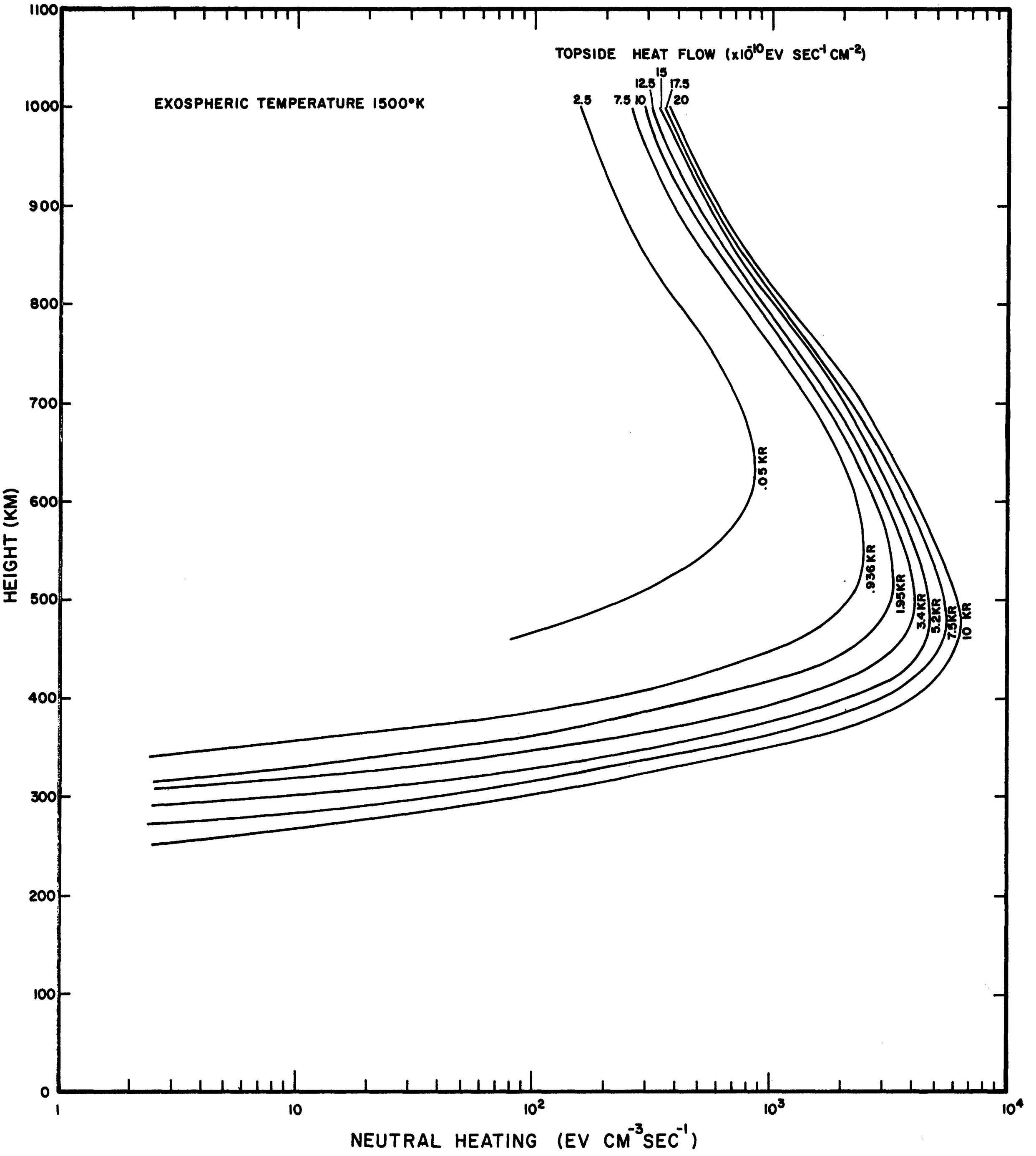

Fig. 66. Neutral heating rate height profiles for SAR-arcs corresponding to case (3) conditions.

density profile is shown in Fig. 5. The electron heat conduction equation is then solved for the same heat flow rates into the ionosphere at 1000 km and the electron temperature profiles are shown in Fig. 67. In comparing these profiles to those of case (2), presented in Chapter 4, the electron temperature profiles are almost identical over most of the upper regions, however at 400 km the electron temperature for case (1) conditions is nearly 300°K greater than the electron temperature in this case. It should be noted that even though the electron density near 400 km, in case (4), is greater by a factor of 2, the increased electron temperature is more effective in increasing the arc intensity, resulting in a brighter arc for equivalent heat flows into the ionosphere. Again the sharp break in the curves of electron temperature is noted in the 200-300 km height range which is due to the changing electron thermal conductivity with respect to height. The volume emission rate for the 6300 Å radiation in this arc is shown in Fig. 68. Compared to the volume emission rate in case (1), it is sharper and has a higher peak value occurring at approximately the same height as in case (1). However, even though the peak value is greater, the integrated emission rate is lower because most of the emission occurs near the peak whereas in case (1) the broader vertical extent of the emission profile gives rise to a higher integrated value. The neutral heating for this arc is shown in Fig. 69. Again, when comparing the results of this arc with those of case (1), a larger peak neutral heating value occurs at a higher altitude, 400 km where the electron density peaks, compared to 360 km in case (1), but the profile is much sharper over the same height interval. Thus, the sharp peak in electron density causes a much more localized region of neutral heating within the SAR-arc.

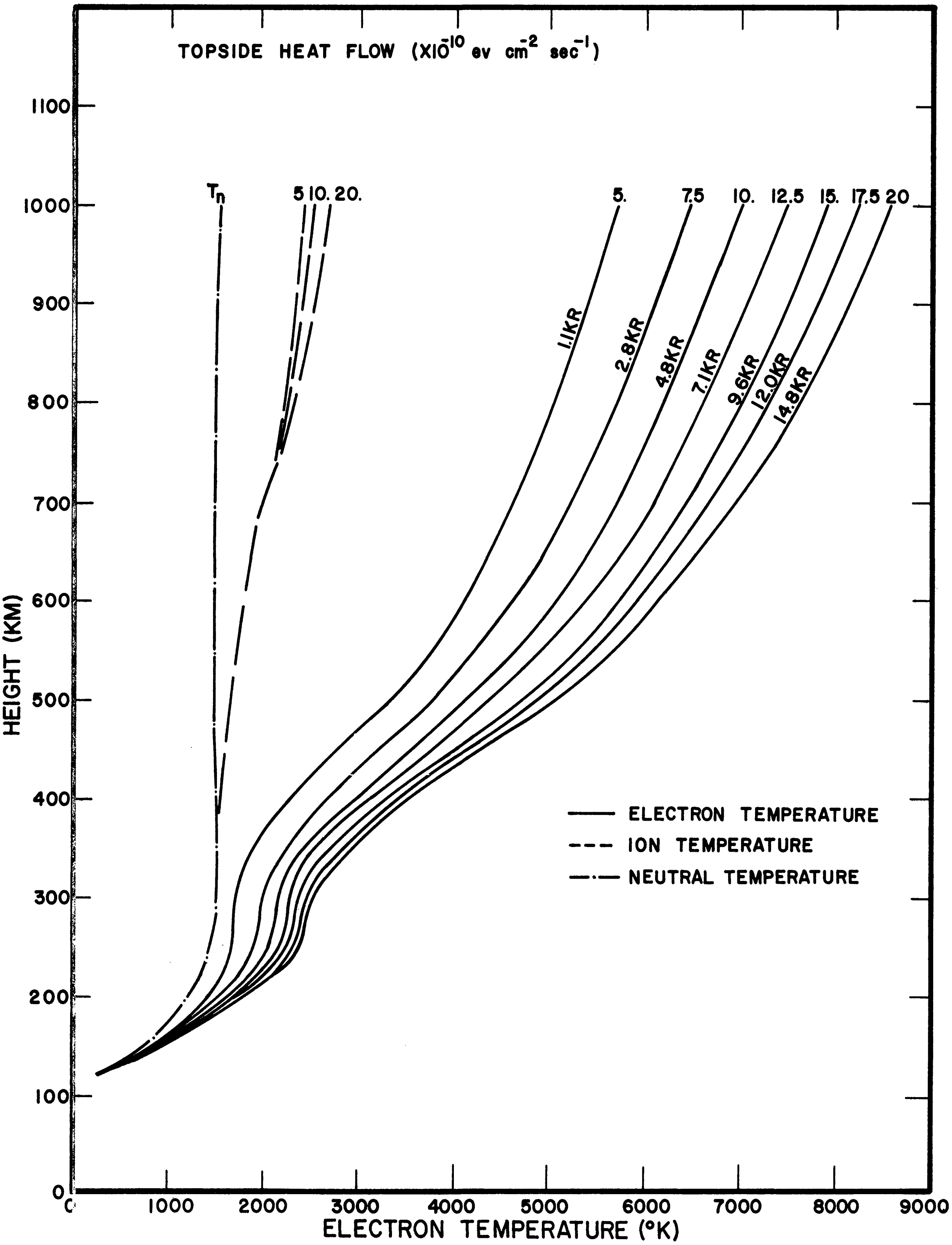

Fig. 67. Electron and ion temperature height profiles for SAR-arcs corresponding to case (4) conditions.

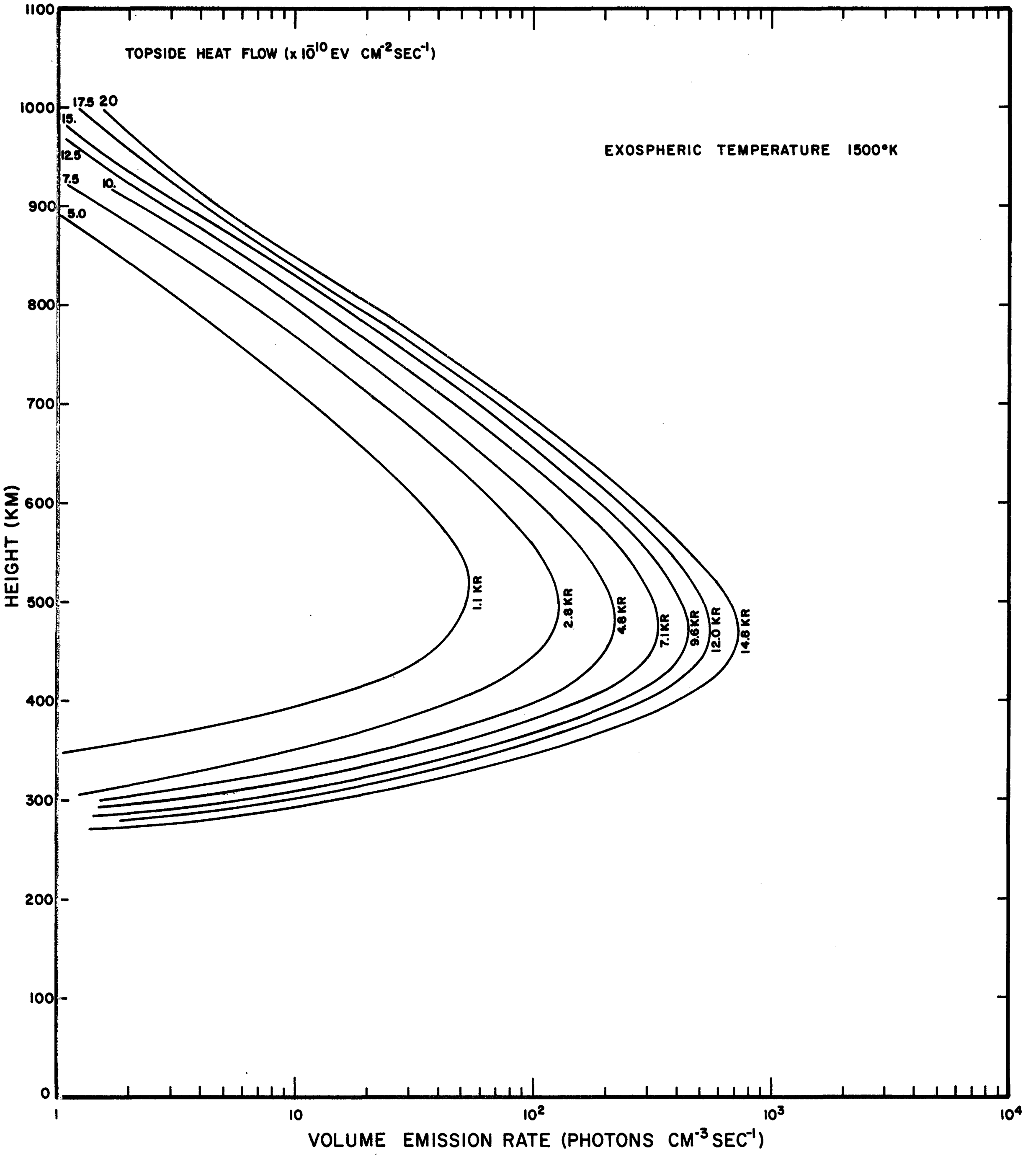

Fig. 68. 6300Å volume emission rate height profiles for SAR-arcs corresponding to case (4) conditions.

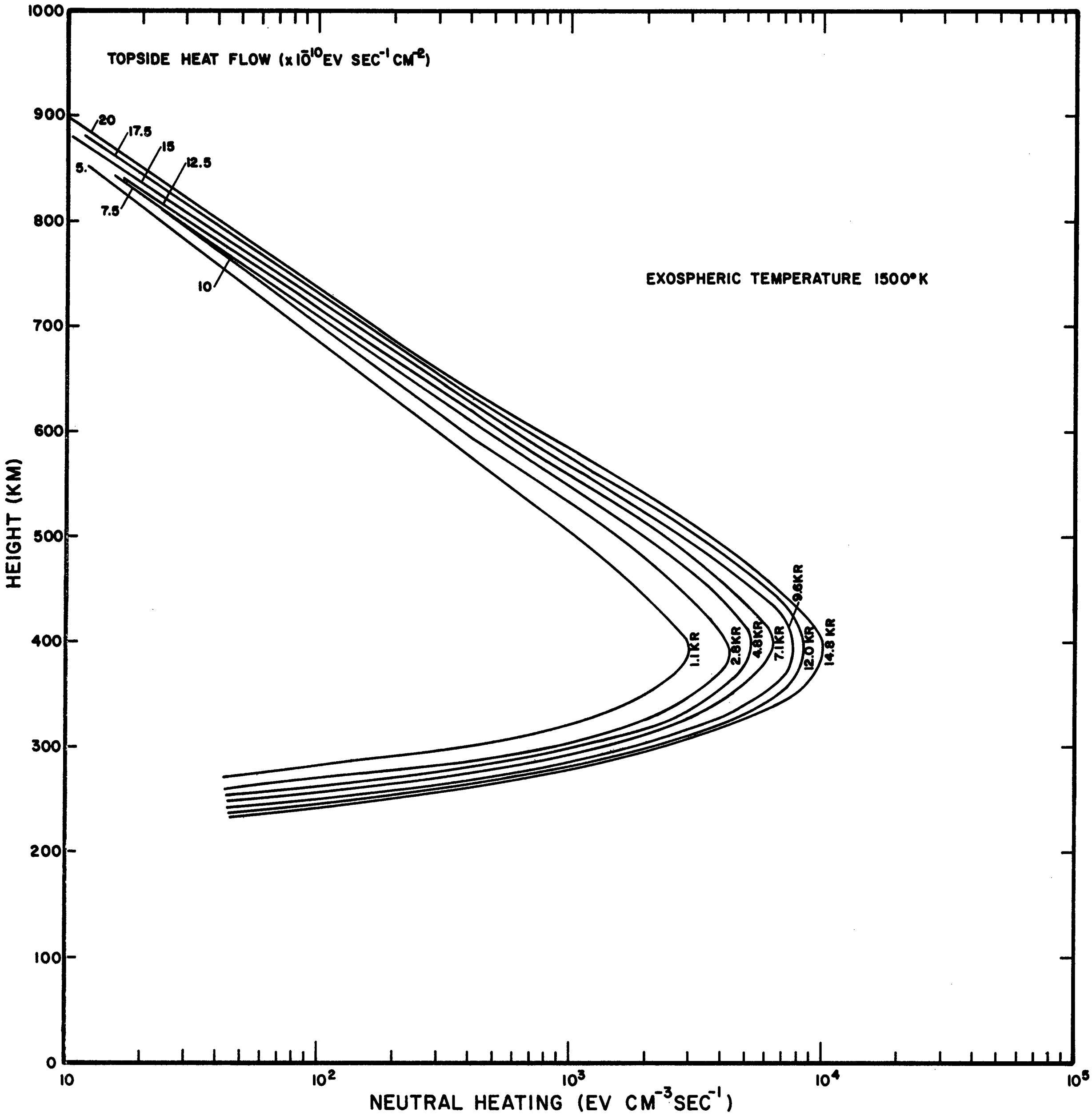

Fig. 69. Neutral heating rate height profiles for SAR-arcs corresponding to case (4) conditions.

Appendix C
SOLUTION TO THE STEADY STATE TWO-DIMENSIONAL NEUTRAL HEAT CONDUCTION EQUATION

The steady state two-dimensional neutral heat conduction equation for neutral heating within the SAR-arc was formulated in Chapter 5 as the following boundary value problem,

$$\nabla^2 \varphi(y,z) = -\frac{3}{2k} Q(y,z) \tag{5-18}$$

with boundary conditions

$$\begin{aligned} \varphi &= 0 && \text{at} && z = z_0 \\ \frac{\partial \varphi}{\partial z} &= 0 && \text{as} && z \rightarrow \infty \\ \frac{\partial \varphi}{\partial y} &= 0 && \text{as} && y \rightarrow \pm\infty \end{aligned} \tag{5-19}$$

The boundary conditions indicate that no heat flows out of the top of the atmosphere and that eventually a lateral boundary is encountered at both the northern and southern extremities of the arc where no lateral heat flow occurs. In addition, the neutral gas temperature at the lower boundary, z_o, is held constant.

The neutral heating contours for the two-dimensional model of the SAR-arc are shown in Fig. 14 and they are seen to closely approximate ellipses. The neutral heating height profile at any given meridional distance can be closely approximated by two Gaussian functions: one large Gaussian curve is used to approximate the region near the peak value and a smaller Gaussian is used for the tail at high altitudes. Therefore, the vertical profile of the neutral heating function is analytically represented as

$$\overline{H}^*(z) = H_{M_1} \mathrm{EXP}\left[-\frac{(z-z_{01})^2}{\delta_1^2}\right] + H_{M_2} \mathrm{EXP}\left[-\frac{(z-z_{02})^2}{\delta_2^2}\right] \tag{C-1}$$

where H_M is the peak value of the Gaussian, z is the altitude, z_o is the height to which the Gaussian profile is referenced, and δ represents the e-folding distance of the vertical profile. Because the two-dimensional neutral heating contours are ellipses, the horizontal distribution is equal to the vertical distribution multiplied by the appropriate ratio of the semi-major to semi-minor axis. The analysis proceeds by considering only the one large Gaussian curve for simplicity, however, in the final answer both Gaussian curves must be included by appropriate superposition. With this assumption, the problem can now be related to one in potential theory where the equation

$$\nabla^2 V = -4\pi\sigma(y,z) \tag{C-2}$$

is solved for V, the potential, due to a charge distribution, σ, by considering it as an ellipsoidal level layer, (c.f. MacMillan, 1958). It was shown that the SAR-arc is a tube extending around the earth at mid-latitudes and therefore the neutral heating contours can be represented by an infinite elliptical cylinder with a Gaussian weighting function and a constant cross section extending in an east-west, or x, direction. The potential function for the infinite homogeneous elliptic cylinder and, in particular, the infinite homogeneous ellipsoidal level layer can be modified and adapted to become the solution of the two-dimensional neutral heat conduction equation in the upper atmosphere. Because the temperature at the lower boundary, 120 km, is unperturbed and remains constant, an image infinite elliptical cylinder is used to satisfy the lower boundary condition. Acting as images, the two infinite elliptic cylinders appear as a dipole at distances far from the arc center. For the dipole, the "potential" and its derivatives approach zero with increasing distances and therefore satisfy the remaining boundary conditions. Fig. 70 gives a geometrical representation of the two elliptic cylinders and the hatched area represents an elliptic shell of neutral heating. If the contribution of each shell at the point P(y, z) is calculated and summed over all shells, the temperature at the point P(y, z) can be determined. Using only one Gaussian function, the vertical profile of the neutral heating is represented by

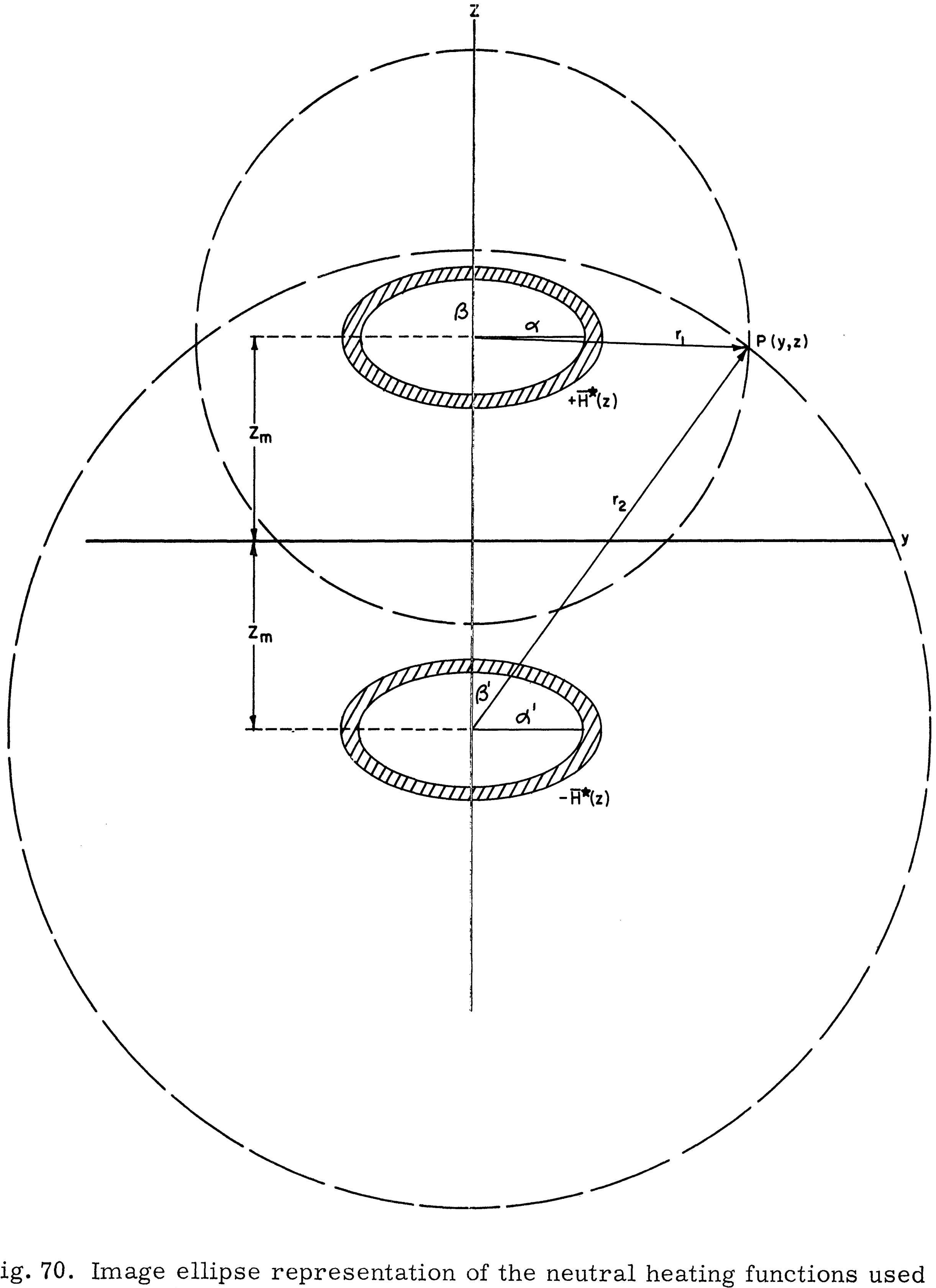

Fig. 70. Image ellipse representation of the neutral heating functions used for the solution to the two-dimensional neutral heat conduction equation.

$$\overline{H}^*(z) = H_M \, \mathrm{EXP}\left[-(z-z_M)^2/\delta^2\right] \tag{C-3}$$

The ellipses, shown in Fig. 14, satisfy the equation

$$\frac{y^2}{\alpha^2} + \frac{z^2}{\beta^2} = 1 \tag{C-4}$$

where α is the semi-major axis and β is the semi-minor axis. The semi-minor axis can be expressed as a function of z:

$$\beta = \delta\sqrt{\ln\left[\frac{H_M}{\overline{H}^*(z)}\right]} \tag{C-5}$$

Because the ellipses also have a similar shape, the ratio between the semi-major and semi-minor axes ($\epsilon = \alpha/\beta$) is considered a constant. Therefore, the analytic expression for the ellipse having a given heat value is

$$\frac{y^2}{\epsilon^2\delta^2 \ln\left[H_M/\overline{H}^*(z)\right]} + \frac{(z-z_M)^2}{\delta^2 \ln\left[H_M/\overline{H}^*(z)\right]} = 1 \tag{C-6}$$

The two-dimensional neutral gas heating function is now approximated by

$$H(y,z) = H_M \, \mathrm{EXP}\left[-\left(y^2/\epsilon^2 + (z-z_M)^2\right)/\delta^2\right] \tag{C-7}$$

The potential of an ellipsoidal level layer has been given by MacMillan (1958) as

$$V = 2\pi\sigma\alpha\beta\gamma\, d\lambda \int_{\kappa^*}^{\infty} \frac{ds}{\sqrt{(\alpha^2+s)(\beta^2+s)(\gamma^2+s)}} \tag{C-8}$$

where α, β, and γ are the axes of the ellipsoidal level layer, σ the charge, and λ a parameter specifying the outer axes of the incremental shell, i. e. $(1+\lambda)\alpha$, $(1+\lambda)\beta$, and $(1+\lambda)\gamma$. Because the shell is part of an elliptic cylinder, then $\gamma \to \infty$ and

$$V = 2\pi\sigma\alpha\beta\, d\lambda \int_{\kappa^*}^{\infty} \frac{ds}{\sqrt{(\alpha^2+s)(\beta^2+s)}} \tag{C-9}$$

where $K^* = K$ when the point for which the potential is calculated lies outside the elliptical shell and $K^* = 0$ when the point lies inside the shell. K is the root of the equation

$$\frac{y^2}{\alpha^2 + K} + \frac{(z - z_M)^2}{\beta^2 + K} = 1 \tag{C-10}$$

and for the case under consideration is

$$K = -\frac{1}{2}\left\{(\alpha^2+\beta^2) - \left[y^2+(z-z_M)^2\right]\right\} + \frac{1}{2}\sqrt{\left\{(\alpha^2+\beta^2) - \left[y^2+(z-z_M)^2\right]\right\}^2 - 4\left(\alpha^2\beta^2 - y^2\beta^2 - (z-z_M)^2\alpha^2\right)} \tag{C-11}$$

From the geometry of the problem $d\lambda$ can be expressed as

$$d\lambda = \frac{dz}{\beta} = \frac{dy}{\alpha} = \frac{\epsilon\, dz}{\alpha} \tag{C-12}$$

The solution to the boundary value problem stated in equation (5-18) for the heating function given by equation (c-7) is now written as

$$\Delta\phi = \frac{3}{4k} H(y,z) \left\{ \alpha\beta\, d\lambda \int_{K^*}^{\infty} \frac{ds}{\sqrt{(\alpha^2+s)(\beta^2+s)}} - \alpha'\beta'\, d\lambda' \int_{K'^*}^{\infty} \frac{ds}{\sqrt{(\alpha'^2+s)(\beta'^2+s)}} \right\} \tag{C-13}$$

It can be seen from figure 70 that

$$\alpha = \alpha' = \epsilon\,(z' - z_M)$$
$$\beta = \beta' = (z' - z_M)$$
$$d\lambda = d\lambda' = \frac{\epsilon\, dz'}{\alpha} = \frac{dz'}{\beta} = \frac{\epsilon\, dz'}{\alpha'} = \frac{dz'}{\beta'} \tag{C-14}$$

Also because $H(y, z)$ is a constant around the infinitesimally thin shell, it can be expressed in terms of the λ and λ' parameters as $H_m \exp\left[-(z'-z_m)^2/\delta^2\right]$, and equation (C-13) then becomes

$$\Delta \phi = \frac{3}{4k}\epsilon H_M (z'-z_M) EXP\left[-(z'-z_M)^2/\delta^2\right] \cdot dz' \int_{K^*}^{K'^*} \frac{ds}{\sqrt{\left[(z'-z_M)^2+s\right]\left[\epsilon^2(z'-z_M)^2+s\right]}} \qquad \text{(C-15)}$$

Integrating this equation, yields

$$\Delta \phi = \frac{3}{4k} H_M \epsilon (z'-z_M) EXP\left\{-(z'-z_M)^2/\delta^2\right\} dz'$$

$$\ln\left\{\left[2K'^* + (1+\epsilon^2)(z'-z_M)^2 + 2\left\{K'^{*2} + (1+\epsilon^2)(z'-z_M)^2 K'^* + \epsilon^2(z'-z_M)^4\right\}^{\frac{1}{2}}\right]\left[2K^* + (1+\epsilon^2)(z'-z_M)^2 + 2\left\{K^{*2} + (1+\epsilon^2)\cdot(z'-z_M)^2 K^* + \epsilon^2(z'-z_M)^4\right\}^{1/2}\right]^{-1}\right\} \qquad \text{(C-16)}$$

Integrating this expression again over all elliptical shells ϕ becomes .

$$\phi = \Big\{ \frac{3}{4k} H_M \epsilon \delta^2 \int_0^\infty x \, EXP(-x^2) \, \ln \Big\{ \Big[2\kappa'^{*} + (1+\epsilon^2)(\delta \cdot x)^2 + 2\big\{ \kappa'^{*2} + (1+\epsilon^2)(\delta \cdot x)^2 \kappa'^{*} + \epsilon^2 (\delta \cdot x)^4 \big\}^{1/2} \Big] \Big[2\kappa^{*} + (1+\epsilon^2)(\delta \cdot x)^2 + 2\big\{ \kappa^{*2} + (1+\epsilon^2)(\delta \cdot x)^2 \kappa^{*} + \epsilon^2 (\delta \cdot x)^4 \big\}^{1/2} \Big]^{-1} \Big\} \tag{C-17}$$

where $X = (z' - z_m)/\delta$ and

$\kappa^{*} = \kappa$ when $\kappa > 0$, otherwise $\kappa^{*} = 0$

$$\kappa = -\frac{1}{2} \Big\{ (1+\epsilon^2)(\delta x)^2 - \big[y^2 + (z - z_M)^2 \big] \Big\} + \frac{1}{2} \Big[\Big\{ (\delta x)^2 (1+\epsilon^2) - \big[y^2 + (z - z_M)^2 \big] \Big\}^2 - 4 \Big\{ \epsilon^2 (\delta \cdot x)^4 - (\delta \cdot x)^2 y^2 - \epsilon^2 (\delta x)^2 \cdot (z - z_M)^2 \Big\} \Big]^{1/2} \tag{C-18}$$

and $\kappa'^{*} = \kappa'$ when $\kappa' > 0$, otherwise $\kappa'^{*} = 0$

$$K' = -\frac{1}{2}\left\{(1+\epsilon^2)(\delta\cdot x)^2 - \left[y^2 + (z+z_M)^2\right]\right\} + \frac{1}{2}\Big[\Big\{(\delta\cdot x)^2 (1+\epsilon^2) - \left[y^2 + (z+z_M)^2\right]\Big\}^2 - 4\Big\{\epsilon^2(\delta\cdot x)^4 - (\delta\cdot x)^2 y^2 - \epsilon^2(\delta\cdot x)^2(z+z_M)^2\Big\}\Big]^{1/2} \qquad \text{(C-19)}$$

The neutral gas temperature increase caused by heating of the neutral gas by the electrons and ions within a SAR-arc is now determined from

$$\Delta T_n(y,z) = \left(T_B(z)^{3/2} + \phi(y,z)\right)^{2/3} - T_B(z) \qquad \text{(C-20)}$$

where $T_B(Z)$ is the basic thermospheric temperature profile given in Appendix A. Equation (C-17) requires only one numerical integration which takes less than one second on the IBM - 360 system.

APPENDIX D

DETAILS OF THE INSTRUMENTS AND THE AIRGLOW OBSERVATORY

The details of the Fabry-Perot interferometer were presented in Chapter 7 where the basic dimensions and equipment requirements necessary for doppler temperature measurements in the normal 6300 Å nightglow were established. In this appendix, the detailed mechanical, electrical, and auxiliary supporting equipment for the Fabry-Perot interferometer and airglow photometer are discussed.

D-1 MECHANICAL LAYOUT OF THE FABRY-PEROT INTERFEROMETER

The etalon plates for the Fabry-Perot interferometer are made of fused quartz. They are 6" in diameter, 1 1/2" thick, and have a 30 minute wedge angle on the uncoated side in order to displace the ghost images which form in the interferometer. The plates are coated with 5 alternate layers of ZnS and cryolite over 5 1/4" of the central diameter of the plates giving a reflectivity of 87% at 6300 Å; this corresponds to a reflective finesse of 23. The outer edges of the plates are uncoated and the plates are separated by a 1 cm precision quartz spacer designed specifically for the etalon plates by Optical Works, Ltd. The spacer consists of a quartz ring having 3 raised 1/8" diameter supports, with rounded tips, and they are located 120° apart and are polished flat to within $\lambda/10$ of the desired spacing.

The plates and spacer are mounted horizontally in an etalon chamber, similar to the one designed by Nilson and Shepherd (1961) and shown in Fig. 71. The central axis of the plates points toward the vertical for night sky measurements. The Fabry-Perot etalon consists of two chambers: the

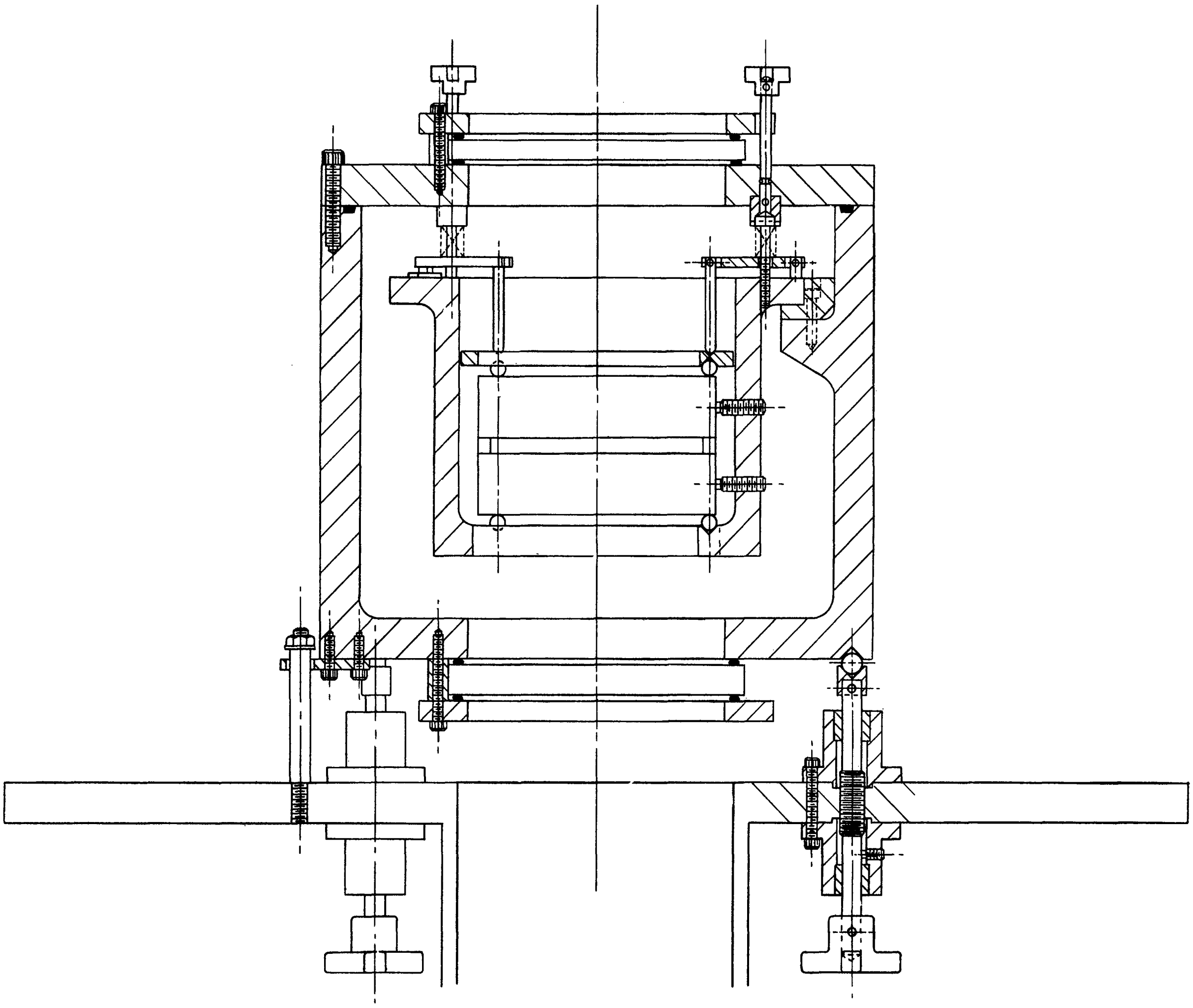

Fig. 71. The Fabry-Perot interferometer etalon chamber and etalon plate holder.

inner plate holder which supports the plates and has the mechanism required to bring the plates into adjustment, and an outer pressure chamber which contains the gas used for scanning the instrument and also provides for a stable thermal environment. The details of the etalon chamber are shown in Fig. 71; for a detailed discussion of the arrangement see Nilson (1960), Nilson and Shepherd (1961), Turgeon (1961), Turgeon and Shepherd (1962), Shepherd (1967). The plates are mounted in a horizontal position and calculations indicated that a differential sagging of $\lambda/80$ between the center and outer edges of the plates would occur due to the weight of the etalon plates alone. However, this did not appear to be objectionable when using 5 layers of dielectric material for the reflective plate coatings because it would only give a defect finesse of 40, whereas the reflective finesse would dominate at 23. If much higher resolution is required, it may be necessary to mount the plates vertically, on edge, in order to reduce the effect of sagging. When the plates were installed in the etalon and brought into adjustment, it was noticed that the fringes appeared to grow in size as one moved his eye from the center of the etalon plates to the edge. This effect, studied in Chapter 7, is due to a nonuniform deposit of dielectric coatings upon the plates, which has a much greater influence on the instrumental broadening that that due to the relatively small plate sagging. Therefore, no apparent advantage would be gained by mounting the plates on edge, unless a more uniform dielectric coating could be applied.

The etalon which was constructed is very stable maintaining the plates in adjustment for weeks at a time and the etalon chamber is pressure tight, holding pressure for several days.

A schematic diagram of the over-all arrangement of the Fabry-Perot interferometer is shown in Fig. 72. The etalon chamber is supported on three large steel balls mounted on adjustable screws which extend through the support base of the tower. The support plate rests on a welded steel tower which in turn is fastened to the 1 1/2" thick armor plate top of a 1600 lb welding table. The upper and lower etalon windows are made of 3/4" thick ground glass having an anti-reflective coating applied for maximum transmission at 6300 Å. Below the lower etalon window an objective lens is mounted in the support plate which focuses the fringe pattern through a 7" inside diameter aluminum tube, properly baffled to eliminate reflections off the tube walls, to an aperture located in the focal plane of the lens. The objective lens is a corrected achromat having a focal length of 121.9 cm. Because the Fabry-Perot interferometer was to be mounted in a trailer-van which has a ceiling of only 7 ft., it was necessary to fold the instrument through 90° by a front surface mirror, having a surface flatness of $\lambda/4$, mounted at 45° inside the 7" inside diameter aluminum light tube. This not only provided the necessary space to mount the photomultiplier and thermo-electric cooler but also provided a convenient arrangement for the optical alignment of the various components. At the end of the tube, but before the aperture plate, an access hole was constructed to allow the insertion of a diffuse screen which would direct the light from a low pressure mercury source through the etalon, from below, for adjustment purposes. After the

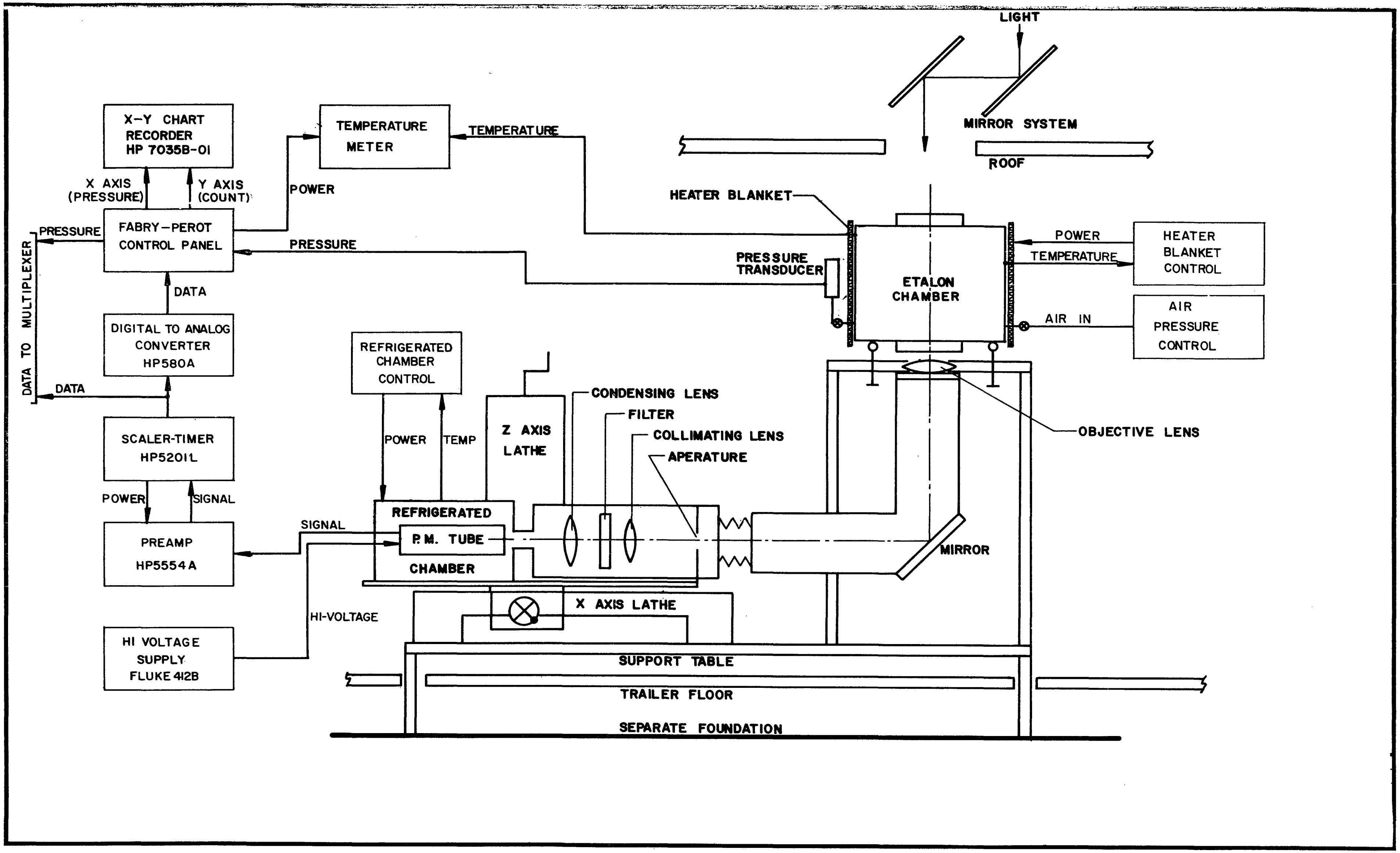

FP-1

Fig. 72. Schematic drawing of the Fabry-Perot interferometer and associated system components.

etalon is adjusted, the diffuse screen is removed and the access hole is clamped shut and covered with a dark cloth to ensure a light tight environment. The optical box is supported on a lathe which rests upon a 1600 lb support table and it is capable of controlled motion in the three axes. The optical box actually rests upon three adjustable screws protruding upward from a rigid support plate which is securely fastened to the vertical axis of the lathe. These adjustable screws are necessary to focus the light from the aperture upon the 1/10" effective aperture of the ITT FW-130 photomultiplier. Within the optical box is a circular aperture plate upon which the fringe pattern is focussed by the objective lens and part of the fringe pattern is transmitted by a 11/64" aperture hole located on the axis of the plate. The aperture plate fits into a precisely machined groove allowing easy removal and replacement, ensuring precise alignment upon re-insertion. The light passing through the aperture is collimated by a 2" achromat having a 7.2" focal length, and then passes through a 4.2Å half-width interference filter which has a transmission peak of 45% at 6302 Å. The peak transmission was centered slightly off the emission line in order to allow for a drift toward shorter wavelengths with age. The interference filter separates out the unwanted orders of the Fabry-Perot interferometer and transmits only the orders under the pass band of the filter to the photomultiplier tube. The light transmitted through the interference filter is condensed by a 2" diameter achromat, with a 3.8" focal length, to the 1/10" diameter effective aperture of the ITT-FW-130 photomultiplier. The lenses and interference filter are placed in adjustable mounts to allow an alignment of the optical system.

An air-cooled thermoelectric cooler, Products for Research model 105TS, houses the photomultiplier which is located directly behind the optical box. It also rests upon the support plate and is positioned in the lateral direction by adjustable screws. A rubber seal is also used to provide a light tight coupling between the cooler and optical box. The ITT-FW-130 photomultiplier, having an S-20 response with a 1/10" effective photocathode aperture, is mounted in the thermoelectric cooler and maintained at a temperature of -15°C which reduces the dark noise of the photomultiplier from 80-90 counts per second at room temperature to 1-2 counts per second. The low dark count rate is particularly important for measurements on the normal 6300 Å emission line from the night sky.

D-2 ELECTRONIC SYSTEM

The high voltage for the photomultiplier is supplied by a John Fluke, Model 412B, high voltage power supply. The voltage is distributed to the dynodes through a standard pulse counting dynode resistance chain and the photocathode is maintained at a high negative voltage. The anode runs at ground potential and the output pulses are fed directly into the preamplifier through a short lead in order to control the stray capacitance of the output circuit which tends to degrade the pulse signals. Only the pulse counting mode of operation is used in this system because the major nightglow emissions are relatively weak and the signal cannot be handled by a DC system. The output of the photomultiplier is fed into a HP model 5544 charge sensitive pre-amp which has a basic time constant of 5 μs. The preamplifier provides a certain amount of pulse shaping and count rates up to 20 KHZ can be handled without danger of a pulse pile up. For higher count rates the pre-amplifier can be used together with a linear amplifier delay line combination allowing count rates of several MHz. The output of the preamplifier provides shaped pulses, with a 0 to 5 volt amplitude, which are fed into the pulse height analyzer of a HP5201 scalar-timer. The counter will count for a pre-set time and display all pulses above a given threshold voltage set by the lower window of the analyzer. After the display, a new counting cycle begins and the process is automatically repeated. The digital output of the scalar timer is fed to a HP-model 580-A D/A converter which provides an analog readout of the data on an X-Y plotter. In addition, the digital output is also fed to a data multiplexer system, to be described in a later section, for recording on paper tape.

The pressure within the etalon is measured by a Stratham model PG731TC pressure transducer attached directly to the Fabry-Perot etalon chamber. The pressure sensor is a strain gauge element excited by a 15 V DC power supply, and the output of the sensor is amplified and fed into the x-axis of the x-y plotter. The pressure transducer was calibrated against a Baratron model 77, pressure gauge and the calibration curve showed a slight nonlinearity which had to be accounted for in the data reduction process. The output of the pressure transducer is also digitized, by a Non-Linear Systems model X-2 digital voltmeter, and fed into the data multiplexer.

D-3 AUXILIARY EQUIPMENT

D-3-1 PRESSURE SCAN SYSTEM

As discussed earlier a wavelength scan of the Fabry-Perot interferometer can be made by varying the index of refraction of the gas. The index of refraction of the gas μ is proportional to the density which can be varied by a pressure change at a constant temperature. The change of wave-number of the radiation is related to the pressure change by $\frac{d\sigma}{\sigma} = -c\,\frac{dp}{p}$ where c is a constant for the particular gas in use. Two separate pressure scanning systems have been installed for use with the Fabry-Perot interferometer: The first scanning system uses a Honeywell time pattern transmitter model Y802A3A which pressurizes the etalon chamber in a manner prescribed by a machined cam rotating at 0.083 RPM. A lever arm following the cam regulates a bellows actuated valve which allows the gas to flow into the chamber at the prescribed rate. The linearity and accuracy of the pressure scan is dependent upon the accuracy with which the cam is cut. However, as long as the pressure is recorded by the pressure transducer, defining the pressure interval for which the photomultiplier counts were obtained, the data can be satisfactorily reduced. The value of the time pattern transmitter lies with its capability of maintaining a constant pressure within the etalon chamber for long periods of time. The cam of the time pattern transmitter can be adjusted to fall on a fringe peak and hold that position while an optical alignment of the instrument is made. Also on the night sky, the 6300 Å fringe peak can be located and held while the mirror system performs a meridian or almucanter scan, thus allowing the Fabry-Perot interferometer to act as an extremely narrow interference filter photometer.

The second scanning system is the one ordinarily used in scanning the Fabry-Perot interferometer and consists of a high precision needle valve, Nupro model SS-4-S, which is adjusted to give a supersonic flow into the etalon chamber. Supersonic flow results in a linear mass flow rate into the chamber which in turn gives a linear pressure scan. A pressure regulator on a dry nitrogen bottle is used to hold the inlet pressure of the needle valve above the critical ratio for supersonic flow. At the end of the scan the etalon is exhausted through the release valve on the time pattern transmitter.

D-3-2 TEMPERATURE CONTROL SYSTEM

The Fabry-Perot etalon, shown in Fig. 71, consists of an outer pressure chamber and inner plate holder. The inner plate holder rests upon three supporting ledges on the inner walls of the pressure chamber but is separated from the ledges by thermal insulating pads. Thus, the etalon plate holder is thermally insulated from the outer chamber with convective heat transfer of the etalon gas being the only thermal contact between the two components. A heater, consisting of fine resistance wires wound within a fiberglass and fiber wool insulating blanket, is wrapped around the outer pressure chamber and maintains the outer surface at a constant temperature. A thermistor sensor is mounted on the outer wall of the pressure chamber and is used together with an Athena, model 51, proportional controller to maintain the temperature to an accuracy of 0.1°F. Due to the large heat capacity of the etalon chamber, with 1" thick walls, the temperature of the inner wall of the pressure chamber is constant and the results of many calibration scans show that the etalon chamber is thermally stable during a scan.

D-3-3 CALIBRATION SOURCES

A mercury 198 single isotope electrodeless lamp with a water jacket was obtained from the Opthos Corp. and is used as a calibration light source because its 5461 Å line is known to be gaussian with a .020 cm^{-1} half-width when the coolant fluid is maintained at 39°F. The lamp is excited by a 100 MHz oscillator and the light from the lamp is directed to a diffuse screen located over the etalon chamber. Because the airglow station will be located in an isolated area, it was necessary to obtain a small camping refrigerator in order to maintain the lamp coolant at a constant temperature. Ethalyne glycol is used as a coolant and it is circulated through the outer jacket of the lamp by a small circulating pump.

A Helium-Neon gas laser is also used as a calibrating source since its line at 6328 Å lies close to the 6300 Å atomic oxygen transition line. The laser beam is directed to fall upon a frosted light globe located above the etalon and due to multiple scattering, the laser light travels around the entire periphery of the globe providing a uniformly glowing surface. The multiple scattering within the frosted globe destroys the laser coherence, thus providing a single frequency non-coherent narrow line source at 6328 Å. The laser, however, does have some intensity fluctuations but at a rapid enough frequency as to not greatly affect a slow scan. In addition, because the laser is not of a single frequency variety, there are several modes under a gaussian envelope; however, the resulting line appears to be quite narrow and is used for rapid evaluation of the instrument adjustment.

D-4 GENERAL ADJUSTMENT PROCEDURE OF THE FABRY-PEROT INTERFEROMETER

The mounting of the optical box on a lathe, with motion in the three axes, enables an easy adjustment of the entire optical box to the fringe pattern formed by the etalon. First, the etalon chamber is aligned so that the access hole in the roof fills the field of view of the etalon when viewed from the focal plane of the objective lens. Then the cover of the optical box is removed and a mirror is used to adjust the box so that the aperture plate falls in the center of the image of the access hole. After this alignment has been accomplished a diffuse screen is placed above the etalon chamber and a low pressure mercury source is used to form a set of fringes in the focal plane of the objective lens and upon a frosted glass screen placed in the machined groove where the aperture plate is installed. The screen has the central hole of the aperture marked on it and by moving the lathe bed and the 45° mirror, the center fringe of the fringe pattern can be centered on the aperture hole. Next a laser beam is used to align the collimating and condensing lenses so that the aperture, collimating lens, interference filter, and condensing lens have a common axis. Then a fringe pattern of the mercury source is projected upon a screen located in the expected position of the photomultiplier which is in the thermoelectric cooler and brought into focus by axially adjusting the collimating and condensing lenses. The screen has a cross hair showing the expected position of the 1/10" effective aperture of the photomultiplier and the central spot of the fringe pattern is aligned to the cross hairs by moving the adjusting screws on the optical box and thermoelectric cooler. In this manner, the instrument is coarsely aligned so that the energy passing through the aperture falls in the immediate vicinity of the photomultiplier effective aperture. The final adjustment is made by using the time pattern transmitter to hold the pressure at a fringe peak and with high voltage on the photomultiplier tube adjusting the optical box vertically and thermoelectric cooler laterally, by means of the adjusting screws, until the maximum count rate is registered on the scalar counter. This method is quite satisfactory and allows a rapid optical alignment of the entire Fabry-Perot interferometer.

D-5 MIRROR SCANNING SYSTEM

Two identical mirror scanning systems were built for the Michigan Airglow Observatory; one for the Fabry-Perot interferometer, and one for the filter photometer. The mirror system is similar to the one designed by Turgeon (1961), Turgeon and Shepherd (1962) which enables the operator to point the instrument to any position in the sky. It utilizes two 11" diameter front surface mirrors; one at 45° to the base and a second at 45° to a plane perpendicular to the base. The mirror system is supported on a base plate which rests upon the roof of the airglow observatory. A 6 3/4", 3/8" thick steel tube extends through the base plate and it is aligned directly over the access hole in the roof of the airglow observatory leading to the instruments. At the top of the tube, a Waydon 7" I.D., 3/8" thick bearing is mounted in order to support the mirror housings. An identical bearing is used for the mirror which rotates parallel to the base and these two bearings give a very smooth motion during the scan. The whole mirror assembly rotates about an axis perpendicular to the base plate and the second mirror rotates about an axis parallel to the base.

The mirrors are driven by two Slo-Syn model SS5U-1008 variable speed stepping motors coupled to two 10" diameter Boston Gears NB-200 having 200 teeth around its periphery. The position readout is obtained by a 10 turn potentiometer, IRC type 7500 with gears directly meshed to the main gear drive. Thus, when an azimuth and elevation angle is dialed-in on the control panel, the position of the mirror system as determined by the potentiometers is compared to the dialed in position, the error signal is amplified, and a Slo-Syn translator drives the stepping motor until a zero error signal is reached indicating that the mirror system is pointing in the desired direction.

The electrical control system has been designed so that meridional and almucanter scans can be made with the photometer mirror system. The Fabry Perot mirror system can be set to a separate position or slaved to the photometer mirror system. Thus, a Fabry Perot measurement can be made at one position while the photometer is operating in the scan mode or both systems can be pointing to the same direction where the photometer can be used to monitor intensity fluctuations during a Fabry Perot scan. This versatility was incorporated into the mirror scanning system in order to be able to search effectively for the SAR-arc. The system is flexible enough so that any prescribed photometer scan mode can be built up on an electronic card and inserted into the control panel.

D-6 AIRGLOW PHOTOMETER

The airglow photometer in use at the University of Michigan Airglow Observatory is of the turret type designed by Purdy, Megill, and Roach (1961) and was built by ESSA at Boulder, Colorado, The basic photometer was modified to make room for six interference filters, instead of the usual four, and a variable speed reversible stepping motor was installed, instead of using the standard continuous speed motor drive. These modifications were necessary to meet our requirements and make the instrument more versatile.

Basically the photometer consists of two turret wheels driven by a Geneva drive mechanism which first positions an interference filter in the lower turret wheel over a telescope and this position is held while the upper turret wheel alternately positions a dark reference, standard light source, and sky opening over the interference filter and telescope. When this process is completed a new filter in the lower turret is moved into position over the telescope and the upper turret then repeats this cycle. A schematic diagram of the cycling sequence is shown in Fig.73. This process is run continuously giving a dark count, standard calibration signal, and sky reading for each filter.

The standard light is a carbon-14 activated, phosphor light source (Kulharni and Sanders, 1964, Blacker and Gadsden 1966) which provides a light of known intensity in the 4000 Å to 8000 Å spectral range. This source was calibrated against a primary standard at the Fritz Peak Observatory and its intensity distribution is shown in Fig. 74. It is desirable to recalibrate the standard light source and color filters every six months, since their properties change somewhat with age. In addition, these components should be maintained in a temperature and humidity controlled environment because their properties are influenced by both.

A block diagram of the airglow photometer system is shown in Fig. 75. The light signal transmitted through the interference filter is collected by a telescope which has a 5° field of view and is focussed upon the photocathode of an EMI-9558-A photomultiplier. The photocathode of this tube has a

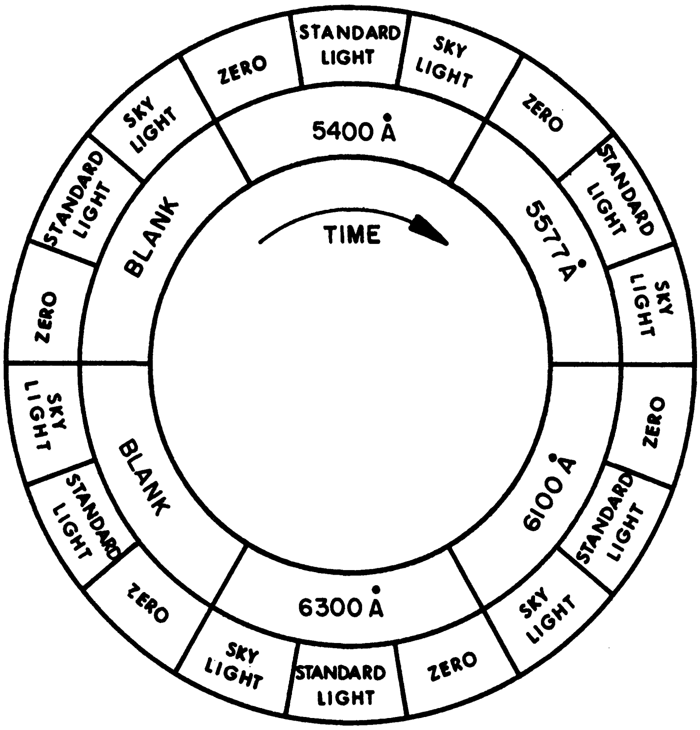

Fig. 73. Cycling sequence of the turret photometer.

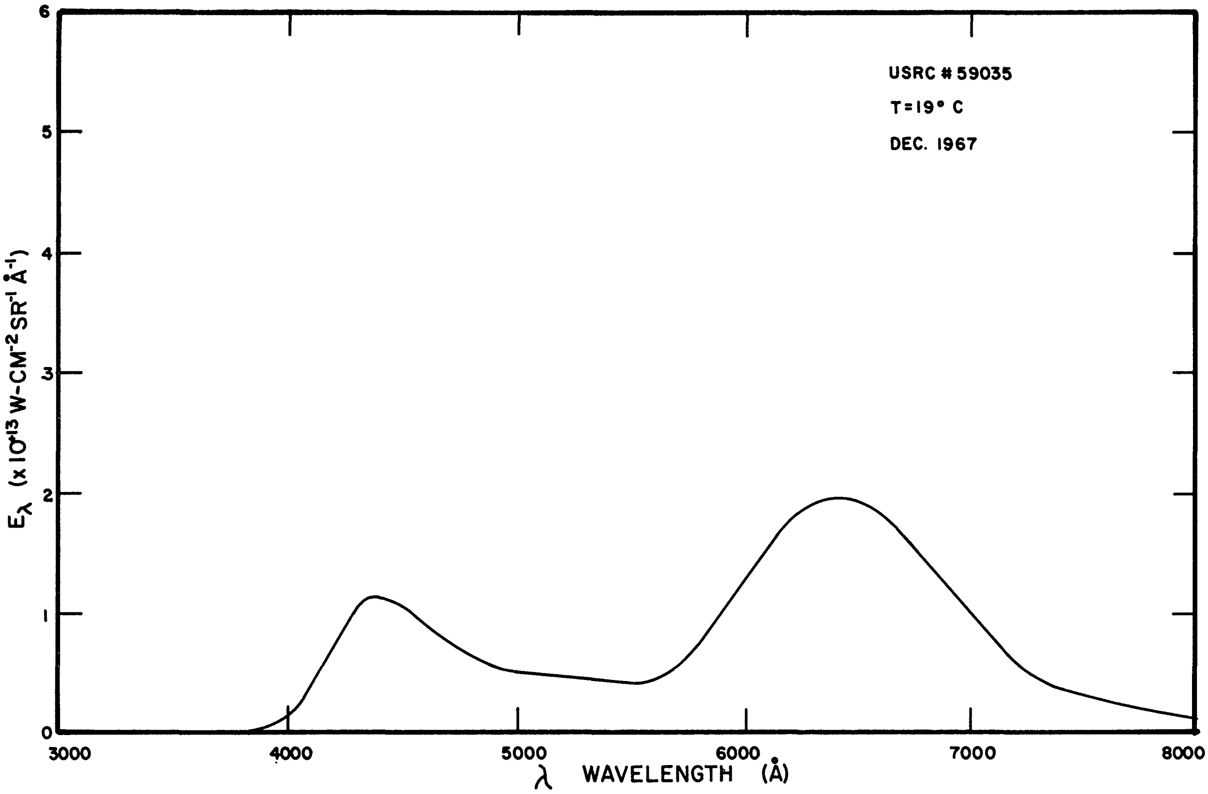

Fig. 74. Spectral characteristics of the photometer calibration light.

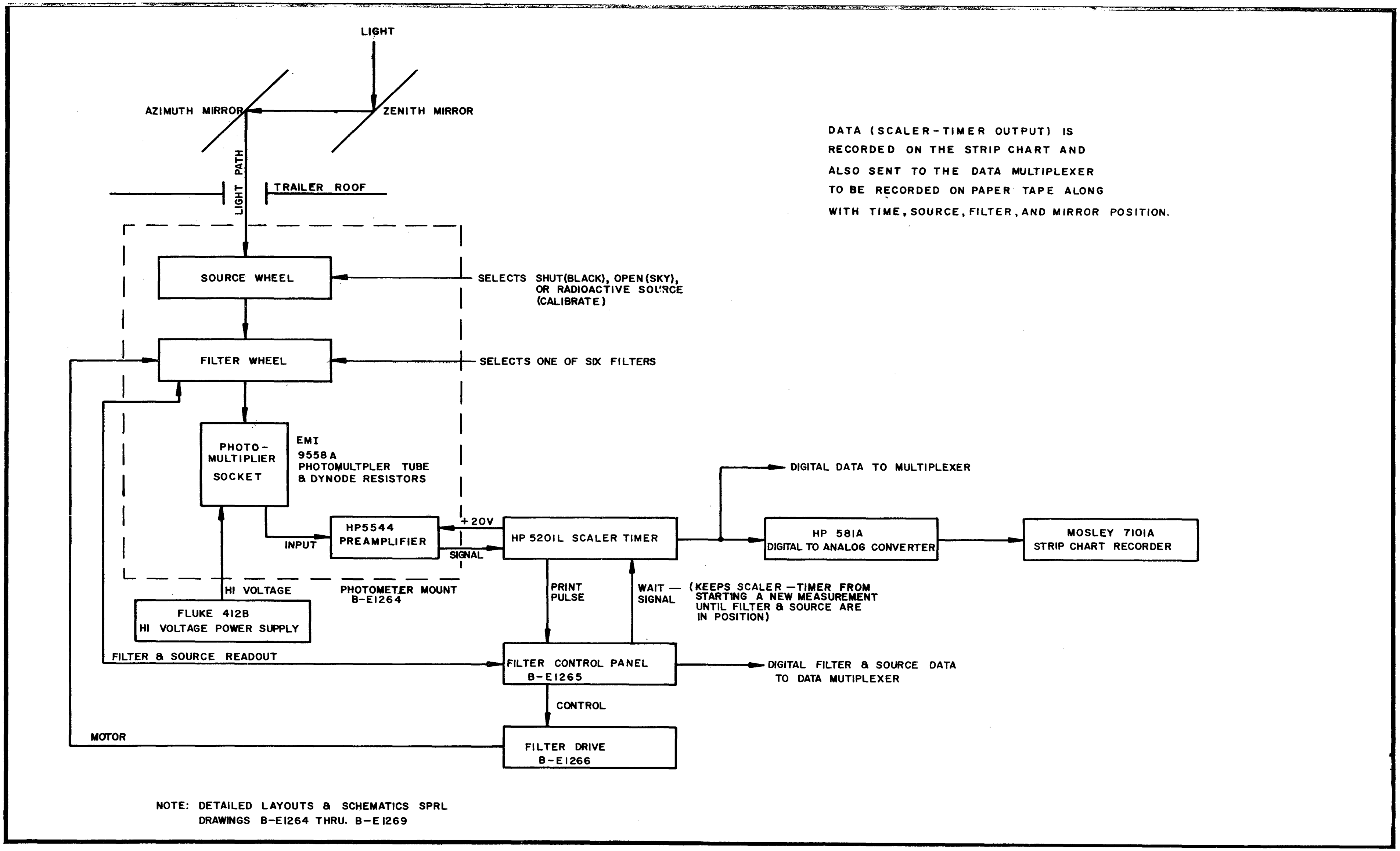

DATA (SCALER-TIMER OUTPUT) IS RECORDED ON THE STRIP CHART AND ALSO SENT TO THE DATA MULTIPLEXER TO BE RECORDED ON PAPER TAPE ALONG WITH TIME, SOURCE, FILTER, AND MIRROR POSITION.

NOTE: DETAILED LAYOUTS & SCHEMATICS SPRL DRAWINGS B-E1264 THRU. B-E1269

PS-1

Fig. 75. Block diagram of the turret photometer.

S-20 spectral response.

Pulse counting is also used for the airglow photometer because the major nightglow emissions are relatively weak. Therefore, an electronic system, identical to the one used for the Fabry-Perot interferometer was used with this system. This includes the high voltage power supply, preamplifier, scalar-timer, and D/A converter. The output signal was recorded on a strip chart recorder and the digital output of the scalar timer was also fed into the data multiplexer for recording on paper tape. The filter position and the type of reading being made, dark, source, or sky, are also recorded on paper tape and visually displayed on the photometer control panel. In operation, the scalar timer will count the number of pulses for a pre-set integration time and display the total number of counts. The total number of counts will be shown on the strip chart recorded and punched on paper tape.

D-7 DIGITAL SYSTEM

The Fabry Perot interferometer fringe profile is recorded on an X-Y plotter and the intensity readings for the various interference filters of the airglow photometer are recorded on a strip chart recorder. A digital system, consisting of an analog data multiplexer, digital data multiplexer, a punch driver, and a 60 cps tape punch, was also constructed which provides a punched tape record suitable for computer processing. The system has a Non-Linear Systems model X-2 digital voltmeter for digitizing the auxiliary information from the photometer, Fabry Perot interferomter, and mirror system and also a Chrono-Log digital clock, model 2500-B, giving time in hours and minutes. The digital multiplexer selects the data from two HP 5201-L scalar-timers, the

NLS X-2 integrating digital voltmeter, the 24 hour digital clock, and the photometer filter positioning system and packs this data in BCD form on a punched paper tape. All data is recorded on 8 level punched tape in the format shown in Fig. 76 with two binary coded decimal digits on each taped line. The beginning of each data record is flagged by a delete code and the time to select and record is 24.5 milliseconds per byte plus any waiting time for DVM integration. The recording cycle is generally triggered by the Fabry Perot scalar-timer at the end of a prescribed counting cycle.

A great deal of versatility is incorporated into the system allowing several modes of operation. The data from the photometer and Fabry Perot interferometer can be recorded independently or in a coupled mode and various selected data can be included or deleted depending upon the data requirements. The maximum time to complete any data logging sequence which includes all inputs is 1.34 seconds.

D-8 STATION

The Fabry Perot interferometer and airglow photometer are housed in a trailer van. The trailer was obtained from U. S. Army surplus and is 40 feet long, 7 feet wide, and 8 feet high. The trailer has 3" of thermal insulation between all outside walls, the ceiling, and the floor, making it easy to provide a controlled environment for the equipment. The trailer was partitioned into three separate rooms, the forward room for the photometer, the middle room for the Fabry Perot interferometer, and the rear room for the electronics. Electric baseboard heating was installed in the three rooms, each individually

PUNCHED TAPE DATA FORMAT AIRGLOW FACILITY DATA MULTIPLEXER

ALL DATA IS BCD CODED EXCEPT FLAGS. ALL EIGHT LEVELS ARE USED.

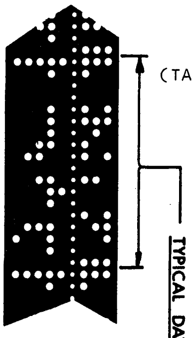

TYPICAL DATA POINT

RECORD ID NO.: 000
TIME: 15:17
PHOTOMETER: SOURCE 1
FILTER 4
COUNT 123465
MIRROR: AZMUTH 003.6
ZENITH 181.0
FABRY-PEROT: COUNT 057391
PRESSURE 1.007 PSIG

BYTE (TAPE LINE)	BINARY BIT NUMBER 8 7 6 5	4 3 2 1	DATA DESCRIPTION AND SCALE FACTORS
1	1 1 1 1 ALWAYS PUNCHED ALL ONES	1 1 1 1	DATA BLOCK BEGIN FLAG
2	2 1 2 1 SKIP SORS	8 4 2 1 FILTER	**DATA SKIP FLAG, PHOTOMETER SOURCE, PHOTOMETER FILTER
3	X X X X	8 4 2 1 X100	BITS 8-5 UNASSIGNED BITS 4-1 IDENTIFICATION NUMBER
4	8 4 2 1 X10	8 4 2 1 X1	IDENTIFICATION NUMBER THUMBWHEEL SWITCHES
5	8 4 2 1 X10	8 4 2 1 X1	HOUR DIGITAL CLOCK
6	8 4 2 1 X10	8 4 2 1 X1	MINUTE DIGITAL CLOCK
7	8 4 2 1 X100000	8 4 2 1 X10000	PHOTOMETER COUNT SCALER-TIMER OUTPUT
8	8 4 2 1 X1000	8 4 2 1 X100	
9*	8 4 2 1 X10	8 4 2 1 X1	
10	S 4 2 1 X1000	8 4 2 1 X100	MIRROR AZIMUTH ANGLE DVM SIGN AND DATA OUTPUT DECI-DEGREES
11	8 4 2 1 X10	8 4 2 1 X1	
12	S 4 2 1 X1000	8 4 2 1 X100	MIRROR ZENITH ANGLE DVM SIGN AND DATA OUTPUT DECI-DEGREES
13*	8 4 2 1 X10	8 4 2 1 X1	
14	8 4 2 1 X100000	8 4 2 1 X10000	FABRY-PEROT COUNT SCALER-TIMER OUTPUT
15	8 4 2 1 X1000	8 4 2 1 X100	
16	8 4 2 1 X10	8 4 2 1 X1	
17	S 4 2 1 X1000	8 4 2 1 X100	ETALON CHAMBER PRESSURE DVM SIGN AND DATA OUTPUT MILLI-PSIG
18*	8 4 2 1 X10	8 4 2 1 X1	

NOTES: *DATA BLOCK LENGTH MAY BE 9, 13, OR 18 BYTES. THE COMPUTER MUST LOOK FOR THE DATA BLOCK BEGIN FLAG.

**THE DATA SKIP FLAG INDICATES CERTAIN DATA SHOULD BE IGNORED.
1 INDICATES MIRROR AZIMUTH ANGLE.
2 INDICATES MIRROR ZENITH ANGLE.

SKIPPING MIRROR ANGLE DATA ENABLES A FASTER DATA LOGGING RATE SINCE THE DATA MULTIPLEXER AND PUNCH DO NOT HAVE TO WAIT FOR THE DIGITAL VOLTMETER INTEGRATION TIME.

TO REPEAT: ALL CHARACTERS ARE LEGAL BCD EXCEPT FLAGS.
ALL EIGHT LEVELS ARE USED.
DATA BLOCK LENGTH IS DETERMINED ONLY BY LOCATION OF THE DATA BLOCK BEGIN FLAG.

K&E 10 8184 11-47

Fig. 76. Digital tape format for the airglow observatory.

controlled by separate thermostats and 1-1/2 ton air-conditioner units were installed in both the interferometer room and electronics room. The photometer and interferometer rooms were made light tight and painted completely black in order to eliminate stray light effects. Power (220 volt, 150 amp) is provided to the trailer and electric power outlet strips are installed along the walls of each room. The photometer and interferometer are positioned below access holes to the roof, where the light from the night sky is directed down the port to the instruments from mirror scanning systems mounted on the roof. The room layout of the trailer is shown in Fig. 77. Incandescent lights are installed in all rooms and four flourescent lights are also installed in the control room. The control room has space available for storage filing cabinets, a work bench, a paper filing cabinet, desk, four electronic racks, and a nitrogen bottle rack for the Fabry Perot pressure system. There is also room for several other instruments when they become available.

The Fabry Perot interferometer is mounted on a 1600 lb steel table located in the middle room of the trailer. The table is supported by three large steel tripod jacks which rest upon the ground beneath the trailer and extend upward through holes in the trailer floor. In this manner, the table is lifted from the trailer floor and no floor motion is transferred to the instrument. Rubber gaskets are used to seal the opening through which the jacks extend, thus providing a weather seal and light-tight environment.

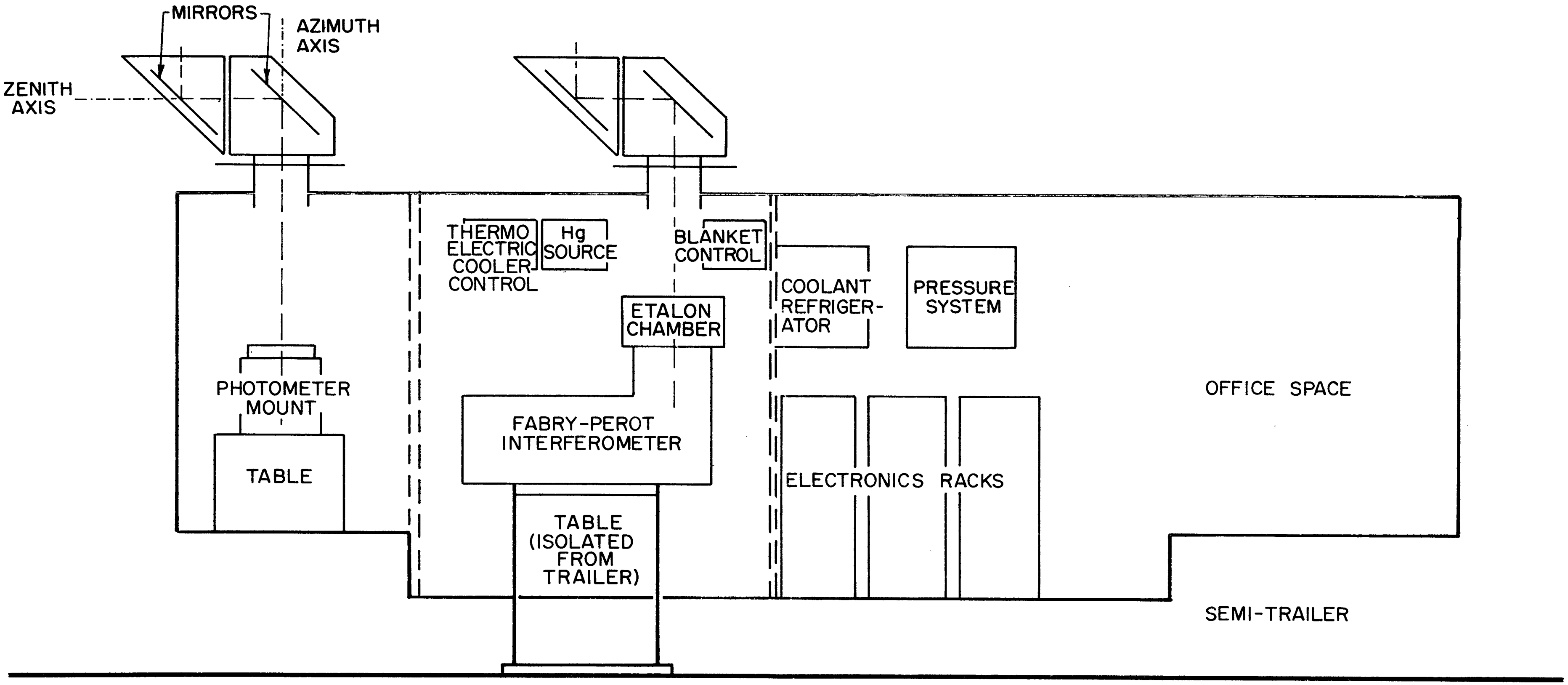

Fig. 77. Schematic diagram of the University of Michigan Airglow Observatory.

UNIVERSITY OF MICHIGAN
3 9015 03525 1191